Anisotropy in Granite and the Effects of Tunnel Excavation in a Controlled Source Shear-Wave Experiment

by

Gordon Murray Holmes

B.Sc.(Hons) Geology and Physics 1991
Queen's University, Kingston, Ontario, Canada

Dissertation submitted for the degree of Doctor of Philosophy
Department of Geology and Geophysics
University of Edinburgh
June 1995

I hereby declare that this dissertation has been composed by myself and that the work described is entirely my own unless explicitly stated in the text.

Gordon M. Holmes

The Earth? I'm going to blow it up. It obstructs my view of Venus.

-Marvin the Martian

Abstract

Observations of shear-wave splitting in signals from a controlled seismic source have never previously been used to parameterize a rockmass in a mine environment. In developing the necessary processing and modelling techniques and interpreting the final results, I demonstrate the usefulness of such a controlled-source shear-wave experiment to parameterize non-destructively a granite rockmass *in situ* and monitor non-destructively the effects of excavation.

A Schmidt Hammer is used to pulse the free end of a nylon rod inserted down a 40cm borehole to create the seismic signals. I show the resulting seismograms to be highly reproducible, with cross-correlation coefficients of 0.90 or greater resulting for repeated raypaths, and that the shear-wave motion produced matches that due to a directional point source in an isotropic medium. I demonstrate that the use of multiple source orientations of a known source for repeated raypaths greatly improves the reliability of picking shear-wave polarizations and time delays. Thus the use of multiple source orientations of a known source is highly desirable in any controlled source shear-wave experiment.

I demonstrate the use of cross-correlation to be effective in detecting temporal changes and that particle motions need only be displayed on the planes perpendicular to the source-receiver directions when interpreting changes in shear-wave particle motions, which is convenient for large datasets. I identify temporal changes due to the advancement of the zone of excavation disturbance, which suggests that Extensive-Dilatancy Anisotropy is at least partially responsible for the *in situ* anisotropy. An increase in the strength of anisotropy suggests that excavation creates an anisotropic fabric of dry cracks with orientations governed by either the *in situ* stress field or mineral alignment. These results suggest that shear waves may be used to remotely monitor a rockmass.

Inversion for the pattern of polarizations produces a best-fitting model to the observed polarizations of strike 023° and dip 35°, broadly agreeing with the orientation of strike 045° and dip 14° expected for Extensive-Dilatancy Anisotropy, and strike 024° and dip 25° expected for anisotropy due to the primary layering. Time delays are consistent with the *in situ* rockmass being intact.

Excavation adds scatter to the measured time delays. I show that, even when accounting for excavation effects, time delay values do not have an obvious pattern and cannot be explained by either extensive-dilatancy anisotropy throughout the rockmass, or the primary layering in part of the rockmass. This prevents a definitive conclusion to the cause of the *in situ* anisotropy.

Acknowledgements

"Then the Persians besieged Barce for nine months, digging mines leading to the walls, and making violent assaults. As for the mines, a smith discovered them by the means of a brazen shield, and this is how he found them: carrying the shield round the inner side of the walls, he smote it against the ground of the city; all other places where he smote it returned but a dull sound, but where the mines were the bronze of the shield range clear. Here the Barcaeans made a counter-mine and slew those Persians who were digging the earth. Thus the mines were discovered and the assaults were beaten off by the townsmen."

-Herodotus, Book 4, section 200 (circa 580 BC)
-first known account of the use of reflection seismology (Liner, 1992)

There is some amusing connection between this account of 'smoting the ground' around tunnels 2575 years ago and this thesis, but at 03:00am I just can't put my finger on it. Rather, I'll follow the advice of everyone who has read rough drafts of my dissertation and get to the point. Those of you who have read the rough drafts will appreciate this.

First and foremost I express my sincere gratitude to my supervisors, Professor Stuart Crampin and Professor R. Paul Young, for their expert guiding of my studies and criticism of my work. Without them, I would not have had the opportunity of studying at the University of Edinburgh. I also express my great appreciation to Dr. Ian G. Main, my second supervisor, for stimulating discussions, ideas, and supervision. I thank all those involved at the British Council and the Association of Commonwealth Universities for the funding and administration of my Commonwealth Scholarship to the United Kingdom.

I have benefited from an inordinate amount of collaboration with research groups. I hope those mentioned do not feel short-changed in the long lists of names. At the University of Edinburgh, I am also grateful to Dr. David C. Booth, Dr. Peter C. Leary, Dr. Xiang-Yang Li, Dr. Enru Liu, Dr. Colin MacBeth, Dr. Robert G. Pearce, and Dr.

Philip Wild for stimulating discussions on anisotropy, reviewing my work, and general help. To my fellow students at the British Geological Survey, Brian J. Baptie, Heng-Chang Dai, Dr. Gerhard Graham, Mark Higgins, Aphrodite Karnassopoulou, Dr. Yun Liu, Helen J. Rowlands, Colin P. Slater, Dr. Gareth S. Yardley, and Dr. Xinwu Zeng, I thank for you for your help and discussions, but mainly your friendship in valiant alas unsuccessful attempts to help me keep my sanity during the more stressful times. I also extend my sincere gratitude at the help and generosity of the British Geological Survey and all members of the Global Seismology Research Group.

I also express great gratitude to all members of the Keele University Applied Seismology and Rock Physics Laboratory past and present, particularly Dr. Stephen D. Falls, Dr. Andrew J. Feustel, Dr. Shawn C. Maxwell, for their continued support, teachings, and collaborations stemming back to my undergraduate days. I give special thanks to David S. Collins for his instrumental role in my experiment (no pun intended).

I thank all members of the Underground Research Laboratory who contributed to acquisition of my data. I give particular thanks to Dr. Derek M. Martin and Dr. Rod Read for their backing and funding of my experiment, and useful discussions.

Lastly, I thank the continuous support of my family and friends, including Alan Choi, Stephen A. Horne, Helen C. R. Jarratt, and Shane S. Sturrock.

Contents

Attached to Back Cover:
Holmes, G. M., Crampin, S., & Young, R. P., 1993, Preliminary analysis of the shear-wave splitting in granite at the Underground Research Laboratory, Manitoba, *Can. J. Expl. Geophys.*, **29**, 140-152.

1 Introduction

1.1 Introduction to Anisotropy

A rockmass is homogeneous when lithology does not vary with position. Homogeneity is therefore a question of scale. An igneous rockmass consists of discrete crystals, but when viewed on scales much larger than that of the grain sizes may appear homogeneous. Seismic homogeneity is also a question of scale. A sandstone rockmass may consist of alternating layers of different lithologies. The elastic deformations within the layers due to seismic waves of wavelengths less than the minimum thicknesses of the layers will be distinctively different, and therefore the rockmass is not seismically homogeneous. For wavelengths much greater than thicknesses of the alternating layers, the deformation involves the combined elastic response of the two layers and the rockmass is seismically homogeneous.

Consider a homogeneous rockmass. The rockmass is seismically isotropic if seismic properties do not vary with direction. In such cases there exist two types of seismic body wave. The faster wave is the *compressional wave* or *P-wave* where particle motion within the rockmass is parallel to the propagation direction. The slower wave is the *transverse wave* or *shear-wave*, where particle motion is orthogonal to the propagation direction.

The rockmass is seismically anisotropic when seismic properties vary with direction. Seismic anisotropy is a three dimensional phenomenom. There is a three-dimensional pattern to the seismic wave propagation in an anisotropic rockmass. In an anisotropic medium, there exist three body waves. Similar to the *P-wave* is the *quasi P*-wave or *qP*-wave where particle motion is parallel or nearly parallel to the propagation direction. Rather than one body wave with shear-motion, there exist two shear waves. The faster shear-wave is the *quasi-shear-wave-1* or *qS1*-wave, and the slower wave *quasi-shear-wave-2* or *qS2*-wave. Particle motions for *qS1*- and *qS2*-waves are generally nearly orthogonal to the propagation direction and orthogonal

or nearly orthogonal to each other. Any consistent pattern that affects wave propagation in an otherwise isotropic rockmass will result in the rockmass being anisotropic. I will use the term *fabric* to refer to such a pattern while making no implications as to its physical cause. Since all rocks are formed under the influence of gravity, it is likely that all rockmasses are to some degree anisotropic for seismic wavelengths greater than grain size. Anisotropy is therefore probably the rule rather than the exception (Tilmann and Bennett, 1973; Crampin, 1985; Zeng, 1994; and many others).

A rough measure of the strength of the anisotropy is *percentage of shear-wave velocity anisotropy, A*, defined as:

$$A = \frac{V_{qS1} - V_{qS2}}{V_{qS1}} \times 100 \; ; \qquad (1.1)$$

where V_{qs1} and V_{qs2} are the velocities of *qS1*- and *qS2*-waves respectively (Crampin, 1989). Some authors use slightly different definitions of *percentage anisotropy*. The context of its use should inform the reader whether the value is expressed for a single seismic raypath or all raypaths or the maximum possible value of the medium.

A more precise and detailed geological interpretation is obtained by accounting for anisotropy when processing seismic data in traditional seismic methods (Mueller, 1992). Another approach is to invert detailed seismic measurements to parameterize the fabrics. Physical interpretations of properties of the rockmass, such as crack structure, may then be made from these values. This latter approach is that used in this dissertation.

It is difficult to determine variations of *qP*-, *qS1*-, and *qS2*-wave velocities in an anisotropic material to the accuracy needed to parameterize accurately an anisotropic fabric when the anisotropy is weak and the change in velocity with direction is small. However, the directions of particle motion of the *qS1*-wave, also called the *polarization,* is sensitive to the anisotropic fabric and is measurable even when the strength of the fabric is weak. The difference between the arrival times of the two quasi-shear-waves can also be determined because the polarization direction of *qS2*-wave is usually nearly orthogonal to *qS1*-wave. This time difference is called the *time delay*. The time delay increases as *qS1*- and *qS2*-waves propagate through the

medium. The phenomenom of time delays increasing with propagation is known as *shear-wave splitting* (Figure 1.1). Polarizations and the time delays are convenient measurements to invert because they are determined mainly by the fabrics and because of the extreme sensitivity of shear-waves to the fabrics (Crampin, 1978). This dissertation focuses on the measurement of the polarizations and times delay and the use of these data as a tool to parameterize the fabrics of a rockmass and then making the subsequent physical interpretation of the fabrics.

The remainder of this chapter summarizes the necessary background information on seismic anisotropy, including seismic theory, the display techniques for polarizations and time delays, and the modelling of seismic anisotropy. The terminology for describing anisotropy is that suggested by Crampin (1989).

Note that geologists use 'strike' and 'dip' to express orientations of planes, and 'trend' and 'plunge' for lines. In most geophysics literature, strike (or azimuth), and dip are used for both planes and lines. I will use strike and dip to describe the orientations of planes and azimuth and dip for lines. I will use the 'right-hand rule' when expressing the orientations of planes. The rule is that the strike is chosen so that

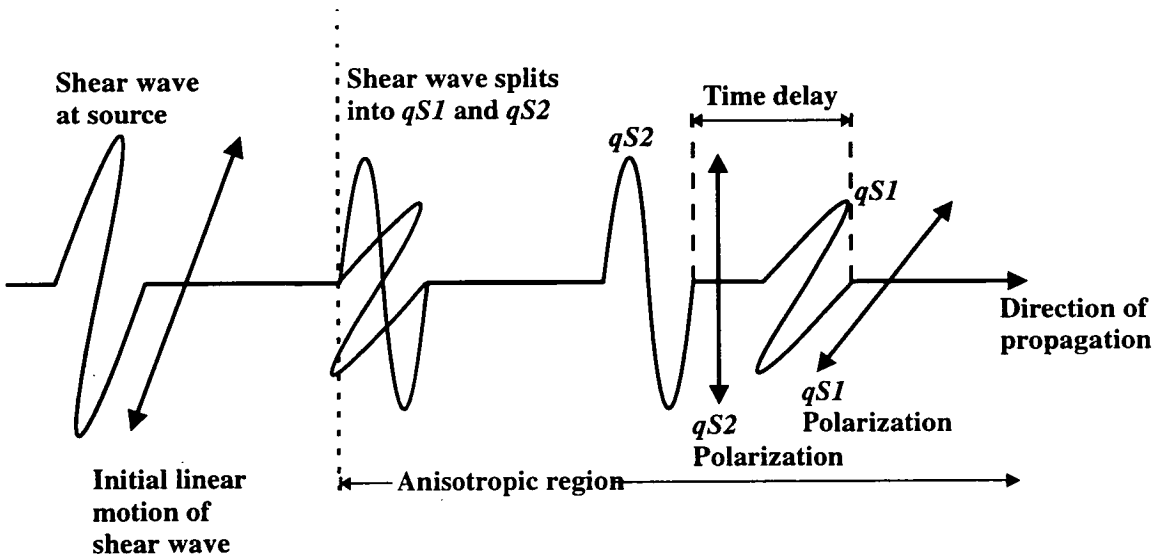

Figure 1.1a: A schematic illustration of shear-wave splitting. Initially there is only one shear-wave whose particle motion direction is determined by the source mechanism. The propagating shear wave enters an anisotropic region and immediately splits into *qS1*- and *qS2*-waves, with polarizations perpendicular or nearly perpendicular to each other. As the shear waves continue to propagate through the anisotropic region, the time delay between the two shear waves increases.

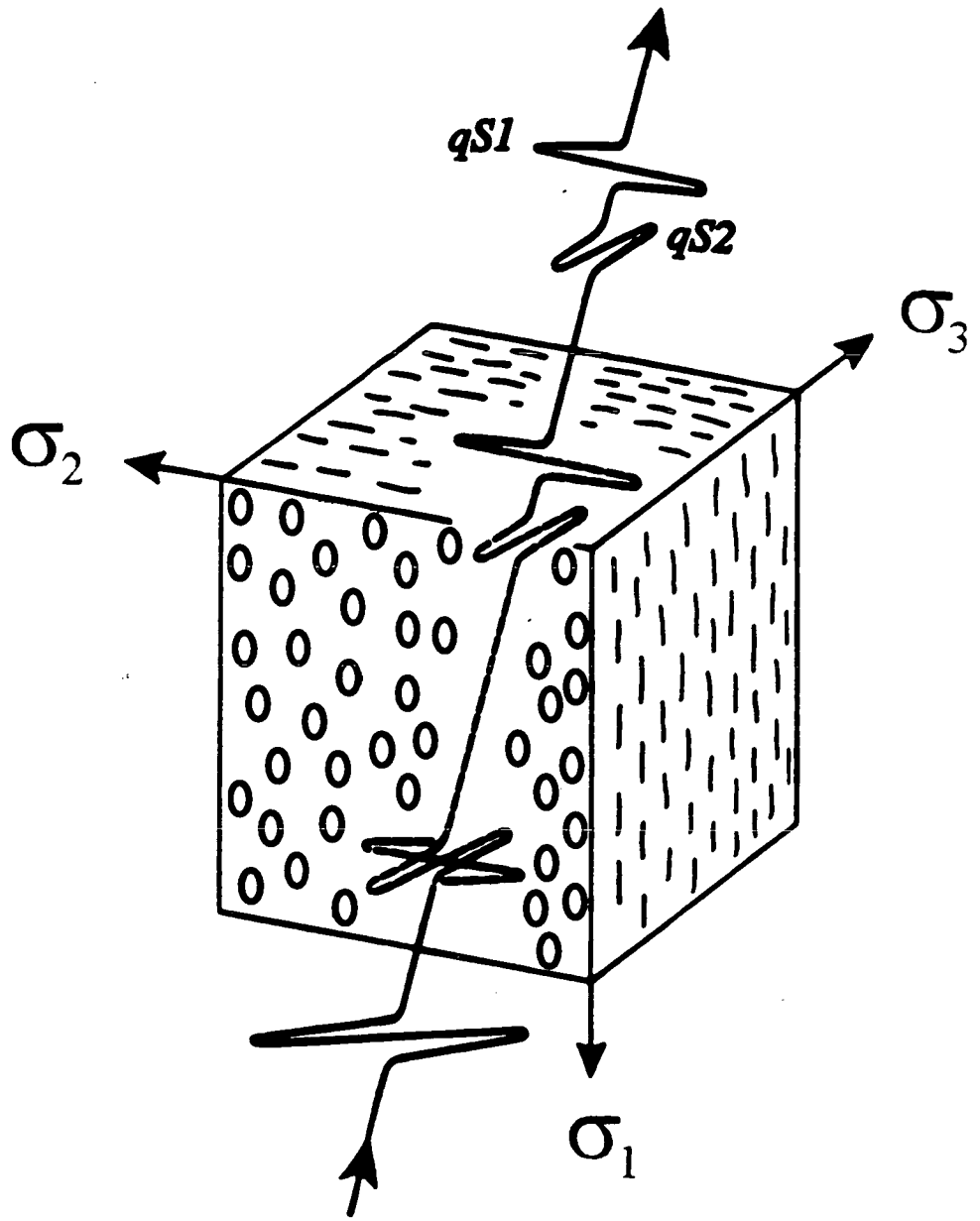

Figure 1.1b: Schematic illustration of shear-wave splitting due to stress-aligned cracks. An unsplit shear-wave enters the anisotropic region and splits into the *qS1*- and *qS2*-waves. The average crack alignment is perpendicular to the minimum stress direction, σ_3. Principle stress directions are marked where $\sigma_1 > \sigma_2 > \sigma_3$.

the dip of the plane is downwards to the right. For example, the orientation a plane striking east-west, but a 30° dip so that north is downwards will be notated 270/30.

1.2 What Causes Anisotropy?

The common physical causes of anisotropy have been described by Crampin et al. (1984b). To summarize, anisotropy in the upper crust has mainly been attributed to four possible causes:

1. Mineral alignment: A preferential alignment of minerals in a rockmass.
2. Aligned cracks and Fractures: A preferential alignment of cracks or fractures (considered to be EDA-cracks (defined below) if aligned by the contemporary stress field).
3. Layering: Alternating layers of different compositions where the thickness of the layers is much less than the seismic wavelength (Postma, 1955). This is commonly referred to as *periodic-thin-layering* or *PTL anisotropy* (Crampin, 1989).
4. Extensive-Dilatancy Anisotropy (*EDA*): Stress-sensitive cracks, microcracks, and pore spaces. The stress field at any point in the earth is described by directions and magnitudes of the three mutually orthogonal stress axes consisting of the maximum principle compressive stress σ_1, the intermediate compressive stress σ_2, and the minimum compressive stress σ_3. Stress may reorient or reshape pore spaces and fluid-filled cracks, open cracks oriented perpendicular to σ_3, and close dry cracks not oriented perpendicular to σ_3, creating a fabric oriented perpendicular to σ_3. I will refer to all such elements of a rockmass that contribute to this type of anisotropy as *EDA-cracks*. It is now understood that EDA is mainly due to fluid-filled, intergranular microcracks, and fluid-filled, intergranular pore space (Zatsepin and Crampin, 1995a,b), and it is hypothesized that EDA exists in almost all rocks of the upper crust (Crampin, 1993a; Crampin, 1994).

1.3 Phase and Group Velocity

The behaviour of wave propagation in an anisotropic media is complicated and the following is a summary. For a detailed discussion, see Crampin (1981a).

The velocity sheets of constant phase for *qP*-, *qS1*-, and *qS2*-waves are easily calculated by solving the equation of motion and the sheets are analytically simple. The shear wave phase-velocity surfaces are analytically continuous over the whole wave surface and the polarizations of the shear-waves are mutually orthogonal. However, the velocity of seismic energy transport, or *group velocity*, is the velocity calculated from the initial arrival of seismic energy as recorded by seismometers *in situ*. Group-velocity sheets are not analytically simple, particularly for *qS1*- and *qS2*-waves. A given group velocity sheet can be calculated from the phase velocity sheet using the Kelvin-Christoffel equation (Musgrave, 1970). The general equation is of a complexity that it is usually solved numerically. The direction of group propagation diverges from the direction of phase velocity so that wave propagation directions are not generally normal to the surface of constant phase. The particle motion directions of the two shear-waves are not necessarily orthogonal, although deviation from orthogonality is only significant for strongly anisotropic materials.

1.4 The Shear-Wave Window

There exists a severe limitation to the analysis of shear-wave data recorded by geophones on the surface. Shear-wave raypaths that travel at greater than approximately 35° from vertical propagation are contaminated by interference with the internally reflected *qP*-wave (Booth and Crampin, 1985). The solid angle of directions for which shear-wave observations are useful is known as the shear-wave window (Liu and Crampin, 1990). This window of raypaths within approximately 35° severely restricts the number of useful measurements and the subsequent interpretation that can be made using data from earthquake sources or reverse vertical seismic profiles.

1.5 Displaying Polarizations and Time Delays

It is necessary to be able to display clearly the polarization vectors and time delays for all possible raypath azimuths and dips. Most past studies of anisotropy either involved only upward travelling waves such as in earthquake studies, or solely downward travelling waves as in vertical seismic profiles (VSP's). In these cases, it is sufficient to display raypaths on equal area polar projections where the splitting from

only upward or downward travelling raypaths could be shown clearly on a single polar projection. As I shall be plotting data from many azimuths and incidence angles, I will plot them using Plate Carée projections which are a type of cylindrical projection. These projections have been used for this purpose previously by Liu et al. (1989), Baptie et al. (1993), and Holmes et al. (1993).

Figure 1.2 gives an example of a set of Plate Carée projections. The polarization is a vector in three dimensions. In using Plate Carée projections to display polarizations, it is necessary to use two plots by taking the components of the polarization vectors and projecting them onto two orthogonal planes. The two planes used are the radial-transverse (R-T) plane and the vertical-transverse (V-T) plane, where the radial is the horizontal source to receiver direction, transverse is the horizontal direction perpendicular to the source to receiver direction, and vertical is straight up-down. Note that this definition of radial is different from that used in the radial, transverse-sagittal, transverse-horizontal co-ordinate system (discussed in section 3.3), but is still used to keep diagrams in this dissertation comparable with those in the literature.

1.6 Reciprocal Symmetry

Figure 1.3a displays the 53 polarizations hand-picked from the Shear-Wave Experiment data set plotted on Plate Carée projections. These polarizations describe the pattern of shear-wave splitting primarily due to the *in situ* rockmass and determining the *in situ* anisotropy from these polarizations is the topic of Chapter Seven.

For an elastic wave travelling through a uniform anisotropic medium, a ray travelling in the opposite direction along a seismic ray is expected to display reciprocal symmetry, so that shear-wave polarizations and time delays between the split shear-waves are preserved. On a Plate Carée projection, this inverted ray plots at an azimuth 180° from the original direction, with the direction of polarization in the R-T plane the same as the original ray. The polarization in the V-T plane is the mirror image about the vertical direction of the polarization of the original ray.

Reciprocal symmetry effectively doubles the data for visual comparison in an experiment with raypaths through a uniform rock mass. Application of such

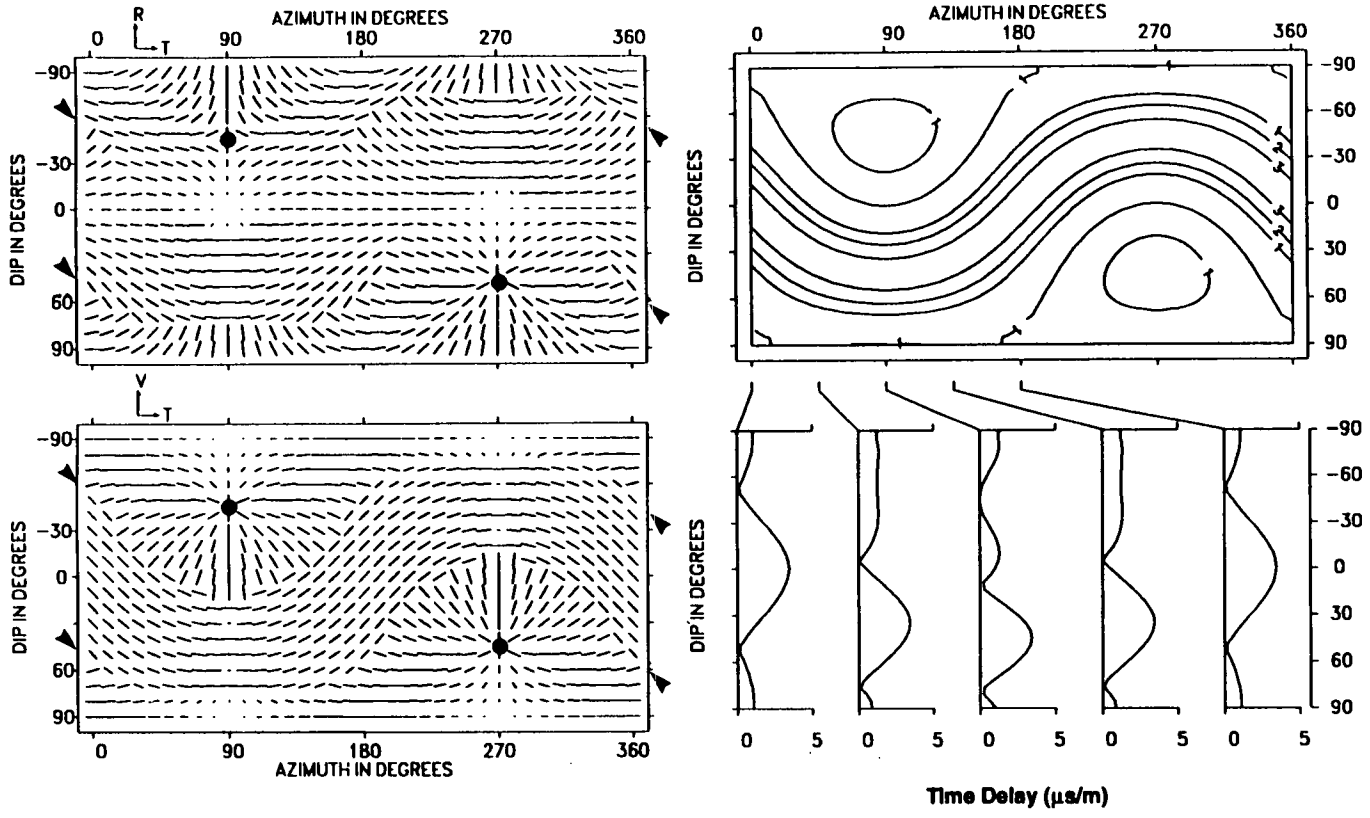

Figure 1.2: The behaviour of shear-wave splitting displayed on Plate Carée projections of water filled cracks in the granite rockmass with crack density ε=0.01 and aspect ratio γ=0.01, striking N000°E and dipping 45° to the West. The vertical axis gives the dips of the raypaths while the horizontal axis gives the azimuth. The top left diagram displays polarizations of the leading split shear wave projected on to the radial-transverse (R-T) plane. The bottom left diagram displays the same polarizations projected on to the vertical transverse (V-T) plane. The top right diagram displays contoured time delays between *qS1*- and *qS2*-wave arrivals normalized to microseconds per metre (μs/m) and the bottom right diagrams display north-south sections of the contours at the indicated azimuths. Arrows mark the directions of line singularities and solid dots mark the directions of kiss singularities.

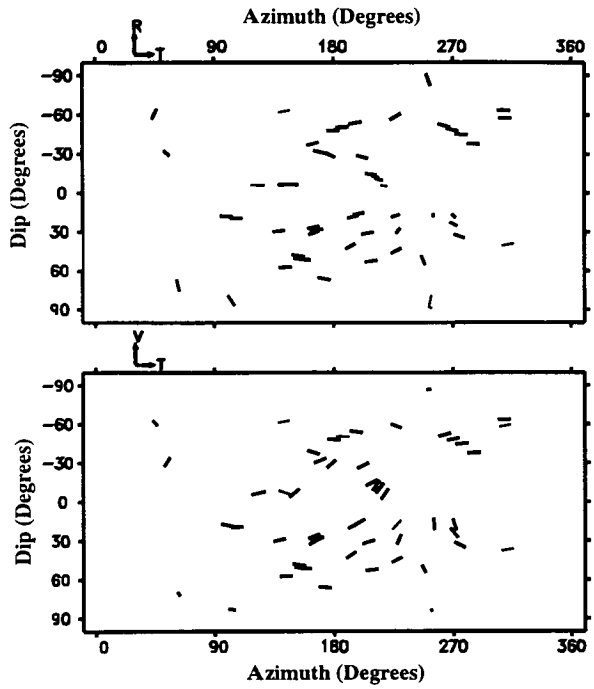

Figure 1.3a: The 53 polarization data from the Shear-Wave Experiment plotted on Plate Carée projections of the Radial-Transverse (R-T) and Vertical-Transverse (V-T) planes.

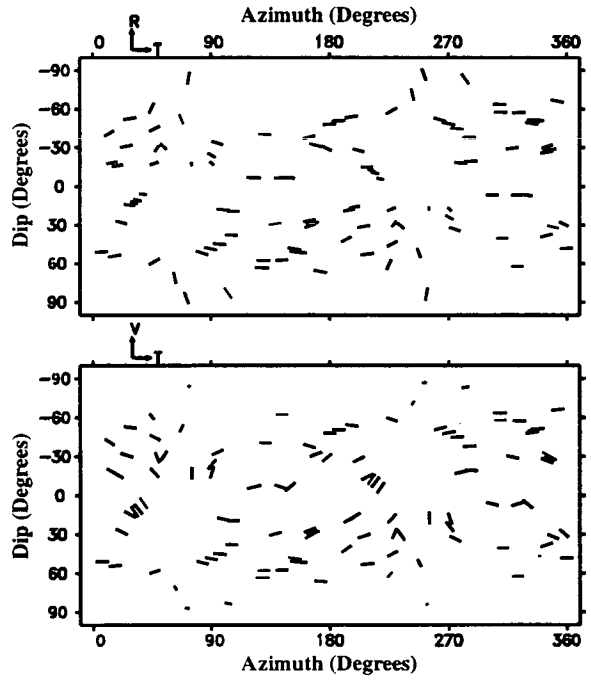

Figure 1.3b: The 53 polarization data from the Shear-Wave Experiment and the 53 polarizations assuming reciprocal symmetry plotted on Plate Carée projections of the Radial-Transverse (R-T) and Vertical-Transverse (V-T) planes.

reciprocal symmetry must be used with caution as it may imprint an apparent symmetry on the data that would be incorrect and misleading if the assumption of reciprocal symmetry does not hold. Nevertheless, reciprocal symmetry can be a useful aid to recognizing anisotropic symmetry patterns in sparse data sets. Figure 1.3b displays the 53 measured polarizations along with the 53 polarization from assuming reciprocal symmetry.

1.7 Linear-Elastic Theory

Most modelling of anisotropic wave propagation uses linear-elastic theory. This theory assumes Hooke's Law that stress depends linearly on strain, which is a valid assumption for small strains («1%). Stated as an equation:

$$\sigma_{ij} = c_{ijkl} e_{kl} \; ; \tag{1.2}$$

where σ_{ij} is the stress in the i direction from direction j. e_{kl} is the strain in the k direction from direction l. c_{ijkl} is the fourth order elastic tensor of eighty-one constants. Assuming wave propagation through a solid and ignoring body forces gives:

$$\rho \ddot{u}_i = \frac{\partial \sigma_{ij}}{\partial x_j} ; \tag{1.3}$$

where ρ is the density of the solid, u_i is the displacement in the i direction and x_i is the unit direction vector. Substituting the equation of Hooke's Law into Equation 1.2 results in the most general form of the wave-equation of motion in a homogeneous, linear-elastic solid:

$$\rho \ddot{u}_i = \frac{\partial}{\partial x_i}\left(c_{ijkl} \frac{\partial u_k}{\partial x_l} \right); \tag{1.4}$$

(Musgrave, 1970), where only twenty-one of the eighty-one elastic constants are independent due to symmetries in stress, strain, and strain energy. Thus, variation of seismic properties of a homogeneous elastic solid can be fully described by 21 independent elastic constants.

Linear-elastic theory is commonly used because the assumptions are reasonable, the constants are physically meaningful, and because of its successful application to

seismology in general. Linear-elastic theory has also been successful in predicting and explaining anisotropic wave behaviour (e.g. Wild and Crampin, 1991; Liu et al., 1993b).

There are eight physically realizable symmetry systems and two sub-systems of anisotropic symmetry, including isotropic symmetry. Common systems are orthorhombic symmetry which has nine independent elastic constants, and hexagonal symmetry, with five independent elastic constants. An isotropic material can be described by only two independent constants such as the bulk modulus and shear modulus.

1.8 Symmetry Systems and Singularities

Shear-wave singularities are propagation directions of the phase-velocity sheets where the velocities of both shear waves are identical. There exists at least two singularities in any anisotropic material, and usually many more (Crampin and Kirkwood, 1981). There are three types of singularities. A point singularity results from the intersection of the phase-velocity sheets other than in a hexagonal symmetry system. A kiss singularity results when the two sheets meet tangentially. A line singularity results when two sheets intersecting in a circle about the symmetry axis. Line singularities can only occur in hexagonal symmetry systems (Figure 1.4).

While singularities are comparatively simple geometrically in terms of phase velocity surfaces, the representation in group-velocity surfaces may be very complicated. Such singularities in group velocity may cause anomalies in shear-wave propagation. These anomalies may extend many degrees to either side of the direction of the point singularity in the phase-velocity surface (Crampin 1981b; Crampin, 1991b). For propagation directions in such a disturbed region, polarization directions of the shear-waves and the time delays can vary rapidly for small changes in propagation.

A common symmetry system is hexagonal symmetry, which is due to a single fabric within a rockmass. There are two possible types of singularities in the case of hexagonal symmetry. The two shear-wave velocity sheets may meet only along the symmetry axis and form two kiss singularities at these points with a region of disturbance around them. Alternatively, hexagonal symmetry may also result in two

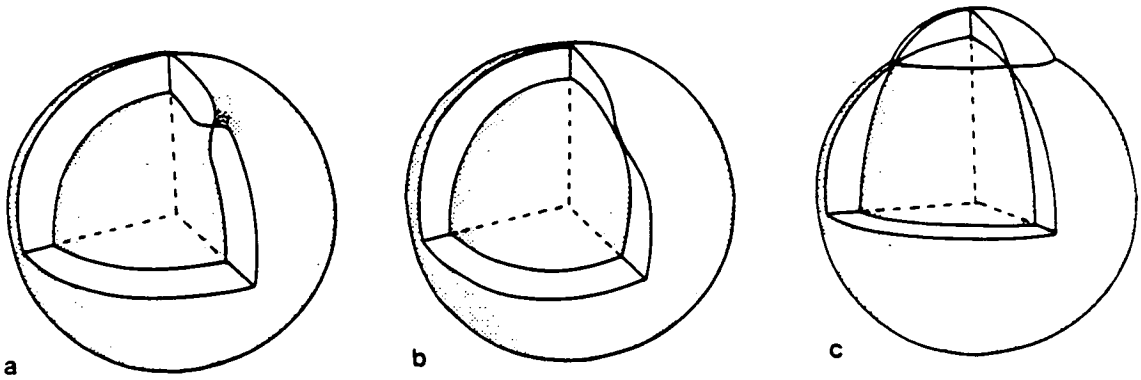

Figure 1.4: Diagrams of the two shear-wave phase velocity slowness-surfaces showing the topology near the various types of singularity:
a) Point singularity
b) Kiss singularity
c) Line singularity
from Crampin and Yedlin (1981).

line singularities. Line singularities exist for parallel fluid-filled cracks while a fabric of parallel dry cracks (e.g. Hudson Cracks, defined in section 1.12) will only have the two kiss singularities (Figures 1.2 and 1.5). There are no disturbances to wave propagation at or around a line singularity (Crampin, 1981b).

Also common is orthorhombic symmetry, which is due to two fabrics oriented perpendicular to one another. This results in up to twenty point singularities (Crampin and Kirkwood, 1981; Wild and Crampin, 1991), depending on the relative strengths of the two fabrics and their crack contents (Figure 1.6).

1.9 Non-Uniqueness

There exists intrinsic non-uniqueness to shear-wave splitting studies where different fabrics may explain observations equally well and this is a fundamental problem. Also, data may contain seemingly anomalous polarization and time delay measurements result due to propagation near singularities. To limit the degree of non-uniqueness it is necessary to have observations for the greatest possible variety of propagation directions and use a priori information.

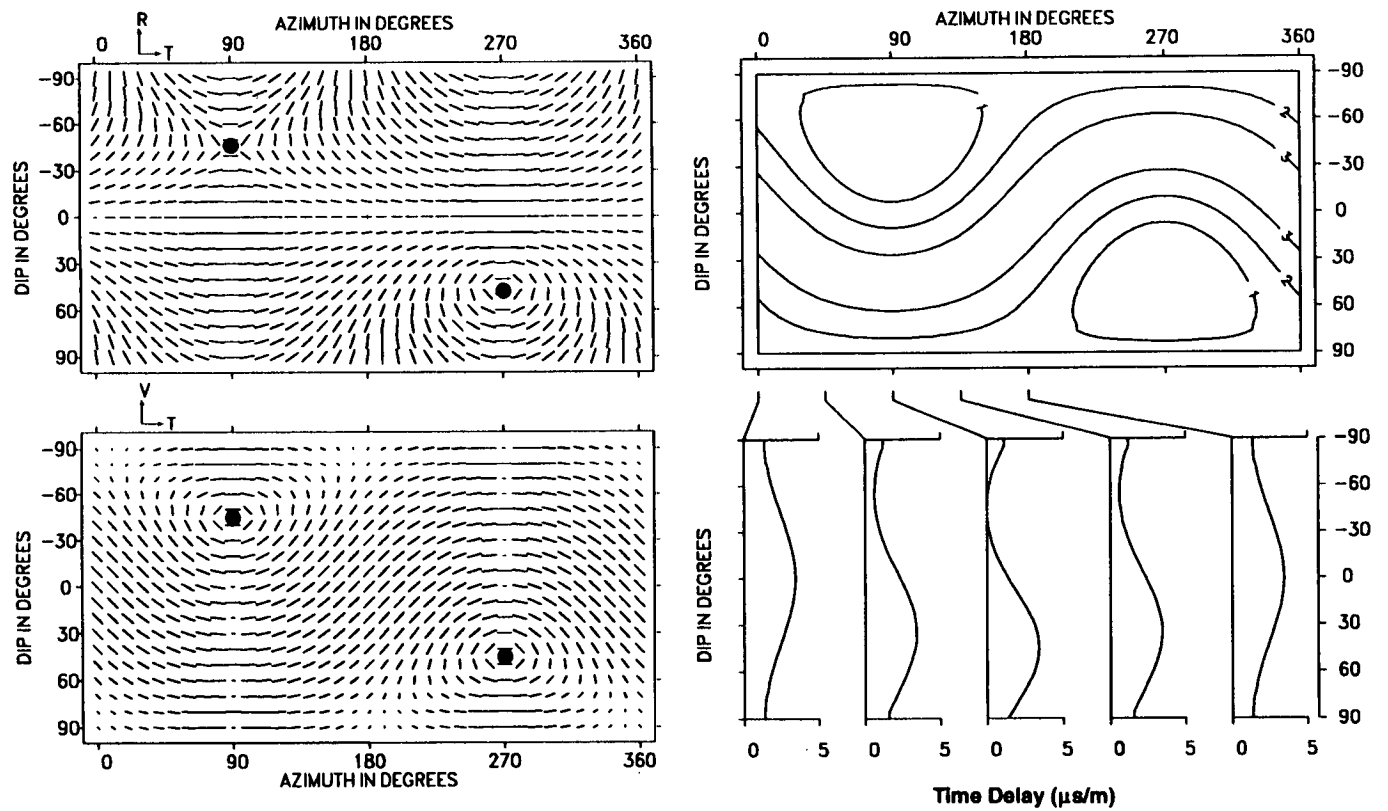

Figure 1.5: The behaviour of shear-wave splitting for the same distribution of cracks as in Figure 1.2 except that the cracks are dry rather than saturated with water. Solid dots mark the directions of the kiss singularities.

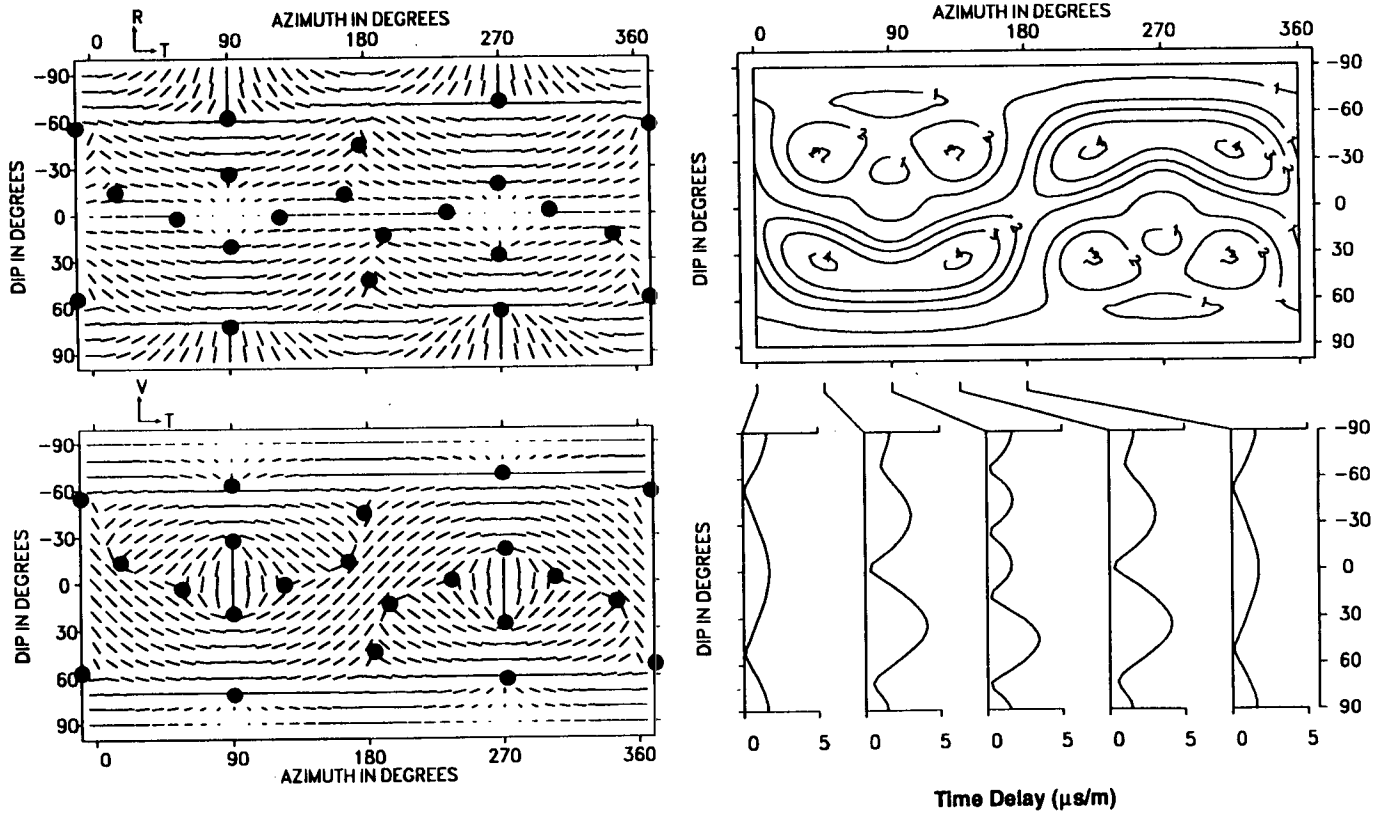

Figure 1.6: An example of the behaviour of shear-wave splitting for an orthorhombic symmetry system. One fabric is a distribution of water saturated cracks oriented 000/45 with crack density ε=0.01 and aspect ratio γ=0.01. The other fabric is a distribution of water saturated cracks oriented 180/45 with crack density of ε=0.005 (half that of the other fabric) and aspect ratio γ=0.01 (the same as the other fabric). Solid dots mark the directions of point singularities.

1.10 Hudson's Theory

One method of calculating the elastic constants for a medium from its physical parameters is using the theory of Hudson (1980; 1981; 1986; 1988). The theory is developed for calculating the effective elastic constants for seismic wave propagation through a sparse arrays of aligned cracks. It shows that the effective elastic constants for a material with parallel aligned cracks are:

$$c_{ijkl} = c^0_{ijkl} + c^1_{ijkl} + c^2_{ijkl} \ ; \qquad (1.5)$$

where c_{ijkl} is the fourth order tensor of elastic constants, c^0_{ijkl} are the elastic constants of the uncracked rock matrix. c^1_{ijkl} and c^2_{ijkl} are the first and second order perturbations due to the presence of the cracks.

The initial assumptions for application are (adapted from Peacock et al., 1994):

1. The cracks are much smaller than the seismic wavelength.
2. Cracks are discrete oblate spheroids.
3. Cracks are thin (aspect ratio, as defined below, of less than 0.3 (Douma, 1988; Crampin, 1991a)).
4. Cracks are filled with a gas, liquid or soft solid with smaller bulk and shear moduli than the matrix rock.

Cracks perfectly described by points one to four above will be referred to as *Hudson Cracks*. A set of Hudson Cracks is described by the parameters of orientation (e.g. strike and dip), crack content, and crack density and aspect ratio (defined below).

The crack density ε is defined as:

$$\varepsilon = \frac{N\langle a^3 \rangle}{\upsilon} \ ; \qquad (1.6)$$

where N is the number of cracks in a volume υ of rock and $\langle a^3 \rangle$ is the average of the cube of the crack radii. The formulations are valid for crack densities of less than about 0.1, which is also the approximate limit of crack density expected for crustal rock away from the near surface (Crampin, 1994). Conveniently, the percentage shear-wave velocity anisotropy is approximately ε x 100. Increasing crack density results in increased time delays but causes only minor changes in polarizations for most raypaths. Thus time delay measurements are necessary to determine the crack

density of a material. The aspect ratio (γ) is the ratio of the thickness to the diameter of the cracks. The crack content is what material is contained in the cracks. Generally the approximation that the cracks are either gas-filled (dry), or saturated with water is valid.

Hudson Cracks are used to create physically interpretable models. The fabrics causing anisotropy will not be perfect Hudson Cracks. However, the elastic constants of an anisotropic fabric can be modelled using Hudson's theory. In doing so, the *equivalent* set of Hudson Cracks to that fabric is also found and inferences can then be made about the real fabric. For example, a fabric of Hudson Cracks with a large crack density that explains the observations where the anisotropy is due to EDA may imply that the actual rockmass has a large crack density.

Observations may be matched to models created using fewer restrictions than Hudson Cracks (e.g. Thomsen parameters (Thomsen, 1988), or elastic constants), but such generality can result in models which are physically unrealizeable or difficult to interpret geologically. Such generality also results in large non-uniqueness. Even the comparatively very restrictive parameterization of Hudson results in considerable non-uniqueness as expected because of intrinsic nonuniques in studies of shear-wave splitting.

1.11 Introduction to The Shear-Wave Experiment

Atomic Energy of Canada Limited is currently investigating excavation damage in highly stressed granite rock as part of the Canadian program in nuclear waste disposal. The experiments are being conducted at the Underground Research Laboratory (URL), a major research facility in south-eastern Manitoba. URL is situated within the roof zone of the Lac du Bonnet Batholith, a granite rockmass of 1800km^2 surface area that crystallized 2670M - 2100M years ago in the Superior Province of the Canadian Shield. It is considered to be representative of many granitic intrusions in the Canadian Precambrian shield (Martin, 1990).

The Mine-by Experiment is the test excavation of a 46m-long, 3.5m-diameter tunnel at the 420-Level (420m below the surface) in an otherwise undisturbed granite rockmass (Figure 1.7). Excavation sequences in which the face was advanced by 0.5m to 1m steps took place between October 1991 and August 1992 within a

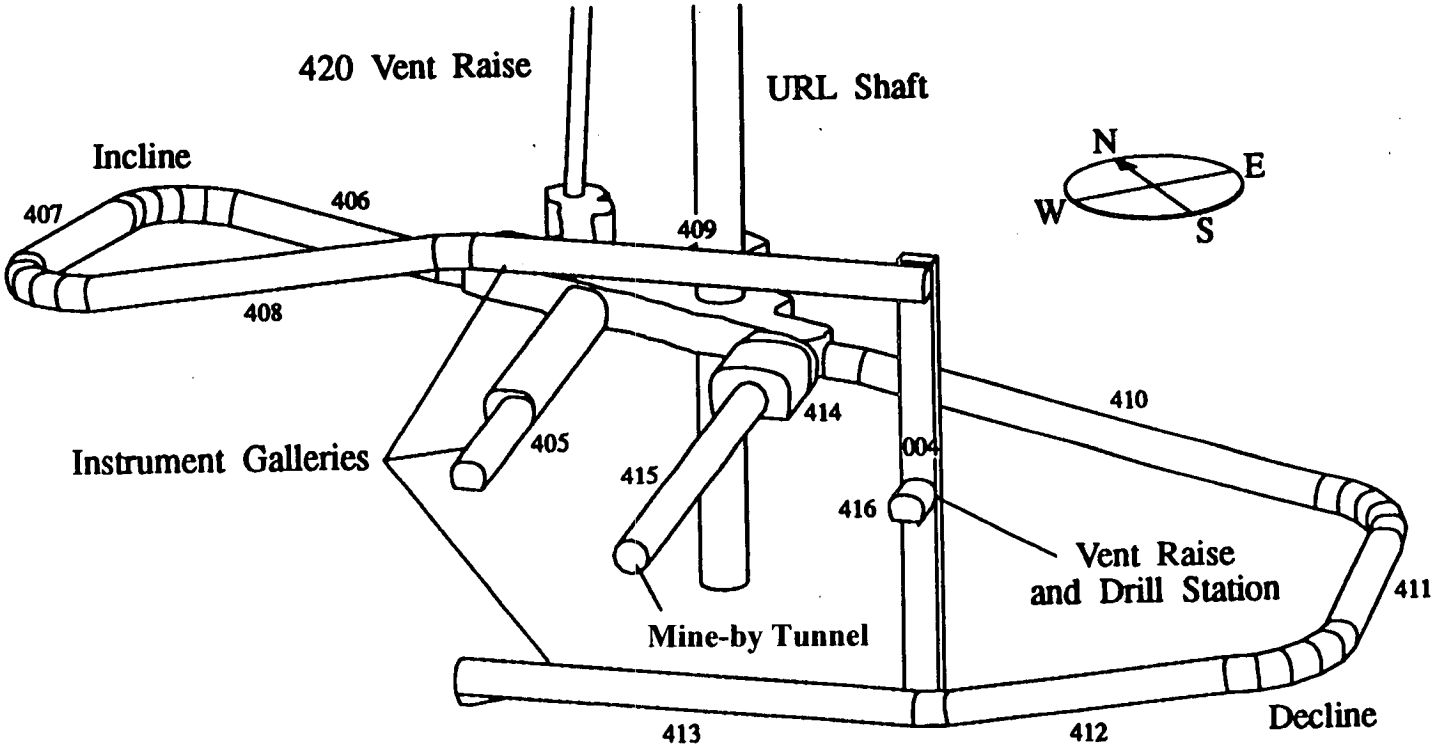

Figure 1.7: The tunnel arrangement of the 420-Level (420m depth) of the Underground Research Laboratory. The room numbers of all outer tunnels and the Mine-by tunnel, Room 415, are marked on the diagram (Read and Martin, 1991).

rockmass monitored with a network of accelerometers, extensometers, strain cells, and thermistors, and convergence arrays measuring the changing shape of the tunnel. The objectives of the Mine-by Experiment include improving our understanding of the behaviour of the *in situ* rockmass, evaluating excavation damage around underground openings, developing and evaluating underground characterization methods, and developing monitoring instrumentation (Read and Martin, 1991).

It was realized that the experimental design of the 420-Level and the deployed microseismic network could be used for a controlled source shear-wave experiment. Seismic signals could be produced near the walls of the outer tunnels of the 420-Level and then recorded using the microseismic network. This dissertation is primarily based on the processing and interpretation of data from this *Shear-Wave Experiment.*

In the past, observations of *in situ* shear-wave splitting have usually been limited by the shear-wave window to raypaths within 35° of vertical in surface recordings above local earthquakes and seismic reflections surveys. Recently, shear-wave splitting has also been studied using data from crosshole surveys (Liu et al., 1991; 1992) which offers records of more nearly horizontal raypaths but with severely limited ranges of azimuths. Similarly, subsurface recordings of VSP's also have a severely limited range azimuths. Thus, all previous recorded data sets showing shear-wave splitting have suffered from limitations in the propagation directions sampled and, in the case of earthquake data, very complicated geology. As a result, the scope for geological interpretation has been limited and the interpretation of the causes of the anisotropy somewhat speculative.

In the Shear-Wave Experiment, actively produced signals in the outer galleries allow shear-wave splitting to be observed over the greatest variety of raypaths of any *in situ* experiment to date. There are also no limitations due to a shear-wave window because the signals were recorded by triaxial accelerometers cemented within the rockmass. Results can be combined and compared with other studies associated with the Mine-by Experiment including other seismic studies. This will allow the most detailed investigation of the causes of the anisotropy to date.

Furthermore, the experiment was repeated as the excavation of the Mine-by tunnel progressed. This allows the observation of the effects of changes of stress upon shear-waves thereby investigating Extensive-Dilatancy Anisotropy (section 1.2) as a

possible fabric. Changes in shear-wave splitting can also be used to investigate the pattern and extent of the damage to the rockmass due to the tunnel excavation.

My analysis and interpretation of the Shear-Wave Experiment data set will provide geological interpretations to the causes of *in situ* anisotropy and the effects of excavation. This is the first controlled shear-wave experiment in a mining environment. Therefore in this dissertation I will develop and assess the use of shear-wave splitting surveys as a technique to parameterize non-destructively a rockmass and monitor excavation effects in a mine environment. This has potential applications in mining engineering where potential planes of weakness need be identified, and in the long term non-destructive monitoring of nuclear waste repositories as a method to indirectly observe any penetration of fluids into the rockmass. It is also important to identify the cause of *in situ* anisotropy in granite for the interpretation of shear-wave splitting in earthquake studies where raypaths travel through granite or a similar lithology. The identification of EDA as a fabric suggests that changes in stress may be monitored using shear-wave splitting so that observations of shear-wave splitting are useful in earthquake prediction.

The experiment was conceived by S. Crampin, P. Young, and myself. I chose the locations of the source stations (section 2.2) and designed the geometry of the four boreholes at the stations (section 2.4). D. Collins tested various ideas for a controlled source thought of by P. Young, S. Crampin, D. Collins, and myself. D. Collins performed the recording sequences of the experiment.

1.12 Objectives

The primary objectives of this dissertation are to;

1. Use measurements of shear-wave splitting to determine the cause of the *in situ* anisotropy.
2. Gain insight into the effects of tunnel excavation upon shear-wave splitting.

Striving to achieve this primary objective facilitates consideration of three other objectives of more general importance. These objectives are to;

3. Develop the methods and techniques necessary to process and interpret the data from the Shear-Wave Experiment such that the methods and techniques are applicable to any future studies of shear-wave splitting in a mine

environment. This requires considering shear-wave splitting measurements for a large variety of propagation directions that are not systematically distributed.

4. Assess the practical value of using of controlled-source shear-wave experiments to test the rockmass non-destructively and monitor excavation effects in a mine environment.
5. Provide insight into causes of seismic anisotropy in the granite rockmass.

1.13 Dissertation Structure

Chapters describing and developing measurement and processing techniques will be followed by the chapters that interpret the results from application of the techniques.

In this chapter I have presented a brief overview of the theory of seismic anisotropy with an emphasis on the information and considerations necessary to interpret measurements of shear-wave splitting, and understand this dissertation. In Chapter Two I present a complete description of the Mine-by Experiment, including all background geological and geophysical information necessary to understand the further chapters. These first two chapters provide all the necessary background information.

Interpretation of shear-wave splitting requires the precise measurement of polarizations and time delays. In Chapter Three I extend the method of hand-picking polarizations and time delays for cases where multiple seismograms are available for comparison and apply this to the Shear-Wave Experiment data set. In doing so, I show that shear-wave splitting clearly takes place within the rockmass and I demonstrate the effectiveness of the method and the desirability of using a controlled source and multiple source orientations.

Time delays are more difficult to measure than polarizations. In Chapter Four presents I compare time delays determined by hand-picking the length of linearity after the *qS1*-wave arrival to time delays determined using the duration between arrivals of similar pulse shapes. Results support the method of hand-picking time delays described in Chapter Three.

Chapter Five is a detailed study of temporal changes in shear-wave particle motion due to tunnel excavation. I first describe methods of detecting possible temporal changes I have developed and then interpret the geological causes of the temporal changes. I show that changes in shear-wave particle motion clearly indicate effects of excavation upon the rockmass.

The quantitative comparison of measurements of shear-wave splitting to models is desirable to reduce subjectivity and is necessary for automated inversion. Previously there has been no study into methods of quantitative comparison for a non-systematic distribution of propagation directions. In Chapter Six I develop an algorithm that is robust and produces a conveniently interpretable misfit value.

In Chapter Seven I use the algorithm developed in Chapter Six in the automated inversion and modelling of the polarizations from the Shear-Wave Experiment and Velocity Survey data sets. I use the results to argue that the *in situ* anisotropy is due to either EDA-cracks or the faint primary layering and suggest that one effect of excavation is the escape of fluids from *in situ*.

I develop a method of quantitatively comparing measured time delays to model in Chapter Eight. I then use this method and the results of inverting polarizations to gain further insight into the cause of the *in situ* anisotropy. I then show that two nearly identical rockmasses may have different *in situ* anisotropy. Most importantly, I present arguments for EDA-crack and the faint primary layering as the causes of the *in situ* anisotropy, but show that the data from this experiment cannot conclusively determine which fabric is responsible.

Lastly, Chapter Nine summarizes the conclusions and suggests applications and useful further research work.

I presented preliminary results of this dissertation at the Fifth International Workshop on Seismic Anisotropy at Banff, Canada, in May, 1992, which I subsequently published (Holmes et al., 1993). This paper is included attached to the back cover. Results of Chapters Three and Seven were presented at the Seventh United Kingdom Geophysical Assembly, at Oxford, United Kingdom, in April, 1993. A summary of the results of Chapters Three, Seven, and Eight was presented at the Sixth International Workshop on Seismic Anisotropy at Trondheim, Norway, in July, 1994.

2 The Shear-Wave Experiment at URL's 420-Level

2.1 Introduction

This chapter describes the Shear-Wave Experiment upon which the majority of this dissertation is based. This is followed by descriptions of the geology, fractures, microcracks, and stress field of the granite rockmass involved in these experiments. The remainder of this chapter discusses previous studies of anisotropy in granite and granodiorite, possible causes of anisotropy in this rockmass, and a discussion of other relevant seismic studies of this rockmass.

2.2 Experiment Procedure

For each recording sequence of the Shear-Wave Experiment, four highly repeatable shear-wave signals (as quantified in section 5.3) were excited at end of 40cm boreholes at thirteen different locations on the walls of the outer tunnels, and recorded by the fourteen triaxial accelerometers (Figure 2.1). I will refer to these thirteen different locations as *source stations* and the tunnels on which the source stations are located as the *source tunnels*. I chose the locations of the source stations in the outer tunnels by calculating the raypath directions that would result from seismic sources located at 0.5m intervals throughout every tunnel of the 420-Level as recorded by the fourteen triaxial accelerometers (see next section). I then selected the thirteen locations that would provide the largest coverage of raypath directions. This serves to limit non-uniqueness (section 1.8). It is believed that the Shear-Wave Experiment has the greatest variety of raypath directions of any *in situ* experiment investigating seismic anisotropy to date. The origin times of the seismic events were not recorded so the experiment could be performed quickly as schedules required.

The excavation of the Mine-by tunnel began before the idea for this experiment was conceived. The first recording sequence of the Shear-Wave Experiments began

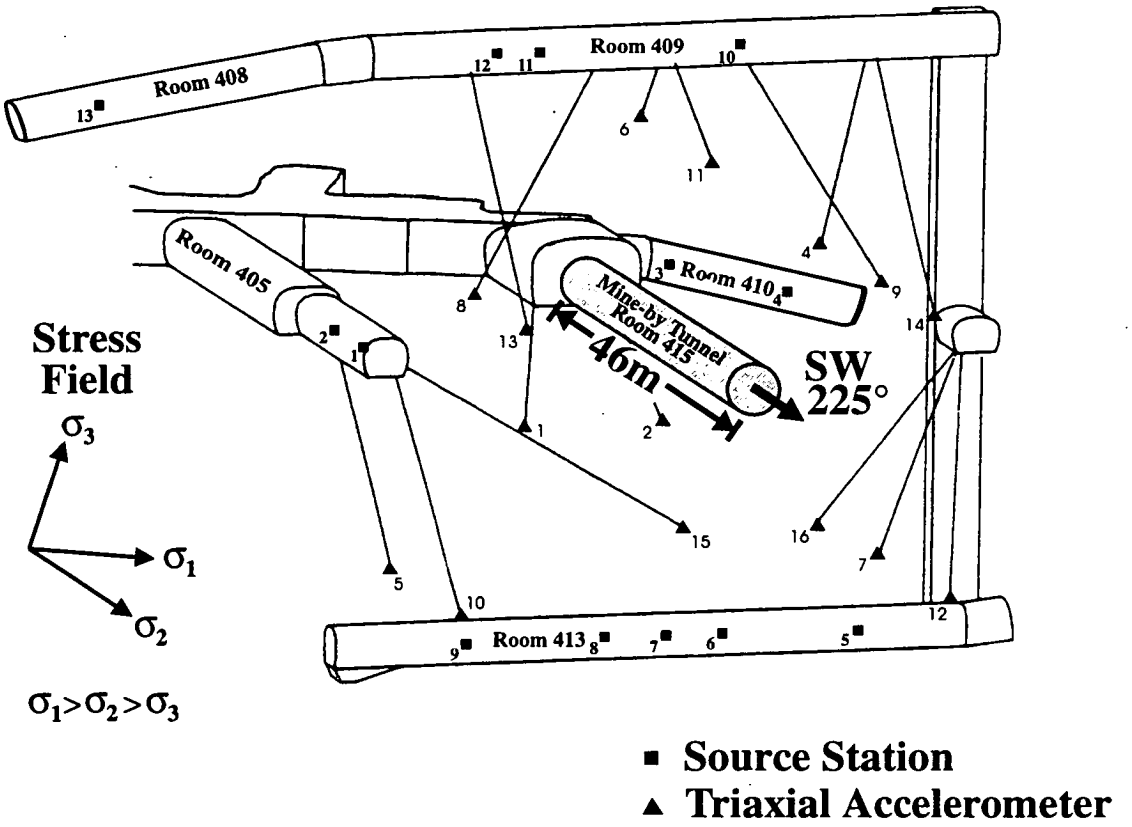

Figure 2.1: Perspective view of the Mine-by Tunnel, coloured grey, and the outer tunnel.

when the tunnel had already been excavated to 29m of the final 46m length. Ten recording sequences took place before the tunnel was completed (not every excavation sequence was monitored), and three additional sequences were recorded at intervals after completion to examine the possible longer-term effects of excavation damage on the rockmass. Excavation of the Mine-by tunnel was either for 3.5m tunnel diameter directly, or an initial 2.5m tunnel diameter followed by repeated excavation to increase the diameter to 3.5m. This was done to investigate the rockmass response to different diameters. Table 2.1 presents the length of the tunnel at each recording sequence for the lengths of both the 2.5m and 3.5m diameters of the tunnel.

Table 2.1: Length of Mine-by Tunnel at Each Recording Sequence

Recording Sequence	Date of Recording Sequence	Chainage* (m) (Values in brackets give limits)	
		3.5m Diameter	2.5m Diameter (if greater than for 3.5m Diameter)
1	May 01	(30.100, 31.170)	
2	May 06	(31.170, 32.260)	
3	May 11	(32.260, 33.180)	
4	May11	(32.260, 33.180)	
5	May 14	(33.180, 34.280)	
6	June 01	34.280	39.020
7	June 05	35.550	40.000
8	June 15	40.000	
9	June 19	40.000	42.060
10	June 30	40.000	(44.060, 45.050)
11	July 22	46.140	
12	Aug. 04	46.140	
13	Aug. 25	46.140	

*Chainage is 0.99m greater than the tunnel length

(Information from Read et al., 1992)

2.3 The Microseismic System and Accelerometer Network

(Adapted from Collins and Young, 1993) The Mine-by Experiment used a full-waveform microseismic system designed by the Queen's University Engineering Seismology Laboratory. The geophone network of the microseismic system consisted of sixteen triaxial accelerometers distributed in the surrounding rockmass at locations chosen to provide full focal sphere coverage of the induced microseismic events and to optimize source location of these events (Talebi and Young, 1989) (Figure 2.1). Each triaxial accelerometer was cemented at the bottom of surveyed NQ-3 size (75.7mm diameter) boreholes diamond-drilled from the outer tunnels of the 420-Level. Special non-reducing cement was used to ensure good coupling between the triaxial accelerometer and the borehole wall (Talebi and Young, 1989). Each triaxial accelerometer was accurately oriented using a mercury tilt switch contained

within the triaxial accelerometer. The triaxial accelerometers (Model 755G) are constructed by Wilcoxon Research. Each contains three orthogonal accelerometers, one in the direction down the borehole and two in the perpendicular plane to the borehole. The maximum separation between two accelerometers in one triaxial accelerometer is 2cm. The sensitivity of the accelerometers is 3 Volts/g with a low noise characteristic of 2μg, where g is the acceleration due to gravity.

When signals are received by the triaxial accelerometers, they are preamplified underground by a gain factor of 3, 30, 300, or 3000 and then transmitted to the surface by a fifty-pair shaft cable. The signals then pass through a differential amplifier and anti-aliasing filter board where they are band-pass filtered in the frequency range of 50Hz or 500Hz to 10kHz (±3 dB) with a frequency roll-off rate outside this bandwidth of 72 dB per octave. Each seismic trace was sampled at 50kHz frequency for 4096 sample points. This system allowed seismic events with magnitudes as small as M_L=-4 (Feignier and Young, 1992) and seismic moments as small as M_0=-6 (Martin and Young, 1993) to be studied.

Two of the sixteen triaxial accelerometers could not be used in this study. Triaxial Accelerometer 3 was replaced by a more distant accelerometer for the recording of larger magnitude seismic events. This more distant accelerometer was too far away from the shear-wave sources to record data useful for this shear-wave analysis. The particle motion recorded by Triaxial Accelerometer 6 was elliptical after both the *qP*- and shear-wave arrivals regardless of the expected particle motion. It appears that this triaxial accelerometer suffered from resonance. It was concluded that data recorded by this triaxial accelerometer is only useful for travel-time studies and was not used in this shear-wave study.

2.4 The Shear-wave Source

I designed the shear-wave source to produce four distinct shear-wave radiation patterns for each source to receiver raypath. The shear-wave splitting can then be compared to improve the accuracy in measuring polarizations and time delays (see Chapter Three). Four 40cm-long 3.2cm-diameter boreholes were drilled at 45° to the surface at the corners of a 29.5cm x 29.5cm template on the walls of the tunnels at each location (Figure 2.2). A rod was inserted in turn into each borehole, and the free

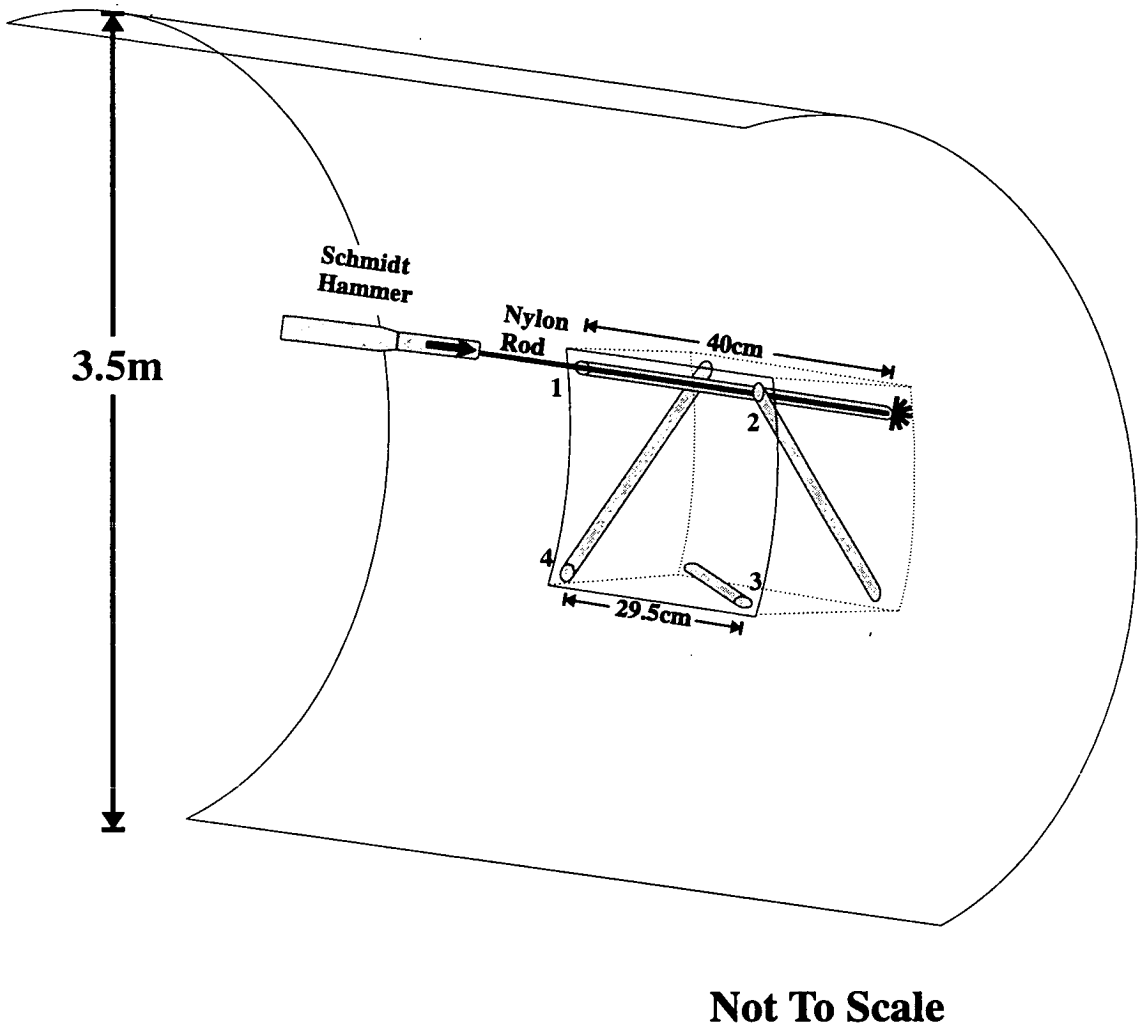

Figure 2.2: The design of the source stations used in the Shear-Wave Experiment consisting of four 40cm-long 3.2cm-diameter boreholes drilled at 45° to the surface at the corners of a 29.5cm x 29.5cm template on the wall of an outer tunnel.

end pulsed with a Schmidt Hammer (Model N, total impact energy 2.207Nm) (A Schmidt Hammer is a spring-load piston designed to test the compressive strength of concrete.).

The orientations and lengths of the four boreholes are arranged so that:

1. The source locations are close enough together that the source to receiver raypaths are virtually the same for all four source locations to any given triaxial accelerometer.
2. The boreholes were not close enough to one another that the excavation damage around the boreholes combines to create a concentration of damage large enough to complicate the source radiation pattern.

The ends of the source boreholes were surveyed to a precision of 2cm and the orientations of these boreholes were surveyed to a precision of 1° in both azimuth and dip.

Figure 2.3 is a graph of frequency amplitude versus frequency for the shear-wave energy created using the nylon rod (see next section). As is typical, there are two distinct peaks at 3.7kHz and 4.9kHz and a relatively narrow frequency range (approximately 3.0kHz to 5.6kHz) contains most of the shear-wave energy. These frequencies correspond to wavelengths between 0.60m and 1.1m (The average raypath length is 35m.). The superposition of these frequencies results in the apparent dominant frequency of 4.2kHz (wavelength 0.81m) for the shear-waves as calculated from the period of the shear-wave cycles displayed on the seismograms. Because the diameters of the source boreholes (3.2cm) are much less than the dominant wavelengths of the shear-waves, the effect of the damage around the boreholes on the seismic signal is expected to be negligible.

2.5 Nylon Rod versus Steel Rod

Rods made of both nylon and steel were tested in the first recording sequence. Figure 2.4 shows the three component seismograms for the same raypath for the shear-wave source created using the two rods. The first seismogram, from using the nylon rod, has relatively impulsive initial shear-wave motion and the maximum amplitude of the seismogram occurs as part of the first cycle of shear-wave motion. This is the desired situation for the study of shear-wave splitting because the arrival of

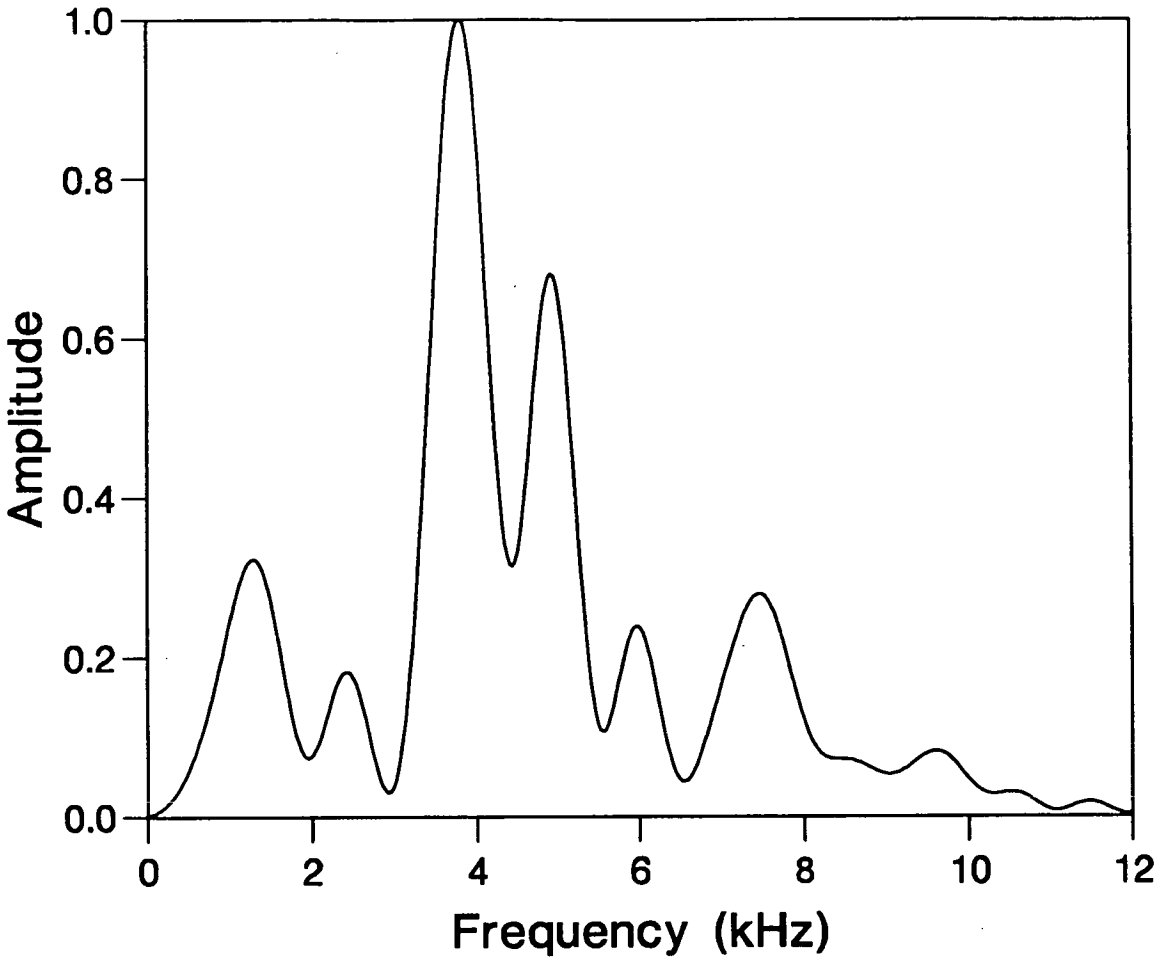

Figure 2.3: Graph of normalized frequency amplitude versus frequency. The two main peaks are at 3.7kHz and 4.9kHz. The seismic energy was created using the nylon rod. To calculate the amplitudes, a three-component seismogram that displayed no shear-wave splitting was rotated to isolate the shear-wave energy on a single channel. Only the seventy-three sample points (1440μs) of this channel, starting at the shear-wave arrival, were used to prevent including any of the shear-wave coda.

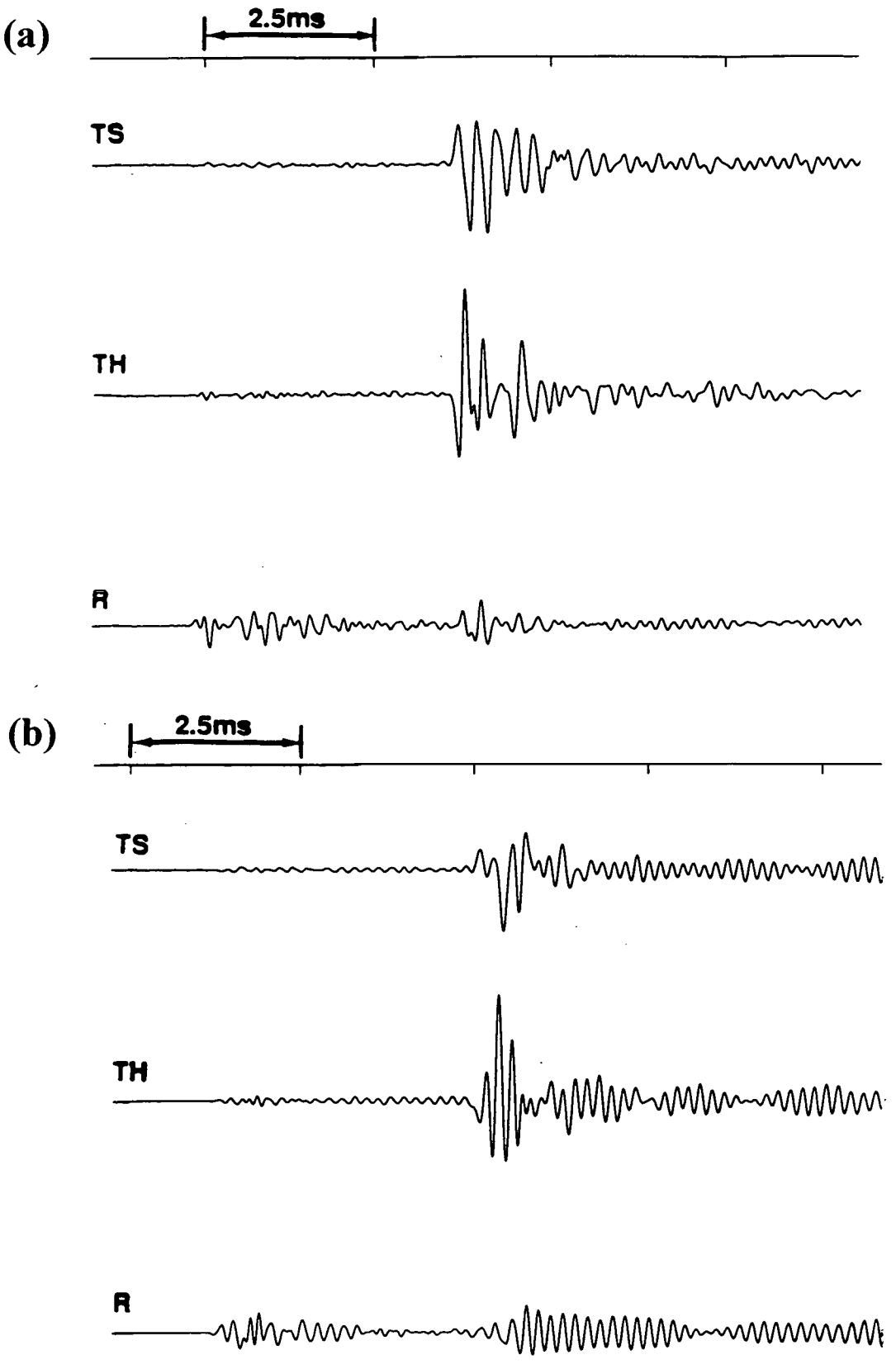

Figure 2.4: Two three component seismograms for the same raypath. In Figure 2.4a, a nylon rod was used to produce to seismic signal. In Figure 2.4b, a steel rod was used. The time scale is given above each set of seismograms with the time interval of 2.5 milliseconds marked.

the first shear-wave is clear and the first shear-wave motion has the highest signal-to-noise ratio of the seismogram. The only advantage of using the steel rod is that it produces a seismic signal of approximately twice the amplitude. However, the steel rod resonates after being pulsed by the Schmidt hammer due to the low acoustic attenuation of steel. The resulting seismograms are contaminated by ringing as seen in the second seismogram. In addition the shear-wave arrival is emergent, having no clear start, and increases to a maximum amplitude after at least one full cycle. This is typical and makes the picking of *qS1*-wave arrivals and time delays unreliable. The ringing on the radial component, which should contain mostly *qP*-wave energy, shows that the motion of the ringing after the shear-wave arrival is not aligned with the *qS1*- and *qS2*-waves. Often the ringing from the *qP*-wave arrival is of long enough duration to completely mask the arrival of shear-wave energy. This ringing appears coherent, but the seismogram cannot be easily processed to remove this ringing because the ringing is approximately the same frequency as the dominant shear-wave signal (A. Feustel, pers. comm.). Consequently, only seismic data created using the nylon rod are analyzed in this dissertation.

2.6 System Calibration

The analysis of shear-wave splitting assumes that all three channels of each triaxial accelerometer have identical system responses so that seismograms may be rotated into any desired co-ordinate system. It is therefore necessary to compare the frequency responses of all accelerometer-to-digitizer channels and determine whether deconvolution of seismic data for system response is necessary. Figure 2.5 shows a typical total system response (Feustel and Young, 1992). As can be seen, the frequency response is approximately flat until 7kHz, and falls off slowly between 7kHz and 10kHz. Total system response did not vary significantly between channels and, as seen in Figure 2.3, the majority of shear-wave energy in seismograms from the Shear-Wave Experiment below this upper limit of a flat frequency response of 7kHz. It is therefore unnecessary to deconvolve the system response for the Shear-Wave Experiment data set.

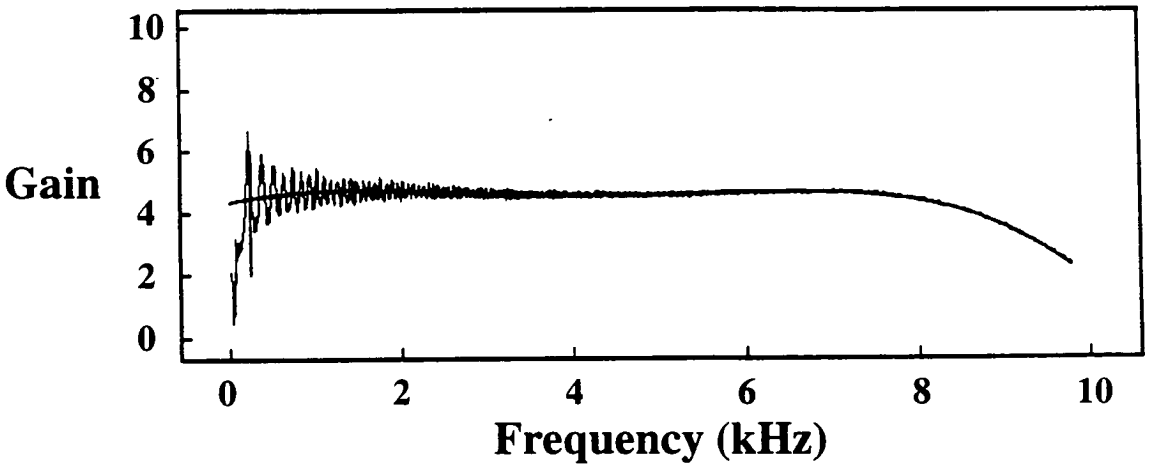

Figure 2.5: The total system response for one channel for frequencies up to 10kHz and the curve of the best-fitting fourth order polynomial to the spectrum (Feustel and Young, 1992).

2.7 Accelerometer Alignment

Seismograms were rotated into the transverse-sagittal, transverse-horizontal, and radial (TS-TH-R) co-ordinate system for analysis (section 3.3). This was performed using the known orientations of all three accelerometers of each triaxial accelerometer. Orientations were measured using the direction of the borehole housing the triaxial accelerometer, and the mercury tilt switch built into the triaxial accelerometer that was used to orient the triaxial accelerometer before cementation.

I discovered that the measured accelerometer directions for Triaxial Accelerometers 1 and 16 were incorrect. In this co-ordinate system the radial channel should contain the majority of *qP*-wave energy and the transverse-horizontal and transverse-sagittal channels should contain the majority of the shear-wave energy. Figure 2.6 is a seismogram recorded by Triaxial Accelerometer 16. Clearly the rotation to the TS-TH-R co-ordinate system was unsuccessful, indicating that the measured triaxial accelerometer orientation was incorrect.

I calculated the correct triaxial accelerometer orientations of all triaxial accelerometers of the seismic network using the data from the Shear-Wave Experiment. I made the approximation that the linear *qP*-wave motion is in the exact

direction as the straight source to receiver raypath. This assumption is reasonable for this relatively homogeneous rockmass (section 2.10) with only weak anisotropy (section 8.8). The accelerometer orientations that maximized the *qP*-wave energy on the radial channel were then found for each raypath. If all assumptions are valid, there exists only one accelerometer orientation such that the *qP*-wave energy is solely on the radial channel for all possible raypath directions. This method requires a minimum of two distinctively different raypath directions for success and more raypaths are needed for greater accuracy and to evaluate the statistical error.

The Shear-Wave Experiment data set was not ideal for this purpose because of the limited variety of raypath directions to some triaxial accelerometers. For example, there were only four source stations where the raypath to Triaxial Accelerometer 1 would not intersect or pass within 2m of a tunnel. However, seismograms from this data set did display clear *qP*-wave arrivals with highly linear particle motion so that even with these restrictions this method should be highly successful. I chose the four raypaths that maximized the variety of raypath directions in calculating each triaxial accelerometer orientation.

The results are presented in Table 2.2. The possible orientations as calculated for each of the four raypaths were compared to find the closest to a common orientation for a given triaxial accelerometer. The *closest to a common orientation* was considered to be the orientation with the minimal average difference between the directions of each of the three channel orientations for four possible orientations. This value of the minimal average difference also gives some idea of the error in calculating the orientation. There is also a significant round-off error in the orientations. The orientations were only measured to three significant digits (to the nearest 0.001) for each of the three co-ordinate directions for each of the three accelerometers of a given triaxial accelerometer. For comparability, the triaxial accelerometer orientations were also calculated to only three significant digits. The maximum error in calculating the difference in direction between two accelerometer orientations is 3.4° due to this precision. Therefore, any difference between measured and calculated triaxial accelerometer orientations less than 3.4° is insignificant. Similarly, any measurement of error less than 3.4° in calculating triaxial accelerometer orientations is also insignificant.

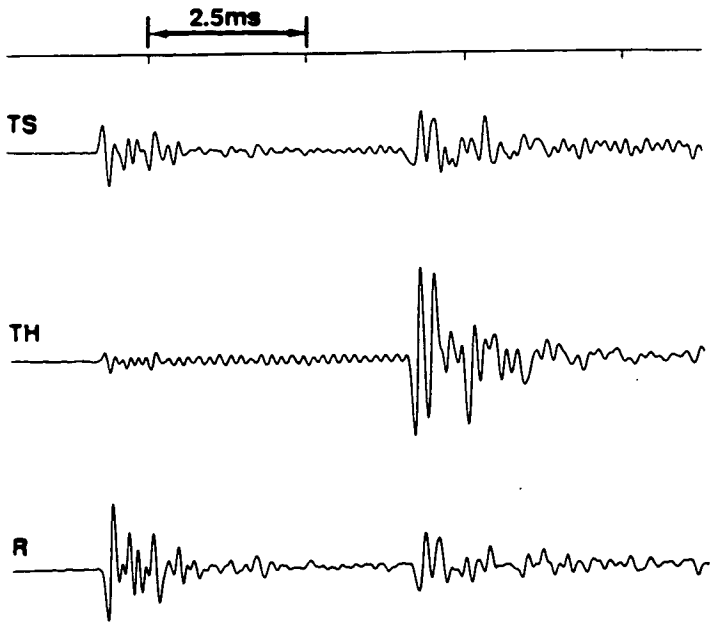

Figure 2.6: Three component seismogram recorded by Triaxial Accelerometer 16 that has been rotated into the TS-TH-R co-ordinate system using the measured triaxial accelerometer orientation. The time scale is given above the seismogram with the time interval of 2.5 milliseconds marked.

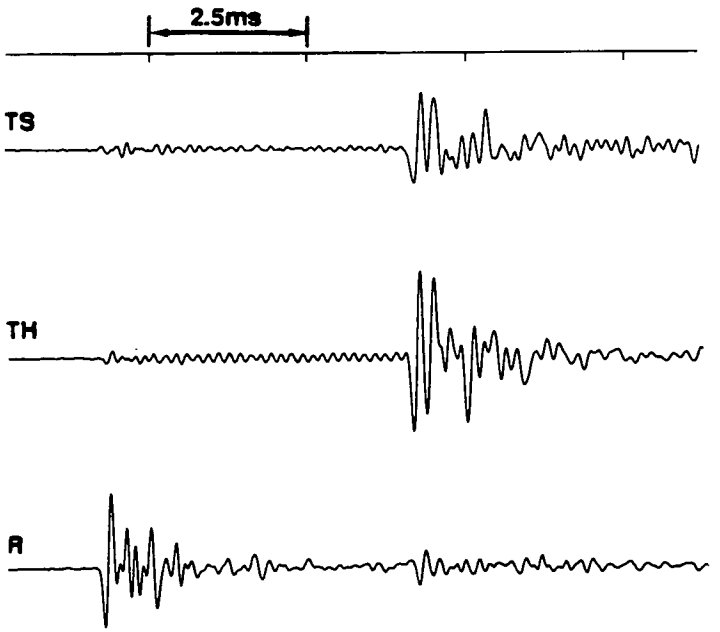

Figure 2.7: The same three component seismogram as in Figure 2.6 rotated into the TS-TH-R co-ordinate system using the calculated triaxial accelerometer orientation. The time scale is given above the seismogram with the time interval of 2.5 milliseconds marked.

Table 2.2: Differences Between Measured and Calculated Triaxial Accelerometer Orientations

Triaxial Accelerometer	Difference Between Measured and Calculated Orientations		Error* (degrees)
	Difference from Down Borehole Direction (degrees)	Rotation in Plane Perpendicular to Down Borehole Direction (degrees)	
1	0.3°	45.8°	±5.5°
2	1.6°	13.0°	±1.2°
4	4.9°	6.3°	±2.6°
5	1.0°	8.5°	±1.2°
7	5.0°	7.8°	±3.0°
8	1.9°	7.8°	±3.0°
9	2.9°	10.5°	±2.6°
10	1.3°	5.7°	±1.2°
11	4.0°	1.4°	±10.2°
12	1.0°	17.3°	±3.0°
13	0.3°	9.9°	±1.6°
14	2.9°	9.5°	±5.7°
15	1.0°	2.4°	±2.2°
16	2.8°	29.3°	±1.9°

*Average angle difference between the orientations of the components calculated from the four raypaths for all three components. Note the orientations were calculated to three significant figures. This results in a round-off error of up to 3.4°. Only errors greater than this value are significant.

Results show that the cause of triaxial accelerometer misorientation is rotation in the source boreholes after the triaxial accelerometers had been oriented using the mercury tilt switch. Of the three accelerometers of a triaxial accelerometer, one is oriented in the direction of the borehole housing the triaxial accelerometer, and the other two are perpendicular to this direction. The cylindrical shape of a housing ensures the alignment of one accelerometer with the borehole direction. The misalignment is due to a rotation of the triaxial accelerometer within the borehole that affects only the other two accelerometers. R. P. Young (pers. comm.) agrees with my

interpretation and elaborated that the triaxial accelerometers may have rotated while the rod used to install the triaxial accelerometer was removed.

The calculated orientations show Triaxial Accelerometers 1 and 16 have rotated by 45.8° and 29.3° respectively. These are the largest rotations of the triaxial accelerometers and this explains the failure of rotation into the TS-TH-R. Figure 2.7 shows the same seismogram as Figure 2.6 except that the calculated accelerometer orientations were used to successfully rotate the recorded seismogram to the TS-TH-R co-ordinate system. One of the accelerometers of Triaxial Accelerometer 1 had the exact opposite polarity expected. This triaxial accelerometer had been disconnected during an experiment and was probably wired in reverse when the triaxial accelerometer was reconnected.

Only Triaxial Accelerometers 11 and 15 had not appreciably rotated. The rotations manifest themselves as errors in measuring polarization directions (section 3.5), although errors as large as the rotation will only occur for raypaths parallel to source borehole directions. Measurement of polarizations and time delays were not made on data recorded by Triaxial Accelerometers 1 and 16 but otherwise no corrections were made for triaxial accelerometer rotations in the analysis of the data from the Shear-Wave Experiment. This is because much of the analysis of the shear-wave data had already been done before the true orientations of these triaxial accelerometers were calculated. Data from Triaxial Accelerometers 1 and 16 were used in the analysis of the Velocity Survey data set (section 2.13.1), and in examining the Shear-Wave Experiment data for temporal changes (Chapter Five). In doing so the calculated orientations of these two triaxial accelerometers were used.

2.8 The Geology

An in-depth analysis of the geology of the rockmass directly surrounding the Mine-by tunnel had not yet been published at the time of the writing of this dissertation. The discussion below is based on preliminary reports, laboratory studies, and personal communications.

The Lac du Bonnet batholith consists of five main rock units: the pink (altered) or grey (unaltered) granite groundmass of the batholith, xenolithic inclusion of variable composition, low-dipping leucocratic granitic segregations, and subvertical

granodiorite and pegmatite dykes (Read and Martin, 1991). Figure 2.8 presents the generalized geological setting at URL.

The average mineral composition of Lac du Bonnet granite is quartz: 30.6±3.9%, plagioclase 37.5±5.7%, potassium feldspar 27.3±6.8%, muscovite 0.5±0.3%, biotite and chlorite 3.5±1.5%, opaque minerals 0.4±0.3%, and other minerals 0.2±0.2% (Robertson and Chernis, 1987). The composition is plotted in the tertiary diagram of Figure 2.9 and clearly shows the average composition is that of granite according to the United States Geological Survey definition. The average density is 2.63gm/cm^3, which is the same as that for Westerly granite (Touloukian and Ho, 1981).

Figures 2.10, 2.11, and 2.12 present the geology of the 420-Level for the Mine-by Tunnel and vicinity. There are two distinct granites in the rockmass surrounding the Mine-by tunnel. The majority of the rockmass consists of unfractured and unaltered medium-grained gneissic grey granite with some coarse-grained porphyritic leucocratic grey granite. A major subvertical, autointrusive, dyke swarm of approximately 100m thick, and striking north to north-west, is present throughout the 420-Level and crosscuts the grey granite (Read and Martin, 1991). The granite of these dykes has a slightly higher density than the grey granite, has a finer grain size, contains a higher proportion of mafic minerals and consequently is darker in colour. It has a composition closer to that of granodiorite (R. P. Young, pers. comm.). For simplicity I will refer to the grey and leucocratic granites as simply granite and the granodioritic granite as granodiorite. Both the granite and the granodiorite have relatively uniform compositions and textures (Read and Martin, 1991), although the granite contains faint primary compositional layering (section 2.15). The geomechanical properties of the granite and granodiorite are summarized in Table 2.3 and show the properties to be nearly identical. No differences in the seismic response of the granite and granodiorite had been observed prior to the Mine-by Experiment (D. Martin, pers. comm.). Some thin pegmatite dykes crosscut other rock types but are mostly confined to the larger granodiorite dykes (Read and Martin, 1991).

2.9 The Stress Field at URL

The stress field at the 420-Level from overcoring and hydraulic fracturing measurements (Martin, 1990) is given in Table 2.4. σ_1 and σ_2 (as defined in section

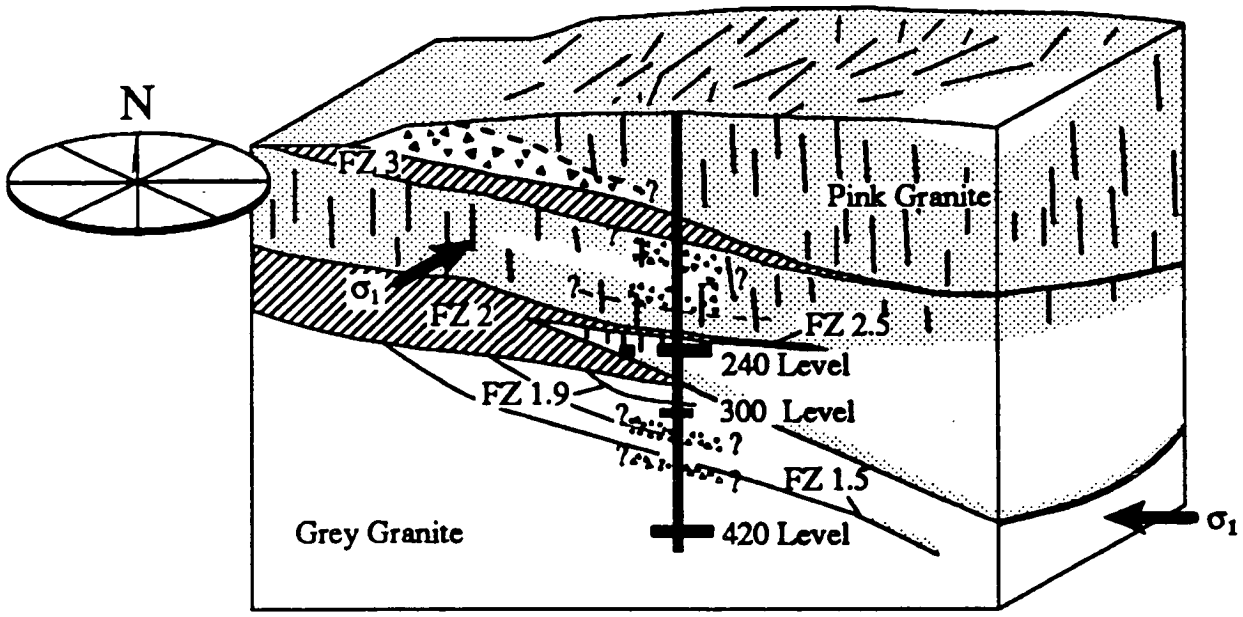

Figure 2.8: The generalized geological setting of the Underground Research Laboratory (Read and Martin, 1991).

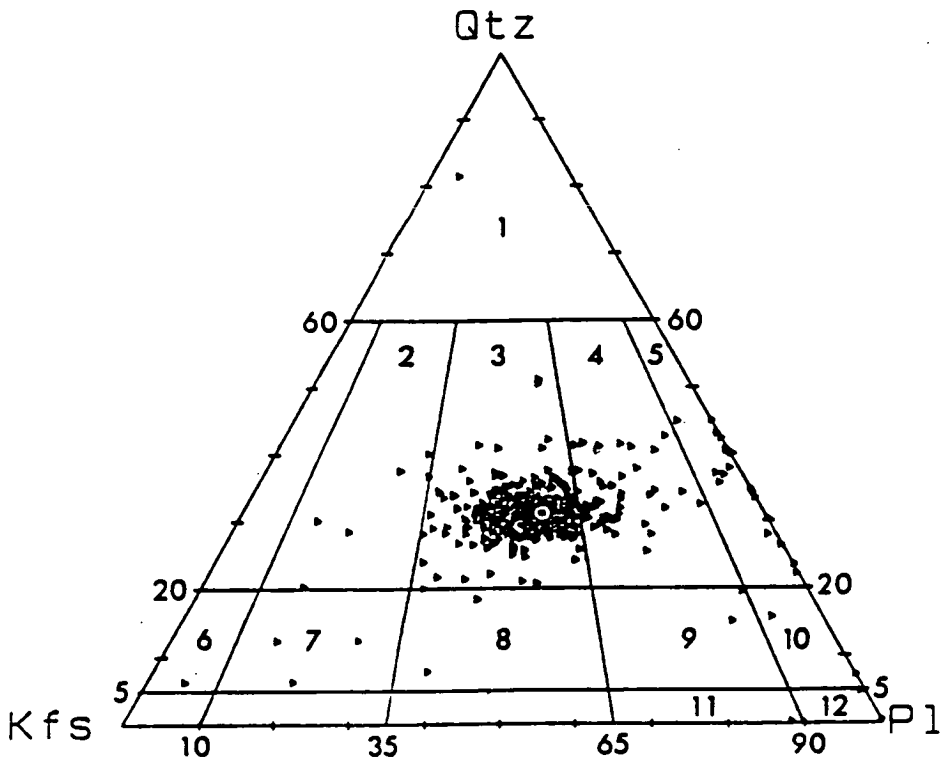

Figure 2.9: The modal composition of 932 core samples from Whiteshell Nuclear Research Establishment and the Underground Research Laboratory boreholes. The contents of each core sample in terms of quartz (Qtz), Potassium Feldspar (Kfs), and Plagioclase (Pl) are marked by triangles on the tertiary diagram. The United States Geological Survey definition of a granite is a rock whose composition plots in region 3. The average composition is marked by a dot and is that of a granite (Robertson and Chernis, 1987).

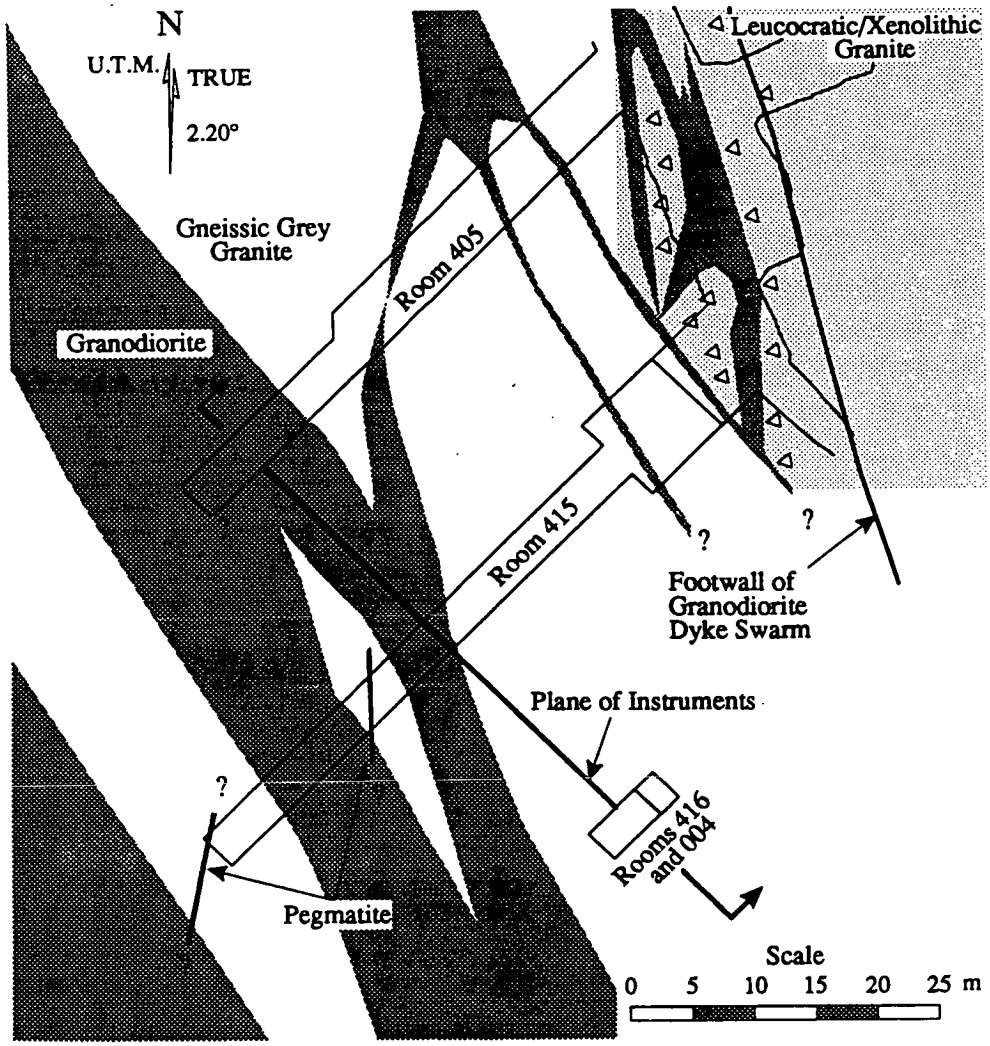

Figure 2.10: Plan view of the Mine-by Experiment showing the projected geology (Read and Martin, 1991).

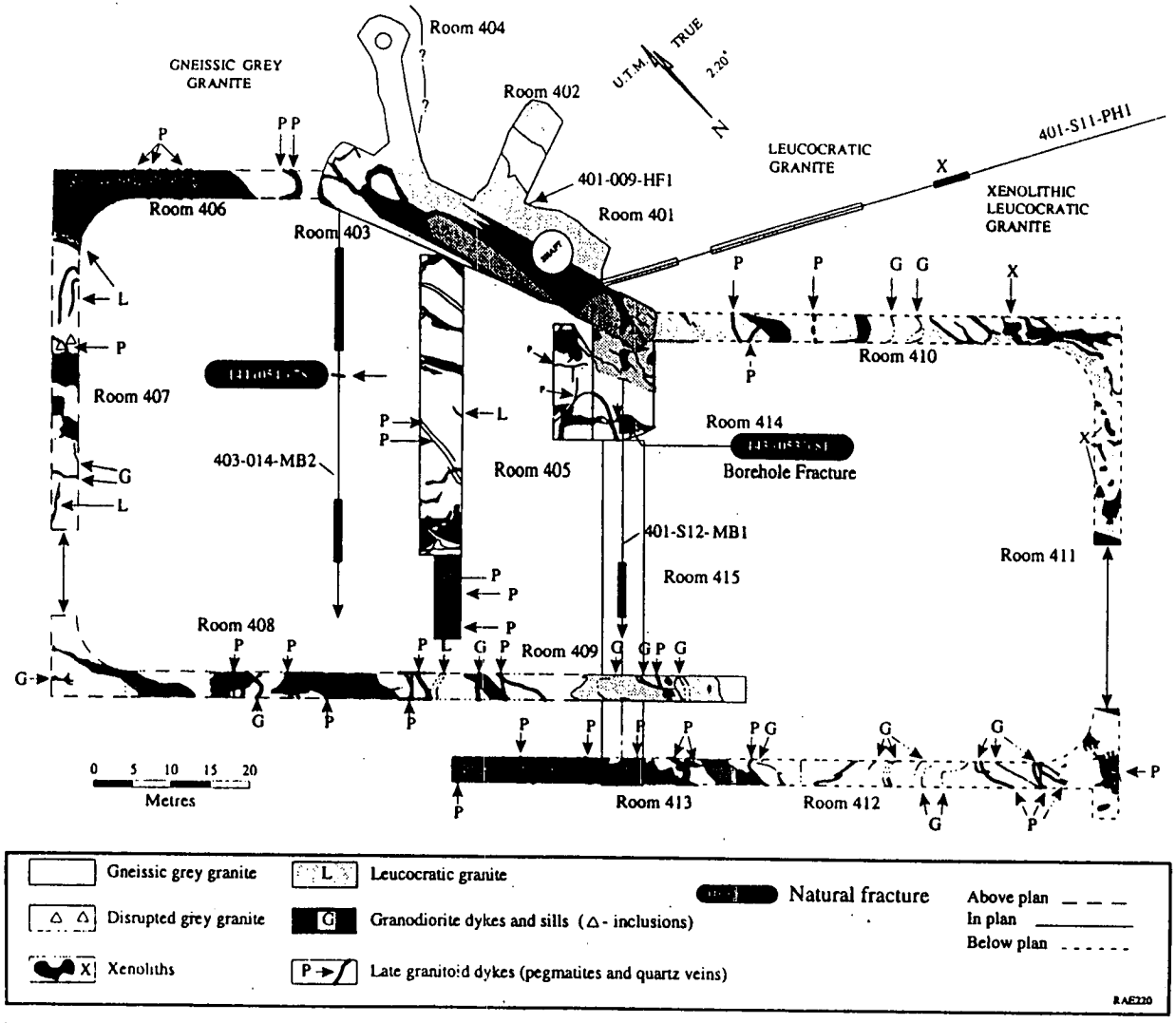

Figure 2.11: Geological Plane of the 420-Level (R. Everitt, pers. notes).

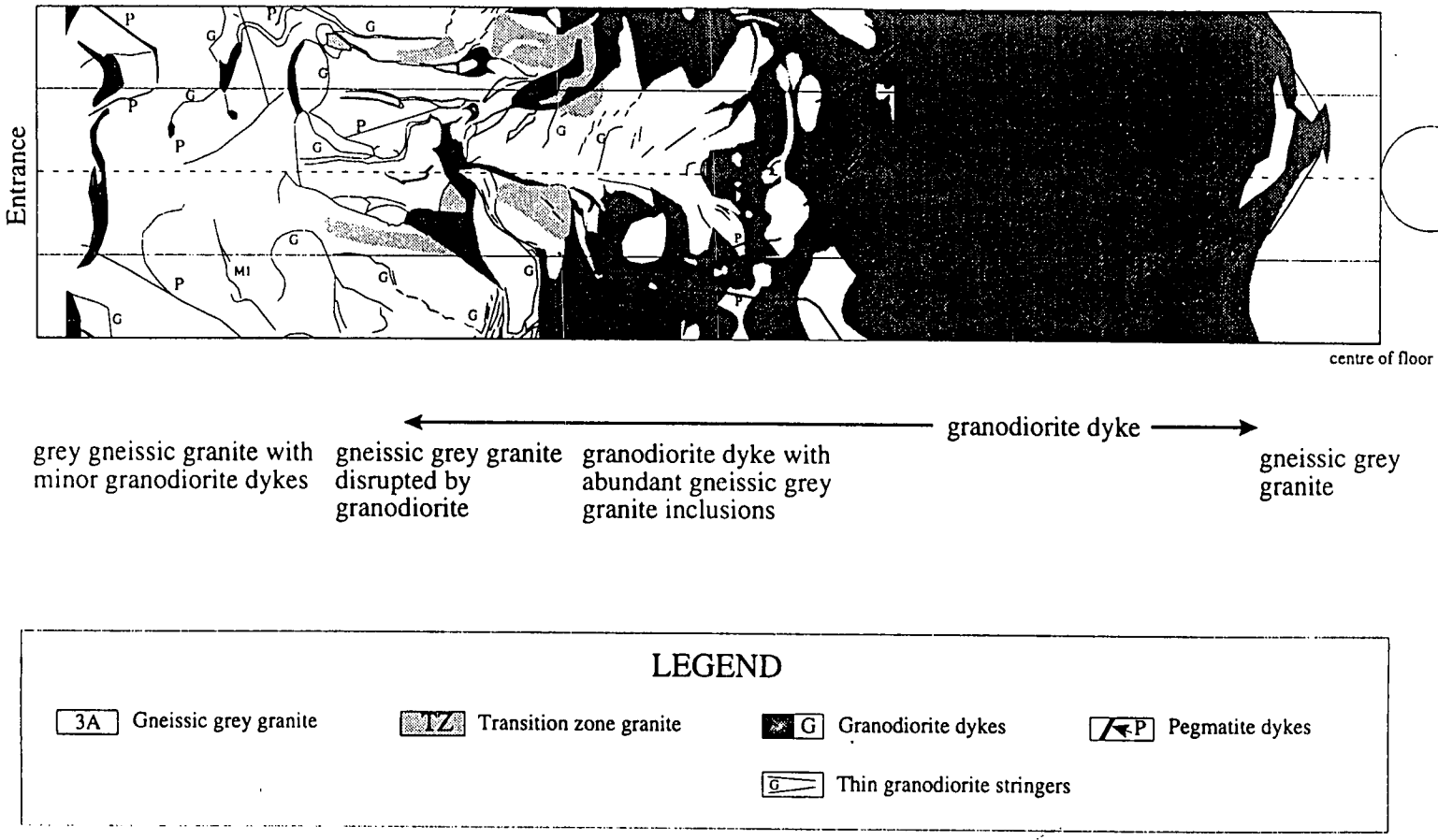

Figure 2.12: Perimeter map of Mine-by Tunnel (Room 415) showing the lithological variation (Read et al., 1992).

Table 2.3: Geomechanical Properties for the 420 Level (Read and Martin, 1991)

Rock Type	Density (g/cm^3)	Unconfined Compressive Strength (MPa)	Tangent Young's Modulus* (GPa)	Poisson's Ratio*
Measured Laboratory Properties				
Grey Granite				
Mean (n = 224)	2.63	171	58	0.28
Standard Deviation	0.01	29	8	0.06
Maximum	2.68	247	74	0.46
Minimum	2.59	111	40	0.13
Granodiorite				
Mean (n = 24)	2.66	225	66	0.28
Standard Deviation	0.02	35	5	0.05
Maximum	2.68	271	75	0.37
Minimum	2.62	155	57	0.19
Pink Granite				
Mean (n = 83)	2.63	187	69	0.25
Standard Deviation	0.01	25	4	0.04
Maximum	2.69	248	78	0.38
Minimum	2.59	134	59	0.17
Best Estimate of Undamaged Sample Properties (45-mm Diameter)				
Granite				
Mean	2.63	213	65	0.25
Standard Deviation	0.01	20	5	0.05
Granodiorite				
Mean	2.66	228	66	0.25
Standard Deviation	0.02	20	5	0.05

* Defined at 50% of Uniaxial Compressive Strength

Table 2.4: *In-situ* Stress State for the Mine-by Tunnel (after Read and Martin, 1991)

Principle stress component	Magnitude (MPa)	Trend (N°E)	Plunge (°)
σ_1	55±5	135±10	10±5
σ_2	48±5	044±10	05±5
σ_3	14±1	290±25	79±5
Stress Ratios	σ_1/σ_2	σ_1/σ_3	σ_2/σ_3
	1.15±0.1	3.93±0.3	3.43±0.5

Estimated Mean Value and 90% Confidence Interval

1.2) are nearly horizontal and almost equal at about 50MPa, with σ_1 oriented to the south-east. Such high levels of stress are typically found between 500m and 1000m depth in the Canadian Shield (Herget, 1987). σ_3 is given in Table 2.4 as oriented 11°±5° from the vertical and is less than a third of the other two stresses in magnitude. It is now known that σ_3 is 14° from the vertical (D. Martin, pers. comm.). Note that the Mine-by Tunnel (Room 415) and Room 405 are orientated approximately parallel to σ_1, and Rooms 408, 409, 410, and 413 are orientated approximately parallel to σ_2 (Figure 2.1). It is expected that EDA-cracks will be oriented perpendicular to the direction of minimum stress (section 1.2) so any EDA should have orientation 045/14.

To maximize potential excavation damage, the Mine-by Tunnel was excavated in the south-west direction, parallel to σ_2. As expected, breakout notches occurred along the entire length of the Mine-by Tunnel as the excavation progressed (except for the last metre before the tunnel face immediately following each excavation sequence). Breakout notches are a common linear feature of boreholes and underground tunnels, generally forming parallel to the direction of weakest stress perpendicular to the length of the cavity (Bell and Gough, 1979). The breakout notches in the Mine-by tunnel generally occurred between 10° and 20° to the vertical towards the south-east, broadly agreeing with the measured direction of minimum stress, σ_3, of 14° from the vertical with azimuth 110°±025°.

2.10 *In Situ* Fractures

Six significant natural fractures were encountered within the area of the Mine-by Experiment. All were closed and dry and confined to the granodiorite dyke swarm (R. Everitt, pers. comm.). Only one of the natural fractures was encountered in the Mine-by Tunnel. The fracture was oriented 040/84 and had a maximum extent of 1.5m horizontally and 0.5m vertically. The volumetric extent of the fractures is expected to be small (Read and Martin, 1991). From a high-resolution subsurface seismic reflection survey at URL, D. Gendzwill of the University of Saskatchewan found that there is the possibility of a splay from a fracture zone in the vicinity of the Mine-by tunnel (D. Gendzwill, pers. comm.). However, no such fractures have

intersected any of the tunnels of the 420-Level. With these exceptions, the *in situ* rockmass around the 420-Level appears to be massive and apparently unfractured.

2.11 Natural Microcracks

The *in situ* Lac du Bonnet granite of the 420-Level at URL exists in a far-field stress field that has a maximum horizontal compressive stress of 55MPa (Read and Martin, 1991). Extensive perturbations to the crack structure of the granite result when the magnitude of the stress field encompassing the granite is significantly released. Such stress-relief occurs by excavation or drilling when there is a zero-stress free-surface, or by complete removal of *in situ* stress in laboratory samples. Changes to structure include opening new microcracks (stress-relief microcracks) to form an additional crack fabric. In granite from the 420-Level, the stress-relief is large enough to break quartz grains (D. Martin, pers. comm.), and the effects of stress-relief alter the pattern of grain boundary cracks and transgranular cracks (cracks that cross grain boundaries) so that the *in situ* pattern of grain boundary cracks is not easily determined. Detailed reports on natural microcracks are being prepared but are not yet available.

Chernis and Robertson (1987) in a laboratory study of microcracks in the Lac du Bonnet granite, found they could discriminate between natural and stress-relief microcracks. The natural microcracks not affected by stress-relief were less than 4μm in aperture with rough and irregular walls and often contain debris. Chernis and Robertson conclude that high pressure alone would not be sufficient to close the natural microcracks. Chernis and Robertson did not report dimensions of the faces of the cracks, but the largest dimensions of *in situ* microcracks are expected to be no more than a centimetre in diameter and possibly much smaller. The dominant seismic wavelength of the shear waves of 0.81m (section 2.6) is therefore much greater than crack size.

They also reported that most grain boundary cracks form around quartz grains, and may have infillings of calcite, iron oxide, or clay. 90% of natural cracks occur along grain boundaries. The remaining cracks that could be distinguished from stress-relief cracks occur as intragranular cracks, chiefly in feldspars. Plagioclase typically contains large numbers of pores less than 5μm in diameter (Sprunt and Brace, 1974),

which may or may not be intersected by fine intragranular cracks. Intragranular cracks within potassium feldspar may be over 1μm in diameter.

2.12 Past Studies of Seismic Anisotropy in Granite and Granodiorite

Tables 2.5 and 2.6, below, summarize all laboratory and *in situ* studies known to this author on seismic anisotropy in granite or granodiorite excluding those based on the Mine-by Experiment. The 'Number of Source to Receiver Paths Examined' is in reference to the orientation of the rock sample rather the stress field. Many laboratory experiments referenced in Table 2.5 involve examining the velocity of a small number of raypaths under numerous stress magnitudes and directions.

2.12.1 Laboratory Experiments

With the exceptions of Thill et al. (1969; 1973) and Babuška and Pros (1984), the twelve laboratory studies employed no more than three source to receiver raypaths at any given stress direction and magnitude to examine the anisotropy. Three or fewer raypaths are entirely inadequate in studying the three dimensional behaviour of seismic wave propagation. Such studies can only provide broad inferences as to the cause of the anisotropic fabrics and cannot parameterize the fabrics in any detail.

The major drawback to laboratory experiments is that the rock samples have been irreversibly altered from their *in situ* state. In removing a rock sample from *in situ*, the sample is altered not only from the excavation of the rocks, but from stress-relief cracking (section 2.11). Of the ten interpretations of the laboratory results presented in Table 2.5 that interpreted the causes of the anisotropy, all but Birch (1961), cited cracks or microcracks as a cause, but the observed fabrics may well have been stress-relief cracks. The change in pressure also alters the shape of pores, causes pre-existing cracks and microcracks to change in shape and increase in size, and allows the movement and possible escape of fluids contained in the rock. These changes in taking the rock from *in situ* to the laboratory permanently alter the rock. Returning the rock to its original *in situ* pressure may reduce or remove only some of these effects so that laboratory samples cannot be expected to have the same seismic characteristics as *in situ* rock. Therefore, the results of laboratory studies cannot be used to directly infer the causes of anisotropy in *in situ* rock at depth.

Table 2.5: Published Laboratory Studies of Seismic Anisotropy in Granite and Granodiorite

Rock Type	Number of Source to Receiver Paths Examined	Attributed Cause of the Anisotropy	Reference
River Sázava Granodiorite	133	mainly cleavage cracks in biotite and amphibole	Babuška and Pros (1984)
granite (source unknown), granulite from Inari, Finland	3	microcracks orientation by grain boundaries, mineral orientation	Kern (1978)
Westerly Granite	2	mineral orientation, cracks	Soga et al. (1978)
Westerly Granite	2	cracks	Lockner et al. (1977)
Westerly Granite	1	stress-algined cracks (EDA*)	Wang et al. (1975)
Westerly Granite	2	orientation and dilation of cracks	Bonner (1974)
Barre Granite (granodiorite rock originally misnamed)	73	microcracks	Thill et al. (1973)
Granite Gneiss, Cross Lake Granite Conglomerate	3	none given	Tilmann and Bennett (1973)
Salisbury Granite	73	microfractures in quartz	Thill et al. (1969)
Barre Granite (granodiorite), Westerly Granite	2	microcracks the only specific cause cited	Nur and Simmons (1969)
Gneiss from Torrington, Conn., U.S.A.	3	pores, cracks, foliation, mineral orientation, possibly gneissic banding	Christensen (1965)
Westerly Granite, Barriefield Granite, Quincy Granite	3	mineral orientation	Birch (1961)

* denotes extensive-dilatancy anisotropy (EDA) for studies published before the fabric of stress-alignment of cracks was formally recognized and given this name.

Table 2.6: Published *In Situ* Studies of Seismic Anisotropy in Granite and Granodiorite

Recording Geometry	Location	Rock Type	Number of Source to Receiver Paths Examined	Attributed Cause of the Anisotropy	Reference
40 surface seismic stations	Japan	Many, including gneiss and granite	>180 - earthquake sources	stress-aligned cracks (EDA), cracks or fractures, intrinsic rock anisotropy from preferred orientation of minerals in the granite -mainly foliation in the gneiss	Kaneshima, S. (1990)
Same as Roberts and Crampin (1986)	Cornwall, U.K.	Carnmenellis Granite	8 induced seismic events and the same 61 events as Roberts and Crampin (1986)	EDA	Crampin and Booth (1989)
VSP -same as Daley et al. (1988), Liu et al. (1988) (below), down borehole seismic log	Cajon Pass, California, U.S.A.	granite, granodiorite, magacrystic granite, quartzite, orthogneisses	Reinterpretation of work of Daley et al. (1988), Li et al. (1988) (below)	fractures and microfractures probably formed before late Miocene-Pliocene	Blenkinsop, T.G. (1990)
VSP -same as Daley et al. (1988) (below)	Cajon Pass, California, U.S.A.	granite, granodiorite, magacrystic granite, quartzite, orthogneisses	Same dataset as Daley et al (1988) (below)	EDA	Li et al. (1988)
VSP with two offsets, geophones every 10m over 590m	Cajon Pass, California, U.S.A.	granite, granodiorite, magacrystic granite, quartzite, orthogneisses	64	Stress-induced fracturing	Daley et al. (1988)

Recording Geometry	Location	Rock Type	Number of Source to Receiver Paths Examined	Attributed Cause of the Anisotropy	Reference
4 down borehole seismometers	Cornwall, U.K.	Carnmenellis Granite	61 induced seismic events	EDA	Roberts and Crampin (1986),
down borehole seismic log and a VSP	Monticello, South Carolina, U.S.A.	Granite and Granodiorite	Continuous down borehole seismic logs, geophone at 30m intervals over 900m depth	mainly macroscopic fractures, but also microcracks, mineral orientation	Moos and Zoback (1983)

Laboratory studies have been useful in determining possible causes of anisotropy. None of the twelve studies in Table 2.5 claimed the observed anisotropy would be the same as *in situ*. Christensen (1965), Nur and Simmons (1969), Bonner (1974), Wang et al. (1975), Lockner et al. (1977), Soga et al. (1978), and Babuška and Pros (1984) all found anisotropy increased with pressure at low confining pressure (<21MPa) and attributed this to fracturing or the dilation or closure of cracks. Kern (1978) found that anisotropy decreased with pressure when rocks were under confining pressures of up to 600MPa. In this high stress, the observed decrease in anisotropy is likely due to the closure of cracks and fractures. These laboratory studies proved that cracks and microcracks can cause a significant fabric that is affected by pressure.

Non-seismic laboratory experiments have also contributed understanding to the possible causes of *in situ* anisotropy. Scholz and Koczynski (1979), showed using strain gauges that dilatancy in a sample of Westerly Granite was controlled by microcracks, and that the pattern of dilatancy was anisotropic even under uniform confining pressure. Siesgesmund and Kruhl (1991) calculated theoretical seismic velocities for a granitic gneiss from the Alpine Roof Zone of the Western Alps. They found that the preferred orientation of plagioclase can explain up to 5% shear-wave anisotropy. This shows that mineral orientation may form an important fabric *in situ*. However, in a study of the velocity of various minerals, Babuška (1981), argued that the orientations of minerals and velocities in crustal crystalline rocks would only result in 'low' seismic anisotropy, although how low was not stated. The exception to this is where a metamorphic fabric, such as gneissic layering, exists. Birch (1961), Babuška (1981), and Siesgesmund and Kruhl (1991) all observe that micas were oriented parallel to the direction of gneissic layering. Gneissic layering is generally oriented so that the normal to the layer is perpendicular to the principle stress direction (Babuška, 1981; Siesgesmund and Kruhl, 1991). Micas are highly anisotropic and may also govern that nearby cracks be parallel to the micas as well as indicating the direction of gneissic layering (Babuška, 1981; Kern et al., 1991). However, it is unknown whether such anisotropy is primarily due to the elastic properties of the minerals, or the effects of cracks whose orientations are governed by the mineral alignments. Also, such mineral-oriented intragranular cracks may be opened or closed *in situ* by changes in stress directions and so may create EDA that is

not perfectly aligned with the stress field. Therefore laboratory experiments have demonstrated that cracks can cause significant anisotropy, and suggested that mineral alignments may correspond in orientation to anisotropic fabrics.

2.12.2 *In Situ* Studies

None of the seven *in situ* studies of four data sets has resulted in an unambiguous interpretation of the cause of the *in situ* anisotropy in granite or granodiorite. Kaneshima (1990) examined shear-waves from seismic signals created by earthquakes. This study involved complicated and varied geology and the uncertainties involved in determining source parameters of the earthquakes, as well as a limited variety of raypath directions because of the shear-wave window (section 1.4). The primary cause of the anisotropy could not be determined because of the limited amount of data and the uncertainties. The studies of Roberts and Crampin (1986) and Crampin and Booth (1989) were based on a common data set from seismicity induced by hydrofracting. Anisotropy was attributed to EDA. However, polarizations directions also corresponded closely to pre-existing planes of weakness in the granite and scatter in the data and a limited variety of raypaths prevents a definitive interpretation. The exact cause of anisotropy observed in the Cajon Pass borehole studies may be due to EDA (Li et al., 1988), stress-induced fracturing (Daley et al.) or paleo-fractures and microfractures (Blenkinsop, 1990), so that the seismic anisotropy may not be clearly attributed to either stress-oriented microfractures or to fault-induced fracture fabric (Leary, 1991). The study of Moos and Zoback (1983) was a study relating acoustic wave velocities to macrofractures. It was demonstrated that shear-wave velocities decrease with increasing density of macrofractures but it could not be determined the effect of microfractures in the neighbourhood of macrofractures upon velocities. Despite these ambiguities, all studies but Kaneshima (1990) attributed the anisotropy to be due to cracks or fractures.

2.13 Velocity and Attenuation Surveys

The Attenuation Survey and the Velocity Survey are two seismic surveys performed as part of the Mine-by Experiment. Both were performed on August 10, 1992, after the Mine-by tunnel had been excavated to its completed length.

Shear-waves of the Velocity Survey data set are analyzed in the dissertation, and the results of shear-wave splitting analysis are compared to travel time analysis of these surveys (Chapters Seven and Eight).

2.13.1 Velocity Survey

The main purpose of the Velocity Survey was to calibrate the velocity structure of the rockmass for the source location of the excavation-induced seismicity. After completion of the Mine-by Tunnel excavation, twenty-seven boreholes were drilled into the Mine-by Tunnel wall. The perpendicular distances of the ends of the boreholes to the Mine-by Tunnel varied between 30cm and 70cm. Also, nine four-orientation sets of source boreholes of the same geometry as the source stations of the Shear-Wave Experiment were drilled into the Mine-by Tunnel wall. All borehole diameters were 32mm as they were for the Shear-Wave Experiment. The locations of the boreholes are as shown on the perimeter map of Figure 2.13. Controlled seismic signals were created by Mark2 seismic caps and the Schmidt Hammer-Nylon Rod sources at the ends of these boreholes. The signals that were recorded by the microseismic system (section 2.3). The time of detonation for the Mark2 cap was accurately recorded for travel time analysis. The nine source stations and the Schmidt Hammer-nylon rod sources were used to provide additional measurements of polarizations and time delays that could be combined and compared with the Shear-Wave Experiment (Chapters Seven and Eight).

2.13.2 Attenuation Survey

The Attenuation Survey was a controlled seismic survey designed to measure the rate of attenuation of seismic signals travelling through the undisturbed rockmass of the 420-Level. In this survey, Mark2 seismic blasting caps and Schmidt Hammer-steel rod sources were used at the end of twelve 1m to 3.5m long boreholes at various locations in the 420-Level (Figure 2.14). The same microseismic system recorded the seismic signals (section 2.3). The primary purpose to this survey is to measure seismic attenuation in the undisturbed rockmass near the Mine-by Tunnel. The data from this survey is of limited use in studying shear-wave splitting because of the use of single source orientation and the use of the steel rather than the nylon rod.

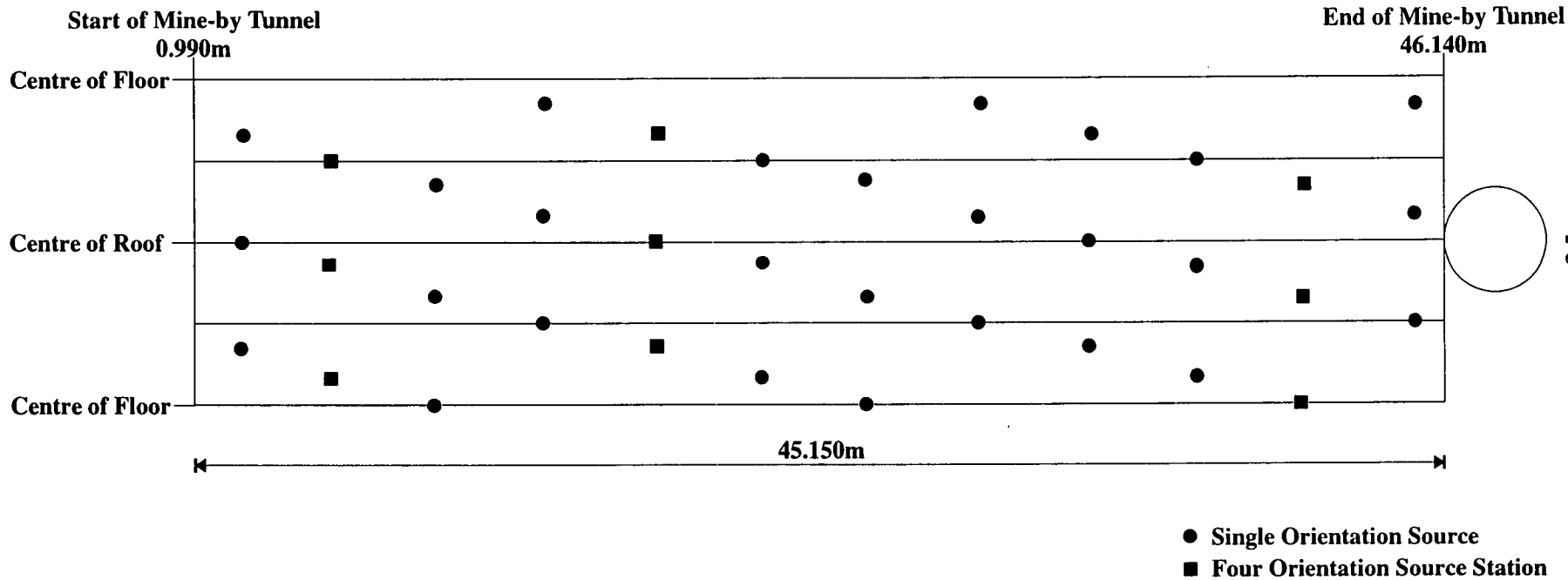

Figure 2.13: Perimeter map of the Mine-by Tunnel showing locations of the source boreholes for the Velocity Survey (after Young and Collins, 1993).

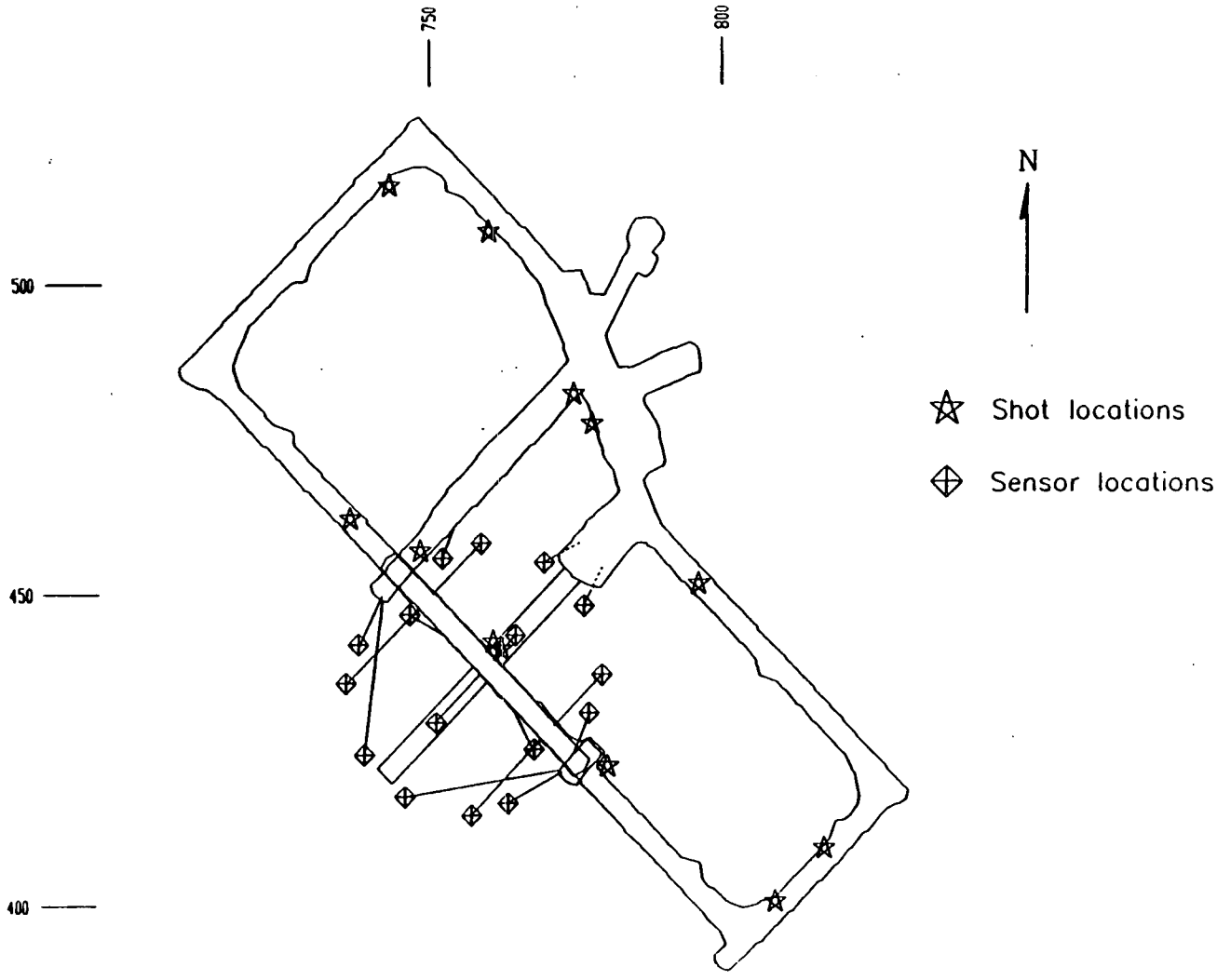

Figure 2.14: Borehole locations for the Attenuation Survey (Young and Collins, 1993).

Consequently, this data set was not analyzed for shear-wave splitting. However, this data set has two distinct benefits. Firstly, the sources were located at the end of longer boreholes than the source boreholes in the Shear-Wave Experiment. The waveforms are therefore less affected by excavation around the source tunnels. Secondly, the raypaths were approximately three times longer on average than those of the Shear-Wave Experiment, so that any damage traversed by the raypaths are smaller proportions of the overall raypath lengths. The seismic signals of the Attenuation Survey will be much less effected by excavation for these reasons.

2.14 Excavation-Induced Velocity Heterogeneity

There have been two studies completed at the time of the writing of this dissertation of the velocity heterogeneities caused by the Mine-by Tunnel excavation. The first of these studies, Carlson and Young (1993), investigates the velocity structure of the granite within the first 1.2m of the free surface of the Mine-by tunnel. The survey used 1MHz compressional transducers to measure *P*- and shear-wave travel times between four parallel 1.2m boreholes perpendicular to a 1m-side square on the tunnel wall. The borehole directions were parallel to σ_1, which is approximately perpendicular to the Mine-by Tunnel side.

The study included examining the change of velocity with distance from the free surface. *P*- and shear-wave velocities increase with distance away from the free surface, particularly within the first 0.40m to the free surface. 0.15m away from the free surface, *P*-wave velocities are within 10% of the *in situ* *P*-wave velocity of 5880m/s as measured by Talebi and Young (1989). 0.75m away from the free surface and greater, *P*- and shear-wave velocities are unchanged from the *in situ* velocities. This is clear evidence that the source locations used in the Shear-Wave Experiment, located within 0.30m from the free surface are within the zone of rockmass affected by excavation and therefore the effects of excavation must be taken into account when interpreting the data from the Shear-Wave Experiment. The velocity changes are interpreted as the effects of cracking due to tunnel excavation.

Compressional velocities are plotted on a lower hemisphere Schmidt stereonet in Figure 2.15. This stereonet indicates two crack fabrics. The direction of lowest velocity is of 155° azimuth and 15° dip, approximately. This suggests there exists a

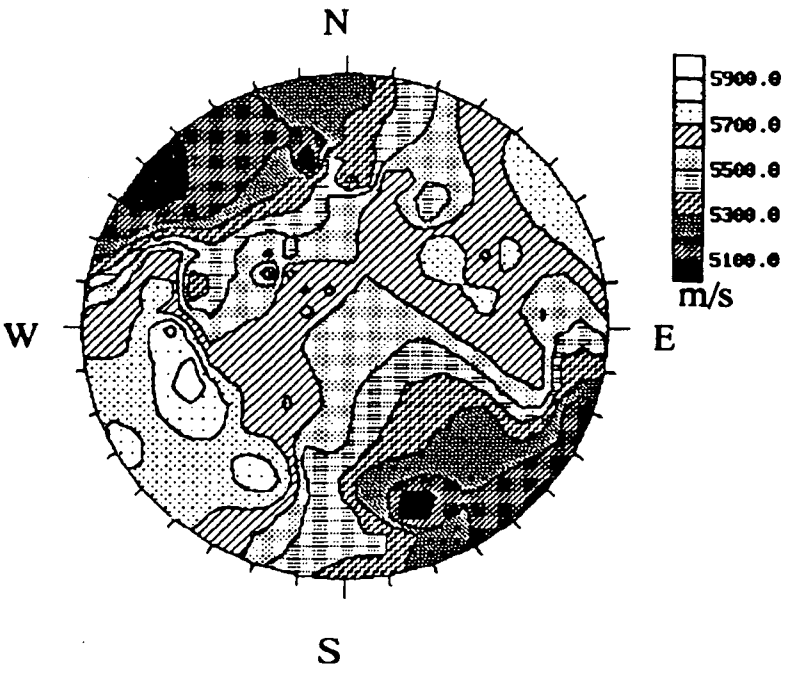

Figure 2.15: Lower hemisphere *P*-wave velocity stereonet Ultrasonic Velocity Survey (Carlson and Young 1993).

fabric of approximately 245° strike and 75° dip. This fabric is parallel to the surface of the tunnel wall and perpendicular to σ_1 and is therefore likely to be cracking due to stress relief during excavation. This agrees with the observed fractures in the discing of core samples (R. Everitt, pers. comm.). The orientation of a second, weaker fabric is indicated by the band in intermediate velocities, indicating a fabric of orientation 050/15. This is approximately the same orientation as the anisotropy expected by EDA, or the primary layering (discussed in the next section) and suggests that the stress field or mineral orientations govern the orientation of this crack set.

The second study is that of Maxwell and Young (1994). It presents contoured equal-area stereographic plots of apparent *P*-wave velocities for data of the Velocity Survey and Attenuation Survey (previous section). Apparent *P*-wave velocity is defined to be the travel time of the first arrival of *P*-wave energy divided by the straight-line raypath distance. Figure 2.16 presents the stereographic plots of apparent *P*-wave velocity from the Velocity Survey. The pattern of velocities implies the existence of two crack sets, one oriented at approximately 046/44, and the other

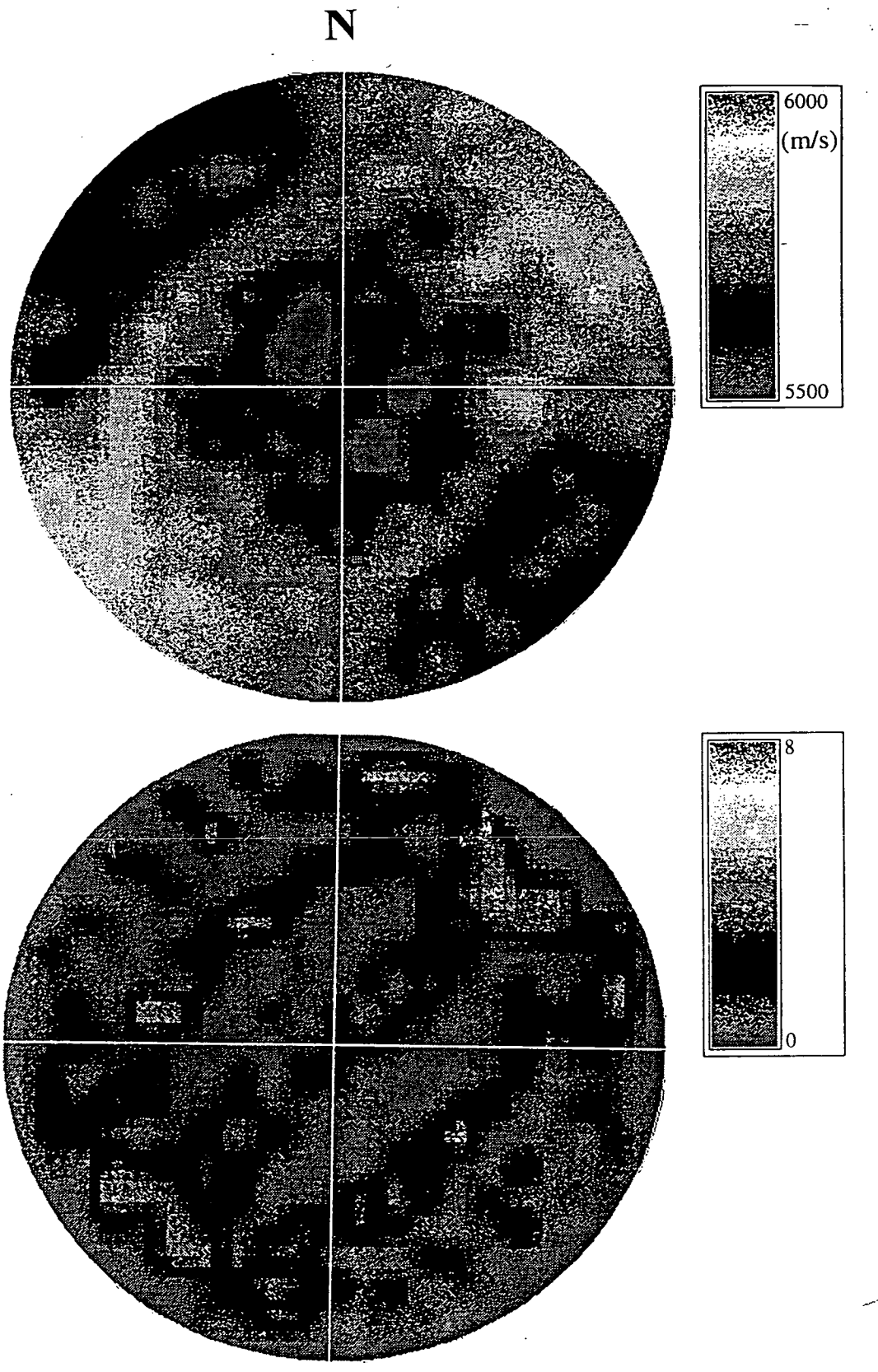

Figure 2.16: Contoured equal-area lower-hemisphere stereographic plot of apparent *P*-wave velocities (top) and the raypath coverage (bottom) for the Velocity Survey (Maxwell and Young, 1994).

perpendicular at 224/46. The pattern is attributed to two observed crack sets with similar orientations (R. Everitt, pers. comm. referenced by Maxwell and Young, 1994). The two crack sets are expected to exist *in situ* but may be enhanced by excavation (S. Maxwell, pers. comm.).

Figure 2.17 is the stereographic plots of apparent *P*-wave velocities as calculated from the Attenuation Survey data set. Raypath coverage is sparse but there appears to be a plane of higher velocities of orientation approximately 045/32 indicated by higher velocities in directions parallel to this plane. The Attenuation Survey is expected to be more representative of the behaviour of the *in situ* rockmass (section 2.13.2). Therefore the apparent *P*-wave velocities from the Attenuation Survey suggest that the *in situ* seismic anisotropy consists of a single fabric orientated approximately 045/32. Again, this is approximately the same orientation as the anisotropy expected by EDA, or the primary layering (next section).

2.15 Possible Causes of Anisotropy

Any consistent pattern that effects the elastic response of the rockmass will result in an anisotropic fabric. Table 2.7 summarises the known patterns in the rockmass at URL. The biotite and hematite alignment, and the faint gneissic banding are part of the primary compositional layering but are listed separated as they were stated by the references. This primary laying does not exist in the granodiorite dyke swarms. The dominant orientation of primary layering is 024/23, but orientation can be highly variable, particularly when disrupted by granodiorite dykes (R. Everitt, pers. comm.). There exists flow banding of variable orientation within the granodiorite. Two sets of aligned microcracks are believed to exist *in situ* (S. Maxwell, pers. comm.), but the results of Maxwell and Young (1994) (previous section) suggest that the anisotropic effects of the microcracks are not seen by raypaths travelling through the undisturbed rockmass. The stress field implies a fabric of EDA-cracks of orientation 045/14 (section 2.9).

The granodiorite differs from the granite only slightly in density and mineral composition (section 2.8). The interface between the two slightly different rock types is diffuse with the two rock types intermixing as is common with intrusive swarms.

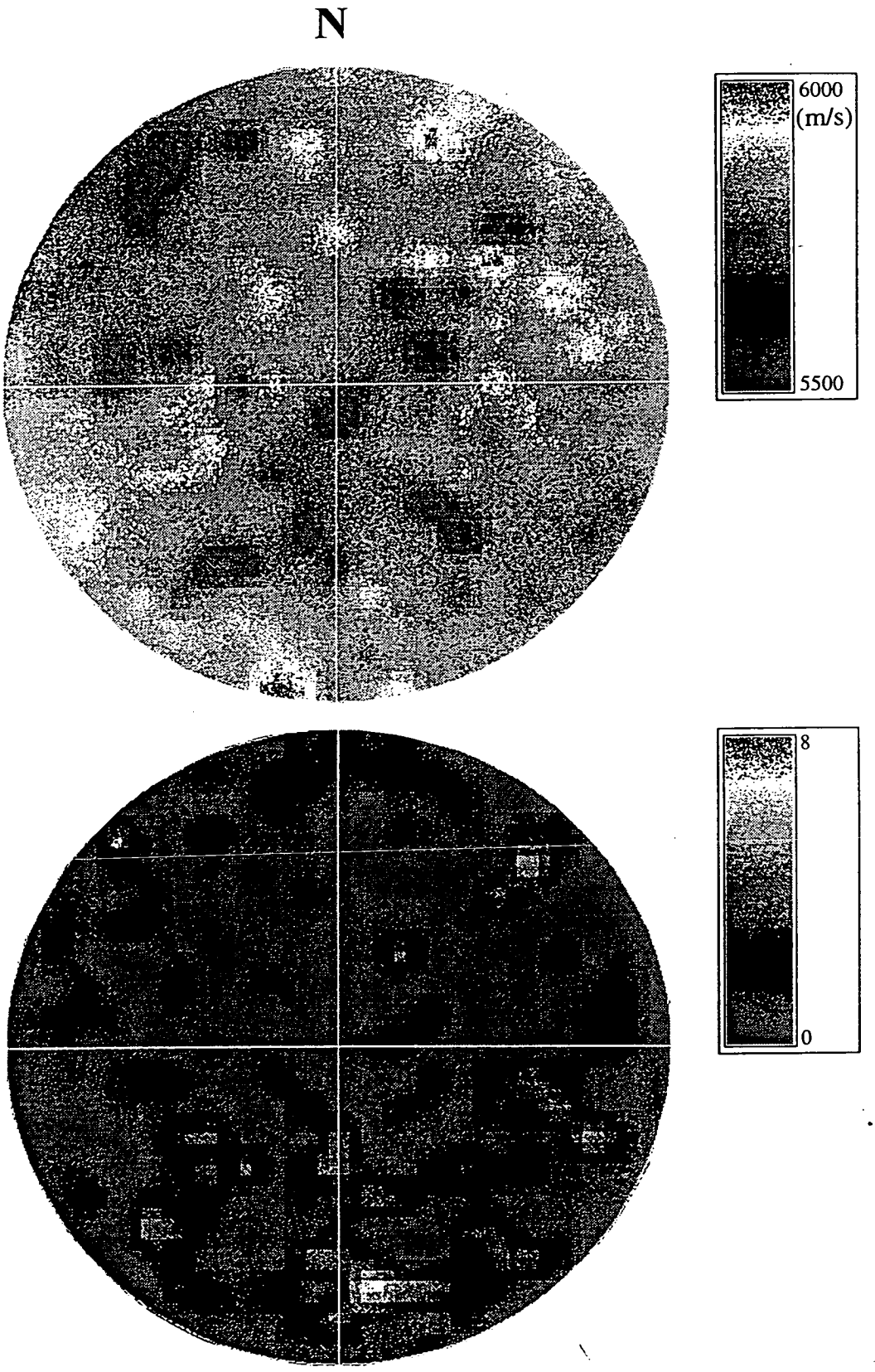

Figure 2.17: Contoured equal-area lower-hemisphere stereographic plot of apparent *P*-wave velocities (top) and the raypath coverage (bottom) for the Attenuation Survey (Maxwell and Young, 1994).

Table 2.7: Known patterns in the Rockmass of the 420-Level

Pattern	Orientation Strike/Dip (°)	Reference
Primary Layering	023/24 035/23	Personal Notes, R. Everitt Read et al.
Granodiorite Dyke Swam	340/(60-70)	Personal Notes, R. Everitt
Biotite, Hematite Alignment	020/20	Personal Notes, R. Everitt
Gneissic Banding	055/25	Read et al.
Flow Banding	040/30	Read et al.
Two sets of aligned microcracks striking NE, moderately dipping in opposite directions. One of the sets may consist of two subsets of cracks with slightly different strikes.	two sets both striking NE with moderate dips in opposite directions	Pers. Comm. with R. Everett referenced by Maxwell and Young, 1994

Therefore, the contact between the granite and granodiorite is not expected to cause detectable reflections.

The two likely causes of any anisotropy within the rockmass are therefore the faint primary (gneissic) layering of dominant orientation 023/24 and EDA-cracks of orientation 045/14. This is supported (section 2.14) by the apparent *P*-wave velocities of the Attenuation Survey and the results of the microseismic study of Carlson and Young (1993). Note that these orientations of 023/24 and 045/14 differ by only 12°. Several studies have found that if two fabrics have similar orientations, then an analysis of shear-wave splitting is unlikely to resolve the separate fabrics. Instead an effective fabric that describes the combined effect of the two fabrics will be found (Winterstein, 1990; Liu et al., 1993b; Crampin, 1993b). Specifically, Liu et al. (1993b) showed models where two sets of biplanar cracks of orientation within 50° to each other form a pattern of polarizations almost indistinguishable from that of an medium containing a single set of cracks. Therefore the pattern of polarizations observed will appear to be that of a single set of cracks if both primary layering and EDA-cracks contribute significantly to the anisotropy.

2.16 Summary and Conclusion

This chapter presented a complete description of the Shear-Wave Experiment upon which this dissertation is based. This experiment is unique. It allows the observation of shear-wave splitting for a greater variety of raypath directions than any previous *in situ* study. The geology is that of a relatively homogenous, unfractured granite rockmass.

I demonstrated that the measured triaxial accelerometer alignments were incorrect and calculated the correct orientations using *qP*-wave particle motion directions. Triaxial accelerometers 1 and 16 had rotated within their source boreholes by 29.3° and 45.8°, respectively, while the other triaxial accelerometers had rotated on average 8.3° within their boreholes.

I also presented a complete review of pass studies of anisotropy in granite and granodiorite. Pass laboratory studies have demonstrated that cracks can be a significant fabric and cracks can be aligned by stress. Past *in situ* studies primarily

attributed the seismic anisotropy to fractures, cracks, and EDA-cracks, but no study could unambiguously explain the cause of the anisotropy.

The experiment is highly controlled. The source and triaxial accelerometer locations were surveyed to a precision of 2cm, and the method of actively producing the seismic signals is highly reproducible (section 5.3) and creates a clear, impulsive shear-wave arrival. Lastly, the experiment was repeated thirteen times as the Mine-by tunnel was excavated. This will help determine the effects of excavation and the changes in the stress field due to the excavation will help determine the importance of EDA as a fabric in the rockmass. This experiment will therefore allow the most detailed examination of the geological causes of anisotropy in a granite rockmass to date.

3 Measuring Shear-Wave Polarizations and Time Delays

3.1 Abstract

The use of a controlled source and multiple source orientations in the Shear-Wave Experiment allows the reliable hand-picking shear-wave polarizations and time delays. The initial shear-wave particle motion due to the controlled seismic source in the Mine-by Experiment matches that expected for a directional point source oriented by the source impact along the source borehole. The raypaths from the four source orientations at a given source station to a given accelerometer are virtually identical. I extend the method of hand-picking polarizations and time delays to include the comparison with four three-component seismograms and comparison to the particle motion expected for an isotropic rockmass. This greatly reduces the chance of mistakes in picking polarizations and time delays and allows the clear identification of raypaths where no splitting occurred.

3.2 Introduction

Chen et al. (1987) gave the first detailed description of how to hand-pick the *qS1*-wave arrival and the time delay using three-component seismograms and particle motion diagrams. The following is a summary for the ideal case where shear-wave splitting is recorded within the shear-wave window by a three-component geophone where the shear-wave energy is mostly contained on the horizontal components:

1. Rotate the horizontal-component seismograms into components that are radial and transverse with respect to the line between epicentre and receiver.
2. Identify the onset of the first shear-wave arrival.
3. Determine the shear-wave polarization by measuring the angle of the first linear motion on the corresponding particle motion diagram.

4. The arrival of the *qS2*-wave is marked by an abrupt change in the direction of particle motion. Time delay is the duration for which particle motion is linear.

This method has serious drawbacks. It is subjective and prone to human bias in what are often difficult judgements in attributing particle motion to be that of the *qS1*- and *qS2*-waves. Applying this method to a large data set is tedious and so may lead to inconsistency in judgement. These problems are particularly acute in earthquake studies where typically complicated seismograms result from inhomogeneous geology. For example, there was a debate over the reliability of the time delay measurements for a data set recorded by the Anza three-component seismic network, California, U.S.A. (see Peacock et al., 1988; Crampin, 1990; Aster et al., 1990; Aster et al., 1991; and Crampin et al., 1991).

The controlled source shear-wave data from the Mine-by Experiment has several advantages over earthquake data for hand-picking polarizations and time delays. These advantages are:

1. Accurately known source and receiver locations. Source and receiver location co-ordinates are surveyed to an accuracy of better than 2cm where the straight source-receiver raypaths varied from 7.70m to 71.79m.
2. A simple, impulsive, and repeatable source (as demonstrated in sections 3.4 and 5.3).
3. Shear-wave particle motion directions and amplitudes that can be calculated from a known source radiation pattern (as demonstrated in section 3.4).
4. A uniform rockmass (section 2.10) so that there are no complications due to trapped waves, or major wave conversions from internal interfaces.
5. The comparison of seismograms for shear-waves from different source orientations but propagated along virtually the same path (The straight source-receiver raypaths varied in direction by no more that 3.0°.).

In this chapter I shall extend the method of Chen et al. (1987) to fully exploit these advantages. I demonstrate that these advantages greatly reduce the chances of misjudgement, inconsistency in judgement, and misinterpretation in hand-picking polarizations and time delays. As necessary preparation, I first introduce the dynamic co-ordinate system necessary for this method, demonstrate that the shear-wave motion due to the source can be determined. I then describe the method and give examples of

its effectiveness. Lastly I discuss complication due to reflected waves. I will use the term *set of raypaths* to refer to the four nearly identical raypaths from a given source station to a given triaxial accelerometer.

3.3 Co-ordinate System for Measurement

The raypaths of the Shear-Wave Experiment span a large variety of directions. No common static co-ordinate system, as commonly used in VSP data sets and earthquake studies, exists that can isolate the majority of shear-wave energy on two channels for all raypath directions. A dynamic co-ordinate system, where each three-component seismogram is rotated to a different set of directions relative to the source-receiver directions, must be used for this data set.

I will use what I call the TS-TH-R co-ordinate system. The seismograms were rotated using the straight source to receiver raypaths into: the radial (R) component; the transverse-horizontal (TH); and the transverse-sagittal (TS) component (Figure 3.1). Because it can be assumed there are no significant internal interfaces within the rockmass (with the exception of the excavation damage), shear-waves are unlikely to be disturbed by interference with internal discontinuities (Liu and Crampin, 1990), and straight raypaths can be assumed. Thus the R component seismograms will predominantly contain the *qP*-wave energy while the TS and TH component seismograms will contain almost all the shear-wave energy. This dynamic co-ordinate system may be used for any study of shear waves including earthquake and VSP studies and therefore is a more general co-ordinate system for use. I expect it to be used more commonly in the future shear-wave studies where not all raypaths are subvertical, such as far-offset VSP's or other experiments in mines.

3.4 Use of a Controlled Source

I claim that the shear-wave source radiation pattern created by the nylon rod-Schmidt hammer source is approximately that of a directional point source in an isotropic medium so that the modelling of such a source can be used to predict particle motions where no shear-wave splitting occurs.

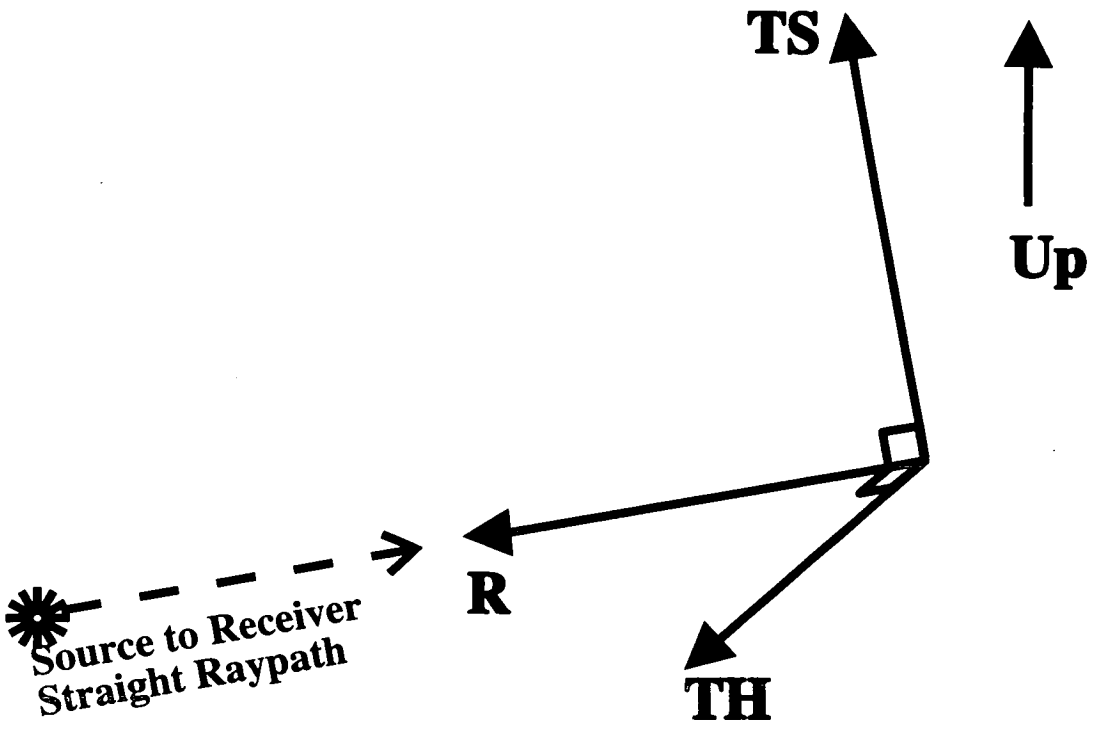

Figure 3.1: Diagram illustrating the co-ordinate system used in examining the seismograms. The radial (R) direction is the source to receiver and contains predominantly *qP*-wave energy. The transverse-horizontal (TH) and transverse-sagittal (TS) channels contain mainly shear-wave energy.

The far-field shear-wave motion due to such a point source is:

$$u_i(\mathbf{x}, t) = \frac{1}{4\pi\rho\beta^2}(\delta_{ij} - \gamma_i\gamma_j)\frac{1}{r}X_0(t - \frac{r}{\beta}); \qquad (3.1)$$

(Aki and Richards, 1980), where $u_i(\mathbf{x}, t)$ is the shear-wave motion at co-ordinates $\mathbf{x}$ and time t and source to receiver distance r, and the rockmass has density ρ, and shear-wave velocity β. X_0 is the source function in the direction of motion. γ_i is the cosine of the angle between the direction of propagation and the direction of movement at the source, and δ_{ij} is the Kronecker delta function.

Such a radiation pattern is expected because the Schmidt Hammer is designed to created on impulsive signal and direction of the source is expected to be parallel to the direction of the nylon rod as one end is pulsed. The approximation of a point source is valid because the area of contact between the nylon rod and the rockmass was no greater than 1.5cm. I calculated both the directions of particle motion and amplitudes

of the shear wave as would displayed on polarization diagrams if no splitting were to occur by using equation 3.1. The success of this modelling is demonstrated in section 3.6.

This modelling of the source assumes an isotropic media. The shear-wave source radiation pattern in an anisotropic medium differs substantially from an isotropic medium, as demonstrated by Gajewski (1993) assuming fluid-filled Hudson Cracks with anisotropic strength of 7%. I suggest the success in approximating the source as isotropic is due to the low anisotropic strength of the rockmass, as modelled using fluid-filled Hudson Cracks (section 8.8).

3.5 Picking Polarizations and Time Delays Using Multiple Seismograms

I now describe the general method for picking shear-wave polarizations and time delays using the comparison of seismograms from four source orientations and the calculated shear-wave particle motions for an isotropic rockmass. The method is an extension of that of Chen et al. (1987) and can be applied to any data set where multiple seismograms with predictable isotropic shear-wave particle motions can be compared.

Figure 3.2 is a flow chart that describes the idealized method used in picking the shear-wave polarization and time delay using four seismograms. The arrival time of the first direct shear wave may be obscured by inference from sensor resonance or the *pS*-wave (section 3.7), which could result in an incorrect pick of the direct shear-wave arrival. Seismograms with such problems are not considered when picking. Also, shear-waves of low amplitudes due to propagation near nodal directions are more susceptible to noise and interference. Such cases are easily identified both by examination of the seismogram and the calculated shear-wave amplitudes, and slightly different apparent polarizations and time delays to the other seismograms of the set. Polarizations and time delays are not measured on such seismograms.

A problem typical to most shear-wave studies using natural seismic sources is that no splitting occurs in an anisotropic rockmass if the shear-wave motion due to the source is aligned with the either the *qS1*- or *qS2*-wave motion. Consequently, if the initial linear motion matched that expected for an isotropic rockmass, then it cannot be determined whether the linear motion is the *qS1*-wave polarization, the *qS2*-wave

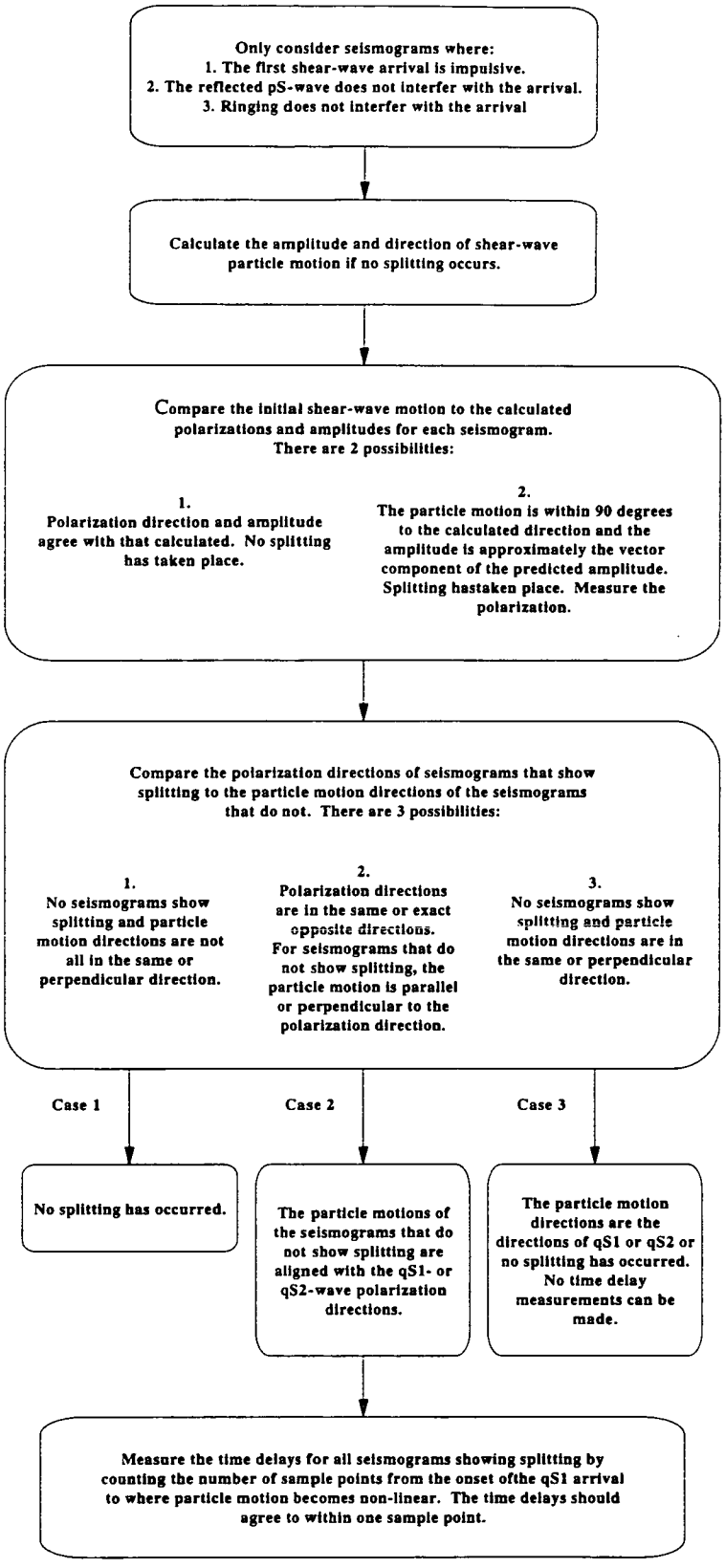

Figure 3.2: Flow chart describing the idealized method used in picking the shear-wave polarizations and time delays using multiple seismograms for the same raypath but different source radiation directions, and expected shear-wave particle motion is there is no splitting.

polarization, or that no splitting has occurred. In such cases no time delay measurement can be made. The orientation of the four source boreholes ensured that this situation is not possible for all four seismograms in a set. Rather, this coincidental alignment is easily identified when the initial linear motion matches that expected for an isotropic rockmass, and this linear motion is parallel or perpendicular to the polarization direction indicated by other seismograms in the set. Polarizations and time delays are then measured using the other seismograms.

I summarize the method as follows:

1. Discard seismograms for which the initial shear-wave arrival is disturbed by the *pS*-wave or sensor resonance.
2. Find the consistent explanation for the shear-wave particle motion. The initial linear motion from the remaining seismograms should either:
   a) Agree with each other, and the amplitudes of the first linear motion are approximately the vector component of the predicted isotropic linear motion (accounting for seismograms where the particle motion predicted for an isotropic rockmass coincidentally agrees with the *qS1*- or *qS2*-wave particle motion direction.). The initial linear motion is therefore the polarization direction of an anisotropic medium. The duration of linear motion after the initial shear-wave arrival should also agree, and therefore indicate the time delay.
   b) Agree with their calculated isotropic linear motion in direction and amplitude, thereby indicating either an isotropic medium or propagation near singularity directions.

Qualitative decisions are inevitably involved. Questions not quantitatively specified include how closely must polarizations agree to conclude that the seismograms show consistent splitting, and how non-linear the initial shear-wave motion must become to signify the *qS2*-wave arrival. To quantify every decision would involve a flow diagram too complex to be applied in practice and too customized to apply to other data sets. Also, the approximation of an isotropic source (section 3.4) will be less successful when applied to media of greater anisotropic strengths and so predicted amplitudes and directions will not closely match observed. The key concept is that a consistent and plausible explanation for the shear-wave

behaviour of all seismograms must be found. The idealized flow diagram acts as a guide.

Consistent and plausible explanations were found for all but two of the 156 sets of seismograms I examined. The two exceptions may be due to anomalous geology along the raypaths or propagation near singularity directions where polarizations vary rapidly for small changes in propagation direction (section 1.8).

3.6 Examples

In this section I present examples to illustrate the method of picking polarizations and time delays. In doing so, I demonstrate the effectiveness of the method.

Figure 3.3 presents the simplest example. The initial linear motion is approximately 038° for a duration of 5 sample points (100μs), and the amplitude of the motion is approximately the vector component of the predicted isotropic amplitude for all four seismograms. I therefore conclude that the direction of linear motion is the polarizations and the duration is the time delay.

In Figure 3.4 the effects of ringing, and the *pS*-wave reflections on the linear motion can be seen by comparing the four seismograms. The linear motion differs only slightly due to the ringing (seismograms 2 and 3) and the *pS*-wave reflections (seismograms 1 and 3) from that of the only seismogram not suffering from interference (seismogram 4). Seismogram 4 indicates a polarization of approximately 067° and a time delay of three sample points (60μs).

Figure 3.5 is an example of a raypath where no splitting occurred. The directions and amplitudes of initial shear-wave motion agree with that of an isotropic rockmass for all seismograms except for seismogram 4, where the shear wave was of very low amplitude due to propagation near a nodal direction.

Figure 3.6 is the most complex comparison encountered. Seismogram 2 displays clear splitting with a polarization direction of approximately 092° with a time delay of eight sample points (160μs) and is the only seismogram that can be used to measure splitting. In seismogram 1, the predicted isotropic shear-wave motion is parallel to the *qS1*-wave direction and no splitting takes place. Similarly, in seismogram 3, the initial shear-wave motion is parallel to the *qS2*-wave. Lastly, seismogram 4 suffers

Figure 3.3: The four 3-component seismograms from source station 2 to accelerometer 13. The direction and approximate amplitude for an isotropic medium are displayed in a single particle motion diagram (PD) below the seismograms. PD's of the TS-TH plane are displayed below this single PD for the 0.25μs time intervals marked above the shear waves on the seismograms. The numbers above the PD's are the numbered time intervals and the relative multiplication factors for scale. Ticks on the PD's are every 0.02μs. Large and small arrowheads denote estimated onsets of the *qS1*- and *qS2*-waves, respectively. All four seismograms show clear splitting with approximately the same polarizations and time delays as expected. In seismogram 4 the shear-wave particle motion from the source was nearly the same as the *qS2*-wave polarization direction. Consequently the amplitude of the *qS1*-wave arrival is relatively low and the polarization is less clearly display. The *pS*-wave arrives after the direct shear waves for all four seismograms.

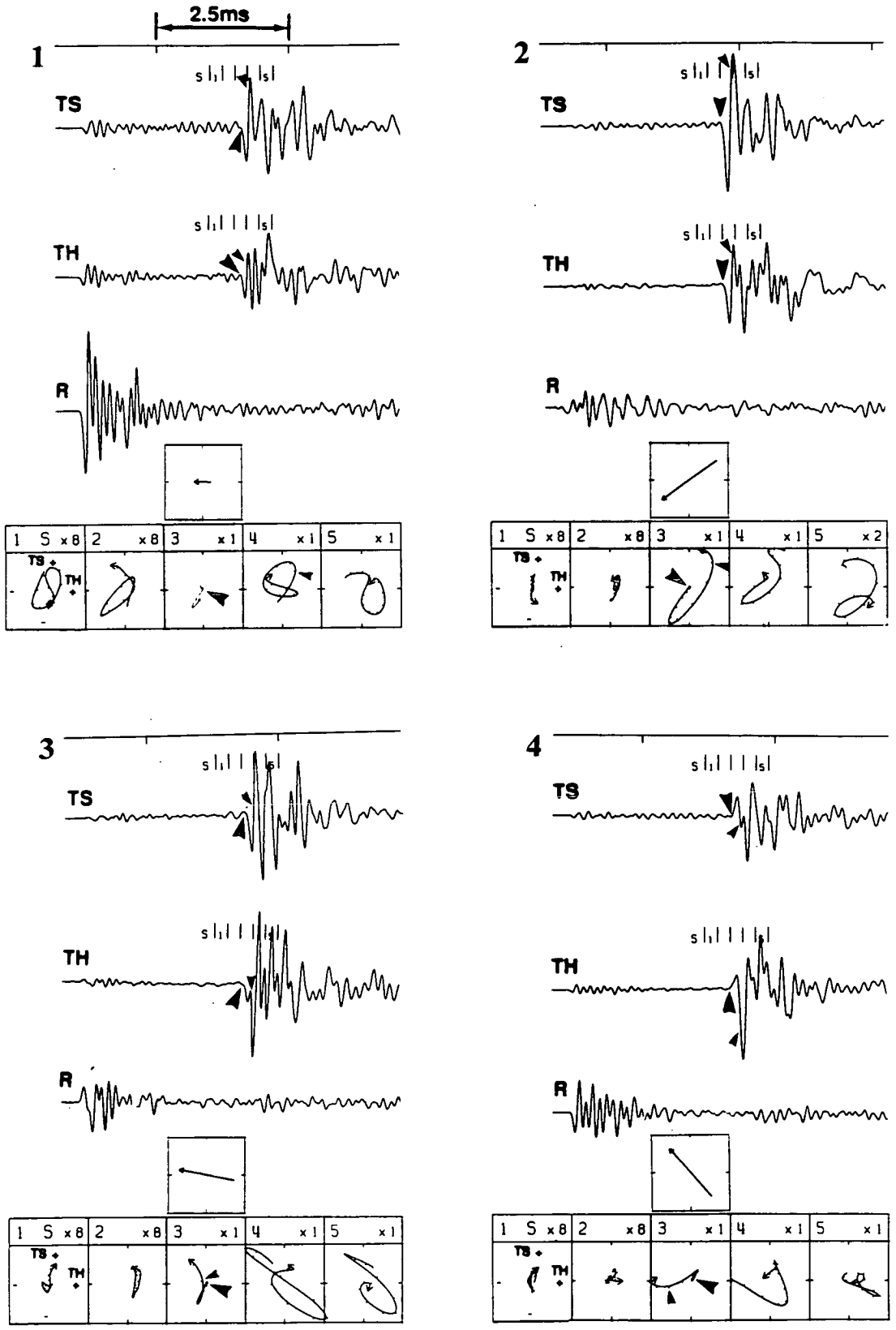
2.5ms
1
TS
TH
R
1 S x8
2 x8
3 x1
4 x1
5 x1
2
TS
TH
R
1 S x8
2 x8
3 x1
4 x1
5 x2
3
TS
TH
R
1 S x8
2 x8
3 x1
4 x1
5 x1
4
TS
TH
R
1 S x8
2 x8
3 x1
4 x1
5 x1

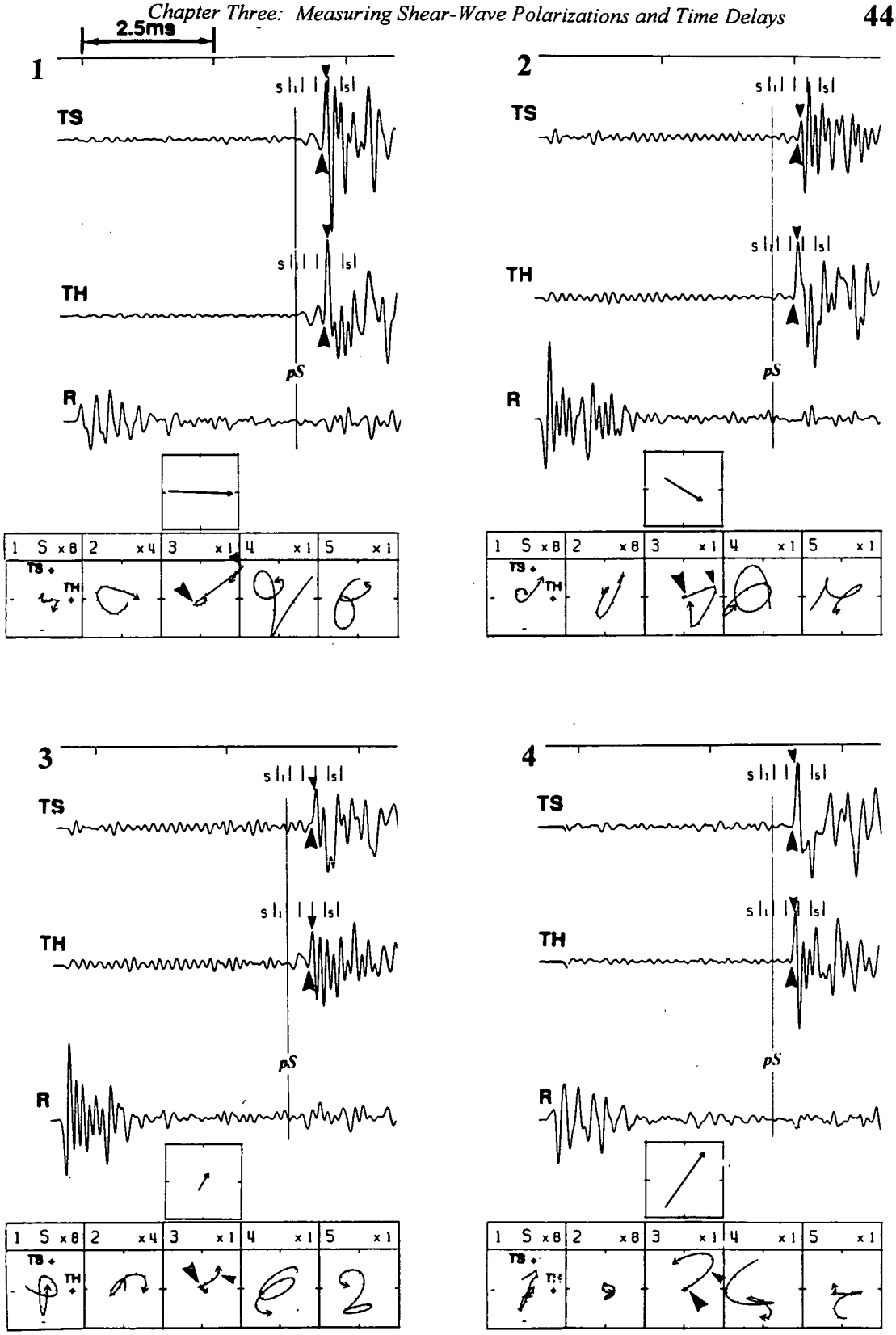

Figure 3.4: The four 3-component seismograms from source station 12 to accelerometer 14. Notation as in Figure 3.3. Vertical lines mark the calculated times of arrival of the *pS*-wave before the direct shear wave assuming an isotropic rockmass. The *pS*-wave arrival can be clearly seen on seismograms 1,2, and 3 and masks the exact arrival of the *qS1*-wave. The *pS*-wave arrival is not seen on seismogram 4 because the initial *P*-wave propagation direction was near a nodal direction in the *P*-wave radiation pattern. Consequently, the *pS*-wave does not affect seismogram 4 and this seismogram is used to measure polarization and time delay.

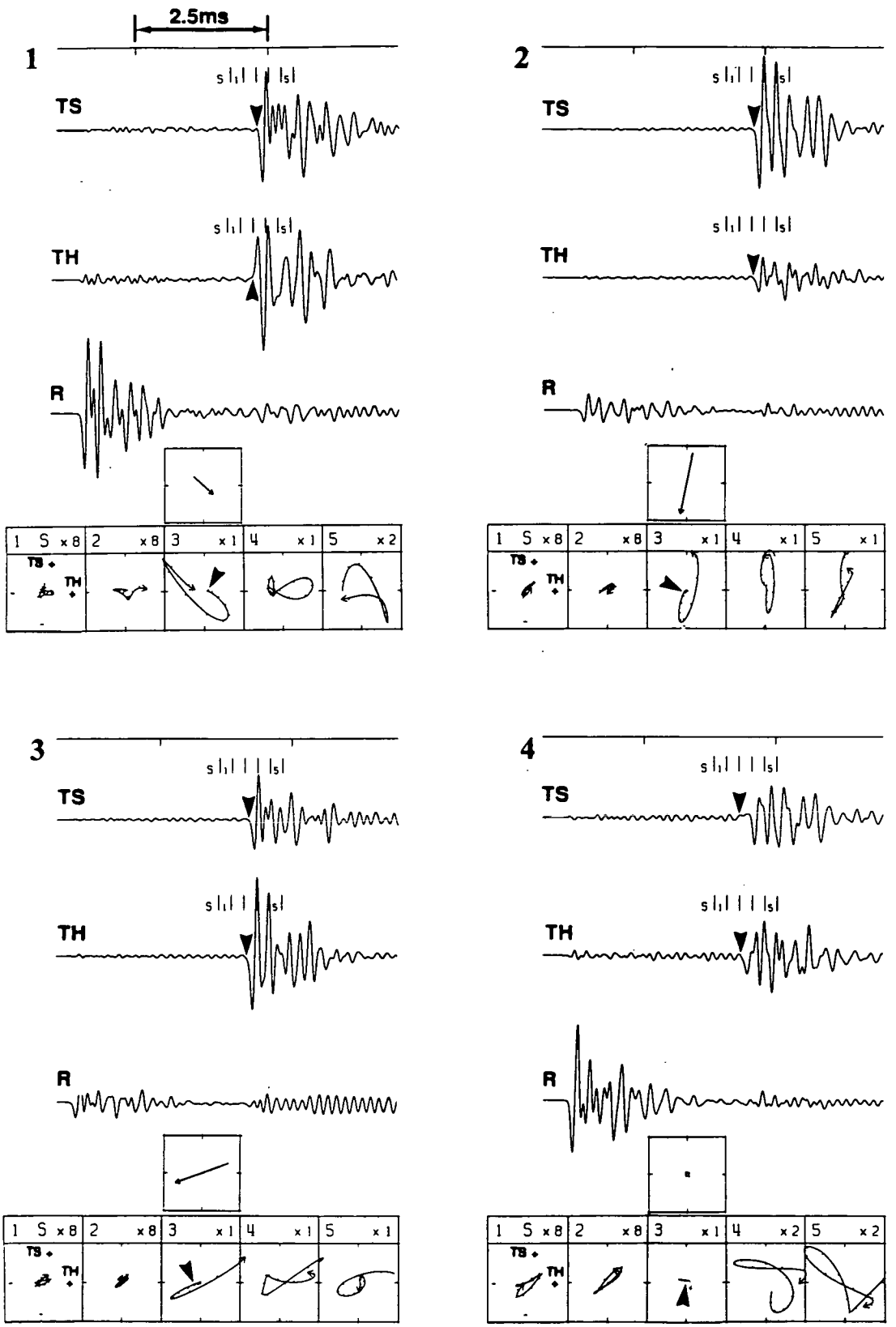

Figure 3.5: The four 3-component seismograms from source station 8 to accelerometer 15. Notation as in Figure 3.3. Shear-wave motion in seismograms 1, 2 and 3 agree with the calculated motion. The direction of the raypath of seismogram 4 was near a nodal direction of the shear-wave radiation pattern and the corresponding the shear wave displays anomalous behaviour. Clearly for this raypath no splitting occurred. The *pS*-wave arrived after the direct shear wave.

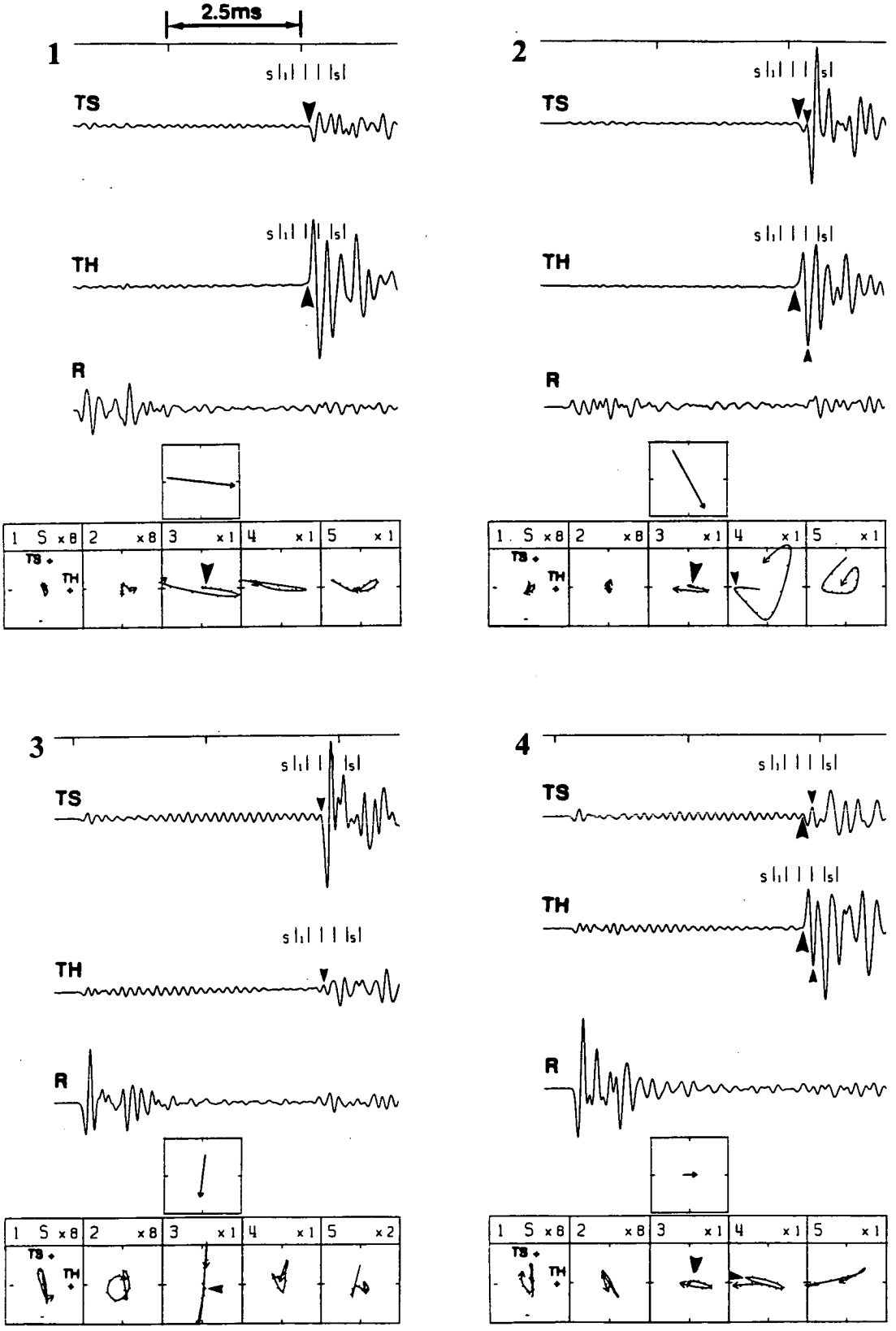

Figure 3.6: The four 3-component seismograms from source station 8 to accelerometer 14. Notation as in Figure 3.3. The *pS*-wave arrives within four sample points (80μs) after the *qS1*-waves. Seismogram 2 shows clear splitting. Seismogram 1 shows no *qS2*-wave because the shear-wave motion due to the source was parallel to the *qS1*-wave polarization. Similarly, seismogram 3 shows no *qS1*-wave. Seismogram 4 is from a raypath direction near a node of the shear-wave radiation pattern and suffers from ringing.

interference from ringing and is of low amplitude because the direction of propagation was near a nodal direction, so that it must be discarded.

Thus I have made a consistent and plausible explanation for the shear-wave behaviour in these examples. Clearly picking using multiple seismograms rather than just one prevents the misinterpretation due to interference, and greatly reduces the chances of miss-identifying arrivals. Therefore results are much more reliable.

3.7 The *pS*-wave and *sS*-wave Reflections from Outer Tunnels

The controlled seismic sources all took place at the end of 40cm boreholes drilled at 45° to walls of the outer tunnel so that all sources were within 29.5cm to a tunnel wall. Therefore waves reflected off source tunnels are of similar path lengths to the direction waves. I will refer to the *P*-wave reflected off an outer tunnel as the *pP*-wave, and the *P*-wave reflected as a shear-wave as the *pS*-wave. Similarly, I will refer to the shear-wave reflected as a *P*-wave as the *sP*-wave and the shear wave reflected as a shear wave as a *sS*-wave. I will not consider the splitting of the reflected shear-waves as their amplitudes are too small for splitting to be identified reliably. The *pP*- and *sP*-waves arrive just slightly after the direct *P*-wave and are of no concern in this study.

3.7.1 Evidence of the Reflected Waves

I claim that the behaviour expected for *pS*- and *sS*-waves is displayed on the seismograms. The amplitudes of the *pS*-waves are expected to be substantially smaller than the direct shear waves if this reflected wave is to interfere with the direct shear waves. This is mainly due to the geometry of the raypaths, for the incident angle of the *P*-wave to the tunnel must be substantial for the arrival time of the *pS*-wave reflection is to be equal or less than those of the direct shear waves. The amplitudes of the *pS*- and *sS*-waves are expected to be smaller than the direct shear waves for three other reasons. Firstly, damage to the rockmass due to excavation is greater nearer the tunnel walls (Carlson and Young, 1993, R. Everitt, pers. comm.). The reflected waves will have travelled through the most damaged rockmass and will have loss greater energy through scattering and absorption. Secondly, the energy of the incident *P*- and shear waves will be divided among the reflected waves. Thirdly, the

curved and rough tunnel walls tend to defocus seismic energy. Therefore the reflected waves are expected to be masked by the direct shear waves and their codas except for the *pS*-wave when it arrives before the direct shear waves.

Figure 3.4 presents an example where the *pS*-wave is calculated to arrive 20 sample points (400μs) before the direct shear-wave arrival. I calculated the arrival times of the *pS*- and *sS*-waves relative to the shear-waves assuming an isotropic rockmass with the average velocities of Vp=5.763km/s and Vs=3.376km/s (Talebi and Young, 1989), and that the tunnels were perfect cylinders. Low amplitude arrivals corresponding to the expected *pS*-waves are clearly seen on seismograms 1 and 3. No such arrivals are seen on seismograms 2 and 4 because of propagation directions of the corresponding incident *P*-waves were near nodal directions of the *P*-wave source radiation patterns. In contrast, the *pS*-waves of the seismograms of Figure 3.3 are calculated to arrive after the direct shear-waves by up to 7 sample points (140μs). *pS*-wave arrivals are not apparent on either the seismograms or particle motion diagrams, suggesting that these arrivals are masked by the larger amplitudes of the direct shear waves, as is also the case for the *sS*-waves in Figures 3.3 and 3.4. These examples are typical and show the expected consistency for arrivals of reflected waves with substantially lower amplitudes than the direct shear waves.

3.7.2 Effects of Reflected Waves on Picking Polarizations and Time Delays

I suggest that interference of direct shear waves with reflected did not cause significant errors in picking polarizations because the *pS*-wave is usually less than a fifth of the amplitude of the first direct shear-wave arrivals. A *pS*-wave of one fifth the amplitude of the *qS1*-wave arrival would only alter the polarization measured by 11.3° in the extreme case where the particle motion of the *pS*-wave is perpendicular to that of the *qS1*-wave. This extreme case is unlikely. The maximum difference in raypath lengths between the direct and reflected waves is only 0.6m and a maximum difference in arrival direction is 2.2°, assuming straight-line raypaths. With such similar raypaths the direct and reflected shear waves are likely to have similar polarization directions. The direct and reflected waves may therefore constructively

interfere so that the direction of initial particle motion will be that of the *qS1*-wave polarizations.

I also suggest that interference did not cause significant errors in picking time delays because multiple seismograms could be compared in picking the *qS1*- and *qS2*-wave arrivals. Occasionally the *pS*-wave interferes with the first direction shear-wave arrival so judgement of arrival of the direction shear waves, making judging of the arrival of the direct shear-wave more difficult. In such cases, the measurements of polarization and time delay are made from other seismograms of the same set (section 3.5). The arrival of reflected waves between the *qS1*- and *qS2*-arrivals may end the linear particle motion from the *qS1*-wave, which would result in a miss-picked time delay. Fortunately the typically consistent agreement in time delays among the four seismograms in a set such as seen in Figures 3.3, 3.4, and 3.6 suggests that the *sS*- and *pS*-wave amplitudes are not great enough to noticeably end the linear motion. This is supported by the agreement of hand-picked time delays to those determined by cross-correlation (section 4.6), where reflected waves will have only minor influences on results because of their small contributions to the shape of the seismograms.

3.8 Conclusions

This chapter presented an extension of the method of Chen et al. (1987) of hand-picking polarizations. This extended method requires that there are seismograms from different source orientations at the same source locations, and that the source mechanism is known so that the initial particle motion for an isotropic rockmass can be calculated and compared to the observed shear-wave motion.

Conclusions specific to the Shear-Wave Experiment are:

1. The Schmidt Hammer-nylon rod source produced the initial shear-wave particle motion expected from an infinitesimal point source with a direction parallel to the source borehole.
2. Reflected waves do not cause significant errors in picking polarizations and time delays.

A flow chart was presented for the general method of picking. However, qualitative judgements are inevitable. The main objective is to find a consistent

explanation of the shear-wave behaviour for all seismograms of the same raypath. The general conclusions from the use of this method are:

1. The method allowed the clear identification of raypaths where no splitting occurred.
2. Seismograms where the recorded shear-waves may have suffered from significant interference, for example ringing or reflections, can conveniently be ignored because other seismograms are available.
3. The method prevents the ambiguity of not being able to determine whether a shear-wave particle motion is that of the *qS1*- or *qS2*-wave, or an unsplit shear wave when the predicted particle motion matches that observed.
4. The comparison of several seismograms greatly improves reliability in picking polarizations and time delays.

4 Are We Measuring Time Delays?

4.1 Abstract

Comparison of hand-picked time delays from the Shear-Wave Experiment data set to those found by cross-correlation shows that the duration of linear particle motion after the *qS1*-wave arrival is approximately the same the time lag between the particle motion of the *qS1*-wave arrival and that expected for the *qS2*-wave. This consistency strongly suggests that both methods are indeed measuring time delays. However, the measurement of time delays by cross-correlation is reliable for this data set only when the predicted ratio of the amplitudes of the *qS1*- and *qS2*-waves are between 0.4 and 2.6 and the cross-correlation coefficient is greater than 0.71.

4.2 Introduction

In the previous chapter I described how time delays may be hand-picked from the seismograms by measuring the time between the arrival of the first direct shear wave and end of the initial linear motion as viewed on the particle motion plots. This seems a reasonable method since:

1. This method is consistent with theory. If a wave that corresponds with the *qS1*-wave has been identified, then the *qS2*-wave is expected to follow as long as the particle motion direction due to the source orientation does not correspond to the *qS1*-wave particle motion direction (section 3.5).
2. Seismograms of the same set had the same duration of linearity when shear-wave splitting was displayed (section 3.6).
3. The time delay values picked suggest a reasonable strength of anisotropy (section 8.8).

However, the hand-picking of time delays must be approached with objectivity. The end of the initial linear motion of the shear-wave may be the *qS2*-wave arrival or the arrival of some other phase, or the start of significant scattered energy (Chen et al.,

1987; Gledhill, 1993a). For the Shear-Wave Experiment data set, there may be concern if the end of linearity is due to sensor resonance or the arrival of a reflected wave (section 3.7.2). I suggest it to be desirable to employ a second method of measuring time delays not based on measuring the duration of linear motion after the *qS1*-wave. The results of the two methods can then be compared for consistency to assess the success in picking the time delays.

The other property of shear-wave splitting that may be conveniently used to measure time delays is the similarity in waveform shapes between the two shear waves. Assuming the effects of the different wavelengths and rates of attenuation between the two shear waves to be small, the *qS2*-wave should display the nearly identical particle motion as the *qS1*-wave when the two shear-waves are displayed on separate seismograms. Therefore time delays can be measured by comparing the particle motion of seismograms to find the time lag of *qS2*-wave seismograms relative to *qS1*-wave seismograms.

In this chapter I demonstrate that the lag between the *qS1*- and *qS2*-waveforms agrees with the hand-picked duration of linear motion after the *qS1*-wave arrival. In preparation I show that the time lag cannot be picked by visual comparison, and I then describe the use of cross-correlation for quantitative comparison. Throughout this chapter I will only use the fifty-three sets of seismograms from the Shear-Wave Experiment data set that display shear-wave splitting and I assume I picked the polarizations successfully.

4.3 Visual Comparison

The most obvious and common approach to confirming time delays is to rotate the two seismograms containing the shear-wave energy, in this case TS and TH, so that the *qS1*-wave is solely one seismogram while the *qS2*-wave is solely on the other. The particle motion directions of the *qS1*- and *qS2*-waves are not strictly perpendicular nor mutually strictly perpendicular to the source-receiver directions, but this is a valid approximation for weak anisotropy, as expected for the intact rockmass of the 420-Level.

Figure 4.1 are the seismograms rotated into the *qS1*- and *qS2*-waves using the assumptions described above for the same raypath as the seismograms in Figure 3.3

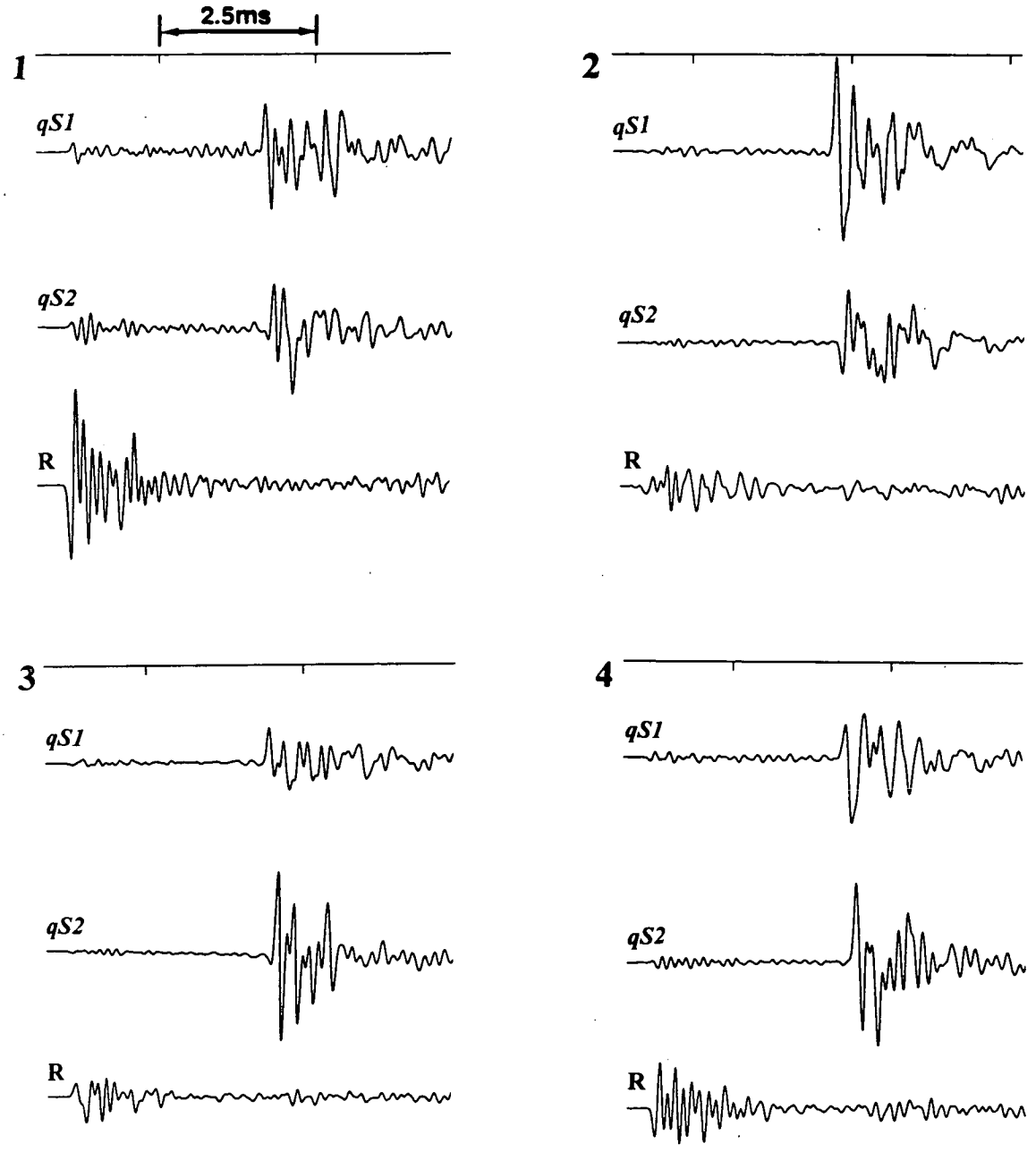

Figure 4.1: The same four 3-component seismograms as in Figure 3.3 except the TS and TH channel have been rotated into the *qS1* and *qS2*-waves using the hand-picked polarization angle.

(The particle motion diagrams for these seismograms are not included because they are the same as those of Figure 3.3 with a 038° rotation.). The seismograms do not look at all similar. A lack of similarity may be expected after the first two cycles because of the lower amplitudes of the shear-waves after the two cycles and interference from reflected waves, coda, sensor resonance, and possible head waves from the source tunnel. Visually comparing only the first cycles on the *qS1*- and *qS2*-seismograms does not produce a clear conclusion as to the similarity. Because of the narrow band width of the seismograms (section 2.6), the character of each waveform appears uniform throughout and it cannot be visually judged whether any agreement between the first cycles of the *qS1*- and *qS2*-seismograms is meaningful or just a coincidence.

Other problems with visual comparison are:

1. It is visually extremely difficult not to be influenced by the rest of seismograms when comparing only two cycles.
2. The amplitudes of the *qS1*- and *qS2*-waves are different. This must be mentally accounted for during visual comparison.
3. Attention is drawn to the visual differences in the shape of the two waves rather than similarities. A small extra peak in one of the two shear waves greatly influences opinion to conclude that the two waves are not similar even if the peak is small compared to the amplitudes of the two waves. Such small differences may result when the rotation into the *qS1*- and *qS2*-wave is not perfect.
4. Visually comparison is very subjective and human judgement inconsistent.

I conclude the method of visual comparison is not useful for judging the time lag for the Shear-Wave Experiment data set.

4.4 Cross-correlation

Similarities in the shapes of the *qS1*- and *qS2*-seismograms can be quantitatively compared using cross-correlation. This method has the benefits of being simple, robust and more sensitive than visual comparison to the shape of the wave. I now describe the use of cross-correlation to find time delays.

The normalized cross-correlation function between two time series is defined as:

$$\chi = \frac{\sum x_i y_i}{N} \; ; \tag{4.1}$$

where χ is the cross-correlation coefficient, x_i and y_i are data points from two time series, and N is the normalizing factor defined to be:

$$N = \left[(\Sigma x_i^2)(\Sigma y_i^2) \right]; \tag{4.2}$$

The cross-correlation coefficient χ is a measure of agreement of the shapes of the two time series. Identical time series result in χ=1, two time series where one is the exact opposite of the other results in χ=-1, and completely random time series gives $\chi \approx 0$. The function does not depend the amplitude of the time series. If the value of a time series is doubled at every point of the series, it would still result in the same coefficient when correlated with the same seismogram as before.

The general method of calculating time delays using cross-correlation is as follows:

1. Rotate the seismograms (in this case, the TS and TH component seismograms) so that one seismogram contains the *qS1*-wave and another contains the *qS2*-wave.
2. Extract the section of the time series containing the *qS1*-wave from the *qS1*-seismogram.
3. Cross correlate the extracted section of the *qS1*-seismogram with all equal length sections of the *qS2*-seismogram starting from the time of the *qS1*-wave arrival.

The basic assumption is that the extracted portion of the *qS1*-seismograms will correlate highest with the *qS2*-wave because of the similar pulse shapes. The time lag between the start time of the extracted portion of the *qS1*-wave seismogram and the start time of the *qS2*-wave seismogram giving the maximum value of χ is then the time delay. This general method has been commonly applied in calculating time delays (Gledhill, 1993a; Yardley and Crampin, 1993; Liu et al., 1993a) and is part of many algorithms for the automatic estimation of polarizations and time delays such as

the Maximum Correlation Method (MacBeth and Crampin, 1991) and the Analytical Synchronous Source Geophone Rotation (Zeng and MacBeth, 1993).

4.5 Practical Considerations and Refinements

Cross-correlation is based on comparing two time series point by point. Two time series may be identical, sampled at a frequency greater than the Nyquist frequency but still not result in a cross-correlation coefficient of χ=1 because the exact points where the seismograms were sampled do not coincide. It is therefore desirable to use the shortest possible sample interval when cross-correlating two seismograms. A short sample interval also helps in preventing the maximum cross-correlation coefficient from occurring not at the arrival of *qS2*-wave but some other part of the seismogram such as the coda that coincidentally has a similar shape to *qS1*-wave. This is known as *cycle skipping* (Yardley and Crampin, 1993), to which narrow band data is particularly susceptible. Cycling skipping is less likely to occur with a shorter sample interval as the greater density of sample points outlines the shape of the seismogram in greater detail. Cross-correlation coefficients between seismograms did not increase significantly once the seismograms were resampled to one sixteenth the original 20μs sample interval (1.25μs) using the Sampling Theorem (section 5.3). All cross-correlation coefficients were determined using this shorter sample interval.

A second problem with cross-correlation is determining the length of the time interval used in comparison. A small time interval of the *qS1*-seismogram, say of only one cycle, is likely to cross correlate well with many sections of the *qS2*-seismogram, giving spurious results from cycle skipping. A large interval may contain significant particle motion not due to a direct shear wave. It is obvious from examining the seismograms in Figures 3.5 and 3.6 that the particle motion of the shear waves seriously differs from that of the *qS1*- or *qS2*-wave after two cycles. This is equivalent to 385 sample points (480μs) and this was the interval length used. Yardley and Crampin (1993) also used two cycles for cross-correlation to find time delays for the same reasons.

The first attempt at using cross-correlation to determine time delays did not result in values that agreed with hand-picked values. Investigation showed that the cross-correlation method had failed for three reasons:

1. Cycle skipping.
2. Low resolution of both *qS1*- and *qS2*-seismograms due to low amplifier settings for some triaxial accelerometers.
3. Interference from sensor resonance on some seismograms.

I added the following refinements into the cross-correlation method to help prevent these problems:

1. The seismograms were rotated such that both the *qS1*- and *qS2*-wave must have positive first motions. This could be done because the particle motion directions for an isotropic rockmass could be calculated. The algorithm then sought the maximum (positive) coefficient rather than the maximum absolute coefficient. This prevents finding time lags due to a high correlation of the *qS*1-wave to particle motion opposite of that possible for the *qS2*-wave.
2. A minimum time delay of sixteen sample points (20μs) was assumed. This prevents finding zero time delays when the *qS1*- and *qS2*-waves were not perfectly separated onto two seismograms.
3. Consideration of the theoretical ratio of the amplitudes of the *qS1*-wave to the *qS2*-wave. This was calculated for each seismogram using the shear-wave particle motion direction calculated for an isotropic rockmass and the hand-picked polarization. Values that differ greatly from unity indicate that either the *qS1*- or *qS2*-wave will have a very small amplitude relative to the other and is therefore more susceptible to interference.
4. The time delay search was limited to a maximum of 129 sample points (180μs) to prevent cycle skipping. Only one of the fifty-three splitting measurements was hand-picked to have a time delay greater than this value so that this value of nine sample points should only rarely cause miss-picks.

This fourth condition restricts what is measured using cross-correlation. The dominant cycle length of 240μs is greater than this maximum delay of 180μs. With this restriction, cross-correlation finds the time lag between the first two cycles of the *qS1*-seismogram and the first two cycles of the perpendicular particle motion isolated on the *qS2*-seismogram. By comparing the results of cross-correlation with the hand-picked values of time delay, it is being ascertained whether the end of the linear

particle motion after the *qS1*-wave arrival is the beginning of perpendicular particle motion similar to that of the first two cycles of the *qS1*-seismogram.

4.6 Results and Comparison of Techniques

I now compare the hand-picked time delays to those measured using the cross-correlation method with the refinements described in the previous section. I present a summary of this comparison in Table 4.1.

From this comparison, it was determined that if;

1. $0.4>S_r>2.6$, where S_r is the ratio of the predicted amplitudes of the *qS1*-wave to the *qS2*-wave, and;
2. The cross-correlation coefficient $\chi>0.71$;
3. The maximum cross-correlation coefficient was not at the maximum allowable time lag;

then for most sets of four seismograms the time delays determined by cross-correlation agree with the hand-picked values.

More specifically, using these parameters thirty-six of the fifty-three time delays determined by cross-correlation were within thirty-two sample points (40μs), and on average 14.7 sample points (18.4μs), to the hand-picked time delays. For all sets of four three-component seismograms, the time delay was taken from the three-component seismogram resulting in the highest cross-correlation coefficient and, if available, within the acceptable amplitude ratio. The acceptable range for parameters S_r and χ were determined by comparison with the hand-picked time delays which biases comparison towards agreement. However, the resulting acceptable ranges for S_r and χ were reasonable and the boundaries between acceptable and unacceptable were distinct. This consistency suggests that these boundaries are essentially determined by the characteristics of the seismograms rather than arbitrarily chosen. The time delay for Station 12 to Accelerometer 12 was hand-picked to be eleven sample points (220μs) and was therefore outside the allowable range of time delays from cross-correlation set to prevent cycle skipping.

In fifteen cases, none of the four seismograms in a set were within the parameters. These cases were usually due to a coincidence of all four seismograms having either lack of *qS1*- or *qS2*-wave energy, noise, or ringing. Lack of *qS1*- or *qS2*-wave energy

Table 4.1: Comparison of Hand-Picked and Cross Correlated Time Delays

Raypath Station to Accelerometer	Number of Sample Points Difference Between Time Delays (1.25μs per point)		Cross-correlation Coeffecient		Calculated Ratio of the Amplitudes of the *qS1*-wave to *qS2*-wave		x Maximum Coeffecient at Boundary of Acceptable Time Delays
	Parameters Within Acceptable Range	At Least One Parameter Outside Range	x Coeffecient Outside Range		x Ratio Outside Range		
1 - 2	22			0.870		1.66	
1 - 5		36	x	0.691		0.58	
1 - 9	10			0.829		0.59	
1 - 11	25			0.822		2.23	
1 - 13	3			0.749		0.40	
1 - 15	23			0.969		1.68	
2 - 2	8			0.767		1.41	
2 - 4	10			0.943		0.47	
2 - 5	31			0.853		2.25	
2 - 9	8			0.945		1.13	
2 - 11	30			0.722		1.01	
2 - 13	16			0.817		0.52	
2 - 15	7			0.930		1.39	
3 - 4	0			0.721		1.38	
3 - 5		64		0.878		0.62	x
3 - 7		4	x	0.523	x	16.47	
3 - 10	4			0.741		1.81	
3 - 14		96	x	0.628		1.36	x
4 - 2		16		0.898	x	0.28	
4 - 7	22			0.932		1.77	
4 - 12		96		0.880	x	3.79	x
5 - 4	18			0.915		2.58	
5 - 13*		69		0.767		1.55	
6 - 13		96	x	0.619	x	0.32	
6 - 14		80		0.886	x	2.89	x
7 - 2		96	x	0.570		1.30	x
7 - 8	8			0.789		1.94	
7 - 9	5			0.799		0.84	
7 - 13	6			0.795		0.47	
7 - 14	12			0.930		0.50	
8 - 8	11			0.948		2.10	
8 - 13	24			0.845		2.17	

Raypath Station to Acceler-meter	Number of Sample Points Difference Between Time Delays (1.25μs per point)		Cross-correlation Coeffecient		Calculated Ratio of the Amplitudes of the *qS1*-wave to *qS2*-wave		x Maximum Coeffe-cient at Boundary of Accept-able Time Delays
	Para-meters Within Accept-able Range	At Least One Parameter Outside Range	x Coeffe-cient Outside Range		x Ratio Outside Range		
9 - 8	0			0.794		1.94	
9 - 13	8			0.821		0.49	
9 - 14	32			0.727		1.47	
9 - 15	8			0.814		0.99	
10 - 8	24			0.817		1.09	
10 - 9	22			0.921		1.26	
10 - 12		19		0.880	x	0.32	
10 - 13	3			0.901		1.99	
10 - 14	25			0.953		1.47	
10 - 15	21			0.966		0.74	
11 - 12		25	x	0.396		0.68	
11 - 14	17			0.942		1.13	
11 - 15	31			0.929		1.68	
12 - 8	32			0.855		1.19	
12 - 9		96	x	0.654	x	3.51	x
12 - 12**		70		0.893		0.60	
12 - 13		11		0.918	x	12.77	
12 - 14	19			0.917		2.08	
13 - 10		111		0.924	x	3.44	
13 - 15	1			0.993		0.91	

The minimum acceptable cross-correlation coeffecient was 0.708 and the acceptable ratios of amplitudes was between 0.386 and 2.592. Cross-correation was restricted to finding time delays of greater than 20μs and less than 180μs. The seismograms used are the one seismogram of each set of four with the largest cross-correlation coeffecient and, if available, was within the parameters.

* Cross-correlation method failed

** Time delay was hand-picked to be 220μs which was 40μs beyond the maximum time delay limit permitted in cross-correlation

was the most common reason and in five of these fourteen cases, the ratio S_r was outside the necessary parameters for least three of the four seismograms. There was only one case where the time delay from cross-correlation differed by more than thirty-two sample points (40μs) from the hand-picked value but was also within the parameters. For this raypath, there was significant ringing after the first shear-wave arrival on the only seismogram of the four within parameters.

These results show that time delays measured using both methods are consistent for most raypaths, and a clear explanation exists for raypaths where the results of the two methods differ. It is therefore consistent with theory that both methods are measuring time delays.

4.7 Precision in Measuring Time Delay

In the previous section I argued that the measuring the duration of linearity after the *qS1*-arrival, and the comparison of wave shapes to find a time lag, both measured the same parameter of time delay. I now exploit this result to calculate an approximate precision in picking time delays as is necessary in determining the strength of the anisotropy in the rockmass (section 8.5). The fundamental assumption is that the different values of time delays measured by both methods are due to a limit in measuring precision common to both methods rather than a systematic difference between the two methods. I will only consider the time delays values where the time delays as measured by both methods were judged to agree, giving thirty-five pairs of time delays values for comparison. I will use the original sample interval of 20μs.

Below are the statistics for the differences between the time delays values determined by the two methods for the thirty-five pairs of measurements:

Average Difference:	0.92 sample points	(18.4μs)
Standard Deviation:	0.66 sample points	(13.2μs)
Maximum Difference:	2.00 sample points	(40.0μs)

For sixteen of these thirty-five sets of raypaths, the parameters for the cross-correlation method were within acceptable ranges on more than one of the four seismograms in a set. The different in the measured time delays using

cross-correlation for each of these sixteen raypaths can also be compared. This gives the following:

Average Difference:	0.95 sample points	(19.0μs)
Standard Deviation:	0.72 sample points	(14.4μs)
Maximum Difference:	2.82 sample points	(56.3μs)

These values are virtually the same as found by comparing delays from hand-picking and cross-correlation. This supports the assumption that both methods have the same precision in picking. It is likely that the precision is determine mainly by inference from reflected waves, sensor resonance, noise, and possible head waves from source tunnels. The 2cm separation between the furthest two accelerometers within a triaxial accelerometer can cause errors of up to 6μs.

I now present two models of the distributions in measurement precision to explain these statistics. The first model is that time delays are measured to within a set interval about the true time delays and that the measured time delay is random within this interval. This model is therefore that of a uniform distribution over an interval. I propose this model because I find that there exists a distinct interval on particle motion diagrams within which linear motion ends, but the exact instance cannot be determine due to interference. The second model is that the measured time delays are of a normal (Gaussian) distribution about the true time delays. This distribution implies that there is no limit to the difference between measured and true time delays, but larger differences are less likely as would be expected.

I numerically found the interval length for the uniform distribution and the standard deviation for the normal distribution that best predicted the average difference and standard deviation between the measured time delays. In doing this, I took into account that time delays were hand-picked to the nearest sample point and delays picked by cross-correlation to one-sixteenth of a sample point. The predicted statistics from the two methods are compared with those of the data in Table 4.2. The predicted statistics of uniform distribution of interval length 2.8 sample points, and the normal distribution with a standard deviation of 0.82 sample points both match the data closely. Most likely the true distribution is a compromise between the two models.

Table 4.2: Comparison of Statistic from Time Delay Measurements to Uniform and Normal Distributions

Distribution	**Comparison of Time Delay Measurements (Number of Sample Points, 1 sample point = 20μs)**	
	Average	**Standard Deviation**
From Comparison of Data	0.92	0.66
Uniform Interval = 2.8 sample points	0.93	0.66
Normal (Gaussian) Standard Deviation=0.82	0.93	0.70

I suggest that the difference in true and measured time delays are usually less than 1.0 sample points (20.0μs). I would expect time delays are hand-picked to within 1.0 sample points to the true time delay because the change from linear motion of the *qS1*-wave to motion due to both shear waves is seen to take place on particle motion diagrams within two sample points (40.0μs) (Figures 3.3, 3.4, and 3.6). This is supported by the uniform and the normal distributions, which predict that only twenty-nine per cent and twenty-three per cent of time delay measurements, respectively, would differ from the true delay by more than 1.0 sample points.

This analysis also shows that a shorter sample interval would not improve the precision in hand-picked time delays appreciably. It would seem beneficial to resample the seismograms to a shorter sample interval when hand-picking time delays because the end of linear motion might be identified to a finer graduation of time. The uniform distribution predicts that the average difference between picked and true time delay for resampled seismograms would remain unchanged at 0.70 sample points. The normal distribution predicts that this average would improve only slightly from 0.69 sample points to 0.59 sample points. Therefore, the limit to the precision in measurement is large enough that a shorter sample interval would not significantly improve the precision in hand-picking time delays.

4.8 Conclusions

I have presented a study to assess the validity and precision of time delay measurements. I showed that visual comparison could not be used effectively to measure time delays, and I introduced cross-correlation as a practical, quantitative method. I conclude that the consistency of the time delays measured by cross correlation with hand-picked delays suggests that both methods are indeed measuring time delays. The effective use of cross-correlation required the refinements of: (1) rotations of the *qS1*- and *qS2*-seismograms so comparison results in a positive cross-correlation; (2) imposing a minimum time delay greater than zero; (3) rejecting measurements where one wave has a significantly lower amplitude than the other; (4) limiting the time delay search to a maximum of three-quarters of a cycle. These refinements were necessary because of the limited band width of the seismic signals and the low resolution of some seismograms, and to overcome the effects of interference from reflections, noise, sensor resonance, and possible head waves. From the results of statistical modelling, I argue that the time delays of the Shear-Wave Experiment data set are usually measured to within 1.0 sample points (20μs) to the true time delay. Statistical modelling also shows that reducing the sample interval of the seismograms would not significantly improve the precision in hand-picking time delays.

5 Temporal Changes

5.1 Abstract

Only three of the 728 sets of repeated raypaths of the Shear-Wave Experiment data set displayed temporal changes presumed to be due to the tunnel excavation. These three were the only raypaths that travelled within 3.0m of the Mine-by Tunnel (of diameter 3.5m) and for which the minimum separation between the raypaths and the tunnel decreased with excavation. Temporal changes are due to the advancement of the zone of excavation disturbance, implying that Extensive-Dilatancy Anisotropy (EDA) is a significant fabric of the *in situ* rockmass, although this result is speculative because of the limited number of raypaths showing temporal changes. The excavation appears to create a crack set with orientations governed by the *in situ* stress field or the primary layering.

5.2 Introduction

Section 2.12.2 summarized past studies of *in situ* anisotropy in granite and granodiorite. In summary, *in situ* anisotropy might be caused by EDA-cracks, fractures and cracks, mineral alignment, and intragranular cracks whose orientations are governed by mineral alignment, but there has never been an unambiguous interpretation as to the cause of *in situ* anisotropy. Any observations of changes in shear-wave splitting that can be solely attributed to changes of stress are evidence that EDA-cracks are at least partially responsible for anisotropy in the rockmass. Also, observations of changes are of importance in evaluating the use of shear-wave splitting as a new technique for parameterizing the stress effects and damage to a rockmass due to excavation and for the long term non-destructive monitoring of nuclear waste repositories.

I demonstrate that the effects of tunnel excavation detected using shear waves are limited to within the known boundary of the zone of excavation disturbance of one

diameter from the Mine-by Tunnel. I begin by developing the method of cross-correlation to detect temporal changes. Following this, I introduce progressive particle-motion diagrams as the preferred technique for displaying shear-wave motion in the visual search and interpretation of temporal changes. Using these two techniques, I identify three situations that result in apparent temporal changes, the most important of which are temporal changes due to the advancement of the zone of excavation disturbance.

I define a *temporal change* for this analysis as a change in the seismic signal for a repeated raypath due to some change in the rockmass through which the seismic waves propagated. I will confine my examination to the initial shear-wave arrivals because changes in shear-wave splitting should be very sensitive to any changes in the rockmass (Crampin, 1993b) and to avoid effects of randomly scattered energy. I will use the term *excavation-induced anisotropy* to refer to the anisotropy within the rockmass where excavation has created anisotropic fabrics or altered the *in situ* anisotropy.

5.3 Reproducibility

Sections 5.4 and 5.6 discuss the methods of visually and numerically searching for temporal changes. The level of reproducibility of seismograms from repeated raypaths must be established before any such search. Only if the changes in seismograms are beyond those expected from lack of reproducibility can the changes be attributed to changes in the rockmass. This conservative approach is necessary to avoid falsely identifying temporal changes where none exist. In this section I quantify the reproducibility using cross-correlation.

The description for cross-correlation to find time delays (section 4.4) was for comparing single component seismograms. The cross-correlation coefficient for a three-component seismogram is given by the equation:

$$\chi = \frac{\Sigma \mathbf{x}_i \mathbf{y}_i}{N}; \qquad (5.1)$$

where χ is the cross-correlation coefficient, $\mathbf{x}_i$ and $\mathbf{y}_i$ are the three component vectors expressed in Cartesian co-ordinates from two seismograms of equal length. N is the normalizing factor defined to be:

$$N = [(\Sigma \mathbf{x}_i \mathbf{x}_i)(\Sigma \mathbf{y}_i \mathbf{y}_i)]^{\frac{1}{2}}; \qquad (5.2)$$

It is desirable to use the shortest possible sample interval when cross-correlating two seismograms because of non-coincidental sampling of the two otherwise identical time series (section 4.5). In practice a limit is reached where cross-correlation does not improve with further reduction is the sample interval. This limit is due to in-coherent noise on the seismograms.

I attempted to find this limit of the sampling interval using the repeated raypaths from Orientation 1 of Source Station 1 to Triaxial Accelerometer 2 and use the results to quantify reproducibility. Figure 5.1 compares the three component seismograms for this raypaths as recorded from the first recording sequence of May 01, the second sequence of May 06, and the final sequence of August 25. The three sets of seismograms are nearly identical suggesting that reproducibility is extremely good. This level of reproducibility is typical. The seismogram from the first recording sequence was used as the reference seismogram and was cross-correlated with all thirteen seismograms. This was repeated five times where each time the sampling interval was reduced to half using the Sampling Theorem, resulting in a final reduction of the sampling interval to 0.625μs, or 1/32 the sampling interval in recording, which I will refer to as a *resampling factor* of 32. The first 480μs of the shear-wave arrival, corresponding to two wavelengths of shear wave, was used in the cross-correlation. The reference seismogram was time shifted by up to half the original sample interval (±10μs) to find the maximum cross-correlation value.

The results are presented in Table 5.1. The table clearly shows the cross-correlation coefficients increased from the previous sampling rate even at a resampling factor of 32 so that the limit to the sampling rate was not found. A resampling factor of 32 is too computationally slow to be used in practice and resulted in cross-correlation coefficients only slightly greater than for a factor of 16 (≤0.0001). Therefore a resampling factor of 16 is adequate and is practical in application.

At this new sampling interval of 1.25μs the minimum cross-correlation coefficient is 0.9585, and the second smallest is 0.9841. These are extremely high values showing that reproducibility was excellent throughout the Shear-wave experiment.

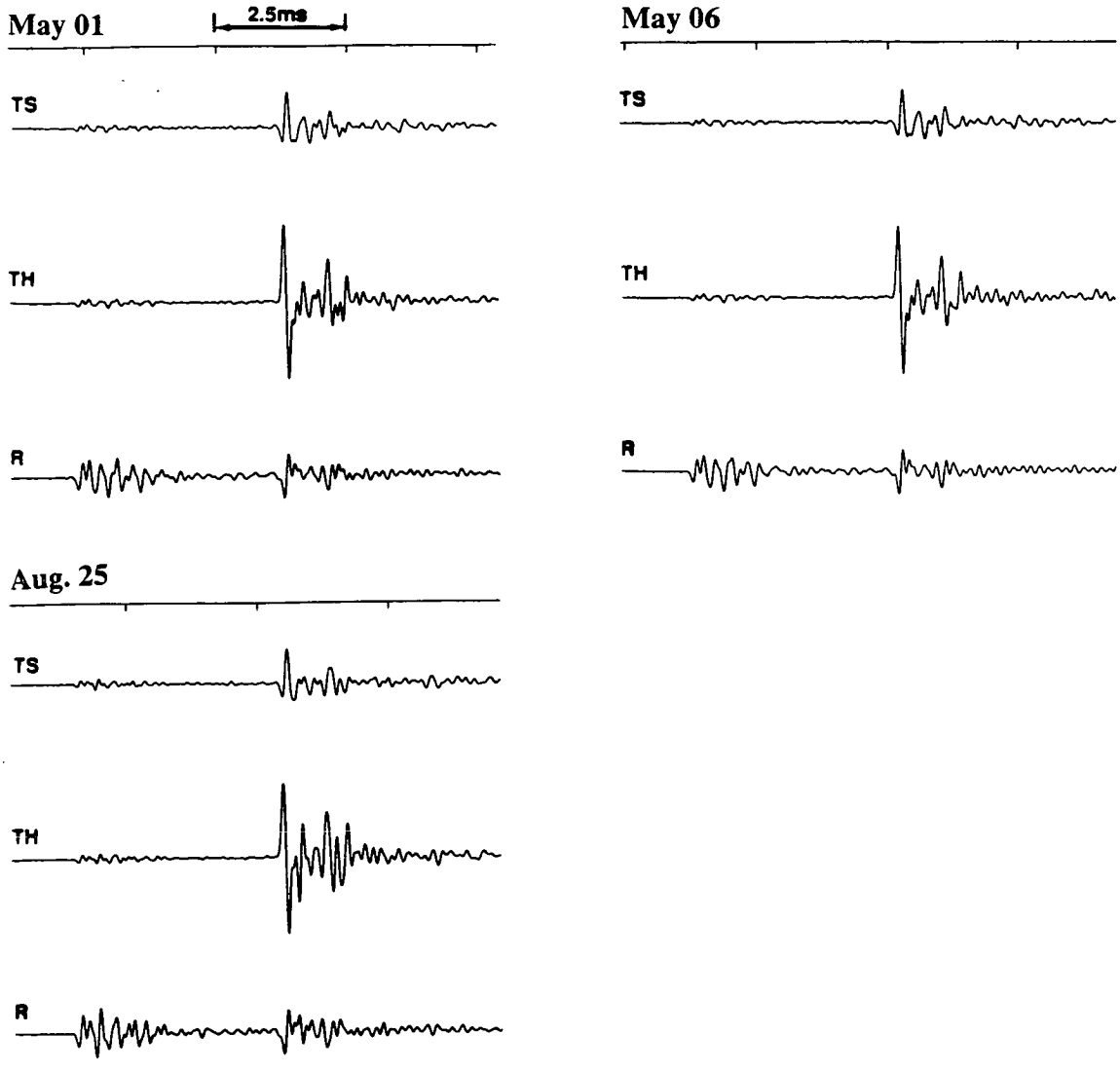

Figure 5.1: Three seismograms from the first, second, and final thirteenth recording sequences for the raypath from Source Station 1, Orientation 1, to Triaxial Accelerometer 2.

Table 5.1: Cross Correlation Coeffecients for raypath from Source Station 1 Orientation 1 to Triaxial Accelerometer 2.

Recording Sequence	Date	Resampling Factor					
		1	2	4	8	16	32
1	May 01	1.0000	1.0000	1.0000	1.0000	1.0000	1.0000
2	May 06	0.9638	0.9964	0.9964	0.9965	0.9967	0.9967
3	May 11	0.9959	0.9959	0.9959	0.9960	0.9960	0.9960
4	May 11	0.9934	0.9935	0.9935	0.9935	0.9941	0.9941
5	May 14	0.9887	0.9887	0.9961	0.9961	0.9961	0.9962
6	June 01	0.9660	0.9946	0.9946	0.9946	0.9951	0.9951
7	June 05	0.9919	0.9920	0.9966	0.9969	0.9974	0.9974
8	June 15	0.9725	0.9911	0.9911	0.9932	0.9932	0.9932
9	June 19	0.9839	0.9840	0.9841	0.9849	0.9850	0.9851
10	June 30	0.9823	0.9825	0.9897	0.9897	0.9897	0.9898
11	July 22	0.9777	0.9777	0.9841	0.9841	0.9841	0.9842
12	Aug. 04	0.9855	0.9858	0.9859	0.9859	0.9861	0.9862
13	Aug. 25	0.9272	0.9576	0.9579	0.9580	0.9585	0.9586

The coefficient generally decreased as the experiment progressed. It is unknown whether this is due to a change in the performance of the Schmidt hammer, nylon rod, or microseismic system, or changes in the rockmass along the raypath. There is a significant decrease in cross-correlation coefficients starting from Recording Sequence 9 (June 19) and another from Recording Sequence 12 (August 04). I do not have an explanation for these sudden decreases in the reproducibility.

5.4 Effects of Amplitude

The data presented in Table 5.1 was for a raypath where the system gain factor was a constant 148 throughout the experiment, resulting in an approximately constant maximum amplitude of 220 units for all recording sequences. Unfortunately, the system gains of seven of the triaxial accelerometers were not kept constant but set to the lower gain setting of approximately 16 for most of the recording sequences. Path length and source orientation both affect seismogram amplitudes and consequently the amount of contamination by noise. The cross-correlation coefficient for seismograms

of different amplitudes must be considered before the cross-correlation method can confidently be employed to search for temporal variations.

To demonstrate the effects of low amplification, I present two three-component seismograms from the same source-receiver raypath from the first (May 01) and second (May 06) recording sequences (Figure 5.2). The gain settings for the first and second seismograms were approximately 160 and 16, respectively. The second seismogram is appreciably contaminated by system noise unlike the first seismogram. This takes the forms of a less smooth seismogram that contains small, sudden, low amplitude changes. The effects of noise are more easily seen on the particle motion diagrams. The diagrams for the latter seismograms show a less linear initial shear-wave motion and the curve connecting sample points is less smooth. The overall visual impression of noise is that the particle motion diagrams appear jittery but it is visually apparent that the general particle motion is only subtly different for both seismograms.

I evaluated the effects of amplitude upon reproducibility by cross-correlating the initial shear-wave arrivals of a variety of identical source-receiver raypaths chosen to present a large range of amplitudes. I used pairs of seismograms from the first and last recording sequences to account for any long term changes in reproducibility. The seismograms were resampled to sixteen times the original sampling rate. Results (Table 5.2) suggest that cross-correlation coefficients remain above 0.94 unless at least one of the pairs of seismograms has an amplitude of less than 60 units so that the value of 0.94 may be used as a cut-off value to search for temporal changes. This also suggests that random noise and poor resolution are appreciable for seismograms of amplitudes less than 60 units. Table 5.2 gives only a limited number of example. In practice a cut-off value of 0.90 was used as it showed to be the critical value when coefficients from all raypaths were examined. Therefore below 60 units, the seismograms resulting in a cross-correlation coefficient less than 0.90 must be examined visually to assess whether the low value truly due to a raypath effect or merely noise.

The window length using in cross-correlation for the data of Table 5.2 was 240μs (one cycle) as opposed to the 480μs window used in Table 5.1. The shorter time interval was necessary to increase the sensitivity of the cross-correlation coefficients

Figure 5.2: Two three-component seismograms from the same source-receiver raypath. The upper seismogram is from the first recording sequence of May 01, as is marked on the seismogram. The lower seismogram is from the second seismogram (May 06). The maximum amplitudes of the first half-wavelength (240μs) of the shear-waves are stated on the diagram. The time interval of 2.5 milliseconds is marked. The particle motion diagrams below the seismograms are in the TS-TH plane and correspond to the five windows marked above shear-waves. Each motion diagram is for an interval of 240μs. Sample points are marked by ticks. The large and small arrowheads mark the arrival of the *qS1*-wave and *qS2*-wave respectively. The lower seismogram was recorded with a gain setting approximately one-tenth that of the upper.

May 01
Maximum Amplitude 247.2

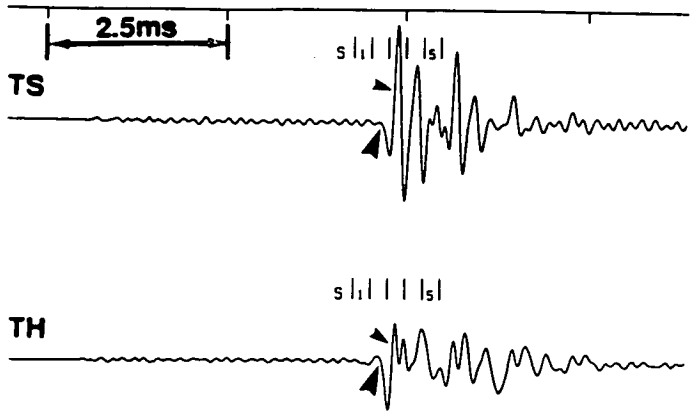

May 06
Maximum Amplitude 24.2

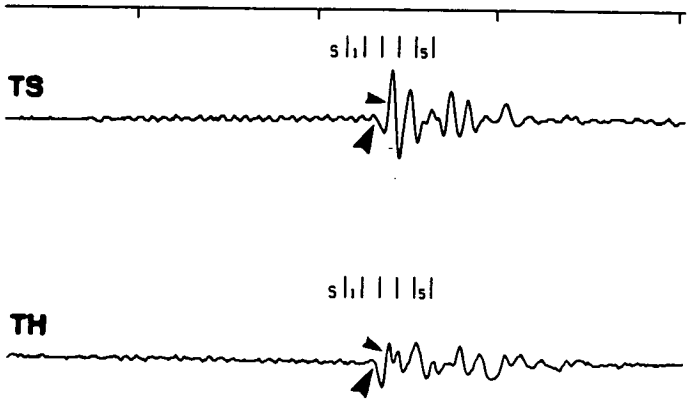

Table 5.2: Typical Cross-correlation Coeffecients for Shear-wave of a Variety of Different Amplitudes. Each set of shear-wave compared were for the same source to receiver raypaths where one seismogram was from the first recording sequence (May 01) and the other from the last (August 25).

Maximum Amplitudes of Shear Waves		**Cross-correlation coeffecient**
Larger Amplitude	**Lesser Amplitude**	
154.7	140.0	0.9966
88.6	86.6	0.9946
425.2	384.4	0.9938
84.7	81.3	0.9878
81.7	68.9	0.9853
195.9	17.8	0.9844
383.9	31.4	0.9796
70.9	66.4	0.9761
47.1	28.2	0.9712
44.0	41.7	0.9695
298.6	31.5	0.9654
306.0	247.1	0.9619
422.0	39.6	0.9609
182.9	146.6	0.9445
105.8	7.7	0.9440
71.9	68.8	0.9429
91.9	9.1	0.9425
100.8	39.0	0.9357
104.6	54.5	0.9214
69.4	4.8	0.8842
42.0	32.4	0.8790
310.8	20.4	0.8539
200.5	15.3	0.8245
20.3	16.7	0.7963
38.0	7.4	0.5931
4.4	2.2	0.3758
31.9	2.2	0.2274

to changes in the initial shear-wave arrivals. Comparison of the results of Tables 5.1 and 5.2 shows no appreciable difference of cross-correlation coefficients due to the shorter window length when there are no temporal changes.

5.5 Displaying Data for Visual Examination

In this section I describe my method of displaying data for the visual search of temporal changes. The visual search is an arduous task. It involves the comparison of seismograms and particle motion diagrams of identical source-receiver raypaths from all recording sequences. I estimate the total number of seismograms for visual examination to be about 7000. For each seismogram and corresponding set of particle motion diagrams, the initial shear-wave motion has to be identified, the effect of noise qualitatively assessed, and the particle motion compared to the other seismograms from the same source-receiver raypaths. Errors in human judgement are inevitable and the time involved makes such a method impractical. It is therefore desirable to minimize the amount of data needed for examination.

I did this by first picking the initial shear-wave arrivals for one complete set of the 728 source-receiver raypaths. The first arrival of a source-receiver raypath from any recording sequence could then automatically be found to within one sample point (20μs) by cross-correlation with the reference set. Temporal changes and general shear-wave behaviour are far easier to examine on particle motion diagrams than seismograms. I will only consider the TS-TH plane of the dynamic TS-TH-R co-ordinate system (section 3.3) as the shear-wave motion is almost entirely confined to this plane. Static co-ordinate systems would require the examination of more than one plane and hence be much slower.

Figure 5.3 displays a set of particle motion diagrams for the same raypath as used to assess reproducibility (section 5.3). The particle motion diagrams on the TS-TH planes are displayed horizontally from left to right. The initial shear-wave arrival is the third sample point of the second particle motion diagram in the row. The first particle motion diagram of each row shows the motion before the shear-wave arrival and aids in interpreting the effect of noise and interference. The fourth diagram is the shear-wave motion well beyond any expected time delay and aids in interpreting the general shear-wave behaviour. The second and third diagrams give the initial

Figure 5.3: The shear-wave motion for the same raypath as in Figure 5.2 displayed on particle motion diagrams of the TS-TH plane. The corresponding diagrams for all recording sequences are displayed chronologically down the page. The relative scale of the diagrams is stated in the upper right corner of each diagram. Ticks mark the position of sample points. The sample interval is 20μs. Arrowheads show the direction of motion at the end of the time window of each diagram. The large arrowhead on the first set of diagram marks the shear-wave arrival. No splitting was observed for this raypath. The maximum amplitudes stated is that for all four sequential diagrams as oppose to just the first half wavelength as in Figure 5.2.

01 1 --> 2 Nylon Rod
source orient. geophone

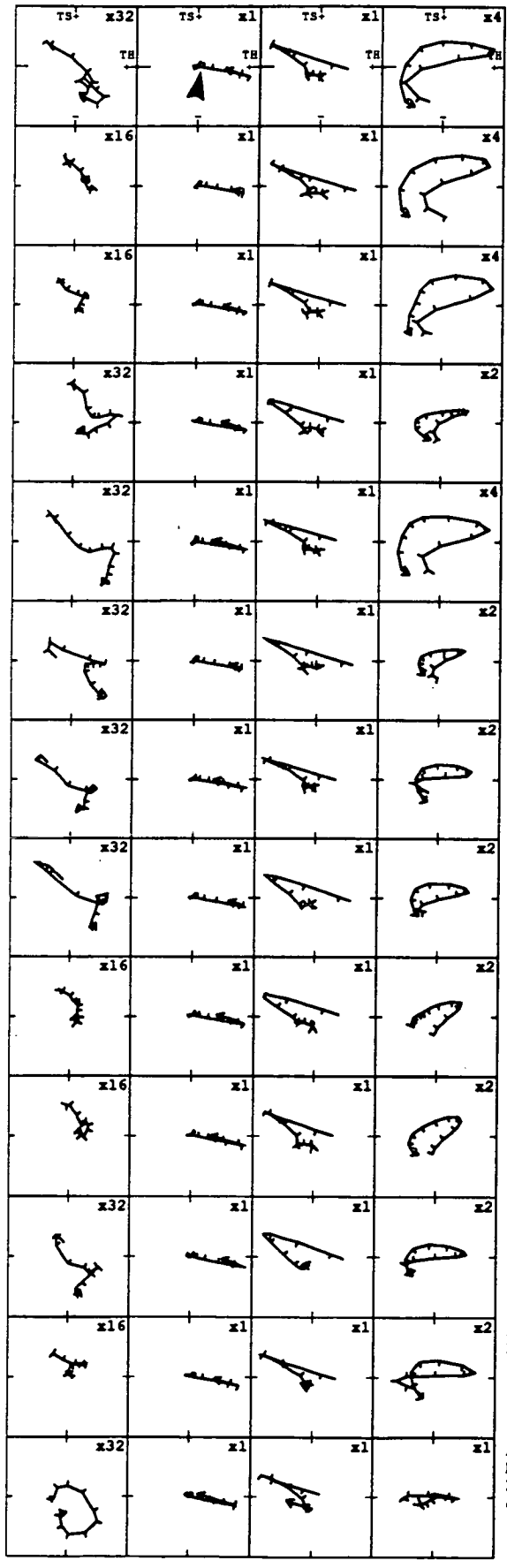

May 1
Max. Amp. 312
Event 086
Julian Day 122

May 6
Max. Amp. 360
Event 053
Julian Day 127

May 11
Max. Amp. 339
Event 026
Julian Day 132

May 11
Max. Amp. 363
Event 058
Julian Day 132

May 14
Max. Amp. 324
Event 022
Julian Day 135

June 1
Max. Amp. 364
Event 006
Julian Day 153

June 5
Max. Amp. 340
Event 044
Julian Day 157

June 15
Max. Amp. 302
Event 017
Julian Day 167

June 19
Max. Amp. 300
Event 038
Julian Day 171

June 30
Max. Amp. 301
Event 081
Julian Day 182

July 22
Max. Amp. 237
Event 034
Julian Day 204

Aug. 4
Max. Amp. 369
Event 082
Julian Day 217

Aug. 25
Max. Amp. 321
Event 080
Julian Day 238

shear-wave motions of the *qS1*- and *qS2*-waves if splitting occurs. Again, subtle changes do take place as was previously discussed with Figure 5.1. However it is quickly seen that no major temporal changes have taken place. I believe this to be the quickest and easiest method of visual examination for temporal changes in a large data set. I will refer to these diagrams as *progressive particle motion diagrams.*

5.6 Visual Examination

I will now demonstrate the necessity of the visual examination in determining the cause of low cross-correlation values and the convenient use of progressive particle motion diagrams to visually examine repeated raypaths for temporal variations. I claim visual examination of data is also helpful in gaining general insight on shear-wave behaviour and is necessary in interpreting any temporal changes found by any method.

Figure 5.2 gives an example of seismograms and particle motion diagrams for a repeated raypath where the amplitude of the second seismograms was well below 60 units. The minimum cross-correlation coefficient of this raypath is 0.8601, but visual examination is necessary to determine whether the low value is due to significant temporal changes or noise because the amplitude of the second seismogram is less than 60 units. The progressive particle motion diagrams for this raypath is shown in Figure 5.4. The particle motion diagrams differ noticeably between one another, but the differences between sets of motion diagrams are not coherent. This visual examination shows the differences causing the low values of cross-correlation are due to ringing, poor resolution, and possibly subtle changes in the rockmass rather than any significant temporal change.

The particle motion diagrams for the first and the final recording sequences (May 01 and August 25, respectively) are of high enough amplitudes that the differences are not due to poor resolution. The particle motion after the *qS2*-arrival is more elliptical for the August 25 recording sequence. This suggests a change in the *qS2*-wave, which suggests a change in the rockmass. The higher attenuation experience by the *qS2*-wave should make it more sensitive to excavation damage than the *qS1*-wave. These subtle changes are typical. Unfortunately, only the conclusion that the rockmass has undergone changes over the time spanned by the recording sequences can be made

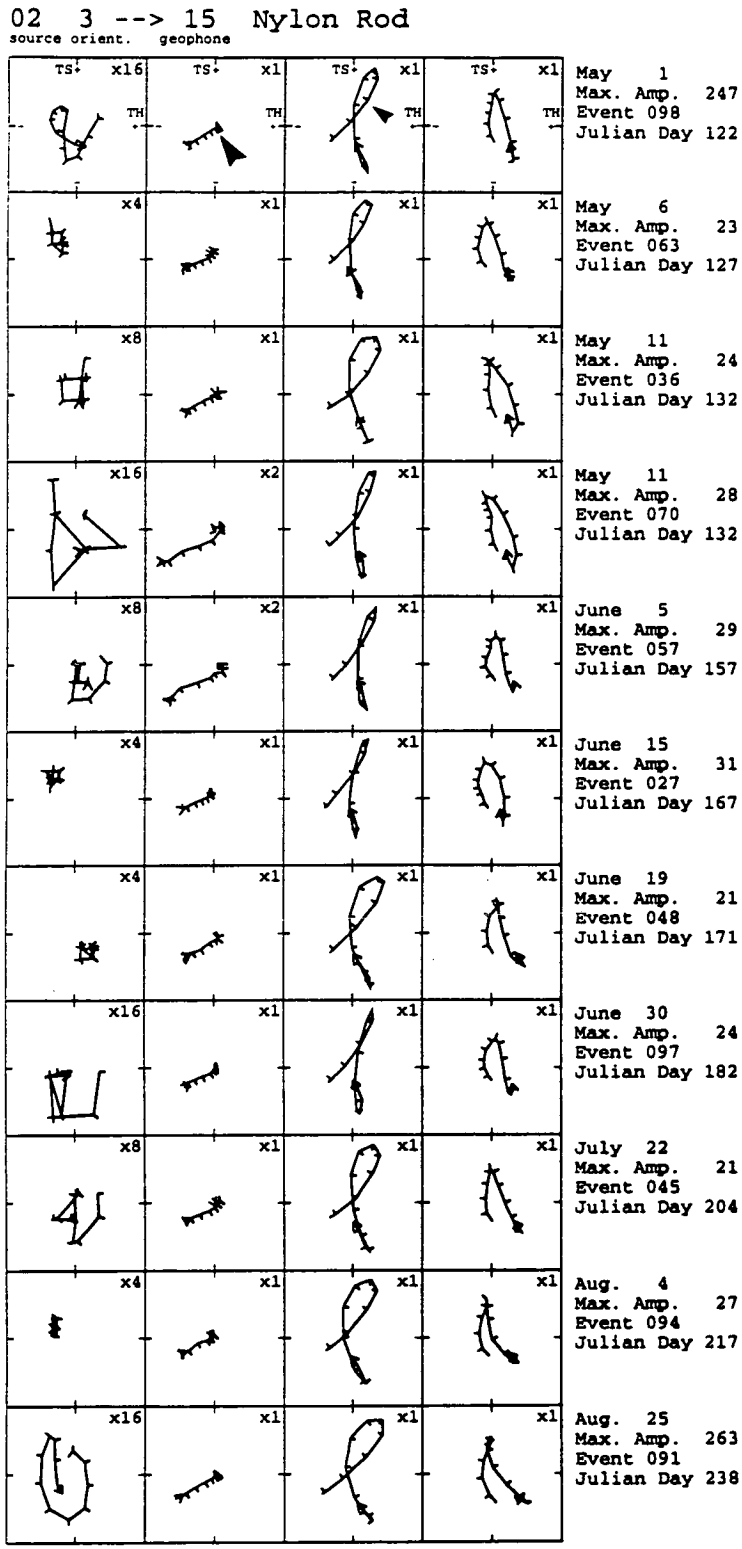

Figure 5.4: The shear-wave motion for raypath from Orientation 3 of Source Station 2 to Triaxial Accelerometer 15. The notation is as in Figure 5.3 except the large arrowhead in the first set of particle motion diagrams marks the *qS1*-wave arrival and the smaller arrowhead marks the *qS2*-wave arrival. The jitteriness of the diagrams for the second (May 06) to second last (August 04) recording sequences is due to low amplitudes. It is easily seen that no coherent change in initial shear-wave motion has taken place.

from such small changes. The cross-correlation coefficient between the seismograms of the first and final recording sequences for the raypath of Figure 5.4 is 0.9296, which is above the cut-off value of 0.90 used in the automated search (next section). Therefore these common, subtle changes are not detected using cross-correlation.

5.7 Searching for Temporal Changes

I performed the search for temporal changes independently using both the visual and cross-correlation methods. For the visual search, the progressive particle motion diagrams were examined for all 728 raypaths created for the four source locations at all thirteen source stations and recorded by all triaxial accelerometers except Triaxial Accelerometers 3 and 6. Likewise, I performed an automated search for temporal variations using cross-correlation for all 728 repeated raypaths. The initial search was performed quickly using a resampling factor of only two. I repeated the cross-correlation using a larger resampling factor for any raypaths where the cross-correlation values were less than the cut-off value of 0.90. This procedure was repeated up to a resampling factor of sixteen.

5.8 Results: Raypaths Showing Temporal Changes

I found eleven raypaths of the 728 that showed temporal variations by visual examination and twenty-two using cross-correlation, including all those found by visual examination. The failure of the visual search to identify eleven raypaths of the twenty-two raypaths was due to inevitable human error. This shows cross-correlation to be more reliable and suggests that potentially all significant temporal variations could be found using cross-correlation if all seismograms had sufficient resolution. Visual examination would then only be needed for interpretation. The seismograms of only fifteen raypaths of the twenty-two had amplitudes above 60 units and visual interpretation was needed to determine if these were temporal changes. For some raypaths, particularly those from Source Station 13, the most remote of the source stations, the microseismic system did not trigger to record the seismic signals of most recording sequences.

5.9 Causes of the Changes

5.9.1 Propagation Near Nodal Directions

I determined the most common temporal variation to be due to raypath propagation direction near nodal directions of the shear-wave source radiation patterns (section 3.6). In these cases, only the one raypath in the set of four showed temporal variations. There were nine such raypaths. Seven of these nine raypaths are within 20.3° to a nodal direction and all nine were within 31.5°. All seismograms from raypaths propagating within 20.8° to a nodal direction either showed these apparent changes or are of amplitudes too low to determine whether any apparent changes had taken place.

Figures 5.5 and 5.6 show a typical example where the raypath is within 7.3° of the nodal direction. Changes are apparent on the seismograms and particle motion diagrams. The seismograms show the emergent, non-impulsive shear-wave arrival typical of all seismograms from raypaths propagating within 20.8° of a nodal direction. Cross-correlation coefficients (Table 5.3) fluctuate without an obvious pattern rather that monotonically decreasing as would be expected from an effect of excavation. The amplitudes are well above 60 units so the changes are not an artefact of poor resolution.

I do not have a definite explanation for the changes, but I speculate it is due to the low amplitude ringing on many of the seismograms. The superposition of the ringing has a significant effect when the shear-wave is of relatively low amplitude and emergent. The other possibility is that much of what appears to be the direct shear-wave arrival is the *pS*-wave (section 3.7) masking the lower amplitude shear-wave. The *pS*-wave is expected to be less reproducible than the direct shear-wave because it travels through the most damage part of the rockmass and is therefore likely to be very sensitive to time dependent effects of excavation.

These observations show that the level of reproducibility of seismograms is dependent upon propagation direction relative to the shear-wave source radiation pattern. Therefore the source radiation pattern should be taken into account in any study examining temporal changes.

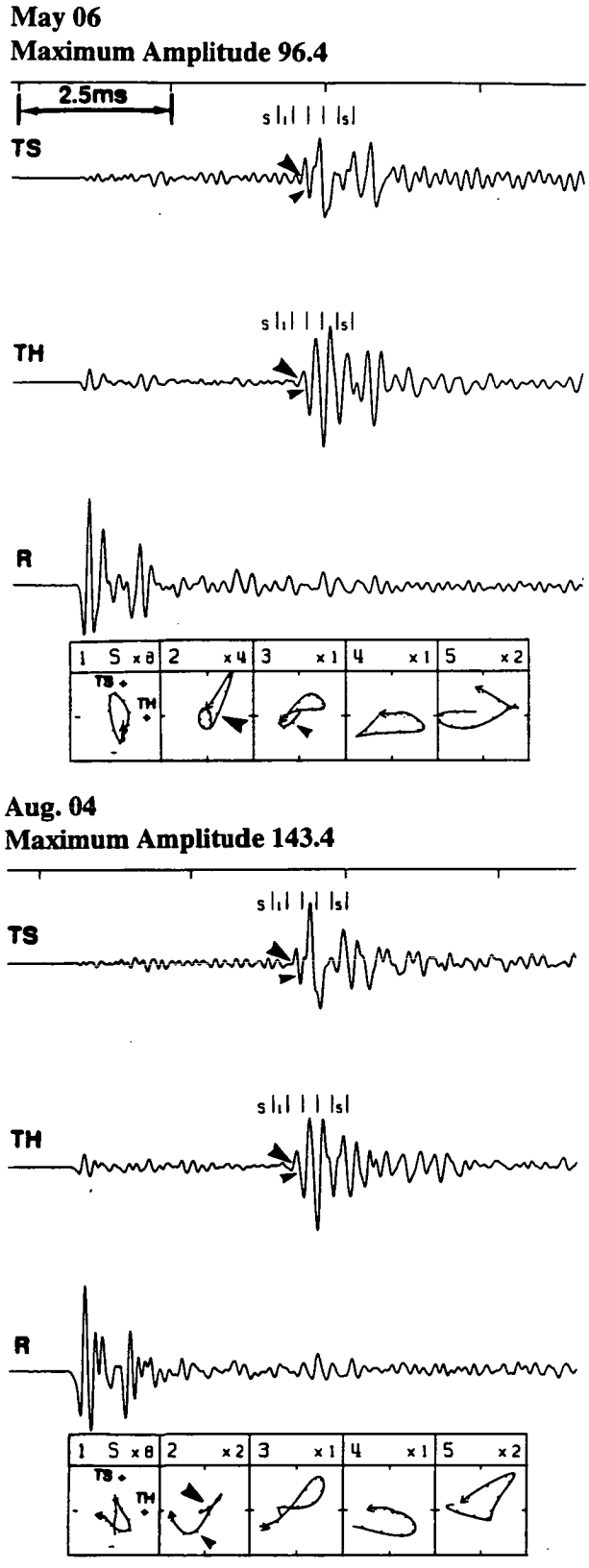

Figure 5.5: Two three-component seismograms from the same source-receiver raypath. Notation is as in Figure 5.2. These seismograms are from a raypath that travelled 7.3° from a shear-wave nodal direction in the source radiation pattern. The emergent shear-wave arrival and slight ringing are typical of seismograms from raypaths that travelled within 20.8° to a nodal direction. The seismograms and particle motion diagrams clearly differ from one another.

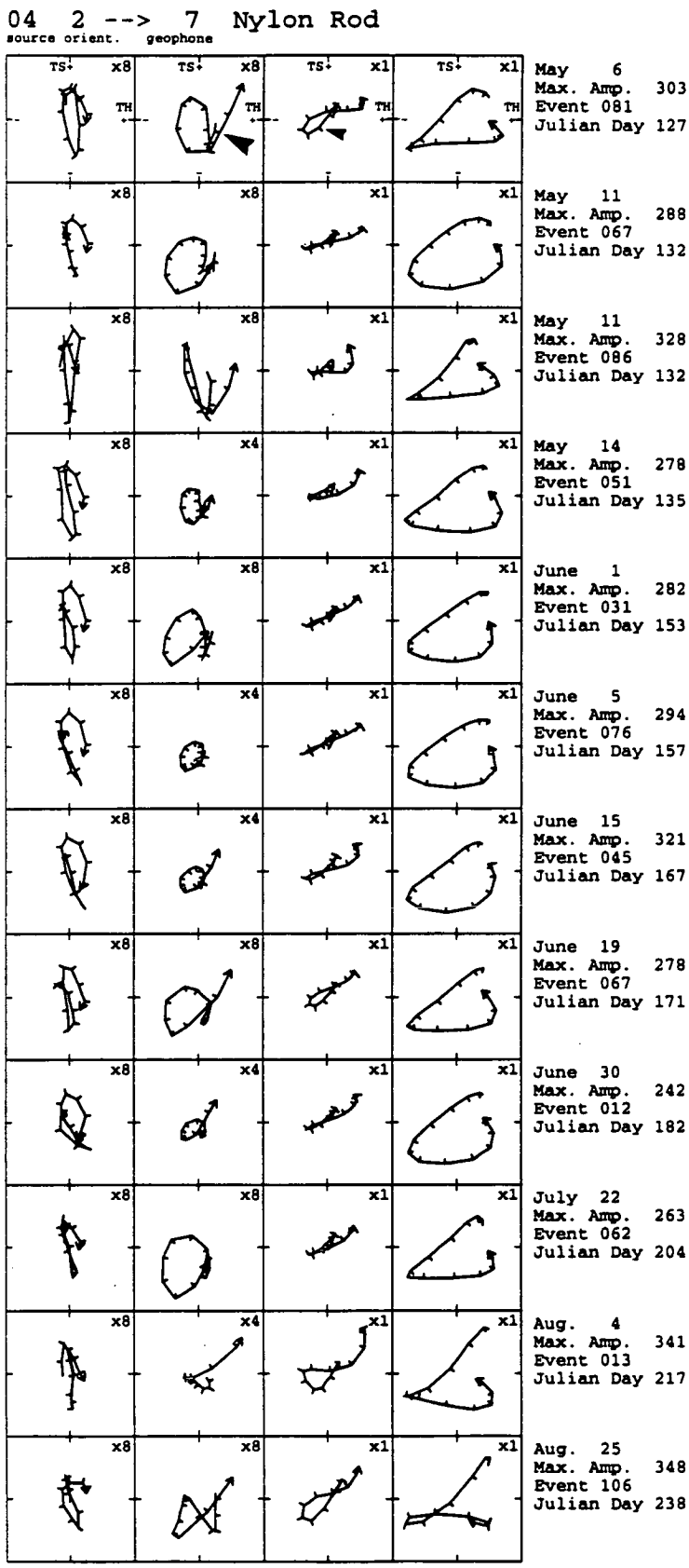

Figure 5.6: The shear-wave particle motion diagrams for the same raypath as in Figure 5.5. Notation is as in Figure 5.3. Clearly the motion differs for different recording sequences, but there is no coherent chronological change.

Table 5.3: Cross Correlation Coeffecients for raypath from Source Station 4 Orientation 2 to Triaxial Accelerometer 7. The resampling factor was 16.

Recording Sequence	Date	Maximum Amplitude of Seismogram Within Window Used in Cross Correlation	Cross-Correlation Coeffecient
1	May 01		
2	May 06	96.2	1.0000
3	May 11	86.0	0.8690
4	May 11	86.6	0.9034
5	May 14	67.2	0.9297
6	June 01	84.0	0.9128
7	June 05	92.9	0.8878
8	June 15	109.2	0.9079
9	June 19	81.1	0.9435
10	June 30	77.0	0.9268
11	July 22	75.7	0.9299
12	Aug. 04	143.4	0.7762
13	Aug. 25	176.1	0.8648

5.9.2 Diffraction Around Source Tunnel

I determined the second cause of temporal variation to be diffraction around source tunnels. For many raypaths the source tunnel directly intersects the straight-line path between source locations and the triaxial accelerometers. The seismic raypath recorded then comprises of seismic energy that diffracted around the source tunnel. Four such raypaths show temporal changes. Two of these raypaths are of the set of raypaths from Source Station 5 to Triaxial Accelerometer 7 and the other two are of the set from Source Station 6 to Triaxial Accelerometer 7. Their straight-line raypath lengths of between 10.5m and 15.7m are the shortest of raypaths that diffracted around their source tunnel. Two seismograms from one of the four raypaths (Orientation 4 of Source Station 5 to Triaxial Accelerometer 7) (Figure 5.7) show the distinctively complicated with non-impulsive *qP*- and shear-wave arrivals

May 01
Maximum Amplitude 227.1

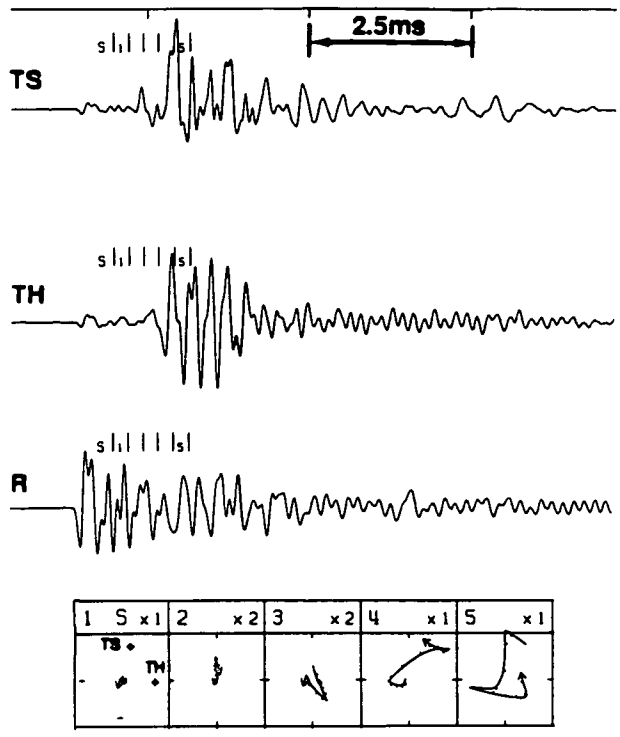

Aug. 25
Maximum Amplitude 299.6

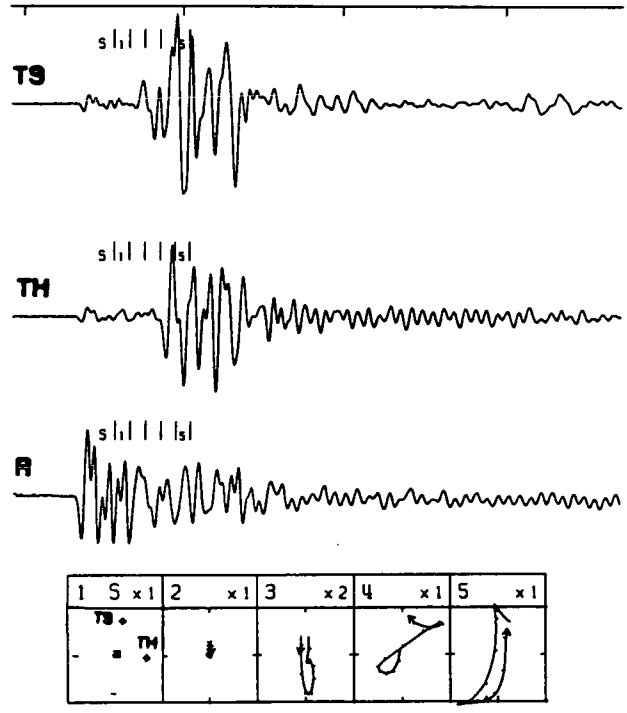

Figure 5.7: Seismograms from the raypath of Source Station 5, Orientation 4, to Triaxial Accelerometer 7 showing temporal changes due to diffraction around its source tunnel. Notation is as in Figure 5.1. Note the emergent shear-wave arrival so that the precise determination of the shear-wave arrival is not possible. The complexity of the seismograms is attributed to the effects of diffraction around the source tunnel and reflections and scattering resulting in the seismic energy travelling through the zone of excavation damage. It is likely that the shear-wave is a conglomerate of shear-waves from travelling in different directions around the source tunnel and the effects of different velocities near the tunnel wall.

typical for all such raypaths. The progressive particle motion diagrams (Figure 5.8) show that the particle motion changes after the third recording sequence on May 11. This agrees with the results of cross-correlation where the coefficient decrease from 0.9736 on May 06 to 0.8348 on May 11 and remained below 0.8800 for all later recording sequences. The results are similar for the other three raypaths.

I do not know the cause of these changes. Raypaths from these to source stations to Triaxial Accelerometer 7 did not travel closer than 21.3m to the Mine-by tunnel so that the changes are not due to the Mine-by tunnel excavation. The changes are likely to be due to changes in the rockmass around Room 413, the source tunnel of Source Stations 5 and 6. Changes may be due to mining activity such as the scaling of loose rock from the tunnel, the installation of rock bolts, or the escape of *in situ* fluids (section 7.9). The changes may also be from longer term effects of excavation such as crack growth, stress redistribution, and the development of the breakout notches. It is an important observation that only half of the raypaths from these source stations to Triaxial Accelerometer 7 show changes. This suggests that either there is a consistent fabric in the rockmass due to these changes so that some shear-wave particle motion directions are less affected, or that changes in the rockmass are extremely localized so that the small differences in source locations are important.

5.9.3 Changes Due to Excavation

I identified the three sets of source stations to triaxial accelerometer raypaths where temporal variations are due to the effects of the Mine-by Tunnel excavation. These are Source Station 10 to Triaxial Accelerometer 15, Source Station 11 to Triaxial Accelerometer 16, and Source Station 12 to Triaxial Accelerometer 16. Evidence of temporal changes is sparse when only considering the results of cross-correlation (Tables 5.4, 5.5, and 5.6). The raypath lengths are all over thirty-nine metres and triaxial accelerometers 15 and 16 were set to the lower gain setting for most recording sequences. Consequently the microseismic system did not automatically trigger to record the data from many recording sequences for these raypaths, limiting the number of raypaths available for comparison. For Orientation 4 of Source Station 12, data was only recorded in the final recording sequence and no comparison can be made. Also the amplitudes of the shear-waves are much less than

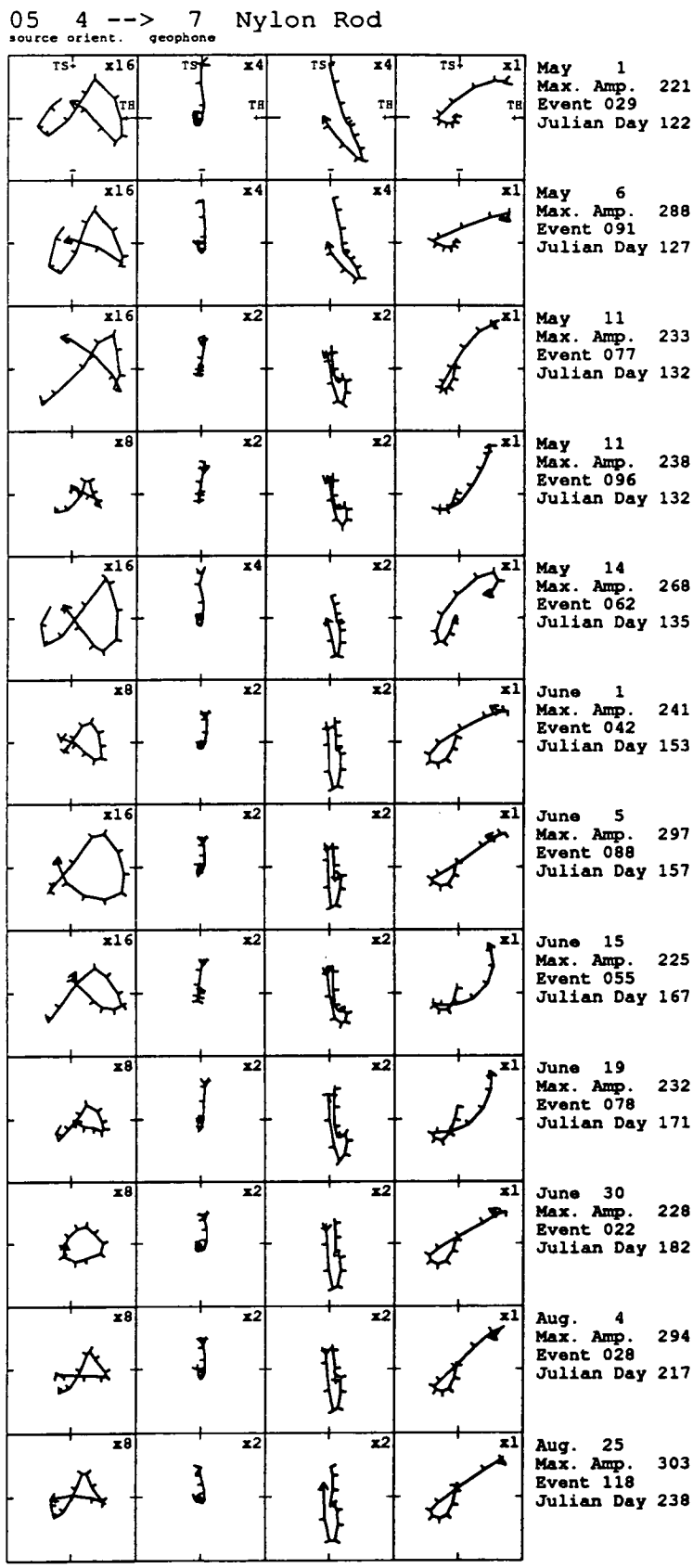

Figure 5.8: The shear-wave particle motion diagrams for the same raypath as in Figure 5.6. Notation is as in Figure 5.3. The initial shear-wave motion from the May 11 sequence clearly differs from that of the previous sequence.

Table 5.4: Cross Correlation Coeffecients for all four raypaths from Source Station 10 to Triaxial Accelerometer 15. The resampling factor was 16.

Recording Sequence and Date		Minimum Separation of Straight Raypath to Mine-by Tunnel (m)	Cross-Correlation Coeffecient (Coef.) and Maximum Amplitude (Amp.) of Seismogram Within Cross Correlation Window for All Four Source Orientations							
			Orientation 1		Orientation 2		Orientation 3		Orientation 4	
			Amp.	Coef.	Amp.	Coef.	Amp.	Coef.	Amp.	Coef.
1	May 01	5.2			78.4	1.0000	117.1	1.0000		
2	May 06	4.4	10.8	1.0000	8.8	0.9367			17.2	1.0000
3	May 11	3.7								
4	May 11	3.7								
5	May 14	2.8			9.7	0.9571	18.7	0.9571	17.3	0.9848
6	June 01	0.7			5.5	0.8872			12.1	0.9504
7	June 05	0.7			6.2	0.8370	11.6	0.9149	13.0	0.9605
8	June 15	0.0			4.4	0.8557	9.5	0.9136		
9	June 19	0.0			3.9	0.5329				
10	June 30	0.0					12.0	0.7619	11.3	0.9509
11	July 22	0.0								
12	Aug. 04	0.0								
13	Aug. 25	0.0	62.8	0.8713	38.7	0.6809	113.8	0.8853	124.1	0.9798

Table 5.5: Cross Correlation Coeffecients for all four raypaths from Source Station 11 to Triaxial Accelerometer 16. The resampling factor was 16.

Recording Sequence and Date		Minimum Separation of Straight Raypath to Mine-by Tunnel (m)	Cross-Correlation Coeffecient (Coef.) and Maximum Amplitude (Amp.) of Seismogram Within Cross Correlation Window for All Four Source Orientations							
			Orientation 1		Orientation 2		Orientation 3		Orientation 4	
			Amp.	Coef.	Amp.	Coef.	Amp.	Coef.	Amp.	Coef.
1	May 01	5.5								
2	May 06	4.6			15.6	1.0000	13.7	1.0000		
3	May 11	3.8								
4	May 11	3.8			14.0	0.9301				
5	May 14	2.9	16.1	1.0000						
6	June 01	0.0	10.6	0.9734	10.3	0.9435	11.4	0.8800		
7	June 05	0.0	12.8	0.9446	12.8	0.8926				
8	June 15	0.0								
9	June 19	0.0							8.6	1.0000
10	June 30	0.0	6.9	0.6691						
11	July 22	0.0			8.9	0.1348				
12	Aug. 04	0.0	6.0	0.6475			8.0	0.4850		
13	Aug. 25	0.0	56.0	0.7306	83.4	0.5292	57.6	0.5793	86.5	0.8938

Table 5.6: Cross Correlation Coeffecients for all four raypaths from Source Station 12 to Triaxial Accelerometer 16. The resampling factor was 16.

Recording Sequence and Date		Minimum Separation of Straight Raypath to Mine-by Tunnel (m)	Cross-Correlation Coeffecient (Coef.) and Maximum Amplitude (Amp.) of Seismogram Within Cross Correlation Window for All Four Source Orientations							
			Orientation 1		Orientation 2		Orientation 3		Orientation 4	
			Amp.	Coef.	Amp.	Coef.	Amp.	Coef.	Amp.	Coef.
1	May 01	5.9			88.5	1.0000				
2	May 06	4.9			9.1	0.9715				
3	May 11	4.2								
4	May 11	4.2								
5	May 14	3.3			11.1	0.8948				
6	June 01	0.0			7.2	0.9115				
7	June 05	0.0	7.5	1.0000	6.9	0.6731	8.5	1.0000		
8	June 15	0.0								
9	June 19	0.0								
10	June 30	0.0								
11	July 22	0.0								
12	Aug. 04	0.0			3.5	0.2483				
13	Aug. 25	0.0	47.6	0.3253	34.1	0.6683	66.2	0.9179	43.4	1.0000

60 units for most of the recording sequences. In particular, the amplitude of the first recording sequence for the raypath of Orientation 1 of Source Station 12 was extremely low and suffered greatly from poor resolution. The final cross-correlation coefficients of three of the raypaths were 0.9179 or greater giving no clear indication of any temporal changes. The raypath from Orientation 4 of Source Station 10 to Triaxial Accelerometer 15 showed no temporal changes for reasons to be explained (section 5.11). Only one raypath both had coefficient less than 0.90 and amplitudes greater than 60 units. However, the coefficients do indicate possible temporal changes for nine raypaths of these twelve.

Visual examination of the seismograms and particle motion diagrams give more concrete evidence. The seismograms for Orientations 2 and 3 of Source Station 10 to Triaxial Accelerometer 15 (Figures 5.9 and 5.10) and the progressive particle motion diagrams for all three sets of raypaths (Figures 5.11, 5.12, and 5.13) show that changes in the initial shear-wave motion has taken place for the ten raypaths where comparison is possible. The changes are not random jitter or the typical subtle fluctuations.

There are common raypath characteristics of these three sets of raypaths that clearly indicate that the observed changes are directly due to the excavation of the Mine-by Tunnel and suggest that no other sets of raypaths should show temporal changes due to excavation. 53 of the 208 sets of raypaths travelled within five metres of the Mine-by tunnel. For 51 of the 208 sets of raypath the minimum distance between the Mine-by tunnel and the raypath decreased as the Mine-by tunnel was excavated. Only four sets of raypaths share both of these characteristics and three of these are these three sets showing temporal changes. The one set of raypaths of the four not showing temporal changes is from Source Station 10 to Triaxial Accelerometer 16. The straight-line raypath for this set of raypaths was never closer than 3.0m to the Mine-by Tunnel. The changes are therefore only seen in raypaths that propagated within 3.0m to the Mine-by Tunnel and propagated progressively closer as the excavation proceeded. This result is consistent with the zone of excavation disturbance extending to only one tunnel diameter from the tunnel wall (next section). Only these temporal changes will be discussed in the remainder of this chapter.

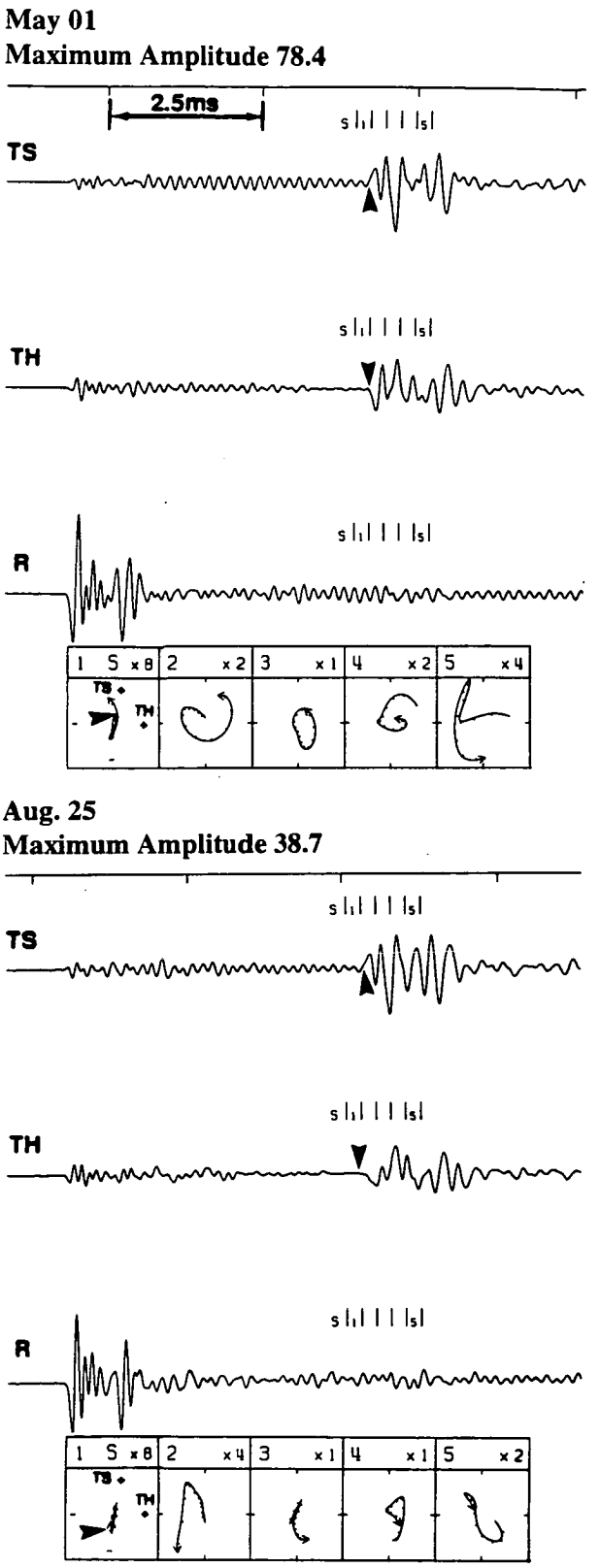

Figure 5.9: Seismograms from the first and last recording sequences the for raypath from Source Station 10, Orientations 2, to Triaxial Accelerometer 15. Notation is as in Figure 5.1. The shear-wave arrivals could not be picked because of the emergent shear-wave arrival and ringing. The large arrowheads mark only the approximate arrivals of shear-wave motion.

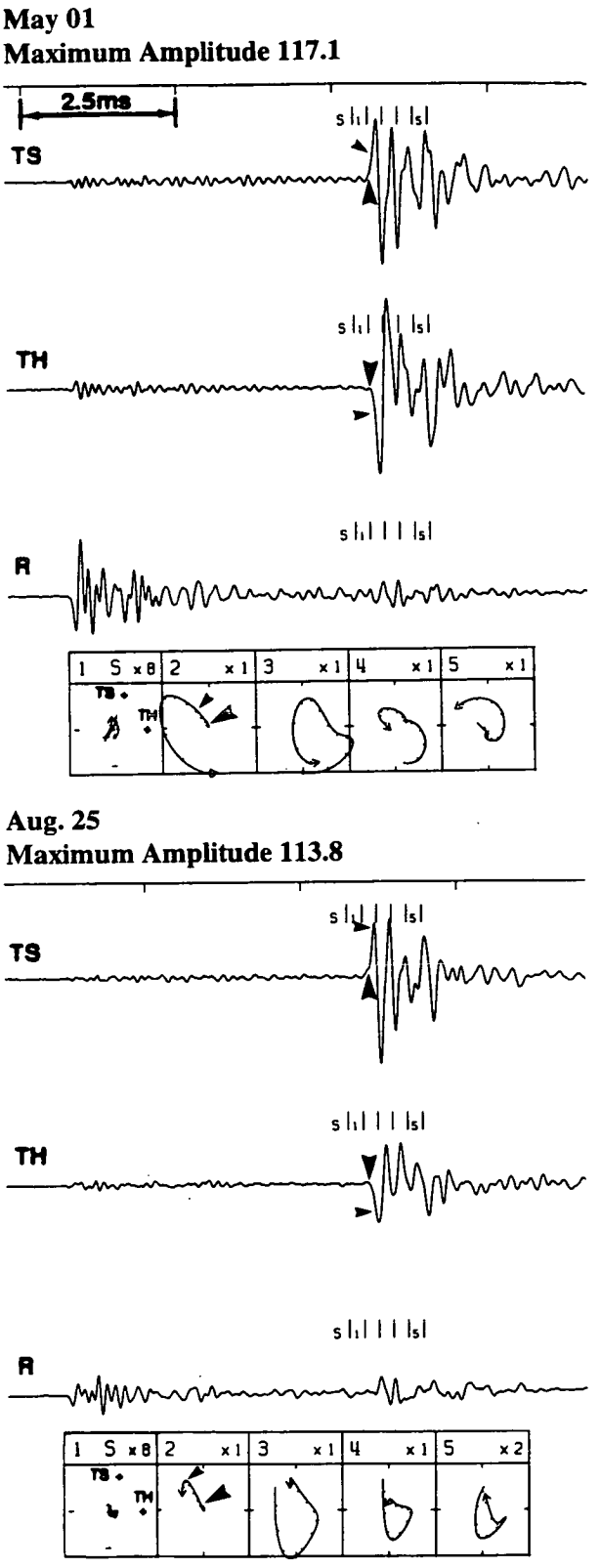

Figure 5.10: Seismograms from the first and last recording sequences the for raypath from Source Station 10, Orientations 3, to Triaxial Accelerometer 15. Notation is as in Figure 5.1. The shear-wave arrivals could not be picked because of the emergent shear-wave arrival and ringing. The large and small arrowheads mark the arrival of the *qS1*-wave and *qS2*-wave respectively.

Figure 5.11 (below): The shear-wave motion for all recording sequences for the raypaths from Source Station 10 to Triaxial Accelerometer 15 for (a) Orientation 1, (b) Orientation 2, (c) Orientation 3, and (d) Orientation 4. The notation is as in Figure 5.3. The large and small arrowheads mark the arrival of the *qS1*-wave and *qS2*-wave respectively when these arrivals could be picked See text for discussion.

(a)

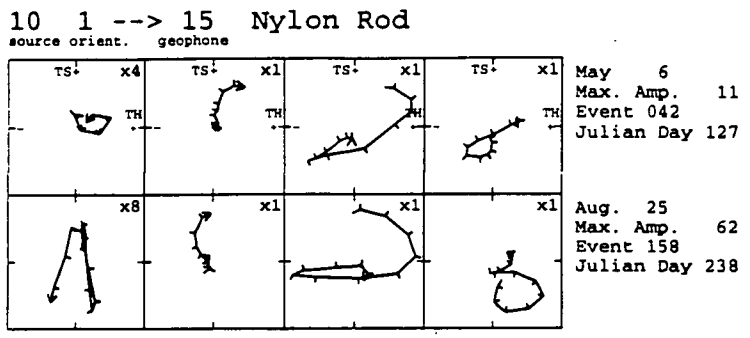

(b)

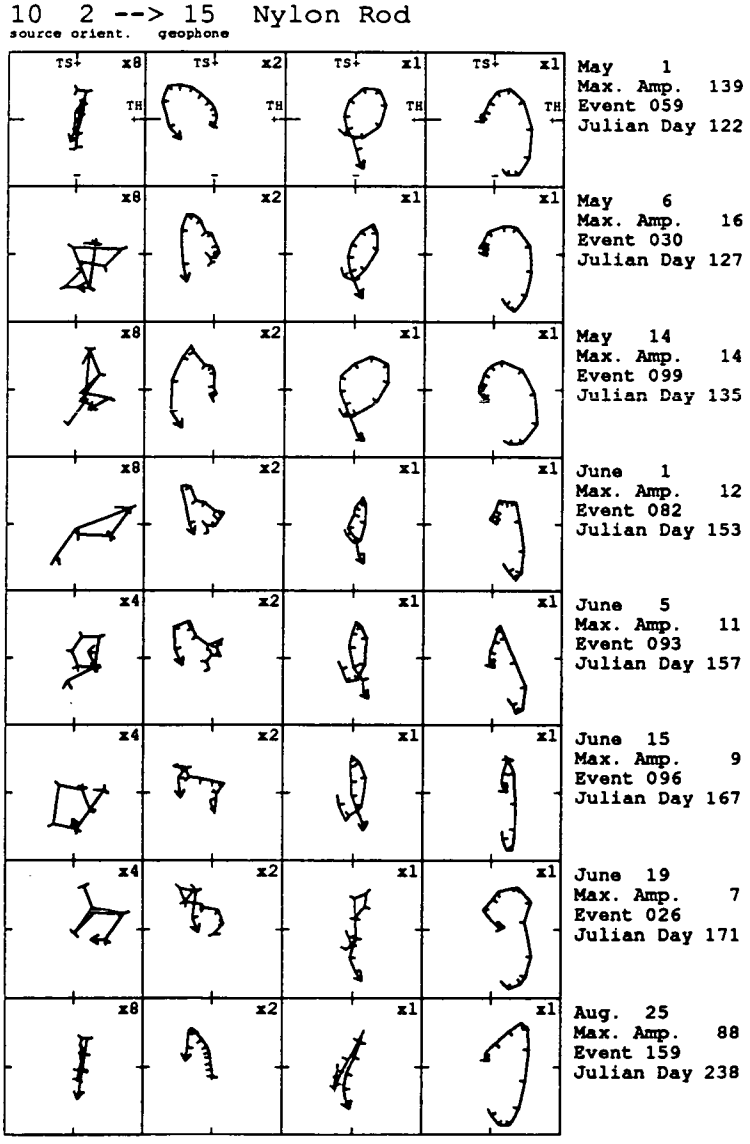

(c) 10 3 --> 15 Nylon Rod
source orient. geophone

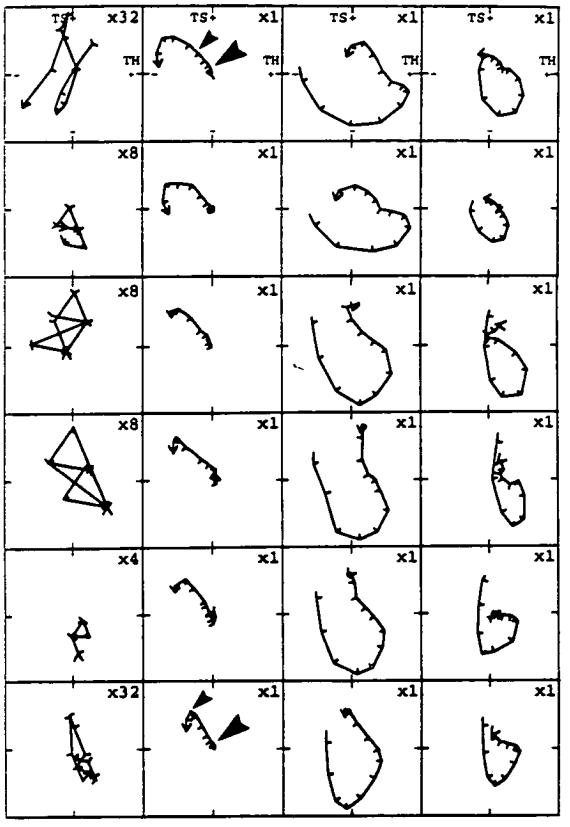

May 1
Max. Amp. 117
Event 060
Julian Day 122

May 14
Max. Amp. 19
Event 100
Julian Day 135

June 5
Max. Amp. 11
Event 094
Julian Day 157

June 15
Max. Amp. 9
Event 097
Julian Day 167

June 30
Max. Amp. 10
Event 069
Julian Day 182

Aug. 25
Max. Amp. 113
Event 001
Julian Day 238

(d) 10 4 --> 15 Nylon Rod
source orient. geophone

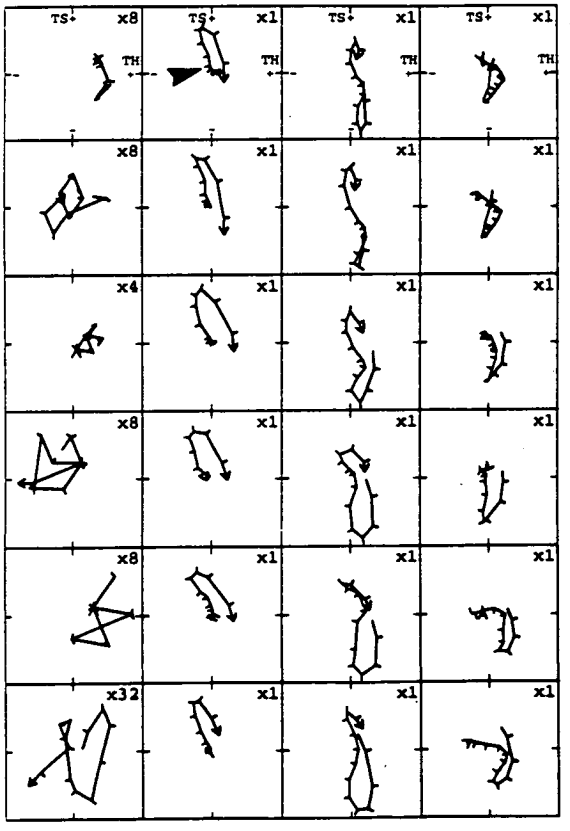

May 6
Max. Amp. 17
Event 031
Julian Day 127

May 14
Max. Amp. 17
Event 001
Julian Day 135

June 1
Max. Amp. 12
Event 084
Julian Day 153

June 5
Max. Amp. 13
Event 095
Julian Day 157

June 30
Max. Amp. 11
Event 070
Julian Day 182

Aug. 25
Max. Amp. 120
Event 002
Julian Day 238

Figure 5.12 (below): The shear-wave motion for all recording sequences for the raypaths from Source Station 11 to Triaxial Accelerometer 16 for (a) Orientation 1, (b) Orientation 2, (c) Orientation 3, and (d) Orientation 4. The notation is as in Figure 5.3. The large marks the arrival of the *qS1*-wave where this could be picked arrival picked See text for discussion.

(a)

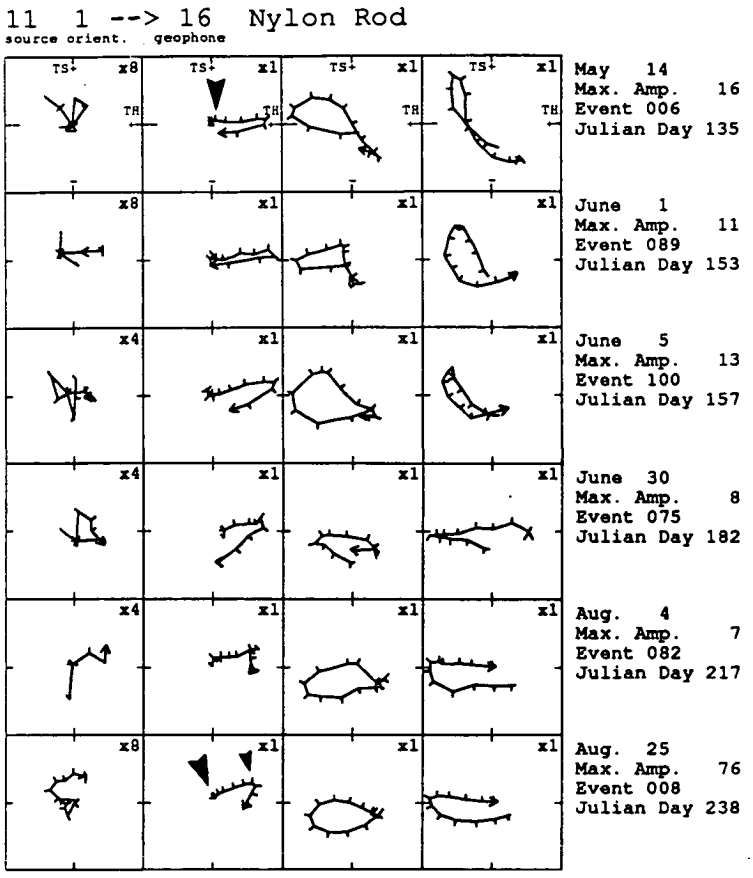

(b)

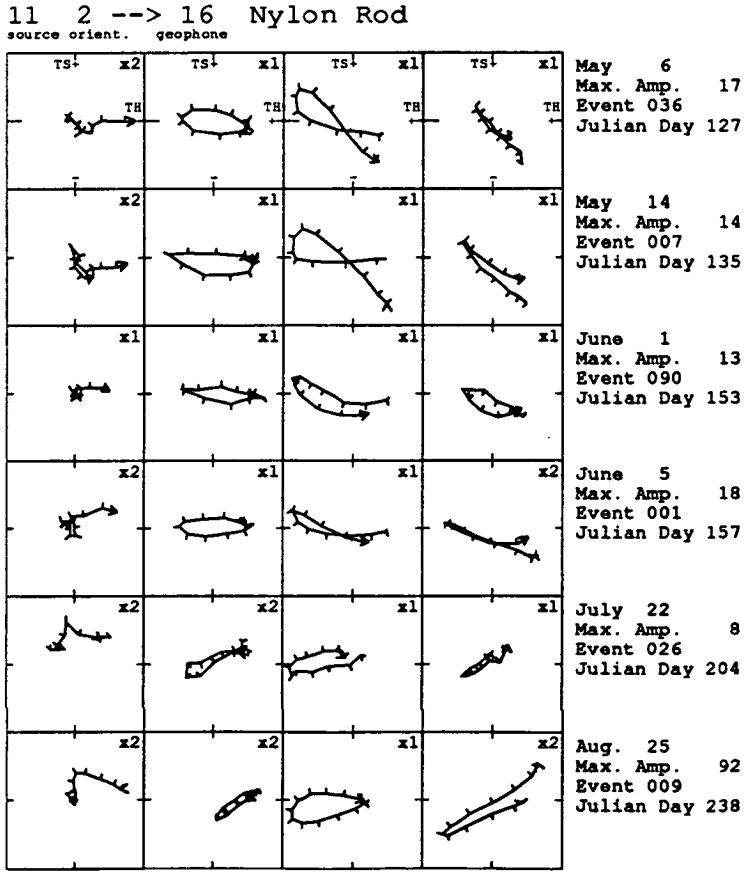

(c) 11 3 --> 16 Nylon Rod
source orient. geophone

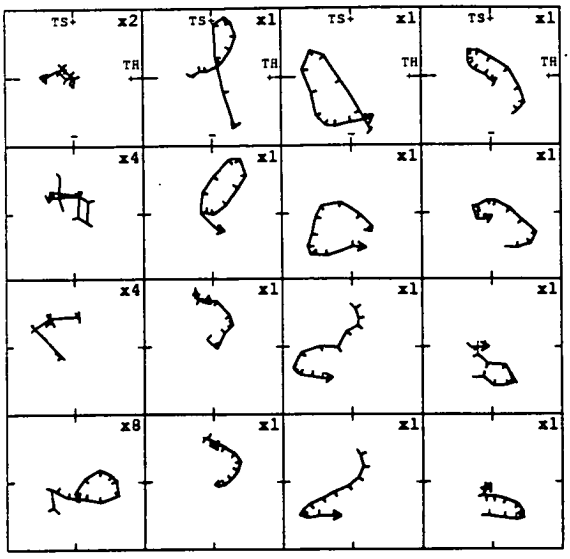

May 6
Max. Amp. 13
Event 043
Julian Day 127

June 1
Max. Amp. 11
Event 091
Julian Day 153

Aug. 4
Max. Amp. 8
Event 084
Julian Day 217

Aug. 25
Max. Amp. 76
Event 010
Julian Day 238

(d) 11 4 --> 16 Nylon Rod
source orient. geophone

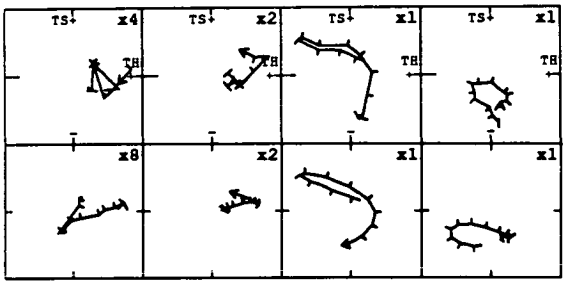

June 19
Max. Amp. 9
Event 040
Julian Day 171

Aug. 25
Max. Amp. 85
Event 011
Julian Day 238

Figure 5.13 (below): The shear-wave motion for all recording sequences for the raypaths from Source Station 12 to Triaxial Accelerometer 16 for (a) Orientation 1, (b) Orientation 2, (c) Orientation 3, and (d) Orientation 4. The notation is as in Figure 5.3. The large marks the arrival of the *qS1*-wave where this could be picked arrival picked See text for discussion.

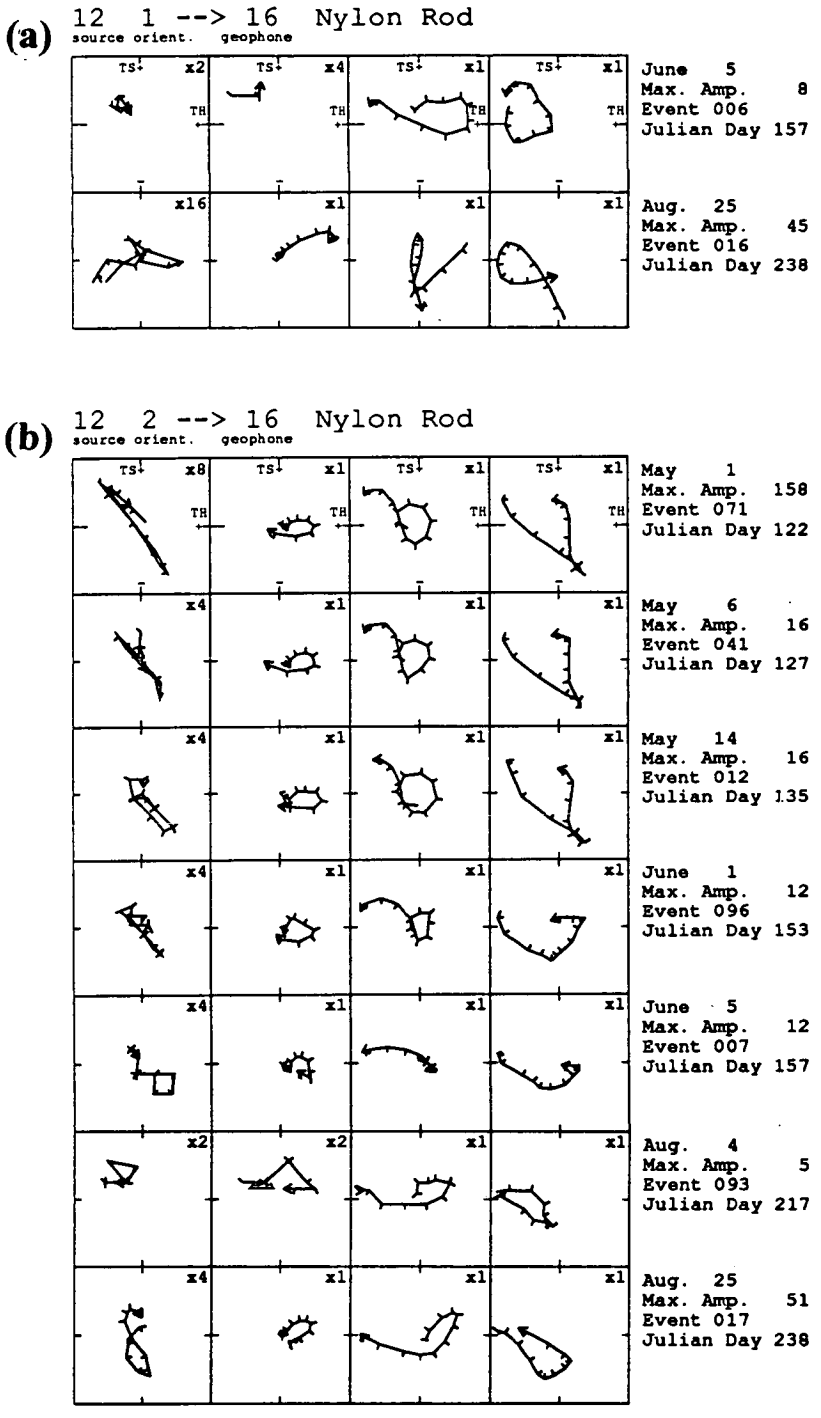

(c)

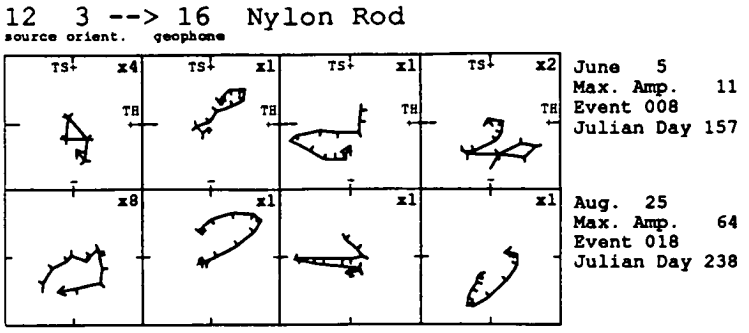

(d)

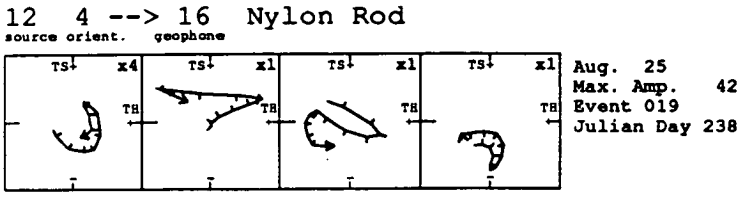

5.10 Distance of Observable Effects

I will now compare the changes in the particle motions of raypaths affected by excavation with the separation between the raypaths and the Mine-by tunnel. I do this to gain insight into the distance of observable excavation effects. First I will introduce three terms. The *zone of excavation damage* around a tunnel is defined as the region where non-elastic deformation occurs because of tunnel excavation and is confined to a skin of 0.5m thickness around the Mine-by Tunnel (Maxwell and Young, 1994; R. Everitt, pers. comm.). The *zone of excavation disturbance* is the zone beyond the zone of excavation damage where elastic stress changes occur (Maxwell and Young, 1994) and extends to a distance of at least a tunnel diameter from the Mine-by Tunnel (P. Young, pers. comm.). I define the *distance of observable effects* to be the maximum separation of the straight-line raypath perpendicular to the Mine-by Tunnel wall for the initial shear-wave motion to be detected due to the excavation-affected rockmass. The distance of observable effects is therefore less than the distance containing the zone of excavation disturbance, and is dependent upon the frequencies of the seismic signals.

I suggest that the onset of temporal change for the raypaths from Source Station 10 to Triaxial Accelerometer 15 was at Recording Sequences 9 (June 01) from the

comparison of cross-correlation coefficients and the particle motion diagrams. This is best seen on the particle motion diagrams for Orientation 2, although the exact onset of temporal changes is not conclusive because of the low amplitude of the seismograms. This suggests that the distance of observable effects to be between 0.7m and 2.8m from the comparison of raypath separations for Recording Sequences 8 and 9 (May 14 and June 01) (Table 5.4). Similarly, I suggest that the onset of temporal changes for raypaths from Source Stations 11 and 12 to Triaxial Accelerometer 16 was at Recording Sequence 6 (June 01), indicating the distance of observable effects to be between 0.0m and 2.9m. This range entirely contains the range of 0.7m to 2.8m and so provides no additional constraints. The position of the Mine-by Tunnel relative to these three sets of raypaths for every recording sequence is presented in Figures 5.14 and 5.15. 0.7m is greater than the extent of the zone of excavation damage so that the initial changes in shear-wave motion are due to the advancement of the zone of excavation disturbance.

Three sets of raypaths are not enough to consider asymmetries. The development of break-out notches shows that the zone of excavation damage is radially asymmetric so the distance of observable effects is also expected to be asymmetric. Microcracking due to excavation does occur ahead of the advancing tunnel face (Martin and Young, 1993) so that distance of observable effects is cylindrically asymmetric for raypaths that travel near the tunnel face.

The true minimum separation of these three sets of raypaths from the Mine-by Tunnel will be greater than that calculated assuming straight-line raypaths because of diffraction around the Mine-by Tunnel. Often clear, impulsive *qP*-, *qS1*-, and *qS2*-arrivals, and relatively simple particle motion behaviour are seen on seismograms where the corresponding straight-line raypath intersects the Mine-by Tunnel, demonstrating that diffraction takes place. This has also been observed is other seismic data sets from the Mine-by Experiment. (Young and Collins, 1993; Maxwell and Young, 1994). Furthermore, diffraction must mainly take place in the zone of excavation disturbance rather than the zone of excavation damage. It is unreasonable that sufficient diffraction could take place mainly within the 0.5m skin of excavation damage (section 5.2) when the raypaths showing temporal changes were for straight-line raypath lengths between 39.3m and 43.0m. A similar argument was

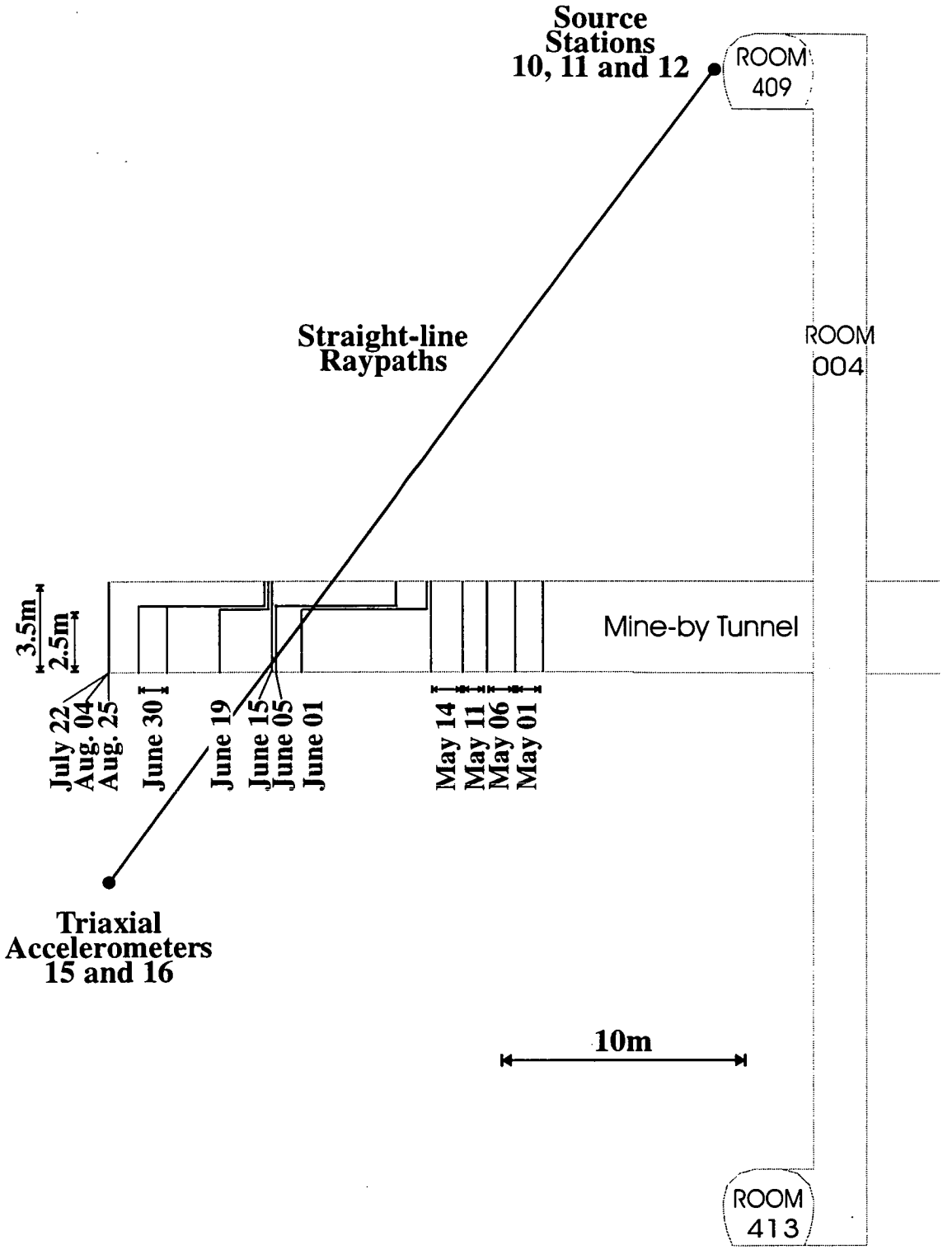

Figure 5.14: Cross-section of the 420-Level around the Mine-by Tunnel looking horizontal and perpendicular to the tunnel drawn to the indicated scale. The location of the tunnel faces during each recording sequence is as marked on the diagram, with arrows denoting the possible ranges where the exact locations are not known. The straight-line raypaths for the Source Station 10 to Triaxial Accelerometer 15 and Source Stations 11 and 12 to Triaxial Accelerometer 16 are projected onto the plane of display.

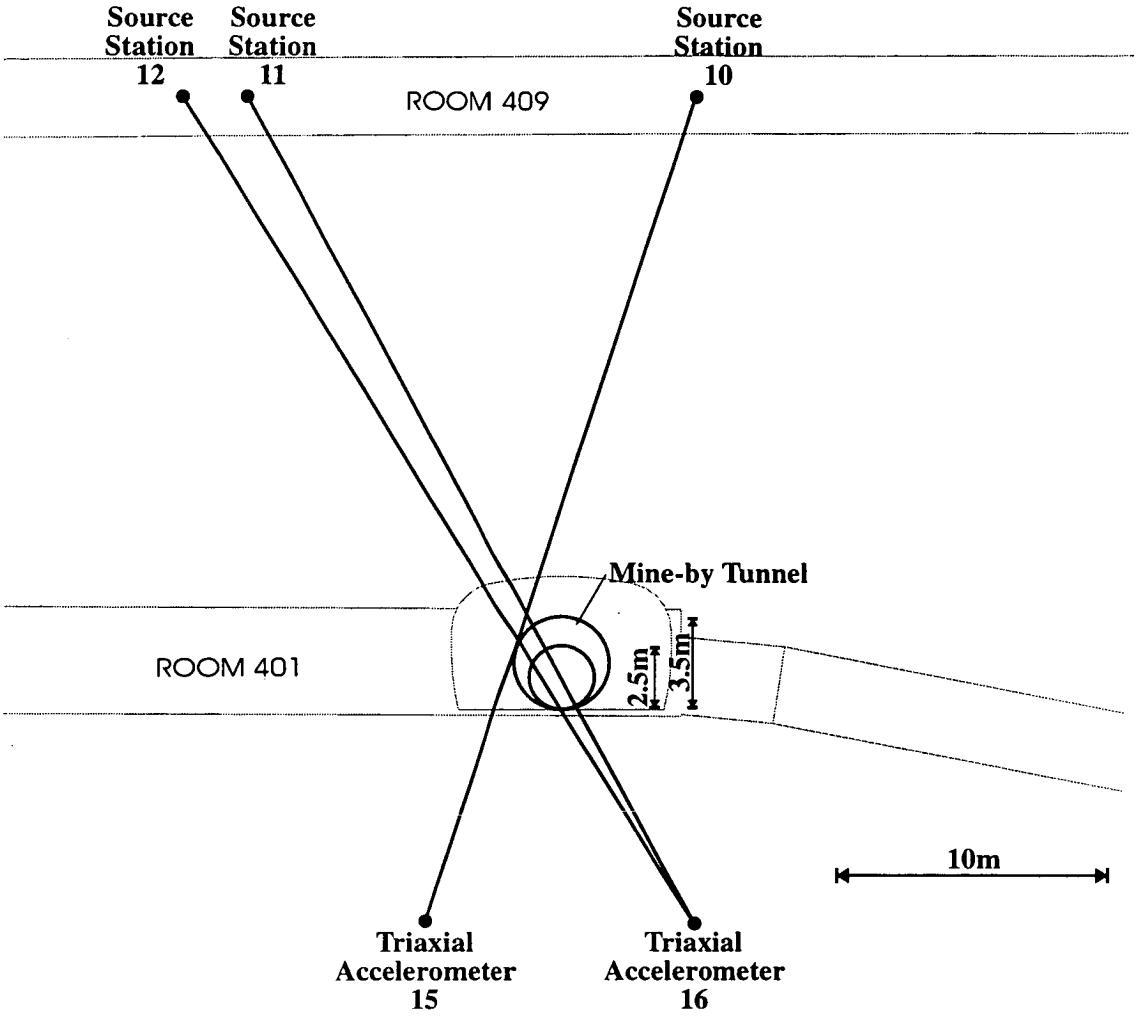

Figure 5.15: Cross-section of the 420-Level around the Mine-by Tunnel looking horizontal and parallel to the tunnel drawn to the indicated scale. The two tunnel diameters used in excavation are shown the diagram. The straight-line raypaths for the Source Station 10 to Triaxial Accelerometer 15 and Source Stations 11 and 12 to Triaxial Accelerometer 16 are projected onto the plane of display.

made by Maxwell and Young (1994). This is supported by the particle motions for the raypaths showing temporal changes. The particle motions of Source Stations 11 and 12 to Triaxial Accelerometer 16 up to Recording Sequence 7 (June 05) and for Source Station 10 to Triaxial Accelerometer 15 for all recording sequences show clear arrivals and relatively simple particle motions despite some straight-line raypaths intersecting the Mine-by Tunnel (Figures 5.10, 5.11, 5.12, and 5.13). More complicated particle motion behaviour due to scattering would be expected if a significant portion of these raypaths traversed the zone of excavation damage, and clear arrivals would not be expected if a significant amount of seismic energy was blocked and reflected by the Mine-by Tunnel. Such behaviour is seen in the particle motions for Source Stations 11 and 12 to Triaxial Accelerometer 16 after Recording Sequence 7 (June 05) (Figures 5.12 and 5.13) where large proportions of the straight-line raypaths were directly through the Mine-by Tunnel (Figures 5.14 and 5.15).

5.11 Interpretation in Terms of Shear-Wave Splitting

The analysis of temporal changes so far has considered observations of changes solely in the initial shear-wave motion between recording sequences. In this section I consider the observation and interpretation of changes in shear-wave splitting.

Unfortunately, the initial particle motion directions of the direct shear-waves cannot be identified for nine of the twelve raypaths. This is mainly due to low gain settings for most recording sequences and the relatively long raypaths of 39.3m to 43.0m. Also, for Recording Sequence 7 (June 05) onwards, a large proportion of the straight-line raypaths from Source Stations 11 and 12 to Triaxial Accelerometer 16 were through the Mine-by Tunnel (Figures 5.14 and 5.15). Onwards from this recording sequence these raypaths display very complex behaviour (Figures 5.12 and 5.13) due to the blocking and reflecting of seismic energy by the Mine-by Tunnel and the propagation of seismic energy through the zone of excavation damage. Also, interference from sensor resonance obscured the initial shear-wave arrivals for two of the four raypaths from Source Station 10 to Triaxial Accelerometer 15.

I suggest that the main effect of excavation upon shear-wave splitting is an increase in time delays due to an overall increase in the strength of anisotropy

traversed by the raypaths without a change in fabric orientation. The initial particle motions can be identified on the raypaths from Orientations 3 and 4 of Source Station 10 to Triaxial Accelerometer 15 and Orientation 1 of Station 11 to Triaxial Accelerometer 16 (Figures 5.10, 5.11, and 5.12). For Orientation 3 of Source Station 10, the particle motion of last recording sequence displays the same polarizations, but an increased time delay of five sample points (100μs) from the original three sample points (60μs) of the first recording sequence. This is the best example of a temporal change in this data set. For Orientation 4 of Source Station 10, there is no obvious change in particle motion for the first half-wavelength (12 sample points) and cross-correlation suggests no temporal changes throughout the tunnel excavation (section 5.9.3). The polarization direction is the same as for Orientation 3, but the time delay is much longer. I interpret this as an example where the *qS1*-polarization direction is the same as the initial shear-wave motion from the source. Therefore no change in the initial shear-wave motion results for an increase time delays without changing polarizations. The initial shear-wave particle motion for seismograms from Orientation 1 of Source Station 11 to Triaxial Accelerometer 16 is that due to the source orientation, but changes with later recording sequences (Figure 5.12) to the polarization direction expected for the *in situ* anisotropy (section 7.7). Again, this is consistent with an increase of the strength of anisotropy traversed by the raypath.

With only three raypaths, it is possible that the changes in particle motions are being misinterpreted as changes in shear-wave splitting. However, such a simple and consistent interpretation would then be unlikely. Also, this interpretation is in agreement with the analysis of Maxwell and Young (1994) who concluded from a comparison of *P*-wave velocities of the Attenuation Survey and Velocity Survey data sets (section 2.15) that excavation amplified the *in situ* anisotropy.

5.12 Geological Interpretation

I suggest that the onset of temporal changes indicates that EDA is at least partially responsible for the *in situ* anisotropy. I argued that the onset of temporal changes is due to the advancement of the zone of excavation disturbance rather than the zone of excavation damage (section 5.10). The three mechanisms likely responsible for these changes are subcritical crack growth, fluid loss by migration to the free surface, and

changes in EDA due to changes in the stress field. However, the effects of sub-critical crack growth are likely to be insignificant because velocity changes due to excavation extend to only 0.75m from the Mine-by Tunnel wall (section 2.14). Changes due to fluid loss show there exists fluid-filled inclusions or microcracks in the *in situ* rockmass that may be stress-aligned and therefore suggest the presence of EDA-cracks.

The onset of temporal changes may be due to changes in the aspect ratio of EDA-cracks. The directions of raypaths from Source Station 11 to Triaxial Accelerometer 16 are 64° from the vector normal to the plane of the *in situ* fabric (section 7.7). This is within the range of 45° to 75° where shear waves are most sensitive to changes in aspect ratios (Crampin et al., 1990), so that changes in time delays maybe be expected even for small to changes in the stress field. Zatsepin and Crampin (1995a) argue that fluid-migration along pressure gradients between neighbouring EDA-cracks at different orientations to the stress field can take place at very low values of differential stress.

An increase in the strength of anisotropy due to excavation (previous section) suggests that excavation produces an anisotropic fabric with an orientation governed by similar processes as govern the orientation of the *in situ* anisotropy. This indicates that the orientations are governed either by the in situ stress field, or the primary layering. Crack growth is expected in the plane perpendicular to σ_3 (Martin et al., 1995). This interpretation is in agreement with the orientation of an excavation-induced crack set in the zone of excavation damage (section 2.14), and suggests that the temporal changes are primarily due to the development of dry cracks (section 7.9).

5.13 Conclusions

I have presented two methods of searching for possible temporal changes: cross-correlation and visual examination. As well as being automated, unbiased, and faster than visual examination, I demonstrated cross-correlation to be more reliable, and therefore the preferred method of searching for temporal changes. I established that resampling the seismic data to one-sixteenth its original sample interval was sufficient to avoid significant effects of non-coincidental sampling of the waveforms.

A cross-correlation coefficient of 0.90 or greater is expected when no temporal changes are present, proving the extreme reproducibility of this experiment. Visual examination allows greater insight into the cause of any perceived temporal change, and allows qualitative accounting for the effects of background noise and the ringing of the source. I demonstrated the use of progressive particle motion plots to be a fast and efficient method for the visual examination of temporal changes because only the necessary information of the initial shear-wave particle motion in the plane perpendicular to the source-receiver raypath direction is considered.

All seismograms from raypaths that propagate within 20.8°, and some that raypaths propagate as much as 31.5°, from a nodal direction display either emergent shear-wave arrival, sensor resonance, or lower levels of reproducibility. These results show that the direction of propagation relative to radiation patterns should be considered in studies of temporal changes to prevent attributing changes in shear-wave motion as being due to significant changes in the rockmass.

I found temporal changes in four of the eight shortest raypaths that diffracted around their source tunnel. Two raypaths of these four had a straight-line raypath length of 10.5m and two raypaths had a straight-line raypath length of 15.7m. The geological cause is unknown but must be due to localized changes in the rockmass around the source tunnel (Room 413).

I observed changes in the initial shear-wave motion due to the Mine-by Tunnel excavation in three sets of source station to triaxial accelerometer raypaths. The three sets of raypaths are the only ones to travel within 3.0m of the Mine-by tunnel and have the minimum separation between the straight-line raypaths the Mine-by Tunnel decreased as the tunnel was excavated. Examination of the onset of temporal changes with straight-line raypaths separations to the advancing tunnel indicates the distance of observable effects to be between 0.7m and 2.8m, as is consistent with a limit to the zone of excavation disturbance of one tunnel diameter (3.5m).

The onset of these temporal changes is due to the advancement of the zone of excavation disturbance rather than the zone of excavation damage. I argued this by considering the distance of observable effects, the spatial limit of the zone of excavation damage, and diffraction effects as implied by the clarity of seismic signals even after the Mine-by Tunnel intersected the straight-line raypaths. This result

demonstrates the potential use of monitoring changes in shear-wave particle motion as a non-destructive method to monitor tunnel excavation and possible longer term changes in a rockmass. I also argued that these initial temporal changes must be due to either the escape of fluids or changes in EDA-cracks, thereby suggesting EDA to be an anisotropic fabric *in situ*.

I interpret the major changes in shear-wave splitting from tunnel excavation as being an increase in the strength of anisotropy due to excavation-induced and altered cracks and microcracks, as is consistent with the observed changes in shear-wave splitting. Therefore the orientations of these excavation-induced and altered cracks are governed by the *in situ* stress field or the primary layering within the rockmass. However, this result is somewhat speculative because shear-wave splitting could only be measured for three of the raypaths showing temporal changes from excavation.

6 The Judgement-of-Fitness

6.1 Abstract

Judgement-of-fitness algorithms comparing shear-wave polarization data to models should measure the number of observations that cannot be explained by the model. An automated inversion program finds the model that minimizes this misfit value. This value may then be used to ascertain whether the misfit is due to incorrect modelling assumptions, invalid physical assumptions, or miss-picked polarizations. The final algorithm presented performs this task quickly even for large data sets by calculating the model polarizations on a regularly spaced grid of orientations and comparing the observed polarization to the four nearest model polarizations of this grid. Rapidly varying polarizations due to singularities are then easily taken into account by determining the range of polarization angles of the four polarizations.

6.2 Introduction: The Limitations of Visual Comparison

The problems of visual comparison of data with models are the same as with any modelling: it is subjective, it does not allow quantitative judgement of accuracy or error, and patterns may be perceived in visual examination from biases judgement. Figures 6.1a and 6.1b illustrate this problem. Both figures display the pattern of polarizations resulting from a single fabric of Hudson Cracks. Superimposed are the fifty-three measured polarizations from the Shear-Wave Experiment data set and the fifty-three polarizations from assuming reciprocal symmetry (section 1.6). The first model is for saturated cracks and has the distinctive line singularity, whereas the second is for dry cracks and has no such line singularity (section 1.8). Despite the distinctive differences, it is not clear solely by visual comparison which model better matches the observed polarizations. Thus the judgement-of-fitness of models to data needs to be quantified. Also, the automated inversion of data requires a quantitative method of judging fitness.

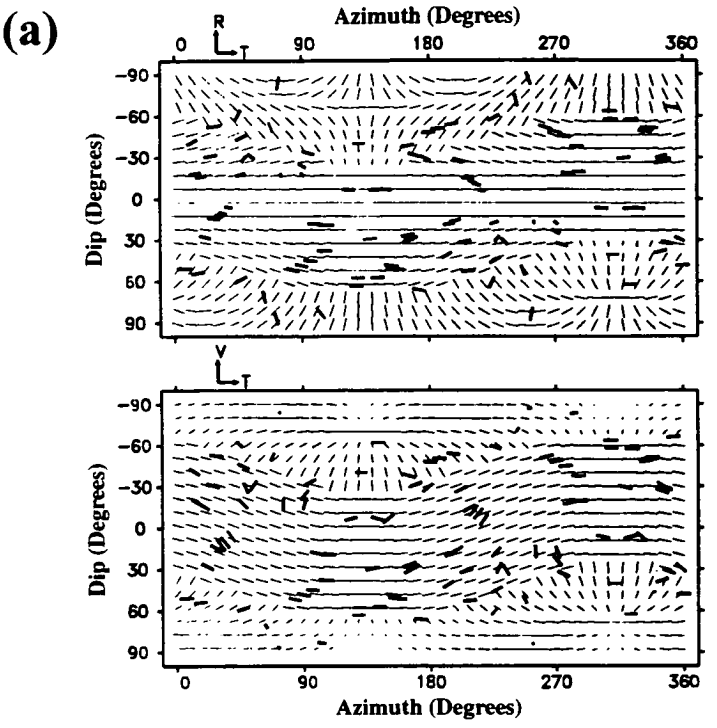

Figure 6.1a: The group velocity polarizations of a model of saturated Hudson Cracks of orientation 045/20, crack density ε=0.020, and aspect ratio γ=0.050. Superimposed are the fifty-three measured polarizations and the fifty-three polarizations from assuming reciprocal symmetry of the Shear-Wave Experiment.

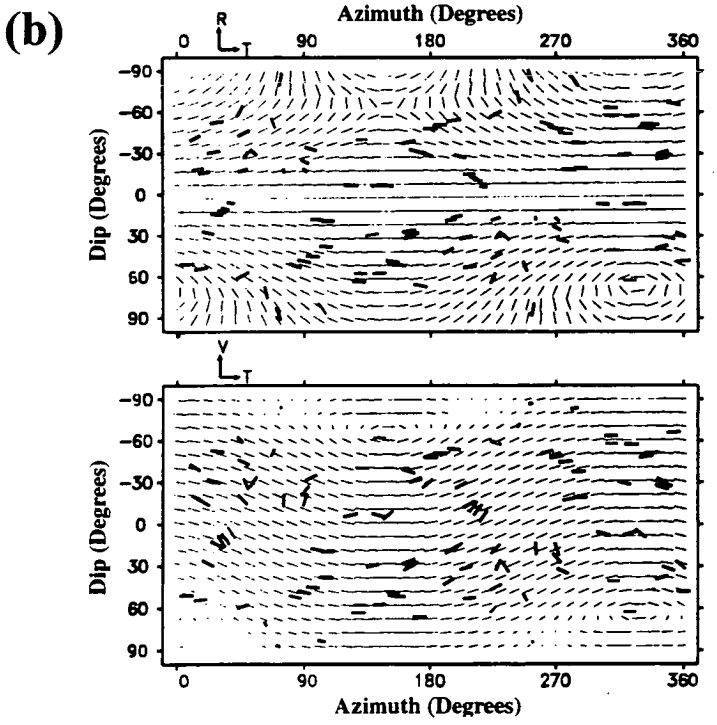

Figure 6.1b: The group velocity polarizations of a model of dry Hudson Cracks of orientation 059/23 (azimuth 059°, dip 23°) and crack density ε=0.070 and aspect ratio γ=0.15. Superimposed are the fifty-three measured polarizations and the fifty-three polarizations from assuming reciprocal symmetry of the Shear-Wave Experiment.

In this chapter I develop a judgement-of-fitness algorithm that accounts for the effects of singularities and produces a conveniently interpretable misfit value. Furthermore, the algorithm allows for some picks of polarizations to be incorrect rather than treating possibly incorrect polarizations as statistical scatter in measurement. I first introduce the method of automated data inversion which requires a judgement-of-fitness algorithm and then describe the program to calculate group velocities as necessary background. I then describe some simple judgement-of-fitness algorithms and demonstrate the problems and drawbacks of their use. Lastly I present the final algorithm and demonstrate its effectiveness. Throughout the chapter I evaluate the algorithms using the polarizations of the Shear-Wave Experiment data set.

6.3 Inversion for Seismic Anisotropy Using A Genetic Algorithm

Automated inversion of shear-wave anisotropy is complicated by the nonlinearity of the problem, but is nevertheless desirable because it is unbiased and faster than visual comparison. I performed the automatic inversions of this data set using the genetic algorithm of Horne and MacBeth (1994), followed by localized grid searches. The genetic algorithm was designed to invert observations of shear-wave polarizations and time delays to find the optimum model assuming fabrics of Hudson Cracks and has been successful in inverting two data sets (Horne and MacBeth, 1994).

6.4 Algorithm to Calculate Polarizations and Time Delays

The inversion and modelling of anisotropic wave propagation requires the ability to calculate the polarizations and time delays for any given set of elastic constants. I use a program based on the subroutines of McGonigle and Crampin (1982), which performs this task for both phase and group velocity. The phase velocity wave fronts are calculated from the Kelvin-Christoffel equation, and the group velocity wavefronts are calculated from the envelope of the phase wave fronts (Musgrave, 1970). The program calculates phase velocities at regular 4.5° intervals of both azimuths and dips, resulting in a 81 by 41 regularly space grid of phase velocities. The group velocity vectors and their polarizations and time delays are calculated for each phase velocity vector of the grid. The propagation direction each group velocity vector is then

approximated to be that of its nearest point on the 81 by 41 grid. The program was modified for greater efficiency and clearer structure by B. Baptie, S. Horne, and myself and I modified the program so the orientation of the fabrics can be conveniently specified.

Unfortunately, the 81 by 41 grid samples propagation directions more densely as dip increases. For example, the nearest neighbour on the 81 by 41 grid for a horizontal phase propagation direction (dip of 00°) is 4.5° where the nearest neighbour for a phase propagation direction with a dip of 85.5° is 0.35°. Any quantitative judgement-of-fitness algorithm will be biased by the different angular separation of grid points for different dips. For example, polarizations vary rapidly for a small change in propagation direction near the kiss singularity in hexagonal symmetry systems. If the fabric being modelled is that of horizontal cracks, the nearest polarization calculated are no more than 0.35° near the singularity. If the fabric is vertical cracks, the nearest polarization can be up to 2.25° away. Such a bias may be overcome by with observations away from singularities where polarizations vary slowly with change in propagation direction. In hexagonal symmetry the line singularities cause no disturbances other than abrupt changes in polarization and there are only two kiss singularities so that this bias will not have an appreciable effect.

6.5 Simple Judgement-of-Fitness Algorithms and Singularities

A fundamental difficulty in quantitative judgement is considering the region of propagation directions near a singularity where polarizations vary rapidly with small changes in propagation directions (section 1.8). It would be convenient for simplicity and speed in a judgement-of-fitness algorithm if special treatment of propagation directions near singularities can be avoided. This would require that the number of polarizations not affected by singularities be sufficiently large that the same best fitting model be found as would be if the effects of singularities were taken into account. I address this question in developing and testing the simplest of the judgement-of-fitness algorithms.

The first and simplest algorithm I tested measured the root-mean-square of the angles between the data and nearest model polarizations when considering the polarizations. No special treatment of propagation directions near singularities was

made. This method is similar to that of the only two publications known to this author describing judgement-of-fitness algorithms (MacBeth, 1991; Horne and MacBeth, 1994). Figure 6.2 shows the best model found using this judgement algorithm with the automated inversion followed by a grid search. Very few data polarizations greatly differ with those of the model, but few agree exactly. I estimate the error in the measurement of polarizations to be approximately ±10° based on the linearity of the *qS1*-wave particle motion, the precision in measurement, and that the effect of triaxial accelerometer misalignment is much less that 10° for most propagation directions (section 2.7). The normalized root-mean-square value of the angles between model and data is 34.7° and the average difference is 27.0°. These values are clearly too large for this model to be a plausible description of the rockmass unless this high value of misfit is due to a few anomalous polarizations. The standard deviation of the difference between the data and model polarizations is the relatively low value of 21.8° which indicates that the high misfit is not due to just a few polarizations. I conclude that this algorithm did not result in an adequate model, as is supported by visual comparison between data and the model.

The second algorithm I tested was identical to the first, except that it calculated the average angle rather than the root-mean-square angle. This made it more tolerant of outlying differences between model and data polarizations, but still treated possible anomalous polarizations as statistical scatter. The best model found (Figure 6.3) is nearly identical to that of Figure 6.2 and the average difference between model and data polarizations is 27.0° with a standard deviation of 22.1°, clearly showing this model is no better. I conclude that this modification gave no significant improvement.

The third algorithm I tested was identical to the first except that special treatment was given to propagation directions near singularity directions. Specifically, any data polarization for a propagation direction within one grid spacing to a singularity of the model was ignored in the judgement-of-fitness. Singularities are easily found in models in the case of hexagonal symmetry. The kiss singularities are in the same direction as the normals to the crack strike, and the line singularities, if present, cause an abrupt change in polarization of close or equal to 90°. The propagation directions of thirteen polarizations of the best model found (Figure 6.4) were within one grid spacing to singularities. The root-mean-square value comparing the remaining forty

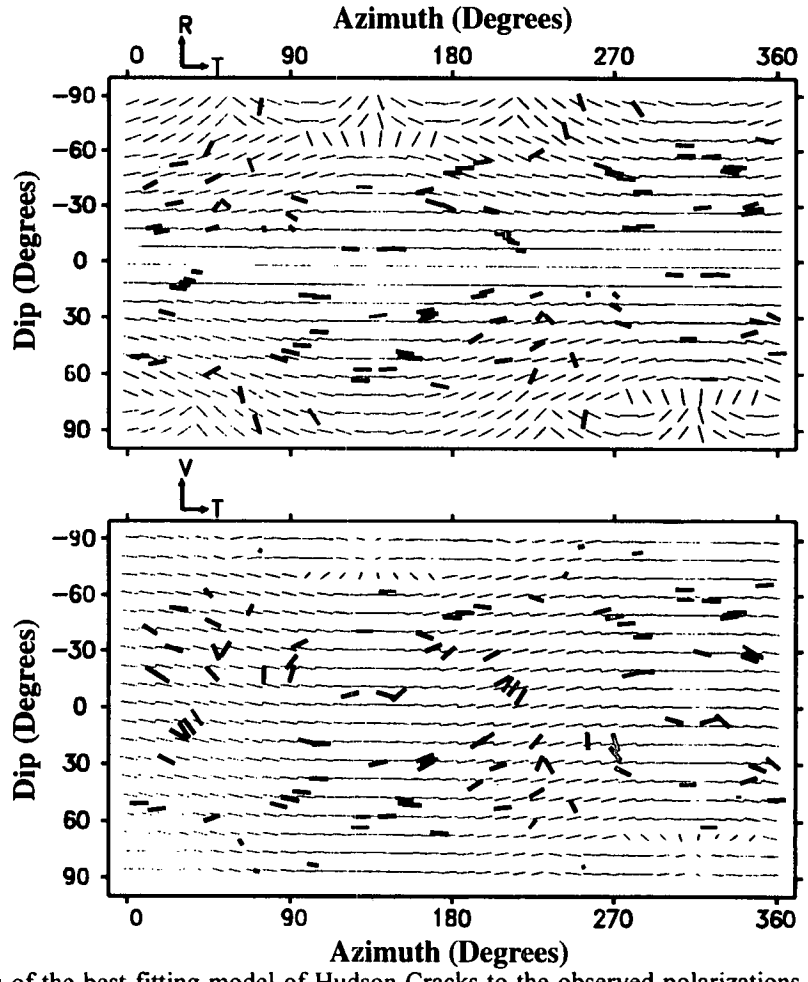

Figure 6.2: The group velocity polarizations of the best fitting model of Hudson Cracks to the observed polarizations of the Shear-wave experiment as judged by the first judgement-of-fitness algorithm. The algorithm found the root-mean-square value of the angles between model and data. No special treatment of singularities is made. The normalized root-mean-square value is 34.7° and the average difference is 27.0°. The model is of dry Hudson Cracks of orientation 047/12, crack density ε=0.1501 and aspect ratio γ=0.13. Superimposed are the fifty-three measured polarizations and the fifty-three polarizations from assuming reciprocal symmetry of the Shear-Wave Experiment.

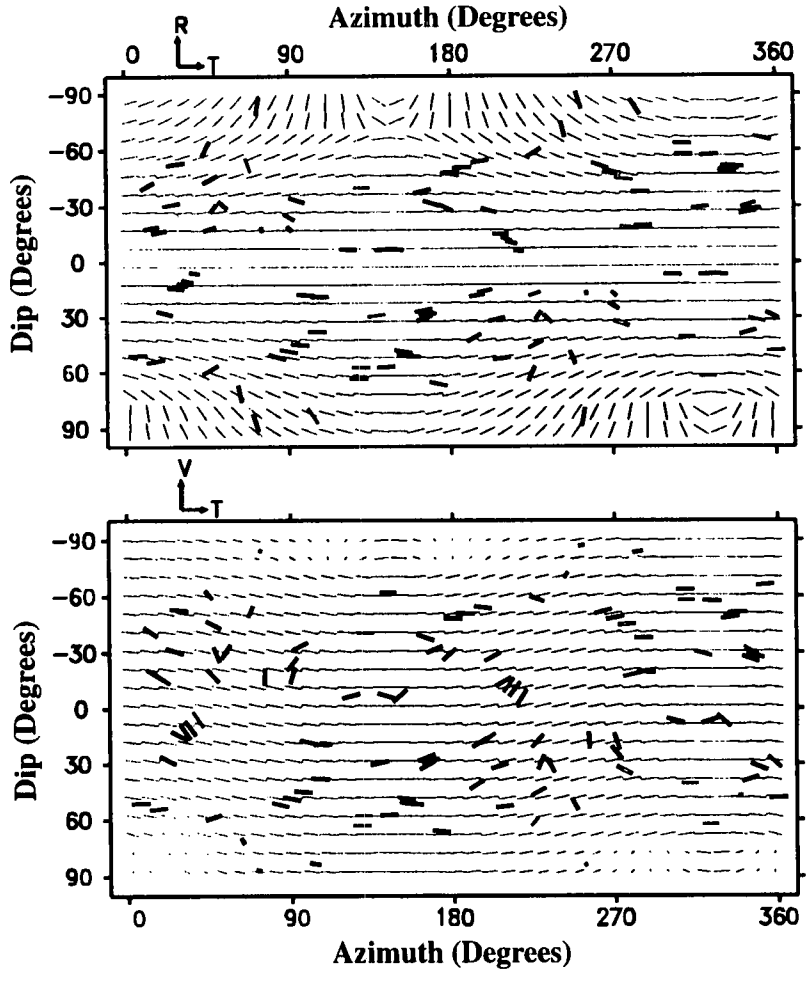

Figure 6.3: As in Figure 6.2 but as judged by the second judgement-of-fitness algorithm. The algorithm found the average value of the angles between model and data. No special treatment of singularities is made. The normalized root-mean-square value is 34.9° and the average difference is 27.0°. The model is of dry Hudson Cracks of orientation 056/12, crack density ε=0.065 and aspect ratio γ=0.040.

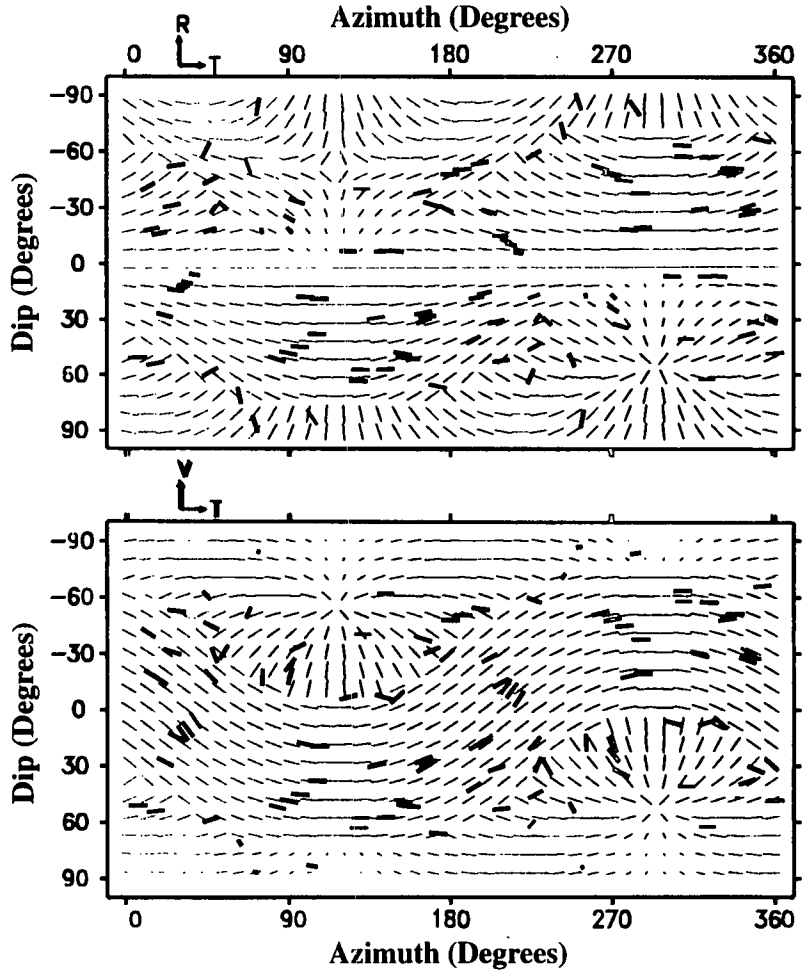

Figure 6.4: As in Figure 6.2 but as judged by the third judgement-of-fitness algorithm. The algorithm found the root-mean-square value of the angles between model and data and ignored observed polarizations within 4.5° of a singularity. The normalized root-mean-square value is 20.0° and the average difference is 20.2°. The model is of saturated Hudson Cracks of orientation 026/36, crack density ε=0.020 and aspect ratio γ=0.030.

polarizations to the model was 27.8° and an average difference of 20.2° with a standard deviation of 20.0°. I suggest that this is the best model so far from visual comparison, and therefore that the effects of singularities should be taken into account when judging fitness.

The root-mean-square value of the best model found from this third algorithm was expected be lower than that of the first algorithm because of the additional freedom to ignore polarizations corresponding propagation directions near singularities. Although this best model visually appears better than those found using the first two algorithms, it does not explain all observations. This raises the question whether the automated inversion using this third algorithm truly found a model that better described the rockmass, or found a model that merely had singularities conveniently located to ignore many of the polarizations. The results of the modelling using the final algorithm show that the former situation is true (section 6.7).

I also suggest that singularities be taken into account for a more in-depth interpretation. It is unlikely any model will explain all polarizations of a large data set to within picking precision because of modelling assumptions and anomalous measurements. No insight is given into the minimum number of polarizations that cannot be explained by the best model found unless the effects of singularities are taken into account. Knowing the minimum number of polarizations that cannot be explained by any model under a given set of assumptions gives insight whether the misfit is mainly due to a few miss-picked polarizations or invalid assumptions.

6.6 The Final Algorithm

The fundamental shortcoming best model found using the third judgement-of-fitness algorithm (previous section) is that the majority of the observed polarizations do not agree to within measurement precision with the best model. However, no insight is given into the minimum number of polarizations that cannot be explained by modelling using the given set of modelling assumptions if misfit values are based solely on statistical scatter. I therefore propose that it is therefore preferable for a judgement-of-fitness algorithm to measure the number of observed polarizations that *cannot be explained* by a given model. An automated inversion would seek the model that minimizes this misfit value. This is the design of this final algorithm,

which is used in all further modelling and inversions of the data sets. I also designed this algorithm to take into account propagation directions where polarizations change rapidly with a change in propagation direction, to be applicable to symmetry systems other than hexagonal, and to not include the assumption of shear-wave motion orthogonal to propagation direction.

In this algorithm, Model and data polarizations are projected onto the TS-TH plane for comparison, rather than comparing polarization vectors in three dimensions. The comparison of polarizations vectors requires calculating the data polarization vector from the angle measurement on the TS-TH by assuming shear-wave motion orthogonal to the source-receiver direction, which is not strictly true (section 1.1). Comparison of the angle on the TS-TH plane is preferable because this assumption of orthogonality is not made.

This algorithm takes the conservative approach of examining the model polarization angles of all four of the neighbouring propagation directions of the 81 by 41 grid to that of the data, rather than just the closest. Both model and data polarizations are restricted to within 0° and 180°. The opposite polarization angles are taken for angles greater than 180°. The minimum range of angles that contains all four model polarization angles then represents a reasonable range of possible values of polarization angles. The measured polarization angle conflicts with the model if it is outside this range by more than the measurement precision of 10° (section 6.5). The best model is then the model that conflicts with the fewest data polarization angles. The ability to determined such a range demonstrates another advantage of comparing data on the TS-TH plane.

The algorithm can be extended to include time delay measurements. The minimum and maximum value of time delays of the four surrounding grid points determine the range that must contain the observed time delay to within picking precision. Outside this range, the observed time delay is not explained by the model.

To distinguish between nearly equal models, the minimum increase in the range of model polarization angles necessary to avoid confliction is determined for all conflicting polarizations. The average of these values is normalized by dividing by 90° and this value is then added to the number of polarizations that conflict with the model. This is the misfit value returned by the algorithm.

Examining the ranges of model polarizations allows for a convenient method of accounting for singularities. Near singularities polarizations can vary rapidly with direction (section 1.8). I found by numerical experiments that if the minimum range of the four angles is greater than 74.5°, then the true change in polarization angle may be the complimentary angle of 180° minus this angle due to propagation near a singularity direction. In these cases no observed polarization can be considered as conflicting with the model. The range of propagation directions where polarizations vary rapidly is dependent upon the strength and symmetry of the anisotropy and the type of singularity, but this method accounts for these difficulties solely by examining the polarizations so that the method is computationally fast.

It would be desirable to find the model polarizations for the exact propagation direction of the observed polarizations. However, model and data polarizations may differ significantly even for a nearly perfect model because of the rapid variation of polarizations near singularities (section 1.8). Also, the use of the 81 by 41 grid will be computationally much faster for large data sets, which is desirable when an automatic inversion compares, in this case, over 40 000 models to the data. In addition, the approximation comparing data to the nearest neighbouring grid points of a model is valid away from directions of singularities. I found by numerical experiments that the maximum difference in propagation directions between observed polarizations and a neighbouring grid point is no greater than 9.5° and is usually much less than 4.9°, assuming anisotropy due to Hudson Cracks.

6.7 The Best Model Found

The model with the smallest misfit value as judged using this final algorithm is presented in Figure 6.5 with the polarization data and reciprocal polarizations superimposed. The model is for saturated cracks with a strike of 023°, dip of 35°, crack density of ε=0.020, and aspect ratio γ=0.025. The misfit value is 20.26, indicating twenty of the fifty-three observed polarizations were not within the acceptable ranges of model polarizations assuming a maximum error in measurement of 10°. These twenty polarizations were on average 23.4° outside of the acceptable ranges. The standard deviation of this average was 19.4° indicating that this average

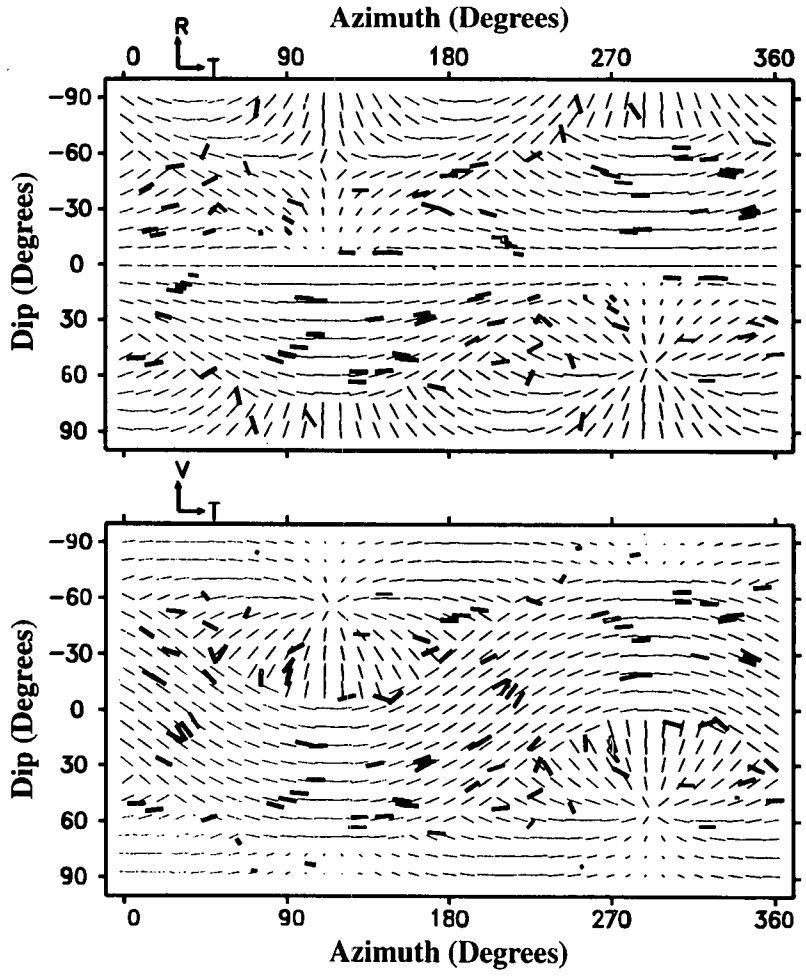

Figure 6.5: As in Figure 6.5 but as judged by the final judgement-of-fitness algorithm (section 6.8). The misfit value was 20.26 meaning twenty of the fifty-three polarizations conflict with the model and are on average $0.26 \times 90^{\circ} = 23.4^{\circ}$ outside the acceptable ranges of model polarizations. The model is of saturated Hudson Cracks of orientation 023/35, crack density $\varepsilon = 0.020$ and aspect ratio $\gamma = 0.025$.

of 23.4° was not due principally to a few polarizations that greatly differed from the acceptable range. Therefore, assuming a slightly larger maximum error than 10° would not have resulted in a significantly different model. Note also that this model is nearly identical to the model found using the third judgement-of-fitness algorithm (section 6.5). This is further shows that the approximation of comparing data to the nearest neighbouring grid point is usually valid (previous section).

Visual comparison between the data and the model show that intuitively this model is the closest of those presented in this chapter. Visually it is more convincing to see many observed polarizations closely match those of the models and fewer polarizations clearly conflicting (Figure 6.5) than nearly all polarizations differing from the model by similar amounts (Figures 6.2 and 6.3). Visual judgement is therefore biased towards this final algorithm.

There may be concern that inversion accounting for singularities may result in a model with singularities conveniently located to ignore many of the observed polarizations (section 6.5). The propagation directions of the majority of data polarizations are not near singularities. There is no doubt that the best fitting model *is not* one where the singularities are merely conveniently located.

This algorithm can be used to compare models of any symmetry system to the data as long as the disturbances of all singularities are over a large enough range of propagation directions that rapid changes in polarizations are apparent on the 81 by 41 grid. The algorithm was successfully applied to modelling assuming orthorhombic symmetry (section 7.5). Numerical experiments show that the grid spacing of 4.5° is not small enough to resolve all point singularities for this symmetry system. This is a fundamental problem that can only be resolved by performing the improvements to the algorithm such as a smaller grid spacing and a method of better resolving the zone of disturbance around a singularity. Time constraints prevented me from pursuing these improvements. Fortunately examination of the models found from automated inversion (section 7.5) shows that the zones of disturbance around the singularities are small enough that the effects of singularities were unlikely to be significant in the inversion.

6.8 Conclusions

I have four conclusions based on this study:

1. Comparison of the polarizations of model to data must be quantified because visual comparison is subjective and time consuming. A quantified comparison is a necessary component of any automated inversion technique.
2. The most useful approach of a judgement-of-fitness algorithm is that it should minimize the number of observations that cannot be explained by a given model. Judgement-of-fitness algorithms should account for the possibility of anomalous polarizations rather than incorrectly treating such polarizations as statistical scatter.
3. It is preferable for judgement-of-fitness algorithms to account for the effects of singularities. Observed data from propagation directions very close to a singularity are best ignored.
4. Model polarizations should be compared to data on the same plane in which data polarizations were measured. This way the approximation that shear-wave motion is perpendicular to propagation direction is no long made.

I developed a judgement-of-fitness algorithm that implemented the recommendations of conclusions one to four and gives an easily interpretable misfit value. I also designed this algorithm to be computationally fast by requiring the evaluation of model polarizations only for 81 by 41 points over a regularly spaced grid. This makes the algorithm practical for use in automated inversion methods. The algorithm was successfully applied to the data from the Shear-Wave Experiment assuming hexagonal (section 7.3) and orthorhombic symmetry (section 7.5). With some refinement, this algorithm may be applied to inversions assuming other symmetry systems.

7 Inverting Polarizations

7.1 Abstract

The inversion of shear-wave polarization measurements assuming seismic anisotropy due to Hudson Cracks results in the determination of all parameters except crack density. The fabric has an approximate orientation of 023° strike and 35° dip. This orientation roughly agrees with the expected orientation of 045° strike and 14° dip expected for a fabric of Extensive-Dilatancy Anisotropy (EDA), and 024° strike and 25° dip expected for anisotropy due to the primary layering. The best model assuming orthorhombic symmetry does not agree with nineteen of the fifty-three polarization measurements, which is not significantly less than that of that of the best hexagonal symmetry, and therefore does not support orthorhombic symmetry as the likely symmetry system. Inversions of polarizations from the Velocity Survey do not result in fabric orientations that agree with any observed or implied patterns in the rockmass, or agreement with the fabric orientations suggest from apparent *P*-wave velocities. The lack of agreement is attributed to most polarizations being determined by anisotropy induced or altered by tunnel excavation rather than the *in situ* anisotropy.

7.2 Introduction

Nearly all previous modelling of shear-wave polarizations and time delays has been performed using the subjective modelling technique of visual comparison (section 6.2) and severely restrictive a priori assumptions on fabric orientations. Such modelling has been successful for data sets recorded using the VSP geometry in sedimentary basins where anisotropy due to (section 1.4) horizontally orientated alternating thin layers (PTL anisotropy) and vertically orientated EDA-cracks has been assumed (Bush and Crampin, 1991; Yardley and Crampin, 1993). Success is partially due to the relatively simple layer-cake geology so that these assumed fabric

orientations are likely correct. Even so, a better fit of model to data should result from quantitative comparison, and modelling without the assumptions on fabric orientations would help test the existence of these fabrics.

The modelling the shear-wave splitting displayed in earthquake generated data sets has only resulted in crude matches between model and data so that modelling results do not so clearly justify the a priori assumptions on fabric orientations. Earthquake data sets are usually from geologically complicated area and do not have precisely known source locations. The range of directions of propagation of the raypaths is more sparse and lacks the systematic distribution of the VSP recording geometry. Also, the seismograms are often of a complexity that time delays cannot be measured reliably. These complications are great enough that all such published studies to date make one of two independent a priori assumptions on fabric orientations to make modelling by visual comparison practical. Some studies assume the strike of the *in situ* fabric to be that of the dominant polarization direction (Kaneshima et al., 1988; Crampin and Booth, 1989; Kaneshima, 1990; Graham et al., 1991; Booth et al., 1992; Liu et al., 1993a; Booth et al., 1993; Rowlands et al., 1993; Graham and Crampin, 1993). This assumption is not necessarily correct and will likely lead to the wrong conclusions in cases where the fabrics are not steeply dipping. Others assume the fabric orientation is similar to that of possible fabrics, such as the orientation of EDA-cracks inferred from the regional stress-field (Crampin and Booth, 1985; Roberts and Crampin, 1986; Kaneshima and Ando, 1989; Savage et al., 1990; Crampin et al., 1990; Yao et al., 1993; Xiong et al., 1993; Yao and Xiong, 1993; Gledhill, 1993a,b). Assuming a fabric orientation biases the modelling, and precludes rigorous testing of the predicted cause of the anisotropy.

In this chapter I use automated inversion (section 6.3) using the final judgement-of-fitness algorithm (section 6.6) to model the polarization data from the Shear-Wave Experiment data set without making subjective comparisons of data to models or a priori assumptions on fabric orientations. This is the first such inversion of an *in situ* data set using polarizations only. Time delays are not used because the time delays of the Shear-Wave Experiment data set are partially determined by the zones of excavation damage and disturbance (section 8.2). This method is suited to

earthquake data sets where the distribution of raypath directions is not systematic and time delays are commonly unreliable and ignored in modelling.

I first invert the polarizations from the Shear-wave data set for hexagonal symmetry, and then orthorhombic symmetry, assuming anisotropy due to sets of Hudson Cracks and then present a preliminary geological interpretation as to the cause of the *in situ* anisotropy based on the results of the inversion. I then invert the polarizations of the Velocity Survey data set and compare these results to the apparent *P*-wave velocities of the Velocity Survey to gain insight into the effects of excavation.

7.3 A Single Fabric of Hudson Cracks

In this section I invert and model the polarization data from the Shear-Wave Experiment assuming the anisotropy has hexagonal symmetry (section 1.7) due to a single set of Hudson Cracks. It is reasonable first to invert assuming Hexagonal symmetry, which is characterized by five parameters using Hudson Cracks, because this avoids non-uniqueness by over-parameterization (section 1.11). Also, the known patterns within the undisturbed rockmass of the 420-Level likely to cause *in situ* fabrics are EDA and the primary layering (section 2.15). Individually either fabric would create a hexagonal symmetry system, and the observed patterns of polarizations would be approximately that of a single equivalent fabric should both fabrics be significant (section 2.15), which would also result in hexagonal symmetry. I will also use hexagonal symmetry to test the automated inversion technique before its application to more complicated symmetry systems, as this can be done conveniently because of the relatively few parameters.

The automated inversion compared a total of 40 400 models to the data. A grid search was then performed with finer increments for values of strike, dip, crack density, and aspect ratio near those values of the best model found by automated inversion to find the model that best fitted the data.

The best fitting hexagonal model (Figure 6.5) was discussed in section 6.7. I now investigate the success of the inversion by presenting the graphs of misfit values against strike, dip, crack density, and aspect ratio separately while holding the other variables constant. Figure 7.1 are the graphs of misfit value versus strike, dip, aspect ratio, and crack density. There is no need to graph misfit values against crack content

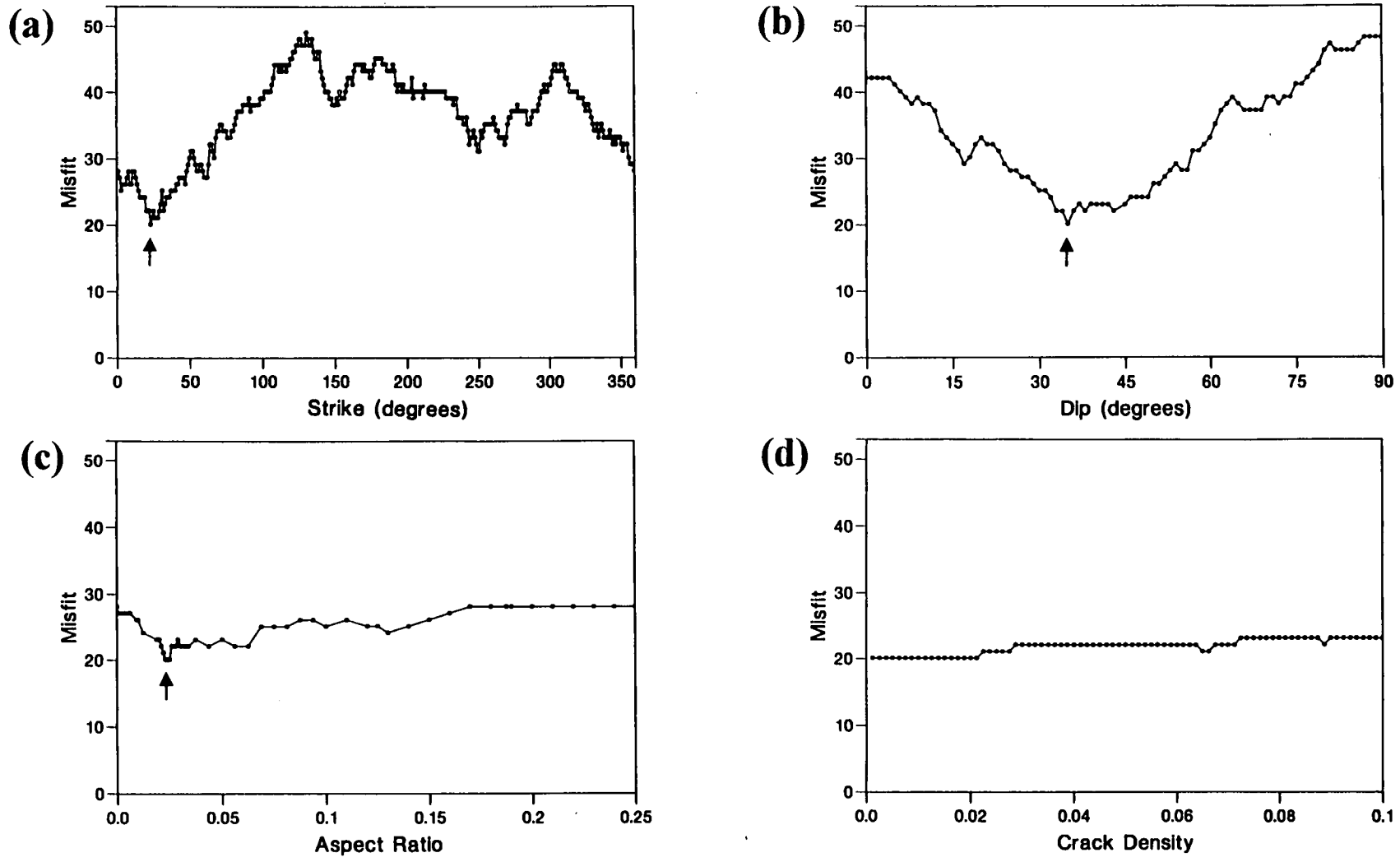

Figure 7.1: Graphs of misfit values against Hudson Crack parameters for the fifty-three polarizations measured from the Shear-Wave Experiment data set. Data is compared to a single fabric of Hudson Cracks. Dots are data points. Graphs are given for the parameters (a) Strike, (b) Dip, (c) Aspect Ratio, and (d) Crack Density. Arrowheads denote values of the best hexagonal model.

because there are only the two values of dry (unsaturated) or fluid-filled (saturated) and all models of dry Hudson Cracks resulted in misfit values significantly greater than that of the better fitting model. The graphs for aspect ratio, strike, and dip all show the global minima in misfit value occur at the parameters of the best model, demonstrating the success of the automated inversion and stability in the judgement-of-fitness. The graph of misfit value versus crack density shows that the misfit value remains almost constant throughout as expected because the pattern of polarizations does not appreciably differ for different values of crack density (section 1.10). The maximum misfit value from varying aspect ratio is 28.320, only 8.06 above that of the best fitting model and values of γ=0.020 to γ=0.069 give misfit values below 23. This demonstrates the limited sensitivity of this parameter.

The two most sensitive parameters are the strike and dip of the Hudson Cracks, allowing me to obtain a more comprehensive judgement of the success of the inversion by simultaneously plotting misfit value against strike and dip on a contour plot (Figure 7.2). The contours are interpolated from 2880 data points where the values of crack density, aspect ratio, and crack content are those of the best model. The average misfit value is 36.342. From this plot that the best hexagonal model, with orientation 023/35, appears to be the global minimum. There are no local minima of misfit value less than thirty outside the depression containing the best hexagonal model, strongly suggesting that the best model has been found.

The errors in determining the parameters of the Hudson Cracks are difficult to quantify. Misfit values of less than twenty-three only occur between strikes 019° to 033°, dips 32° to 39°, and aspect ratios γ=0.020 to γ=0.069 where misfit values fluctuate apparently randomly. However, with only fifty-three polarization measurements, the misfit value is strongly dependent on each measurement. Therefore the true errors are probably larger and must be a judged qualitatively in absence of a much more detailed understanding of the errors in determining these parameters.

7.4 Orthorhombic Symmetry

There is a need to investigate orthorhombic symmetry for the Shear-Wave Experiment data set because apparent *P*-wave velocities suggest the rockmass to have

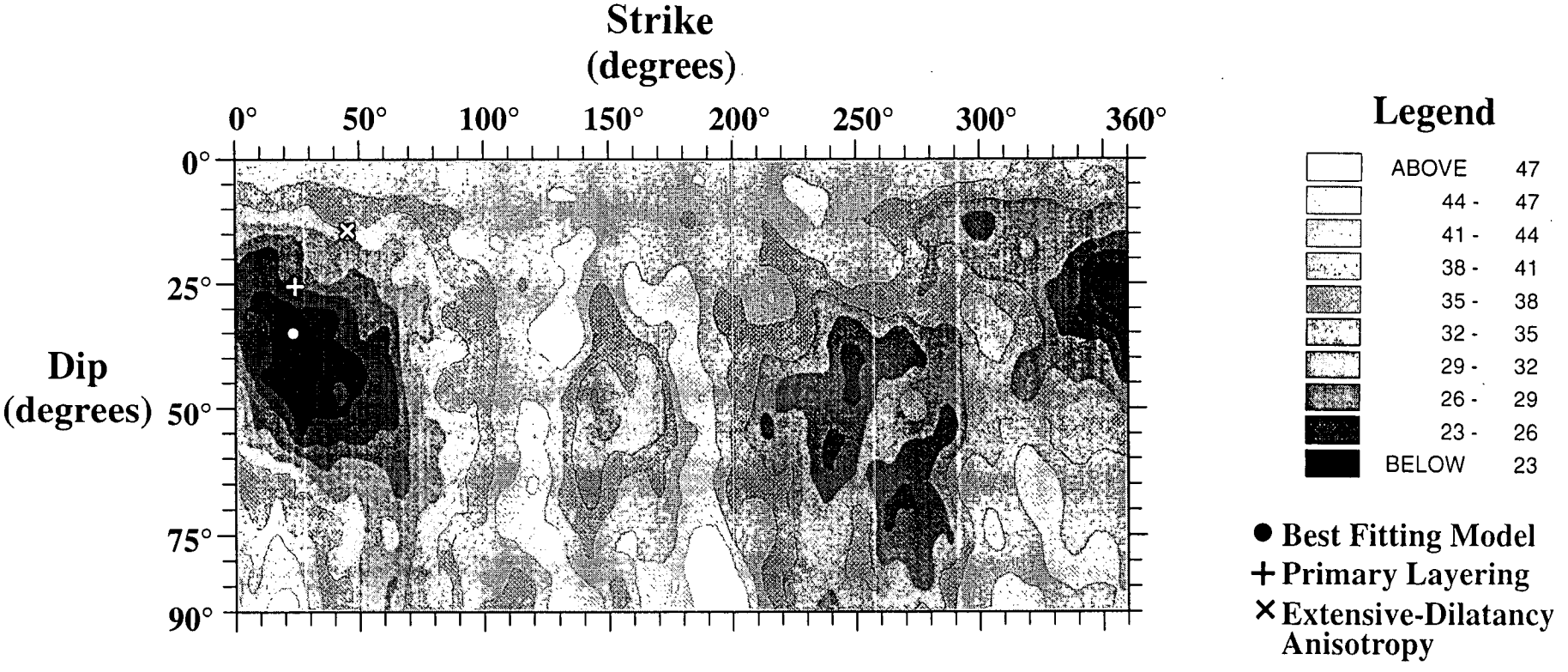

Figure 7.2: Contoured plot of misfit values against strike and dip for all possible fabric orientations. The fifty-three polarizations from the Shear-Wave Experiment are compared to a single set of Hudson Cracks, where all other parameters are those of the best fitting hexagonal model (saturated cracks, crack density ε=0.020, aspect ratio γ=0.025). Contours are extrapolated from 2880 data points. Marked on the figure are the orientations of the best fitting model, primary layering, and EDA as implied by the *in situ* stress field.

excavation-induced orthorhombic symmetry (section 2.14). In this section I briefly described orthorhombic symmetry in preparation interpreting the results of inversion (next section). Physically, orthorhombic symmetry possesses two perpendicularly oriented planar fabrics, and is described by nine independent elastic constants as opposed to five for hexagonal symmetry. Orthorhombic symmetry due to two sets of perpendicular Hudson Cracks is described by the eight parameters of the crack densities, aspect ratios, and crack contents of both set of cracks, and the orientation, such as strike and dip, of one crack set. As with hexagonal symmetry, crack densities can only be determined using time delays. Inversion using polarizations only can determine the ratio of the crack densities of the two crack sets. Inversion for orthorhombic symmetry is therefore undesirable without independent geological constraints because of the larger range of physically realizable models resulting in greater non-uniqueness (section 1.9). The inversion was performed by the same procedure as for hexagonal symmetry (previous section).

7.5 Results of Inversion for Orthorhombic Symmetry

The orientations of the two crack sets of the best model found (Figure 7.3) are 060/27 and 240/63 and the ratio of crack densities is 0.57 where is former crack set has the lower crack density. The misfit value was 19.248, which is only slightly better than the misfit value of 20.260 of the best fitting hexagonal model. With the additional freedom of three more parameters, only a significantly lower misfit value for the best orthorhombic model would suggest that the pattern of anisotropy has orthorhombic symmetry. Also, the former crack set is unsaturated whereas the latter is saturated. It is unlikely that the two sets should be so distinctly different if the geological causes are similar.

I further investigate possible agreement between the fabric orientations inferred from this Shear-wave Experiment and those from the *P*-wave Velocity Survey by restricting modelling to cracks fabrics of the same orientations as those suggested by the *P*-wave velocities. I performed forward modelling by a grid search to find the best orthorhombic model with cracks orientations of 046/44 and 226/46. The misfit value of the best model (Figure 7.4) is 23.324. The fit is therefore significantly worse than that of the best hexagonal model and the comparison of data polarizations to the

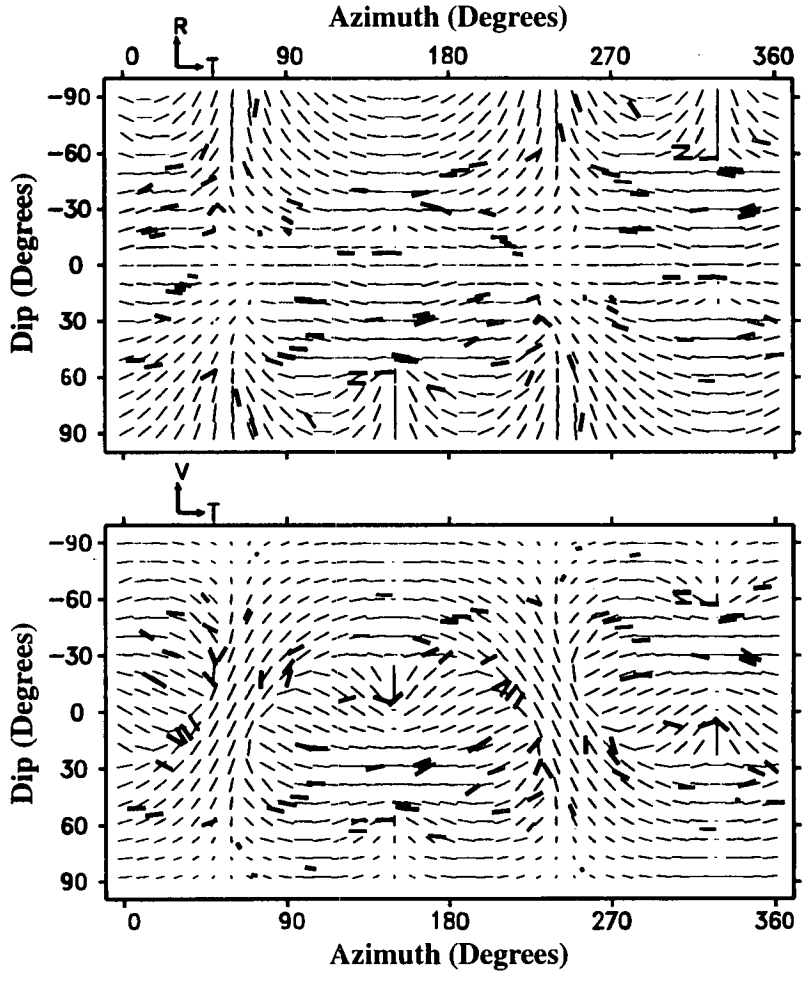

Figure 7.3: The fifty-three polarizations from the Shear-Wave Experiment superimposed upon the best fitting orthorhombic model of Hudson Cracks. The misfit value is 19.248. The first crack set is of unsaturated cracks of strike 060°, dip 27°, crack density ε=0.035, and aspect ratio γ=0.084. The second crack set is of saturated cracks of strike 240°, dip 63°, crack density ε=0.061, and aspect ratio γ=0.0050. The ratio of the crack densities of the first crack set to the second is 0.57.

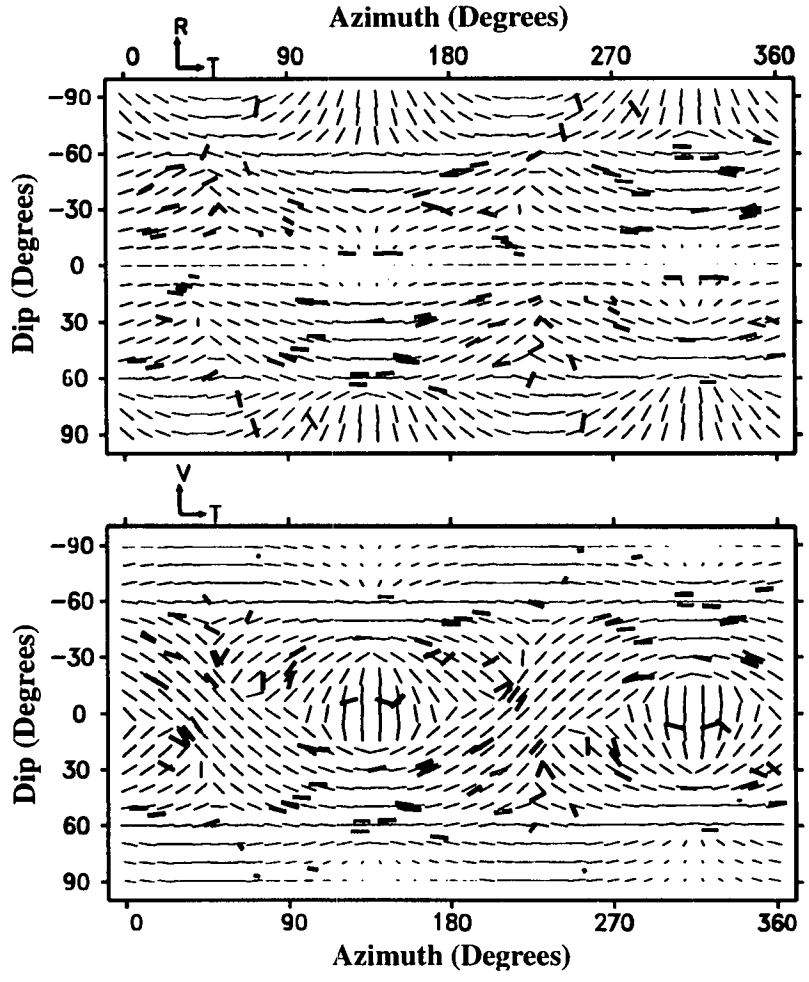

Figure 7.4: As in Figure 7.3, but for the best fitting orthorhombic model of Hudson Cracks with the orientations indicated by the apparent *P*-wave velocities from the Velocity Survey. The misfit value is 23.324. The first crack set is of saturated cracks of strike 046°, dip 44°, crack density ε=0.017, and aspect ratio γ=0.0001. The second crack set is of saturated cracks of strike 226°, dip 46°, crack density ε=0.0064, and aspect ratio γ=0.0001. The ratio of the crack densities of the first crack set to the second is 2.7.

model is unconvincing, particularly for polarizations near 00° dip and, 135° and 215° strike.

I conclude that the observations do not support orthorhombic symmetry as the symmetry system that determined the polarizations. Orthorhombic symmetry is expected if the effects of excavation are significant. Otherwise hexagonal symmetry is expected (section 2.14). Therefore the lack of support for orthorhombic symmetry strongly suggests that the observed polarizations are due to the original *in situ* anisotropy rather than excavation-induced anisotropy.

7.6 Monoclinic and Triclinic Symmetry Systems: Discussion

It may seem desirable to try to invert the polarizations for two or more fabrics without the restriction of specific orientations of the fabrics relative to one another. Such situations are physically realizable. The automated inversion at the time of the writing of this dissertation had not yet been developed to consider symmetry systems other than hexagonal and orthorhombic. In practice, however, the results of such inversions may be of limited use.

The problem with such inversions is the large number of parameters. Monoclinic symmetry is that possessing two fabrics that are not necessarily perpendicular to one another. It is described by thirteen elastic constants and by ten parameters as Hudson Cracks. Triclinic symmetry is that possessing three or more fabrics without restrictions on fabric orientations and is described by twenty-one elastic constants and by fifteen parameters as Hudson Cracks. These large numbers of parameters would result in considerable non-uniqueness. Many models may be found the match the observations and any well fitting model found that corresponded to observed geological patterns may due so only coincidentally. No modelling results assuming monoclinic or triclinic symmetries have been published either from *in situ* or highly controlled laboratory data sets.

Inversion for these two symmetry systems may be practical if additional restrictions on parameters are included such as a priori restrictions on fabric orientations. The precise geological causes of anisotropy in the crust are not yet fully understood but I foresee that the causes will soon be understood well enough that geological survey of a rockmass will provide a list of all possible anisotropic fabrics

and their orientations. If the number of possible fabrics is small, inversion of shear-wave data may be performed assuming the fabric orientations from the survey and produce interpretable results. Until the causes of *in situ* anisotropy are well established it is preferable not to make such assumptions that may bias inversion. Therefore inversion for these symmetries is not yet practical.

7.7 Geological Interpretation

The results of inversions using polarizations already allow me to make some important geological interpretations that I present now in preparation for the latter sections of this chapter. The results of inversions assuming hexagonal and orthorhombic symmetry suggest that the *in situ* anisotropy is due to a single fabric of orientation approximately 023/35. This orientation differs with the fabric orientation of 045/32 suggested by the *P*-wave velocities from the Attenuation Survey (section 2.14) by only 12°. This orientation of the best-fitting hexagonal model differs from the primary layering of orientation 024/25 by only 10° and from the expected orientation of EDA-cracks of 045/14 by only 23° (section 2.15) . These are the two fabrics most likely to cause the *in situ* anisotropy and there are no other patterns known within the rockmass of similar orientations (section 2.15). I conclude that this consistency shows that the dominant *in situ* anisotropy has hexagonal symmetry that is caused either by the primary layering or EDA or both.

7.8 The Velocity Survey

The results of *P*-wave travel time analysis using data from the Velocity Survey (section 2.13.1) suggested an orthorhombic symmetry (section 2.14). It is therefore desirable to analyze the shear-wave splitting of the Velocity Survey data set using the same procedure as for the Shear-Wave Experiment data set to compare results.

7.8.1 Processing

I examined the seismograms for all raypaths from the twenty-seven isolated boreholes and nine four-orientation source stations to the sixteen triaxial accelerometers. The method of measuring polarizations and time delays was exactly the same as described in Chapter Three with one major exception. The great benefit

of comparing seismograms when picking was not possible for signals created in the twenty-seven isolated boreholes. Therefore greater scatter is to be expected for measurements from this data set. Furthermore, many seismograms from signals created at these locations display initial shear-wave motion in the same direction as expected for an isotropic rockmass. For these cases, it was not possible to determine whether splitting had taken place (section 3.5).

The Velocity Survey employs thirty-six source stations as opposed to thirteen in the Shear-Wave Experiment, resulting in much more data. However, the average raypath length is 30m as opposed to 35m for the Shear-Wave Experiment, and many raypaths travel sub-parallel to the axial direction of the Mine-by Tunnel. Consequently, the raypaths of the Velocity Survey are likely to traverse a greater proportion of rockmass affected by excavation and this is a fundamental difference between the two data sets. The two data sets may be combined to create a larger, more comprehensive data set accepting the greater effects of excavation damage and greater scatter in the data from the Velocity Survey. The correct orientations for Triaxial Accelerometers 1 and 16 had been calculated (section 2.7) prior to processing this data set so that I included data recorded by these triaxial accelerometers in this analysis.

I measured a total of 146 polarizations and time delays from this data set, including forty-five from the nine four-orientation source stations. I found the best-fitting models of Hudson Cracks for hexagonal and orthorhombic symmetry using the automated inversion and grid searches (section 7.3). Again, time delays are partially determined by excavation so I only used polarizations in the inversion.

7.8.2 Results of Inversions

The misfit value of the best-fitting hexagonal model (Figure 7.5) is 74.360 for the 146 polarizations so that just over half the polarizations conflict with the model. The misfit is proportionally significantly worse than the best fitting hexagonal model for the Shear-Wave Experiment polarizations where the misfit value is 20.260 for fifty-three polarizations. The best fitting orthorhombic model for the Velocity Survey data set (Figure 7.6) has misfit value of 72.329, which is only slightly lower than that of the best hexagonal model.

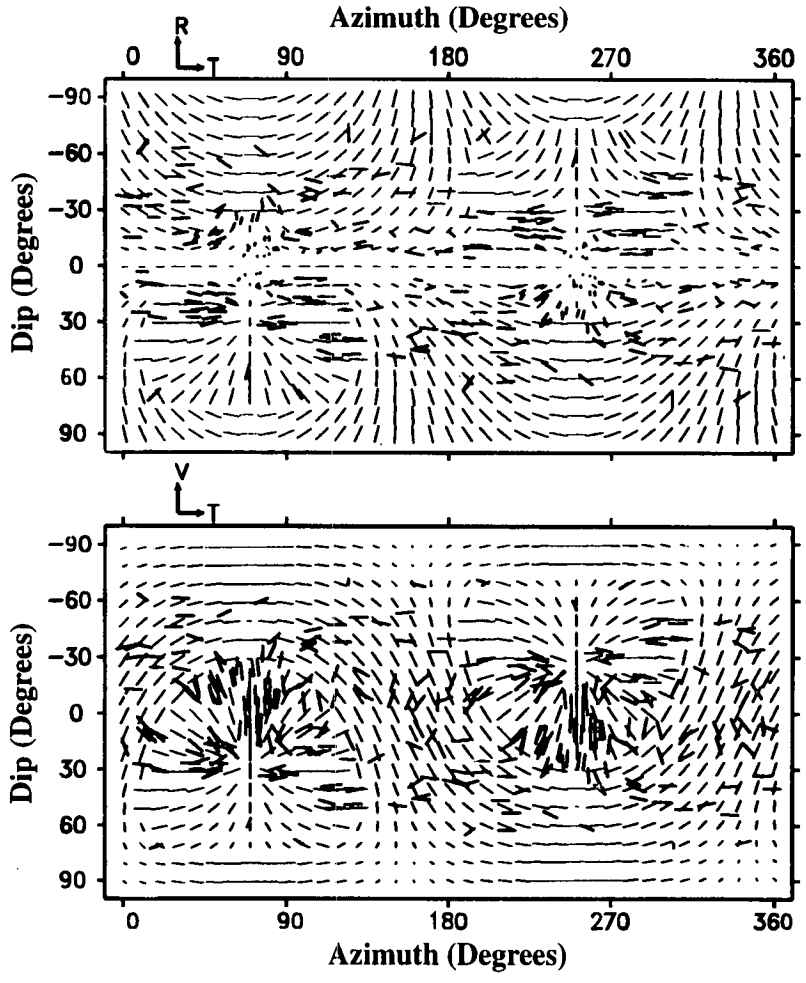

Figure 7.5: The 146 polarizations from the Velocity Survey upon the best fitting model of a single fabric of Hudson Cracks. The misfit value is 74.360. The model is of saturated cracks of strike 160°, dip 64°, crack density ε=0.020, and aspect ratio γ=0.020.

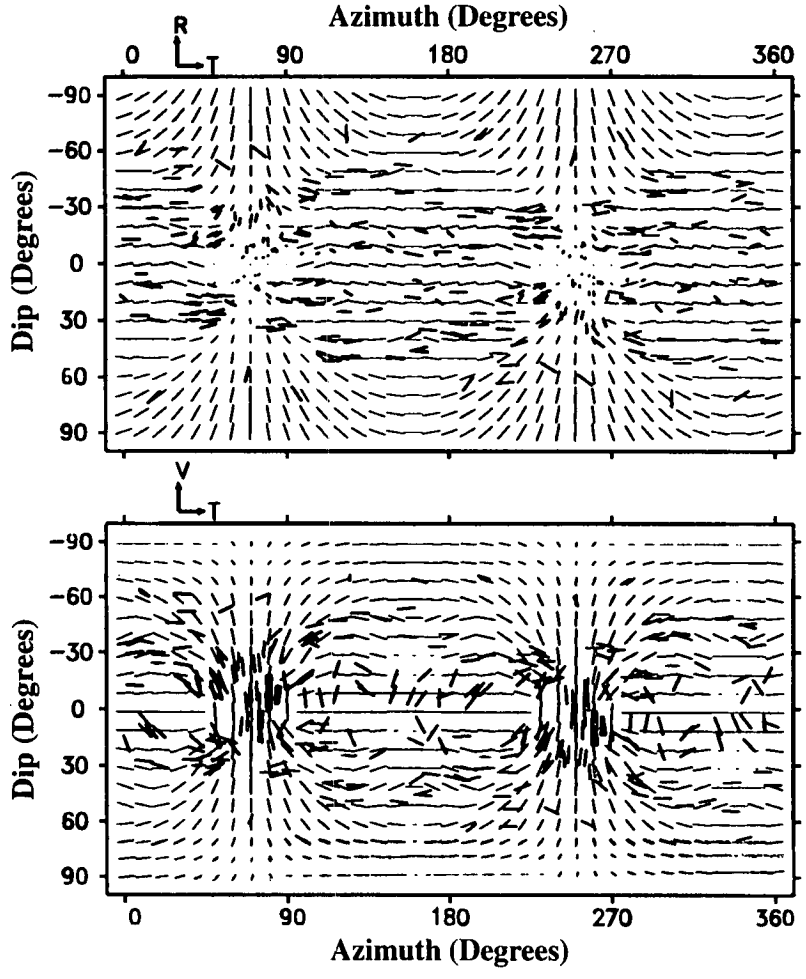

Figure 7.6: The 146 polarizations from the Velocity Survey superimposed upon the best fitting orthorhombic model of Hudson Cracks. The misfit value is 72.329. The first crack set is of saturated cracks of strike 070°, dip 87°, crack density ε=0.016, and aspect ratio γ=0.015. The second crack set is of saturated cracks of strike 250°, dip 03°, crack density ε=0.012, and aspect ratio γ=0.015. The ratio of the crack densities of the first crack set to the second is 1.3.

The fabric orientation suggested by the best hexagonal model does not agree with any that may be expected. The orientation of the cracks for the best hexagonal model of 160/64 clearly does not agree with 023/35 as found for the Shear-Wave Experiment (section 7.3) and there is no observed or implied consistent geological pattern of orientation near 160/64 (section 2.15). I performed a grid search with the restriction of a fabric orientation of 023/35. The lowest misfit value was 103.294 for the 146 polarizations, showing that the pattern of polarizations is distinctly different from that inferred from the Shear-Wave Experiment.

Similarly the fabric orientations suggested by the best orthorhombic model do not agree with any that may be expected. The orientations of crack sets for the best orthorhombic model of 070/87 and 230/03 differ significantly from 046/44 and 226/46 as suggested by the *P*-wave velocities of the same data set (section 2.14) and from 060/27 and 240/63 of the best orthorhombic model of the Shear-Wave Experiment data set (section 7.5). The modelling for orthorhombic symmetry with fabric orientations restricted to 046/44 and 226/46 resulted in a minimum misfit value of 98.294. There are no observed or implied consistent geological patterns of orientations near 070/87 and 230/03 (section 2.15).

7.9 Velocity Survey: Geological Interpretation

The results of the inversions and modelling offer no clear interpretation. The polarizations (Figures 7.5 and 7.6) clearly form a pattern but the orientations of the cracks sets of the best hexagonal and orthorhombic models do not correspond to any fabric that may be expected including the orientation suggested by the best hexagonal model of the Shear-Wave Experiment data set. Furthermore there is a contradiction between the fabric orientations indicated by the inversion of polarizations for orthorhombic symmetry and those indicated by apparent *P*-wave velocities (This contradiction is the topic of the next section.).

I suggest this unexpected result is primarily due to the effects of tunnel excavation. The raypaths of the Velocity Survey have traversed proportionally more of the zones of excavation damage and disturbance (section 7.7.1). Tunnel orientation may also be an important factor. The azimuthal orientation of the Mine-by Tunnel was chosen to be parallel to the direction of the intermediate stress axis σ_2. In this

way, the maximum and minimum stress axes, σ_1 and σ_3 respectively, are perpendicular to the axis of the tunnel, causing the maximum possible excavation effects (section 2.9). In contrast, Rooms 409, 410, and 413, which are the source tunnels for eleven of the thirteen Shear-Wave Experiment source stations, have azimuthal orientations perpendicular to the directions of σ_2 and σ_3. Even though σ_2 is only 7MPa less than σ_1 (section 2.9), the excavation effects are significantly less as indicated by much less developed breakout-notches in these tunnels. The difference pattern of apparent *P*-wave velocities of the Velocity and Attenuation Surveys shows that the seismic signals of the Velocity Survey have been significantly affected by excavation (section 2.14). Therefore the induced anisotropy is greater for the Mine-by Tunnel than for most of the source tunnels of the Shear-Wave Experiment, and I conclude that the shear-wave polarizations of the Velocity Survey data set do not represent the *in situ* rockmass.

I suggest that the anisotropy determining the polarizations varies with propagation direction. Excavation effects are not cylindrically symmetric around the tunnel (section 5.10), and the strength and orientations of the fabrics will vary with direction radially away from the tunnel axis. Therefore the polarizations from the Velocity Survey data set are not those of a single set of fabric orientation. I interpret the apparent pattern of polarizations as evidence that the effects of excavation are consistent along the length of the tunnel for any given direction.

The different results of the *P*-wave velocity analysis and the inversion of polarizations also strongly suggest that the *in situ* fluids escape as a consequence of excavation. Fluid-filled cracks have little effect on *P*-wave velocities, whereas dry cracks have a much greater affect on *P*-wave velocities than on shear-wave velocities (Crampin, 1993b). The *P*-wave velocities of the Velocity Survey clearly indicate two crack sets whereas the shear-wave polarizations of both the Velocity Survey and the Shear-Wave Experiment do not. The escape of fluid to cause dry cracks is expected. Fluid-filled microcracks causing EDA (section 5.12) are likely to be altered or burst (as pore fluids are possibly explosively released) near the free surface due to stress-relief and the additional excavation induced cracking. Any fluids in the rockmass may migrate towards the free surface due to diffusion along new pathways created by microcracking. Thus the excavation may alter the geometry of the cracks

and pore spaces and reduce the fluid content in both the zones of excavation damage and disturbance. The direction of one set of induced cracks in the zone of excavation damage is aligned with the stress direction and direction of primary layering (section 2.14), so that these cracks form a network that aids fluid escape. I therefore suggest that the variations in *P*-wave velocities are due to dry cracks caused by excavation.

7.10 *P*-wave Velocities and Polarizations

I further explain the different results of the *P*-wave travel time analysis and the pattern of polarizations of both the Shear-Wave Experiment and Velocity Survey data sets by the fundamental differences of the two methods within heterogeneous rockmasses. *P*-wave travel times are determined by the integral sum of the *P*-wave slowness over the entire raypath. In this case, the zones of different and changing slownesses throughout the zones of damage and disturbance and the *in situ* rockmass all contribute to the *P*-wave travel times. Thus the dry cracks encountered by the seismic signals at the start of propagation have the greatest influence on the pattern of *P*-wave velocities (previous section). Polarizations are determined by the last set of fabrics traversed by the shear-waves for a long enough portion of the raypaths to cause measurable splitting. For the Shear-Wave Experiment data set, results of inversion are due to the *in situ* anisotropy (section 7.7). The majority of polarizations measured in the Velocity Survey data set are primarily due to cracks created or altered by excavation (previous section).

7.11 Conclusions

In this chapter I have inverted and modelled the polarizations of the Shear-Wave Experiment and Velocity Survey data sets and compared the results to the *P*-wave velocity analysis of the Velocity Survey. My main conclusions for geological interpretation are:

1. The *in situ* anisotropy is consistent with hexagonal symmetry due to EDA-cracks, the primary layering, or both. Specifically, the best hexagonal model of Hudson Cracks is of saturated cracks of 023° strike, 35° dip, with an aspect ratio of γ=0.025. This conclusion is supported by the close correspondence of the model's fabric orientation to those expected (section

2.15), the stability of the inversion, and the consistency of this conclusion with the interpretation of all results.

2. Fabrics in the zones of excavation damage and disturbance determine many of the polarizations of the Velocity Survey. This explanation is consistent with the failure of inversions and modelling to produce reasonable results, the disagreement with the inversion results of the Shear-Wave Experiment data set, and the evidence of excavation effects upon the *P*-wave velocities.
3. Excavation has almost certainly resulted in the escape of fluids from the *in situ* rockmass. This is suggested by different results of the shear-wave inversions and the *P*-wave velocity analysis of the Velocity Survey data set. The *P*-wave velocity analysis indicates the presence of two crack sets, while the shear-wave inversions do not.

This study is the first involving the inversion and detailed modelling solely using polarizations from a non-systematic distribution of propagation directions. Confidence in results required the testing of inversion and modelling techniques. My evaluation of the success in the inversion and modelling assuming a single fabric of Hudson Cracks is more thorough than any yet published. My conclusions of general importance to shear-wave studies are;

1. Polarizations alone can be used to determine *in situ* fabric orientations.
2. It is desirable to first test automated inversion and modelling techniques assuming hexagonal symmetry. The success of the inversion and the resolution of the modelling can be assessed more easily than symmetry systems of more elastic constants or parameters.
3. Results strongly suggest that the automated inversion of Horne and MacBeth (1994), followed by a grid search (as is now included as part of their inversion), does find the best-fitting models. This is supported by the convincing fit of data to models found by inversion and the detailed evaluation of the success in inverting the Shear-Wave Experiment data set for hexagonal symmetry. Such success is important because automated inversion is necessary for symmetry systems involving too many parameters for modelling by hand to be practical. I suggest that even modelling orthorhombic symmetry by hand is impractical without a priori restrictions on fabric orientations.

8 Time Delays and Geological Interpretation

8.1 Abstract

Time delay measurements are scattered but do indicate an *in situ* strength of differential shear-wave anisotropy consistent with an intact rockmass. However, seismic signals from nine raypaths do not display shear-wave splitting where splitting would be expected based on inversion results. Eight of these nine raypaths are wholly or almost wholly within granodiorite rather than the granite and indicate a lower *in situ* and excavation-induced anisotropy in the granodiorite. However, time-delay measurements do not indicate any differences of the seismic anisotropy between the two slightly different lithologies. This contradiction prevents a conclusion whether the *in situ* anisotropy is due to Extensive-Dilatancy Anisotropy, or the faint primary layering.

8.2 Introduction

Recent modelling strongly suggests that the geometry intergranular cracks are extremely sensitive to stress and that changes in differential stress affecting intergranular cracks will affect shear-wave propagation (Zatsepin and Crampin, 1995). Such sensitivity is beneficial for the monitoring of a rockmass, but also suggests that appreciable scatter to measurements of shear-wave splitting may result from inhomogenieties with a rockmass.

There is strong evidence that the shear-wave splitting in the Shear-Wave Experiment and the Velocity Survey is affected by the zones of excavation damage and disturbance around the source tunnels. Results of inversion for polarizations give clear evidence that the *in situ* rockmass has hexagonal symmetry (section 7.7), but 20 of the 53 polarizations from the Shear-Wave Experiment data set conflict with the best hexagonal model (section 7.3). Similarly, the polarizations of the Velocity

Survey data set suggests that the majority of these polarizations are not determined by the *in situ* anisotropy (section 7.9). Affects due to excavation are expected as the source locations of the Shear-Wave Experiment were 0.30m from the free surfaces of the source tunnels' walls, and between 0.30m and 0.70m for the Velocity Survey. The zone of excavation damage is limited to a skin of 0.5m thickness around the Mine-by Tunnel, while the zone of excavation disturbance extends to 3.5m from the Mine-by Tunnel (section 5.12). These zones are likely of similar extent around the source tunnels. Therefore, all seismic signals of these two experiments initially propagated through rockmass affected by excavation.

Greater scatter is expected for time delays than for polarizations as time delays cumulate with propagation. The success in inverting polarizations suggests that most polarizations are determined by the *in situ* anisotropy (section 7.3). However, time delays cumulate with propagation and are therefore affected by the velocity heterogeneities around the source locations. Greater scatter of time delays also explains inversion results. Inversions were initially performed for both polarizations and time delays using the two first algorithms (section 6.5) as part of the development of the final algorithm (As discussed in section 6.5, the final algorithm did not consider time delays but could be modified to do so.). No model fitted the time delays well and the final anisotropic fabrics found were virtually identical to those found solely using polarizations and the failure to match the pattern of time delays produced high misfit values.

In this chapter I use time delay measurements to find an approximate strength of the *in situ* differential shear-wave anisotropy by assuming that the scatter in time delays is due to the effects of excavation. I then use the result to gain further insight into the cause of the *in situ* anisotropy. I first show the inadequacies of contoured time delay diagrams and then develop a quantitative method of comparing time delay data to models that accounts for the effects of the zone of excavation damage. I then investigate why the seismic signals of several raypaths do not display shear-wave splitting. Lastly, I combine all observations in making the final geological interpretation.

8.3 Displaying Time Delays Using Plate Carée Projections

The method of displaying polarization using Plate Carée projections (section 1.7) may also be used for plotting time delays. Only one plot is needed to display time delays because time delays are a scalar quantity as opposed to polarizations, which are vectors and require projection onto two planes. Figure 8.1 displays the contoured group velocity time delay plot for the best fitting hexagonal model with the polarizations as shown in Figure 6.5. Cross sections along lines of constant azimuth display profiles of the time delay behaviour. The contours were based upon a 81 by 41 grid of model time delays. The grid spacing is fine enough that both the line singularities and kiss singularities are accurately mapped and visually easily seen both in the Plate Carée projections and in the cross sections. Clearly this technique is effective at displaying the pattern of time delays for models (e.g. Liu and Crampin, 1990; Holmes et al., 1993; Baptie et al., 1993; and Liu, 1995). Creating such a contour plot using real data is not so simple. Data points are irregularly spaced and the spacing between data points will be large enough in many places that the locations of contours are not well restrained. This section describes my method of contouring real data to minimize these problems.

The interpolation algorithm should be based on interpolating over a sphere rather than a plane as is conventionally assumed in interpolation algorithms. Interpolation on a sphere will account for the symmetries involved with raypath directions, such as an azimuth of 000° is the same as 360° and azimuth being undefined for vertical propagation directions. I searched for such an algorithm in three separate mathematical algorithm libraries (IMSL, 1987; Numerical Algorithm Group (NAG), 1991; and Numerical Recipes (Press et al.), 1992) and made various inquires but found no such interpolation algorithm available. I did not consider the writing and refining of such an algorithm as an economical use of time.

I instead based the contouring over a plane. The algorithm used was E01SEF from the Numerical Algorithm Group library (1991). This algorithm creates a regularly space grid of interpolated data from irregularly spaced data. The function defining the grid is continuous and has a continuous first derivative. Interpolation for a given grid point is performed locally within a user defined radius.

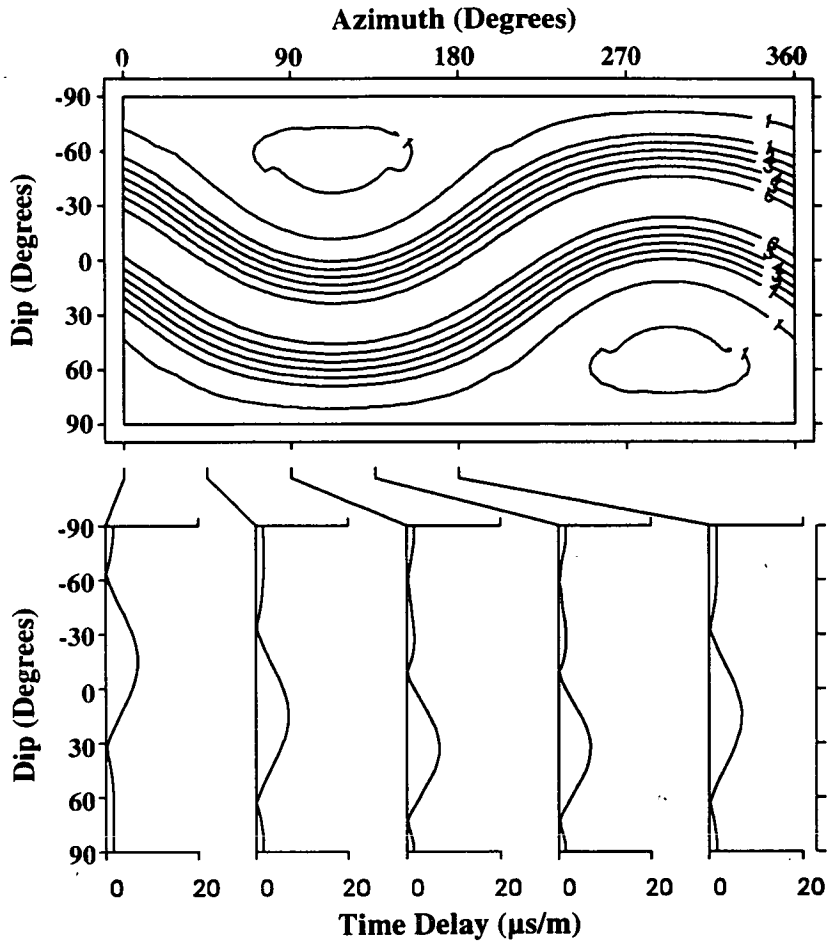

Figure 8.1: Contoured time delays of group velocity (microseconds per metre, equivalent to milliseconds per kilometre) plotted on a Plate Carée projection with cross sections for constant azimuths. Contours are extrapolated from a grid of 41x81 data points. The contours are in 1μs/m intervals. The model is of saturated Hudson Cracks of orientation 023/35, crack density ε=0.020 and aspect ratio γ=0.025. This is the best fitting model of a single set of Hudson Cracks found for the fifty-three polarizations of the Shear-Wave Experiment The plot of polarizations for this model is presented in Figure 6.5.

Contouring over a plane such as on a Plate Carée projection would not account for the symmetries of a sphere. Specifically, it would not account for the symmetry about 000° or the stretch of data point separations with increasing dip. Such stretch is seen on world maps where land masses near the poles are displayed as anomalously large compared to land masses near the equator. I account for symmetry about 000° by repeating each data point three times, assigning data points the same dips, but equivalent azimuths within the range of -360° to 000° and 360° to 720°. I also transformed data points closer together with increasing dip to exactly compensate for the north-south stretch. This method produces the approximate pattern expected if interpolation was performed over a spherical surface rather than a plane. It is not perfect because compensating for the stretch prevents perfect symmetry in the surface when accounting for symmetry about 000°. The approximation improves with larger data sets and greater varieties of propagation directions.

The interpolation is improved by assuming reciprocal symmetry (section 1.8). This doubles the amount of data for interpolation and makes the data set less sparse. Also, time delays less than zero are by definition not possible. Interpolation resulting in grid points less than zero was prevented by determining all local minima less than zero of the interpolated grid. The interpolation was then repeated with added data points with values set to zero at the location of these minima.

Figure 8.2 displays the contoured Plate Carée projections and cross sections of the fifty-three time delays measurements from the Shear-Wave Experiment. The contours were determined from a grid of 81 by 41 point which is the same size grid as using in the model (Figure 8.1). The grid was interpolated from time delay measurements by the method described in this section.

8.4 The Shortcomings of Contouring Real Data

An attempt to visually compared the model (Figure 8.2) to data (Figure 8.1) shows the shortcomings of this method of display. Visual comparison subjective and difficult and any pattern seen to roughly match between the two figures may only be coincidence. This display method does not indicate in which propagation directions data are sparse or contain gaps so that the contouring is less restrained by the observed time delays.

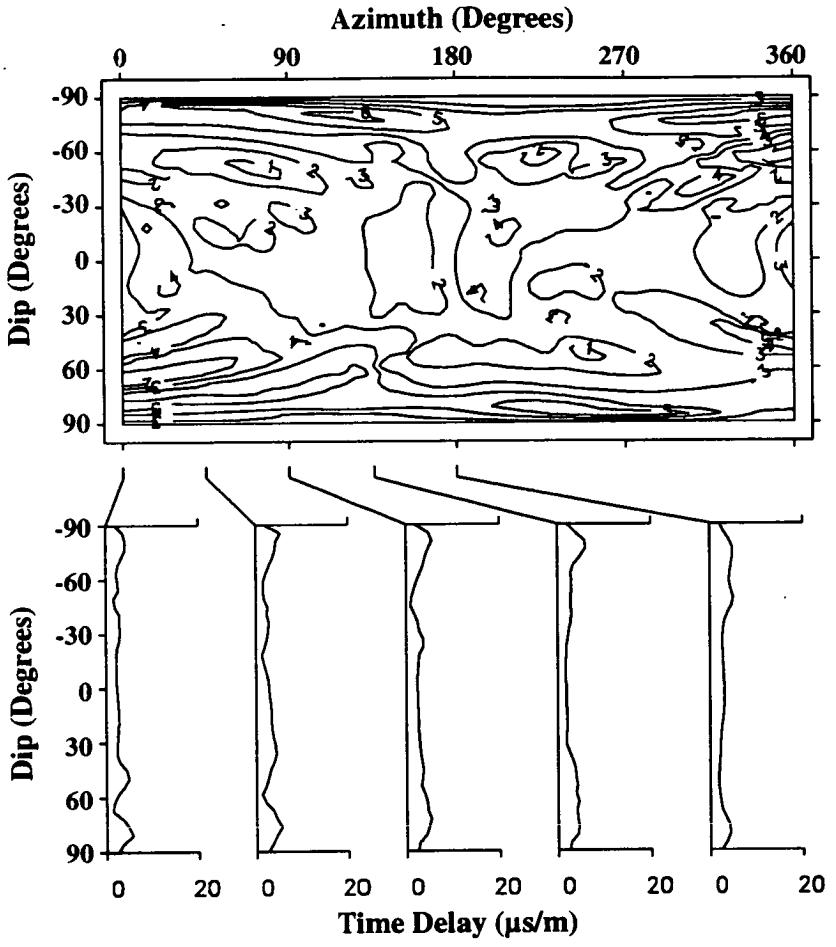

Figure 8.2: Contoured time delays (microseconds per metre) extrapolated from the fifty-three time delays measured from the Shear-Wave Experiment plotted on a Plate Carée projection.

These problems are fundamental to this method. Figure 8.3 is the contoured time delay plot where the time delay values are exactly those of the model of Figure 8.1. There are 166 data points for randomly generated propagation directions and the 166 reciprocal directions (332 is presently the maximum number the program is capable of using in extrapolation). Even for this data that matches the model exactly, comparison is difficult because of the irregular shape of the contours particularly near the directions of singularities.

Singularities are unlikely to be seen. Near zero time delays around singularities will only be interpolated if relatively small time delays are observed near the singularity. However, the closer the propagation direction is to a singularity, the less likely the time delay will be great enough for splitting to be observed. This problem is demonstrated in Figure 8.4, which displays the contour plot for fifty-three randomly generated propagation directions and corresponding reciprocal directions where the delays values are also exactly those of the model of Figure 8.1. Fifty-three is the same number as measured time delay in the Shear-Wave Experiment and is more realistic of the number of time delay measurements expected in studies. Only time delays where at least 1.5 sample points (30μs) delay time for a 30m raypath are included because this is realistic of the minimum time delay that can typically be measured in the Shear-Wave Experiment. Figure 8.4 does not indicate the locations of singularities, and again this figure is difficult to compare to Figure 8.1 despite the perfect match of the fifty-three values used in contouring to the model.

The precision in time delay measurements is not displayed by this method. Precision for the Shear-Wave Experiment data set is approximately ±1 sample points (section 4.7). The average time delay measured is 4.7 sample points. Therefore the precision indicates very large relative errors, of which Figure 8.2 gives no indication.

8.5 Quantitative Comparison of Time Delays

The previous section demonstrated the inadequacies of plotting measured time delays on Plate Carée projections. I now develop a quantitative method of comparing time delays to models.

Ideally an observed time delay can be compared to a model by dividing the observed time delay by the time delay of the model for the same propagation

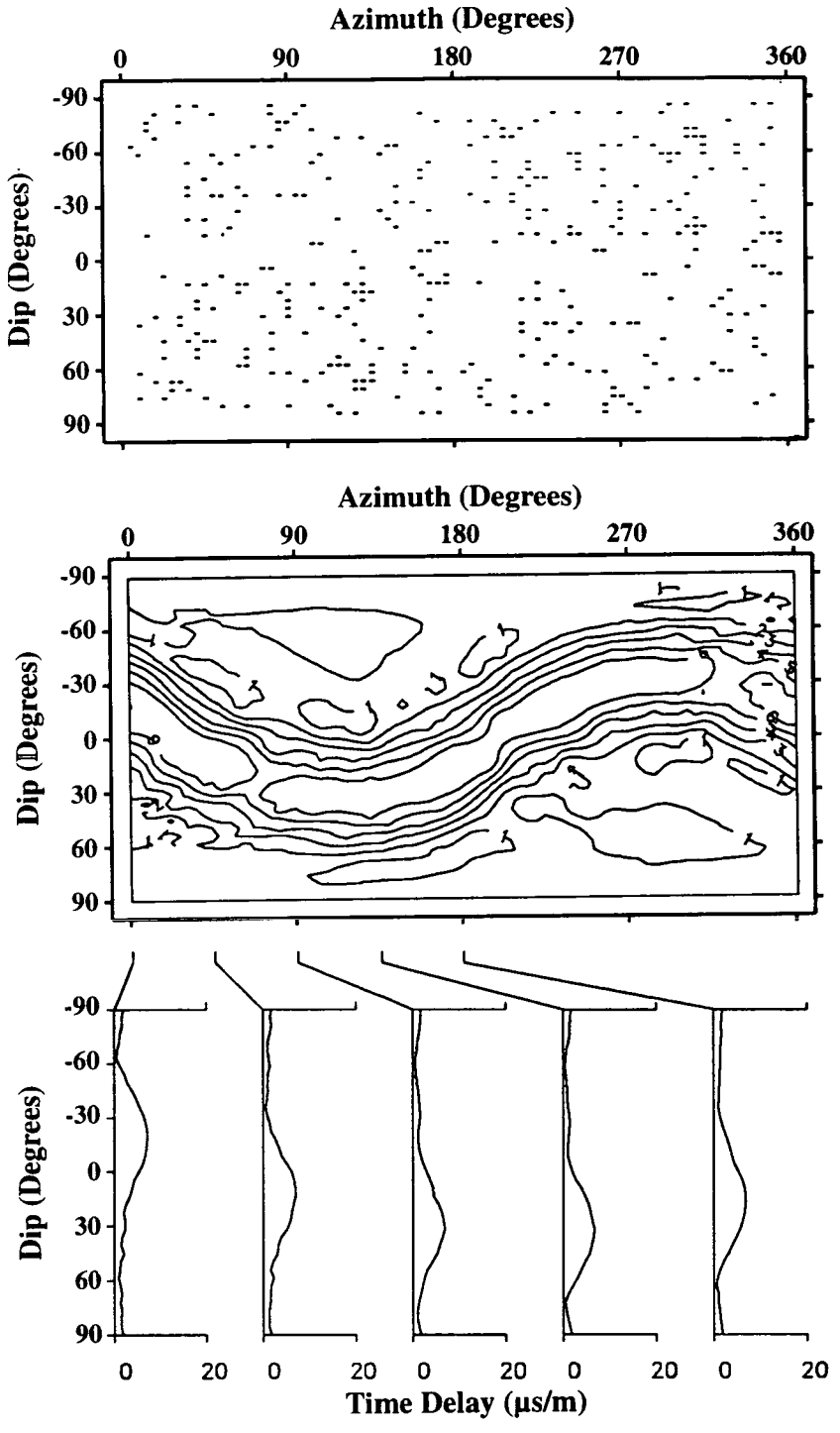

Figure 8.3: Contoured plot of time delays extrapolated from 166 data points and the 166 reciprocal data points plotted on a Plate Carée projection. The data points are for the randomly chosen propagation directions denoted by the location of ticks on the upper projection. The values of time delays exactly match those of Figure 8.1.

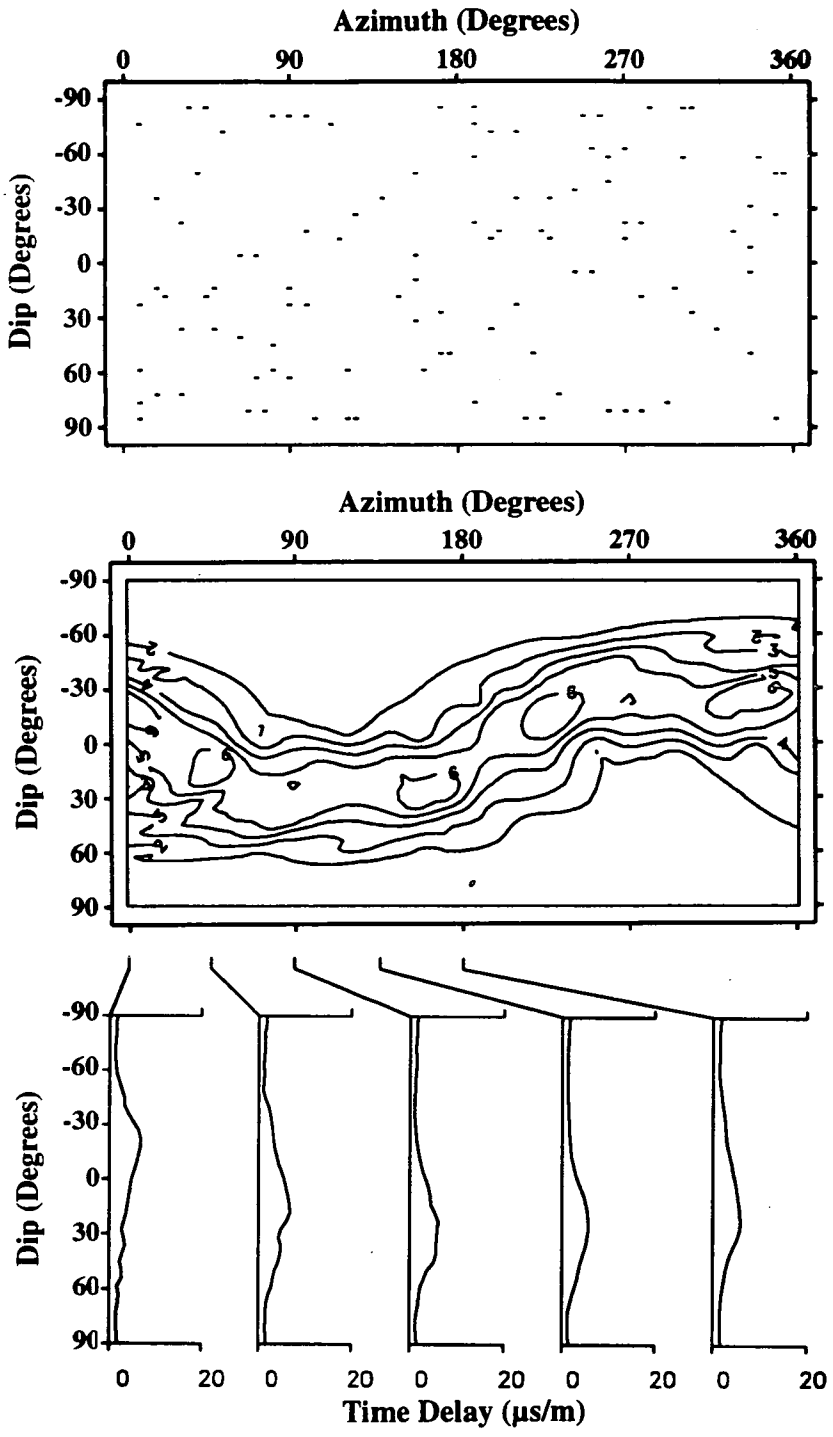

Figure 8.4: Contoured plot of time delays extrapolated from fifty-three data points and the fifty-three reciprocal data points plotted on a Plate Carée projection. Only time delays of greater than 1µs/m (equivalent to a time delay of 1.5 samples points (30µs) for a 30m raypath) are included. The data points are for the randomly chosen propagation directions denoted by the location of ticks on the upper projection. The values of time delays exactly match those of Figure 8.1.

direction. I define the resulting value as the *normalized time delay.* A perfect match between model and data would result in a value of '1' for all normalized time delays. Crack density cannot be determine solely from inverting polarizations (section 7.3), but crack density is approximately proportional to time delay (section 1.10). Therefore, a constant value for all normalized time delays would result if a model matches the data other than for crack density, and this value would be approximately the ratio of the true crack density to that of the model tested. In this way, models may be compared to observed time delays to determine if the model explains the time delays and to determine the crack density.

In practice, there are complications in dividing the observed time delay by that predicted by the model. The algorithm used (section 8.3) does not determine time delays for a specified propagation direction, but over a grid. Small miss-orientations in determining propagation directions and small variations on fabric orientation also must be accounted. Also, time delays can only be measured to a limited precision. Therefore determining discrete values of normalized time delays is not practical.

It is more useful to determine the range of possible values for the normalized time delays. These ranges are calculated using the minimum and maximum data time delays as determined by the measured time delays, the picking precision of ±1 sample point, and the maximum and minimum model time delays as found from the 81x41 grid within 9° of the propagation direction. A common value to all ranges of normalized time delays indicates the ratio of the true crack density to that of the model. If there exist no value is common to all ranges of normalized time delays then either the model does not explain the observed time delays or there are anomalous time delay picks.

8.6 Initial Comparison of Data to Model

Twenty of the corresponding polarizations do not agree with the best hexagonal model. Assuming the hexagonal model to be correct, these twenty polarizations are not determined by the *in situ* anisotropy and are either determined by the excavation-induced anisotropy, or are anomalous. The time delays corresponding to these twenty polarizations should not be included when time delays are normalized by the best hexagonal model. The hand-picked and automatically picked time delays

agreed for twenty-three of the remaining thirty-three observations. I will only us these twenty-three time delay measurements to reduce the number of possible miss-picked time delays.

Figure 8.5 is the graph of normalized time delay versus raypath length for the twenty-three measured time delays. The time delays were normalized using the best hexagonal model found (Figure 8.1) using a crack density of ε=0.017. Many normalized time delays are greater than the maximum of the time delays axis. These are observed time delays whose corresponding propagation directions were near singularities in the model. Consequently the measured time delays are divided by a value near zero to find the maximum normalized time delay values resulting in unreasonably large values. The maximum value of '4' for the *Normalized Time Delay* Axis of Figure 8.5 was chosen because the minimum values of all ranges of normalized time delays were less than '4' and a normalized time delay of '4' suggests an unreasonably large crack density of ε=0.068. I chose *Straight Raypath Length* to be the other axis of Figure 8.5 to examine the data for greater scatter in shorter raypaths. The graph clearly shows there exists no common value within the ranges of all normalized time delays and this cannot be attributed to a few anomalous polarizations. All but four of the twenty-three ranges contain values between 0.50 and 1.0, corresponding to crack densities of ε=0.0085 to 0.018. These values are less than the maximum of ε=0.045 expected for an intact rockmass (Crampin, 1994).

The number of observations for this analysis can be increased by including time delays from the Velocity Survey data set, where the corresponding polarizations agree with the best hexagonal model. Additional scatter is expected because some polarizations may coincidentally agree with the hexagonal model even if the polarizations were determined by excavation-induced anisotropy, and the lower reliability of picks from the Velocity Survey data set (section 7.8.1). This resulted in sixty-five normalized time delays (Figure 8.6).

8.7 Accounting for the Zone Of Damage

The zone of damage can be taken into account by calculating the maximum and minimum effects of the zone of excavation damage upon time delays. To do this I will assume the maximum anisotropy to be no greater than ten per cent as this is the

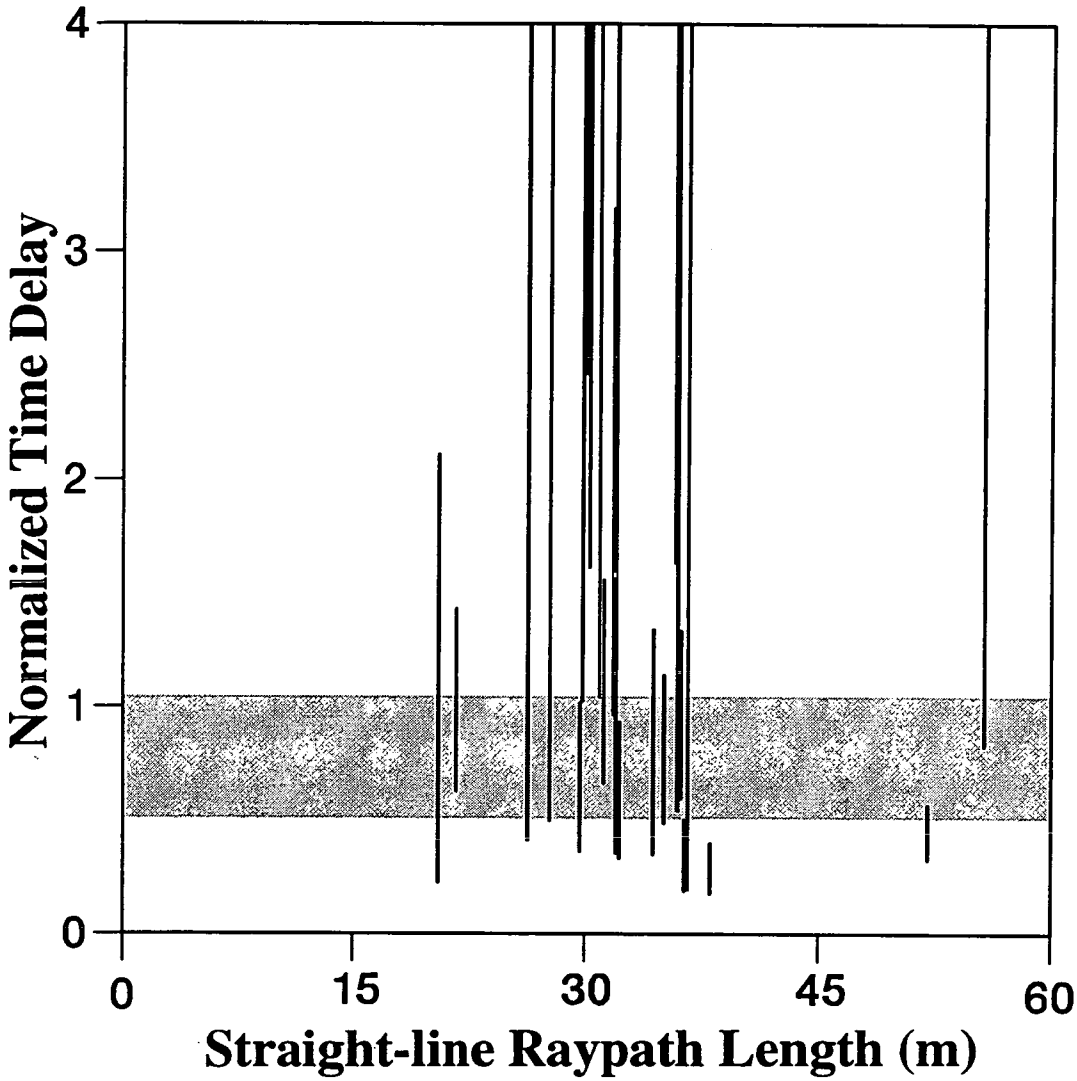

Figure 8.5: The graph of normalized time delays versus raypath length corresponding to the twenty-three polarizations from the Shear-Wave Experiment that do not conflict with the best fitting hexagonal model of Hudson Cracks, and the values of hand-picked and automatically picked time delays agree. The model used to normalized the time delays is that of the best fitting model of a single set of Hudson Cracks (saturated Hudson Cracks of orientation 023/35, crack density ε=0.017 and aspect ratio γ=0.025). The model is the same as that of Figure 8.1 except for a lower crack density of ε=0.017 rather than ε=0.020. The shaded horizontal band indicates a range of normalized time delays from 0.5 to 1.0 where values of all but four ranges are included.

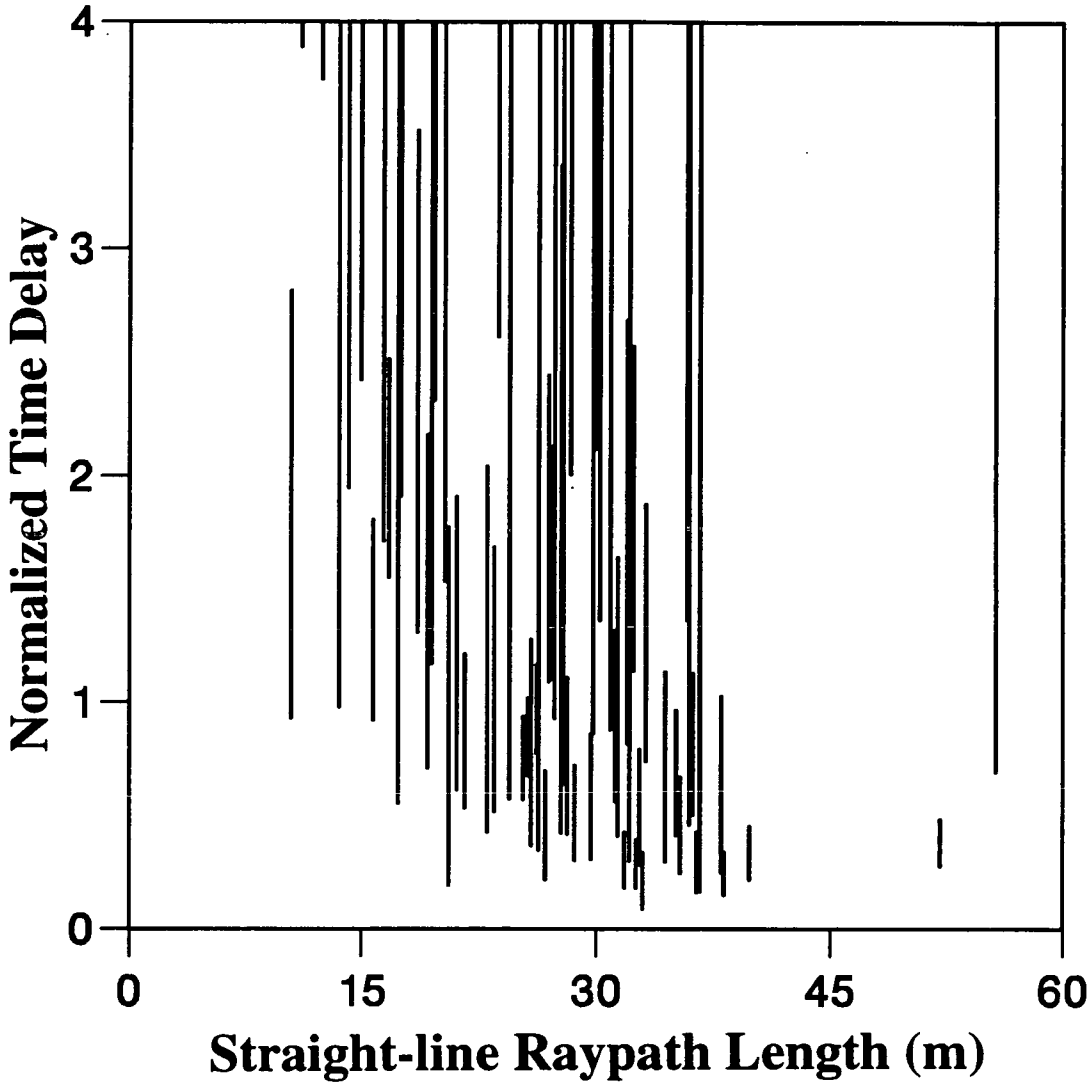

Figure 8.6: The graph of normalized time delays versus raypath length corresponding to the twenty polarizations as in Figure 8.6, and the forty-five polarizations from the Velocity Survey that do not conflict with the best fitting hexagonal model of Hudson Cracks. The model used to normalize the time delays is that of the best fitting hexagonal model, as used in Figure 8.5. Some values of raypath lengths have been slightly altered (typically 0.30m) to prevent overlapping of ranges.

maximum strength expected for an intact rockmass (Crampin, 1994). I will also estimate the extent of the zone of excavation damage to be a skin of 1.0m around each source tunnel despite a known limit of 0.5m around the Mine-by Tunnel. This is because Carlson and Young (1993) observed velocity changes up to 0.75m from the Mine-by Tunnel and the lesser care taken in excavating the source tunnels.

The proportion of the total length of every raypath within one metre of its source tunnel was numerically calculated using the surveyed co-ordinates of the source and receiver locations and the interpolation of surveyed locations on the tunnel walls. I estimate the precision at determining this length to be ±0.1m. The time delay through a homogeneous rockmass is given by;

$$t = \frac{d}{V_{qs2}} - \frac{d}{V_{qs1}}; \tag{8.1}$$

where V_{qs1} and V_{qs2} are the velocities of the *qS1*- and *qS2*-waves respectively, d is the straight raypath length, and t is the time delay. Substituting equation 1.1 into equation 8.1 gives;

$$t = \frac{d}{V_{qs1}(1-A)} - \frac{d}{V_{qs}}; \tag{8.2}$$

where A is the percentage anisotropy. Ten per cent anisotropy results in a time delay of 32.9μs/m, assuming a *qS1*-wave velocity of 3376m/s as measured by Talebi and Young (1989). It is therefore assumed that the contribution of the zone of excavation damage to the total time delay measured is between 0μs/m and 32.9μs/m for the length of raypath within 1.0m to the source tunnel. These values are subtracted from the measured time delay for each raypath to find the range of time delays that can be solely attributed to shear-wave splitting outside of the zone of excavation damage.

This is a very crude method that takes no account variation of damage with propagation direction. Breakouts in the Mine-by Tunnel show that the zone of damage is not cylindrical symmetric about the tunnel axis. However there is not enough known about the fabrics in the zone of excavation damage to confidently estimate their orientations, extent, or anisotropic effects. A maximum of ten per cent anisotropy is assumed in all directions so not to underestimate the effects of the zone

of damage and so place lower and upper bounds on the possible effects of the zone of excavation damage.

8.8 Strength of *In Situ* Anisotropy

Figure 8.7 displays the sixty-five normalized time delays as determined by the same method as for Figure 8.6 except for that the maximum and minimum effects of the zone of excavation damage have been accounted. Twenty of the sixty-five normalized time delays range from zero to over four. Most values greater than four are due to many raypaths of the Velocity Survey being subparallel to the Mine-by Tunnel so that large proportions of the raypaths are within 1.0m to the tunnel. Values of zero result from being able to attribute all the measured time delay to splitting within the zone of excavation damage. Accounting for the zone of damage has also reduced the scatter in normalized time delay ranges for raypaths less than twenty-five metres in length. This result is consistent with the zone of damage contributing significantly to the time delays of these shorter raypaths.

There is no value of time delay common to all sixty-five ranges, and scatter displayed in the time delay ranges prevents any detailed interpretation of the strength of the *in situ* anisotropy. However, normalized time delay values of less than 1.7 are common to all ranges. This corresponds to a crack density of $\varepsilon=0.029$ as is consistent with the rockmass being intact (Crampin, 1984).

No accounting for the effects of the zone of excavation disturbance upon time delays have been made because the effects are expected to be small compared to those from the zone of excavation damage. Changes in the stress field due to excavation will cause reorientation of EDA-cracks, but will not increase the overall strength of anisotropy assuming that EDA-cracks have the maximum possible alignment from the *in situ* stress field. Anisotropy due to primary layering will remain unchanged. Therefore, the anisotropy in the zone of excavation disturbance for a given raypath can range from 0% to 2.9% assuming the *in situ* crack density to be no greater than $\varepsilon=0.029$. This is only a third of the range possible in the zone of excavation damage. Also, the differences in orientations and magnitude of the stress field in the zone of excavation damage from *in situ* decay rapidly with distance so that the effects of this zone are likely compensated by the overestimation of the effects of the zone of

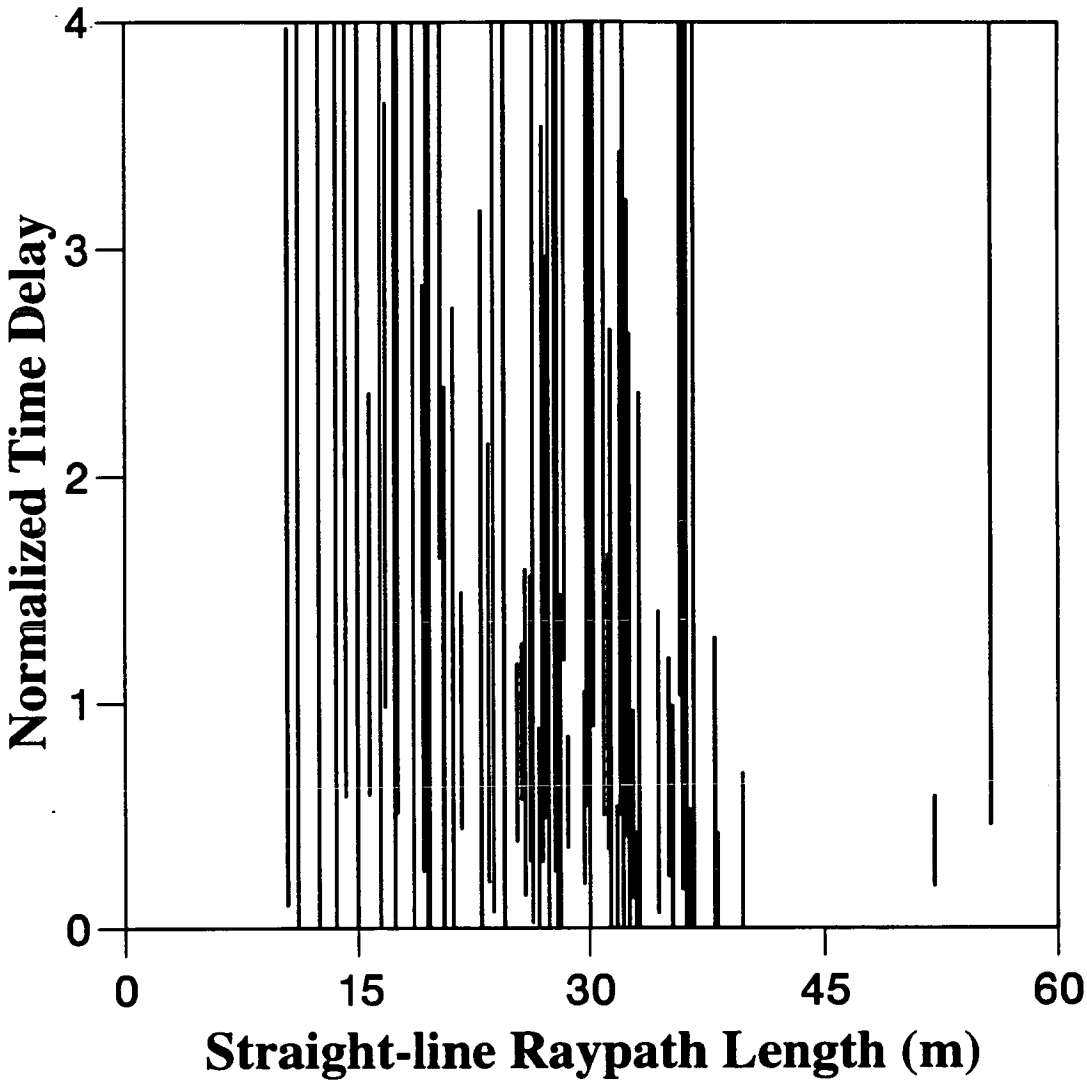

Figure 8.7: The graph of normalized time delays versus raypath length for the same sixty-five values as in Figure 8.6, but the ranges calculated to included the effects of 0% to 10% anisotropy for the portion of each raypath within one metre to its source tunnel. The model used to normalize the time delays is that of the best fitting hexagonal model, as used in Figure 8.5. Some values of raypath lengths have been slightly altered (typically 0.30m) where necessary to prevent overlapping of ranges.

excavation damage (section 8.7). Effects of the zone of excavation disturbance will add some scatter to the ranges of normalized time delays and may partially explain the lack of a single common value to the time delays.

8.9 No Shear-wave Splitting

Polarizations and time delays could be clearly measured on the seismograms from fifty-three sets of raypaths of the Shear-Wave Experiment data set. There were also eighteen sets of raypaths where the corresponding seismograms clearly indicated that no shear-wave splitting had taken place. Seismograms recorded by Triaxial Accelerometer 16, originally ignored because of incorrect accelerometer alignments (section 2.7), were also examined using the calculated triaxial accelerometer orientation. Two raypaths to this accelerometer showed no splitting. Any large data set is expected to included seismograms that display no shear-wave splitting even in a strongly anisotropic fabric because of short raypaths or propagation near singularity directions. I show in this section that the lack of splitting for all twenty raypaths cannot be explain solely by raypath length and propagation direction.

To be thorough I will compare these twenty raypaths to the time delays predicted for the best hexagonal and best orthorhombic models of the Shear-Wave data set (Figures 6.5 and 7.3, respectively) and the best orthorhombic model with the fabric orientations suggests by *P*-wave velocities of the Velocity Survey (Figure 7.4). The crack density ε=0.017 will be used for the best hexagonal model. I estimated a minimum likely crack density of the orthorhombic models to be the average of the minimums from the ranges of normalized time delays without accounting for the zone of excavation damage. The minimum likely crack densities for the best orthorhombic model are ε=0.010 and ε=0.017 for orientations 059/31 and 239/59 respectively. The minimum crack densities for third model are ε=0.0082 and ε=0.0030 for fabric orientations of 046/44 and 226/46, respectively.

All three models predict clearly measurable splitting (time delays of least two sample points) for at least four of the twenty raypaths. I argue that the hexagonal model best represents the *in situ* anisotropy (section 7.7), which predicts that at least nine of the raypaths should show clear splitting and the crack density would have to be lower than ε=0.0030 to explain the lack of splitting for all twenty raypaths.

8.10 Why the Lack of Splitting?

The previous section established that the models do not explain the lack shear-wave splitting for nine raypaths. This section relates these raypaths to lithology.

The lithology of the 420-Level consists mainly of the granite and granodiorite. Compositionally, these two rock types are very similar although the granodiorite has a slightly greater proportion of mafic minerals, a slightly higher density, and is finer grained (section 2.8). Examination of the three-dimensional lithology (Figure 8.8) and comparison of raypaths to the lithology on the plan view (Figure 8.9), and cress-sectional view (Figure 8.10) show a relationship of these raypaths to lithology. Specifically, eight of the nine raypaths predicted to show splitting are wholly or almost wholly within granodiorite as opposed to granite, the one exception being the raypath from Source Station 3 to Triaxial Accelerometer 2. This consistency suggests that the anisotropy in the granodiorite is different from that of the granite.

Other studies also find the behaviour of the two rock types noticeably different despite similarities in strength and composition. Collins and Young (1994) measured the decay in the rate of seismic events with time after each excavation sequence. The rate of induced seismicity in the granodiorite is initially less than in the granite but decays at a much slower rate. Figure 8.11 is the perimeter maps of the induced seismicity source locations and the break out contours. Comparison of this figure to the geology of the Mine-by Tunnel (Figure 2.12) shows that there is less induced seismicity and a less developed breakout notch in the granodiorite (Young and Collins, 1993).

These differences in the two lithologies may be due to the finer grain sizes of the granodiorite. The development of excavation-induced microcracks may be impaired by the greater number of grain boundaries that must be crossed (P. Young, pers. comm.). There may also be differences in the rate of fluid escape from the rockmass due to the different grain sizes and the possible differences in the excavation-induced crack structures. There may also be *in situ* differences in the seismic responses of the two lithologies, as investigated in the next two sections.

I presented a preliminary study of the splitting of the Shear-Wave Experiment from data of the first recording sequence (Holmes et al., 1993). In this preliminary study the direction of shear-wave motion due to the source was not considered. The

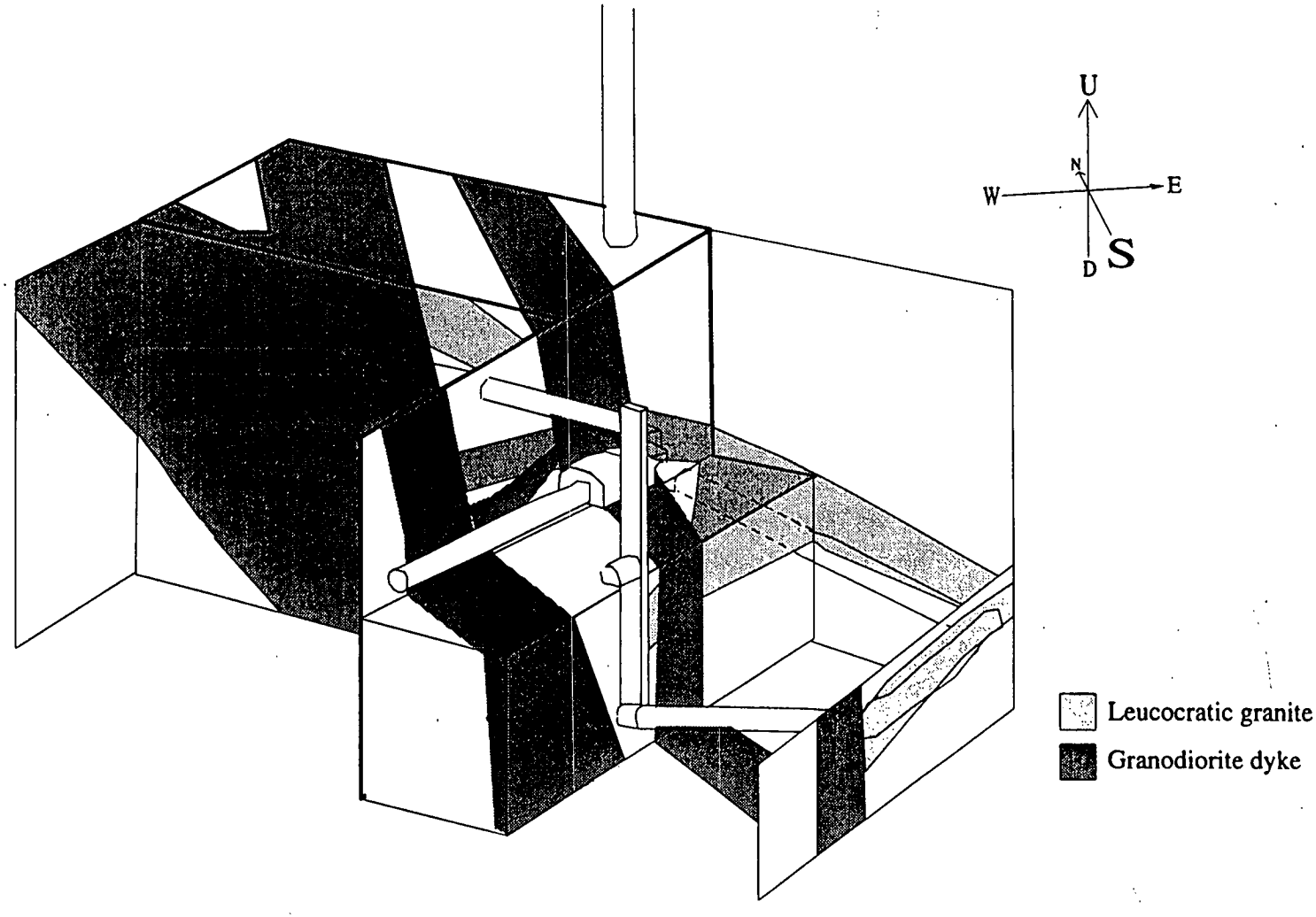

Figure 8.8: Block diagram depicting the geological setting of the Mine-by Experiment (R. Everitt, pers. notes).

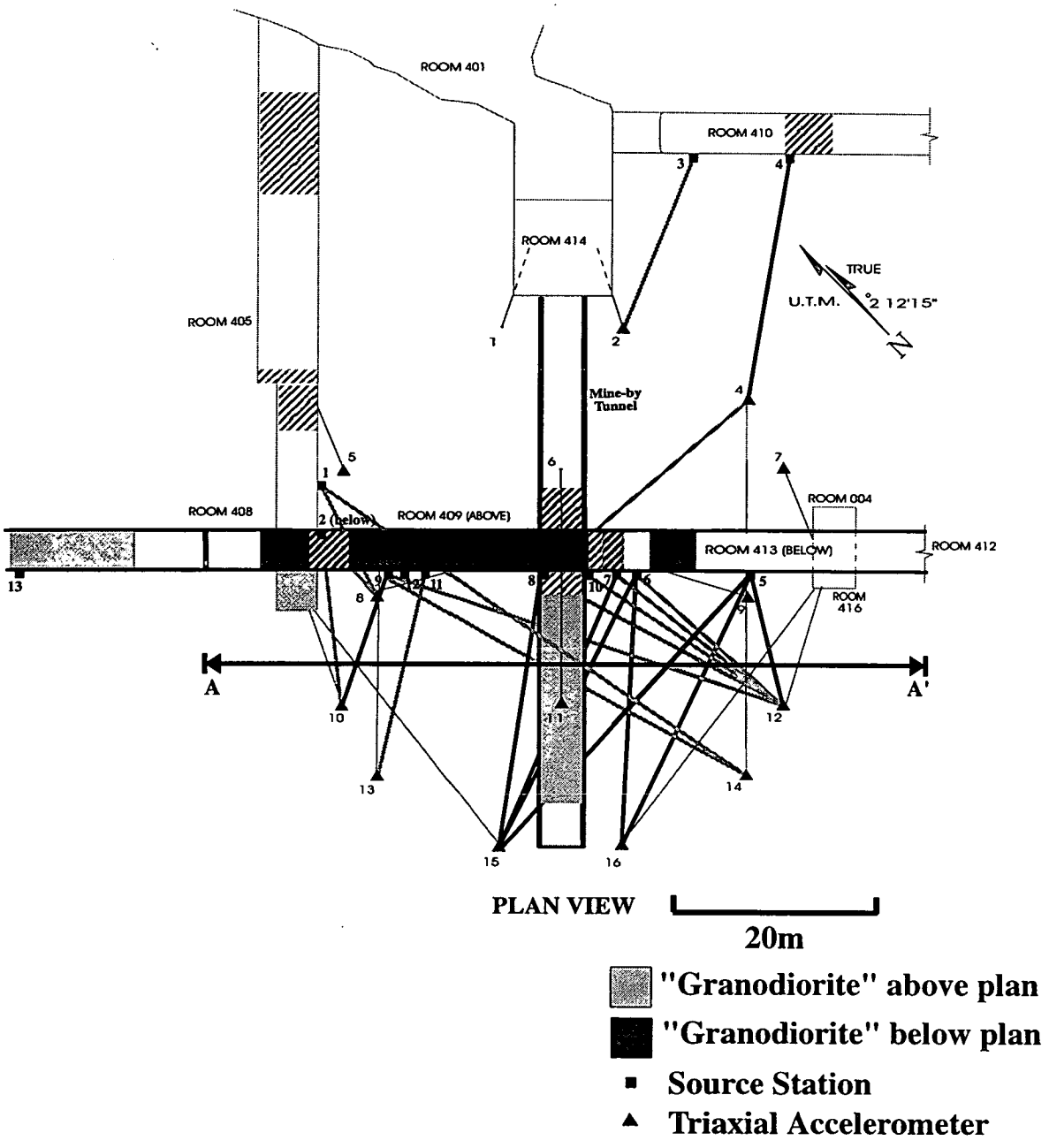

Figure 8.9: Plan view of the 420-Level around the Mine-by Tunnel showing the geology of the tunnels. Striped areas depict intermingling between the granite and granodiorite. The darker shading is used to indicate granodiorite for Room 413 where it is directly below Room 409. The twenty raypaths corresponding to the seismic signals without measurable splitting are shown. The nine raypaths denoted by darker shading are those where splitting is expected based on the best fitting hexagonal model. The line **A** to **A'** denotes the location of the cross section of Figure 8.11. Geology from R. Everitt, pers. notes.

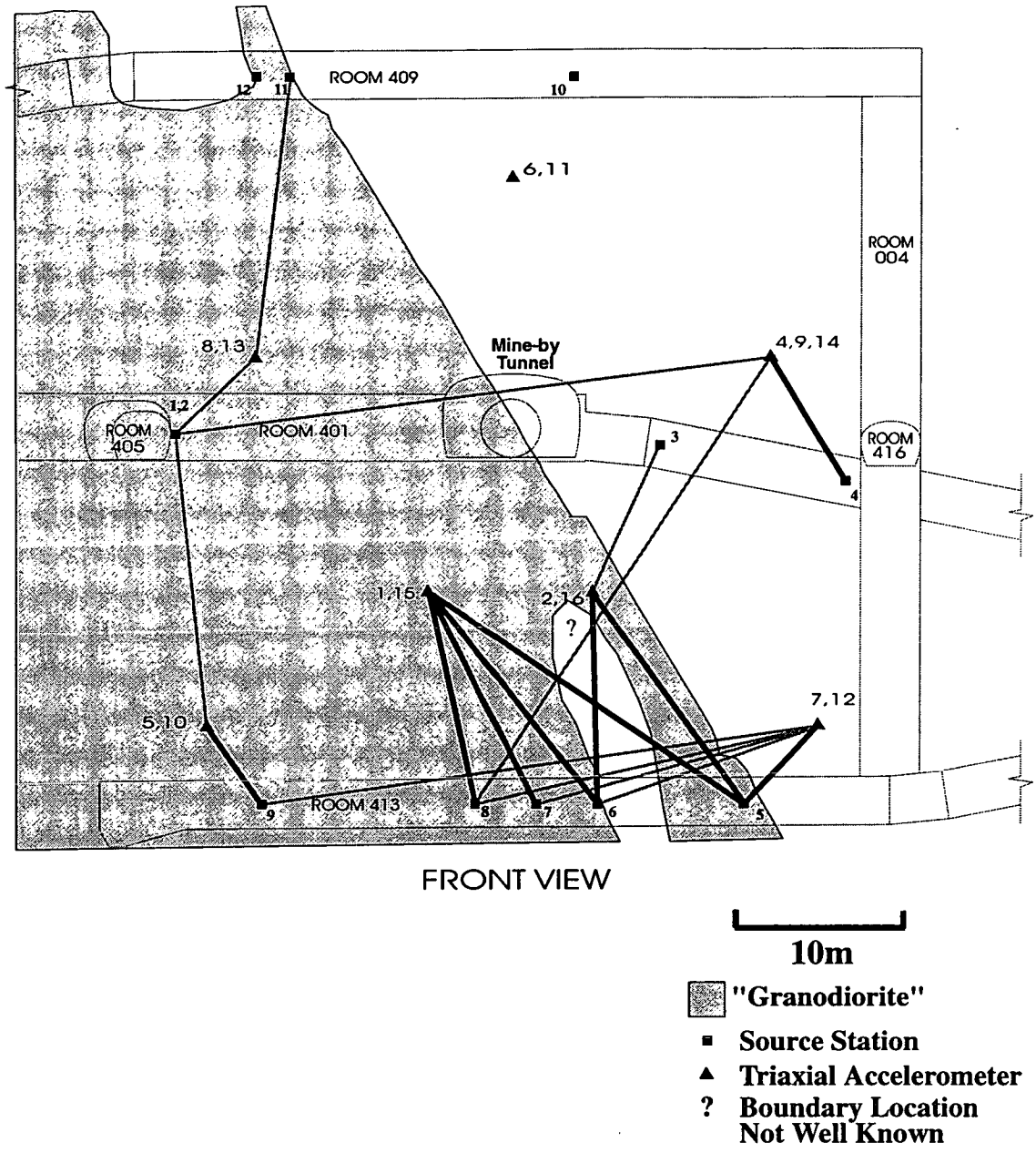

Figure 8.10: Cross section of the Geology of the 420-Level near the Mine-by Tunnel. The twenty raypaths corresponding to the seismic signals without measurable splitting are shown. The nine raypaths denoted by darker shading are those where splitting is expected based on the best fitting hexagonal model. Modified from Read and Martin (1991).

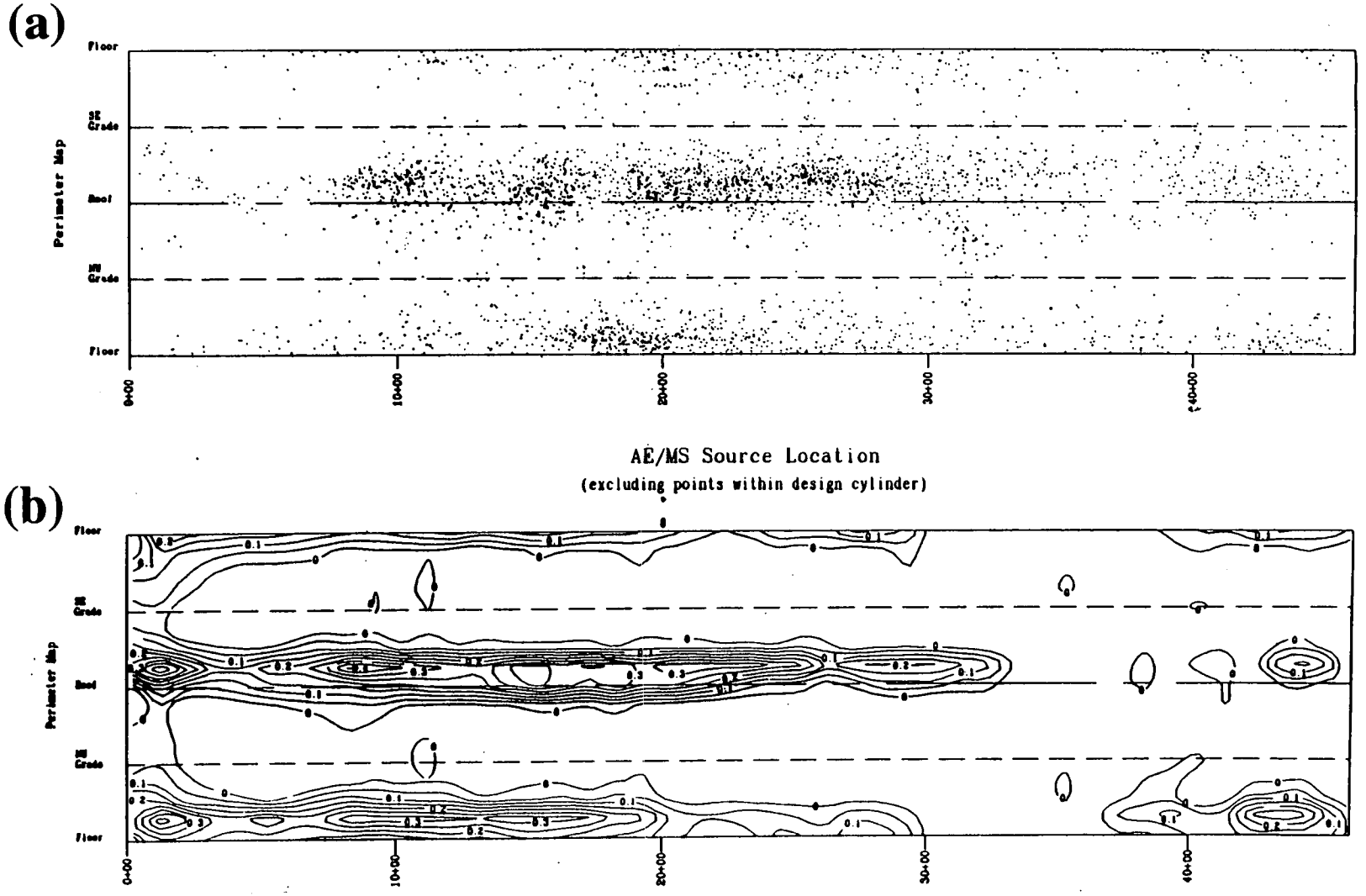

Figure 8.11: Perimeters maps for the Mine-by Tunnel showing (a) the auto source located induced microseismic events following the excavations of the fifty excavation rounds, and (b) the breakout contours (Young and Collins, 1993).

observation was made that the seismic signals from many raypaths that were near the Mine-by Tunnel's face had anomalous shear-wave polarization directions. These polarizations have now been identified as the shear-wave particle motions where no splitting had taken place. The first recording sequence took place when the Mine-by Tunnel face was within the granodiorite. This coincidence of apparently anomalous polarizations and the location of the tunnel face led to the incorrect interpretation that the anomalous stresses around the tunnel face cause the anomalous polarizations rather than lack of splitting from raypaths within the granodiorite.

8.11 Lower *In Situ* Anisotropy in Granodiorite

I will investigate the possibility of lower *in situ* anisotropy in granodiorite by considering the time delays. Limited geological information of the *in situ* rockmass prevents determining the proportions of each raypath that are within the two lithologies. Instead, I used Figures 8.8, 8.9, and 8.10 to identify raypaths from both the Shear-Wave Experiment and Velocity Survey data sets that are predominantly in only one of the two lithologies and that the corresponding polarizations agree with the best hexagonal model.

Figure 8.12 is the graph of normalized time delays accounting for the zone of excavation damage for the ten raypaths that are clearly predominantly in granite. The smallest range that includes values common to all ranges of normalized time delays corresponds to cracks densities between ε=0.0094 and ε=0.014. Figure 8.13 is the graph for eleven raypaths that are clearly predominantly in granodiorite, also accounting for the zone of damage. The smallest range of common values suggests a crack density between ε=0.013 and ε=0.018. The crack density in the granodiorite appears to be slightly greater than in the granite, but this is probably due to the limit amount of data. There are no distinct differences between the pattern of normalized time delays of the two graphs. Therefore time delays do not suggest there exists any differences in the *in situ* anisotropy of the two lithologies.

8.12 Less Excavation-induced Anisotropy in Granodiorite

I now investigate whether there is less excavation-induced anisotropy in the granodiorite than the granite. Less excavation-induced anisotropy in the granodiorite

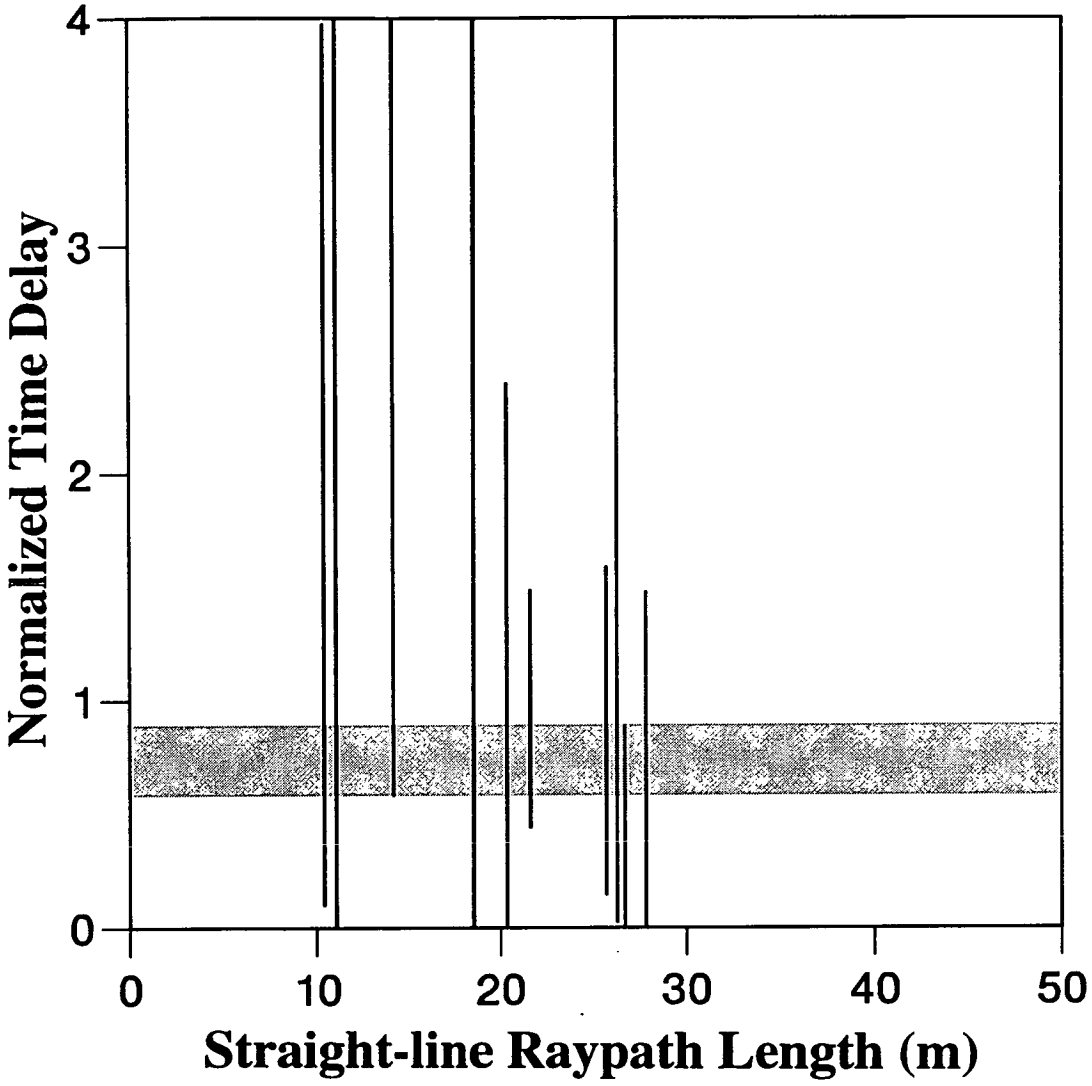

Figure 8.12: The graph of the ten of the sixty-five time delays of Figure 8.8 where the raypaths were predominantly within granite. The ranges were calculated to included the effects of 0% to 10% anisotropy for the portion of each raypath within one metre to its source tunnel. The model used to normalize the time delays is that of the best fitting hexagonal model, as used in Figure 8.5. The shaded band contains values from all ranges and corresponds to crack densities ε=0.0094 to ε=0.014.

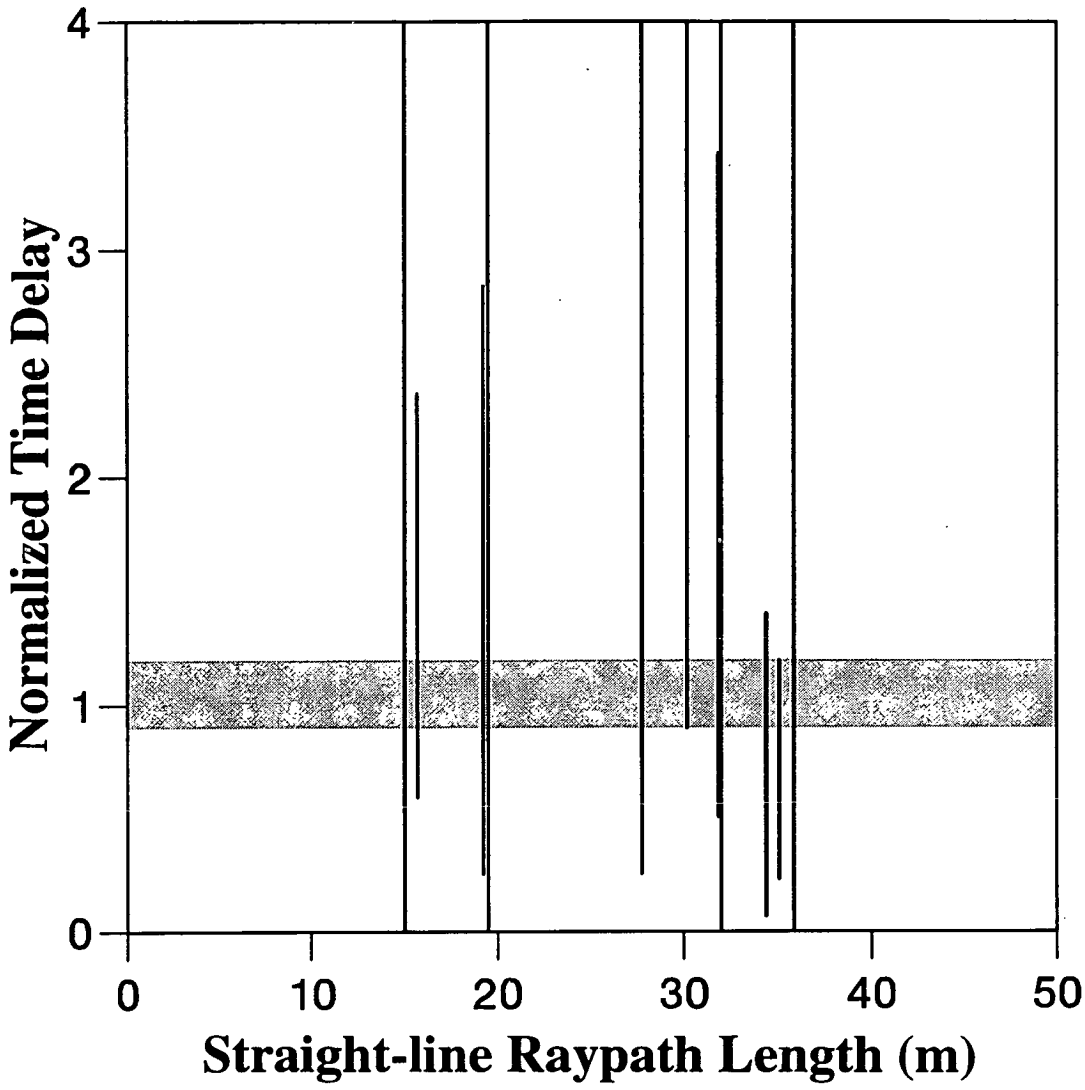

Figure 8.13: The graph of the eleven of the sixty-five time delays of Figure 8.8 where raypaths were predominantly within granodiorite. The ranges were calculated to included the effects of 0% to 10% anisotropy for the portion of each raypath within one metre to its source tunnel. The model used to normalize the time delays is that of the best fitting hexagonal model, as used in Figure 8.5. Some values of raypath lengths have been slightly altered (typically 0.30m) where necessary to prevent overlapping of ranges. The shaded band contains values from all ranges and corresponds to crack densities ε=0.0013 to ε=0.018.

may be expected because of possibly less excavation effects in the granodiorite (section 8.10). I will consider raypaths from both the Shear-Wave Experiment and Velocity Survey where the source locations are clearly within either granite or granodiorite. Only raypaths where the corresponding polarizations agree with the best hexagonal model are included so that the best hexagonal model can be used to normalize the time delays.

Figures 8.14 and 8.15 show the normalized time delays for sixteen raypaths with source locations clearly within granite and twenty-three raypaths with source locations clearly within granodiorite, respectively. No accounting of the zone of damage is made. If there is less excavation-induced anisotropy in the granodiorite, then the normalized time delays for shorter raypaths would be less scattered and generally lower than for the granite. Such behaviour is not seen. The time delays therefore do not suggest that there is less excavation-induced anisotropy in the granodiorite.

8.13 Geological Interpretation

The examination time delays presented in the two previous sections failed to reveal differences due to lithology to explain the lack of splitting of raypaths expected to show splitting or explain the scatter in normalized time delays. Similar examinations of subsets of the Shear-Wave Experiment and Velocity Survey data sets based on raypath length, separation of raypaths to tunnels, raypath directions, time delay measurements, and source tunnel orientations, as well as lithology, failed to resolve the scatter or explain the lack of splitting for some raypaths. There are several explanations that may resolve these conflicting results, but not enough data to substantiate them.

An explanation consistent with all observations is that there is negligible *in situ* anisotropy where the rockmass consists wholly of granodiorite, but that even minor intermingling of granite with the granodiorite results in the same *in situ* anisotropy as in the granite. The impure granodiorite would also be more susceptible to excavation effects. The amount of splitting therefore depends on the proportion of the raypath within wholly granite or intermixed lithologies. This situation could be due to extragranular cracks (cracks outside of grains including grain-boundary or intergranular cracks) within the *in situ* granite which are fluid-filled and stress-aligned

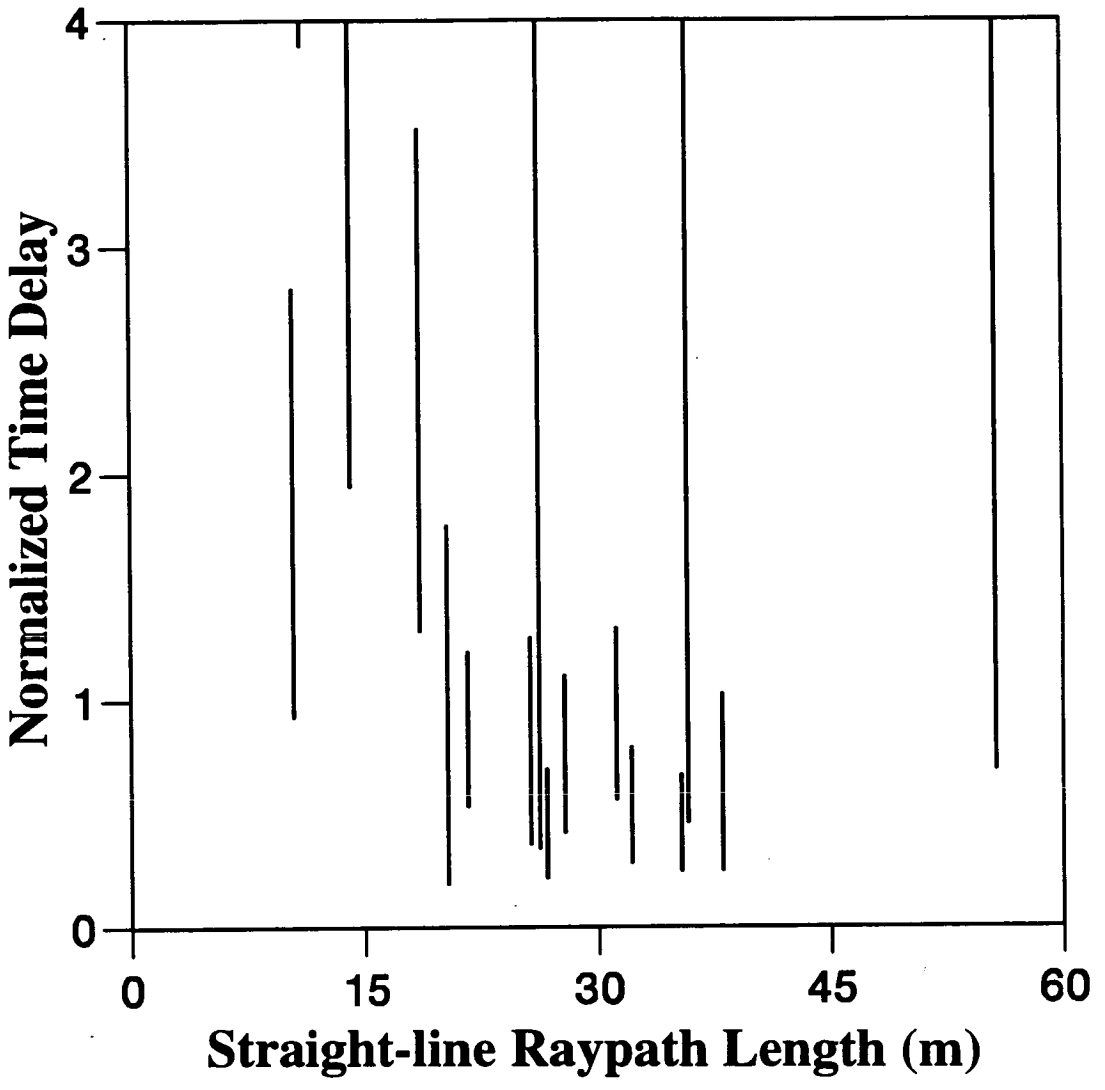

Figure 8.14: The graph of the sixteen of the sixty-five time delays of Figure 8.8 where the source locations of the seismic signals were clearly within granite. The model used to normalize the time delays is that of the best fitting hexagonal model, as used in Figure 8.5.

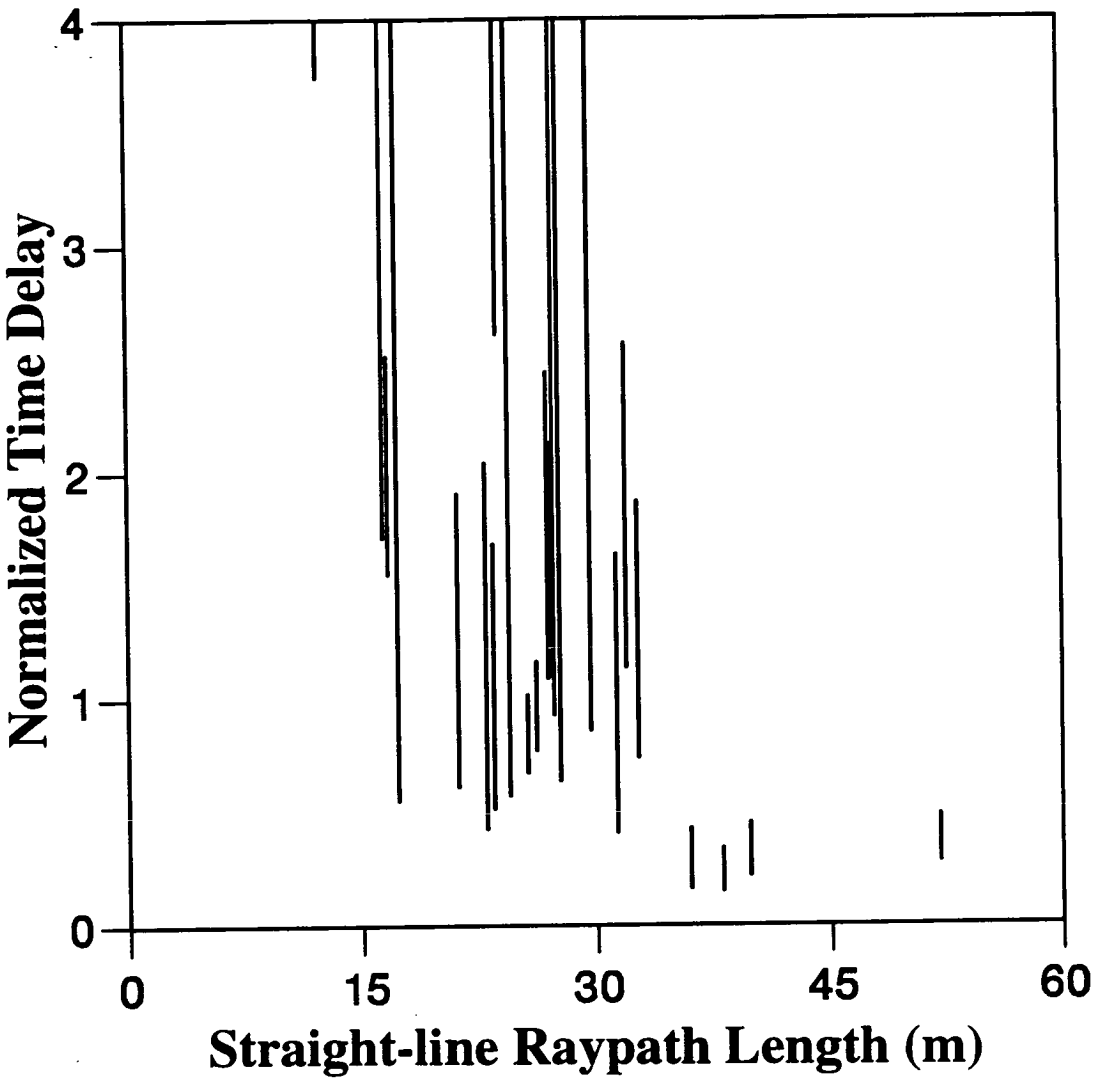

Figure 8.15: The graph of the twenty-three of the sixty-five time delays of Figure 8.8 where the source locations of the seismic signals were clearly within granodiorite. The model used to normalize the time delays is that of the best fitting hexagonal model, as used in Figure 8.5. Some values of raypath lengths have been slightly altered (typically 0.30m) to prevent overlapping of ranges.

and are primarily responsible for the *in situ* anisotropy (and are therefore EDA-cracks). The development of such cracks may be inhibited within the granodiorite by the finer grain sizes, but may form near where the two lithologies intermingle so that such cracks extend into the granodiorite for a finite distance before the rock matrix prevents their further development. There is no direct evidence to substantiate this explanation, although it is worthy of investigation.

I proposed this may be investigated by using tomographic techniques by using normalized time delays rather than the more traditional *P*-wave travel times. The addition restriction would be made that there are only two types of grid cells in the inversion grid. One type of call would be wholly isotropic while all the second type of cells would contain the same anisotropy. Success in relating the tomogram of time delays to geology would introduce a new method of non-destructively parameterizing a rockmass in a mine environment. Unfortunately, sixty-five raypaths do not provide enough raypath coverage to produce a meaningful tomogram (S. Maxwell, pers. comm.).

I suggest that the major reason for the lack of a precise explanation for the time delays is a combination of the assumptions in modelling, the complex pattern of excavation damage, and the extreme sensitivity of shear-waves. The modelling may not have resulted in the precise determination of the *in situ* fabric orientation and the fabric is unlikely to behave exactly as a set of Hudson Cracks. This creates errors in the normalization of time delays. It was also necessary to combine the data of the Shear-Wave Experiment with the less reliable data of the Velocity Experiment so there were enough observations for graphs such as Figure 8.7 to be meaningful (section 8.6). The most substantial complications are the extreme sensitivity of shear-wave splitting and the effects of excavation. The exact extend, symmetry, and pattern of zones of damage and disturbance are unknown and may differ between the two rock types. The intermingling between granite and granodiorite causes extreme reorientation of the primary layering, possibly causing anomalous polarizations and time delays, and there may exist differences in the anisotropy of the two lithologies. The rockmass also contains some smaller dykes and quartz veins and may contain other inhomogeneities that cause anomalous polarizations or time delays. These

effects may add enough scatter to data to mask fabrics that exist throughout the rockmass or within the zones of damage and disturbance.

8.14 Cause of the *In Situ* Anisotropy

8.14.1 Arguments for EDA

The strongest argument for EDA as the cause is the consistency of the results to an *in situ* fabric of EDA-cracks. The orientation of the best hexagonal model differs from that predicted for EDA by only 23° (section 7.7). Time delays indicate the strength of differential shear-wave anisotropy of significantly less than the upper limit of 4.5% (Crampin, 1994). Temporal changes also suggest that the *in situ* anisotropy is at least partially due to EDA (section 5.12).

Anisotropy due to extragranular EDA-cracks is also consistent with the porosity of the rockmass. The porosity of a rockmass, assuming all porosity is due to Hudson Cracks, is given by;

$$\Phi = \frac{4}{3}\pi\gamma\varepsilon\,; \tag{8.3}$$

where Φ is the porosity of the rockmass. Assuming a maximum crack density of ε=0.029 (section 8.8) results in an upper limit to the porosity of 0.3% using the aspect ratio of γ=0.025, although aspect ratio is a relatively insensitive parameter (section 7.3) so this upper limit is poorly determined. This value of porosity agrees with the porosity of Lac du Bonnet granite of between 0.2% and 0.4% as measured in laboratory samples, accounting for the effects of stress-relief cracking (Chernis and Robertson, 1987). This method of calculating porosity is also likely to underestimate the true porosity because porosity likely exists in cracks not aligned by stress, and EDA-cracks will not be perfectly ellipsoidal. However, this near agreement is consistent with an *in situ* anisotropy due to extragranular EDA-cracks.

There are two strong arguments against EDA as the *in situ* fabric. Firstly, the eight raypaths through granodiorite that are predicted to show splitting but do not suggest that the strength of the EDA anisotropy must be extremely weak in the granodiorite, but not the granite. This would make the granodiorite of the 420-Level

the second rockmass found to have negligible *in situ* crack-induced anisotropy, the only other one being 1200m of fine-grained shale or shaley clay in the Caucasus Basin, Russia (Slater et al., 1993). This contradicts the minimum strengths of anisotropy expected (previous paragraph). Secondly, EDA is aligned by the stress field and therefore should cause a very consistent anisotropic fabric throughout the undisturbed rockmass. The misfit value of 20.260 for fifty-three polarizations indicates the *in situ* anisotropy does not have this expected consistency.

8.14.2 Arguments for Primary Layering

There are three arguments that suggest the *in situ* anisotropy is due to the mineral alignments within the primary layering, or intergranular cracks whose orientations are governed by the primary layering (section 2.14.1). Firstly, it would explain the lack of splitting for the eight raypaths within the granodiorite expected to show splitting because the primary layering exists solely within the granite. Secondly, it explains the high number of polarizations that do not agree with the best hexagonal model. The orientation of the primary layering varies slightly throughout the granite and varies greatly when disrupted by the intermingling of the two lithologies (R. Everitt, pers. comm.). Thirdly, the orientation the best hexagonal model differs to the primary layering by only 10° as opposed to 23° to the orientation expected for EDA (section 7.7). However, *in situ* anisotropy due to the primary layering would not explain the lack of observable differences in normalized time delays between raypaths predominantly in either the granite or granodiorite (sections 8.11).

Interpretation of this explanation is severely restricted by the lack of knowledge of the possible effects of the primary layering. The effects of gneissic layering have never been theoretically deduced, although Babuška (1981) argued that the orientations of minerals and velocities in crustal crystalline rocks would only result in 'low' seismic anisotropy. The highly anisotropic platy minerals typical in gneissic layering, such as biotite, and the intergranular cracks whose orientations are governed by the mineral alignment, must cause some anisotropy. Kern et al. (1991) attributed the anisotropy observed between 1610m to 3575m depth of the German Continental Deep Drilling Project (KTB) drill hole to the highly foliated paragneiss at those depths. By observational field geology standards, the gneissic primary layering is very

faint and hardly noticeable. I do not know whether the faint gneissic layering within the granite of the 420-Level is anisotropically strong enough to cause the observed time delays and polarizations.

8.14.3 Summary and Alternative

There are no clear conclusions as to the cause of the *in situ* anisotropy. It is also possible that gneissic layering and EDA anisotropy both contribute appreciably to the anisotropy and the orientations of the two fabrics are too similar for them to be resolved separately (section 2.15). I suggest that the anisotropy is primarily due to EDA, but the orientations of the EDA-cracks are influenced by the primary layering. This explains both the initial onset of temporal changes (section 5.10) and the closer agreement in orientation of the primary layering to the best-fitting hexagonal model (section 7.7). Peacock et al. (1994) observed in a laboratory study of Carrara marble that the stress alignment of cracks were partially governed by grain boundaries so crack normals were not exactly aligned with the minimum stress axis, σ_3.

8.15 Conclusions

In this chapter I used time delays gain further insight to the cause of the *in situ* anisotropy. I demonstrated that graphs of normalized time delays are a useful, quantitative method of comparing measured time delays to models that accounts for the precision in measuring time delays. This method of comparison is much preferable to qualitative, visual comparisons of contour plots.

Time delays values are consistent with the rockmass being intact. The scatter in time delays prevents a determination of the *in situ* strength of differential shear-wave anisotropy.

Examining the effects of two lithologies produced apparently contradicting results. Nine of the twenty raypaths where there was no measurable splitting (time delays greater than approximately 1.5 sample points, or 30μs) should show clear shear-wave splitting, as calculated using the best hexagonal model. Eight of these nine raypaths appear to be wholly or almost wholly within granodiorite, indicating that the excavation does not cause an appreciable fabric in granodiorite and the *in situ* anisotropy in granodiorite is negligible. In contrast, examination of the time delays

for raypaths predominantly within a single lithology, or for raypaths with source locations clearly within a single lithology, indicate no clear differences in the anisotropy between the granite and granodiorite. I speculate that this may be due to EDA-cracks within the granite whose development in granodiorite is impaired by the finer grain size so that they only occur in granodiorite near where the two lithologies intermingle. However, the scatter of time delays is at least partially due to the assumptions of modelling, the effects of the zone of excavation disturbance, and possibly small inhomogeneities in the rockmass. This scatter prevents more definite conclusions.

The exact cause of the *in situ* anisotropy could not be determined because of the apparent contradiction as to whether there exist distinct differences in the two lithologies. All observations are entirely consistent with anisotropy due to EDA-cracks except that EDA-cracks are predicted to be significant fabric throughout virtually all the crust and the purely granodioritic rock appears not to have this expected fabric. The faint primary layering will be an anisotropic fabric, but it is unknown whether the strength of this fabric is significant.

9 Conclusions, Implications, and Further Research

9.1 Conclusions

I have used observations of shear-wave splitting from a controlled source shear-wave experiment to parameterize the *in situ* anisotropy of a granite rockmass, and gain insight into the cause of the anisotropy and the effects of excavation. In doing so, I have developed the necessary processing and interpretation techniques such that they may be applied to future shear-wave experiments in a mine environment. The greatest variety of raypath directions of any *in situ* experiment to date has been used for quantifying the anisotropy. I state my major conclusions:

9.1.1 The *In Situ* Anisotropy

1. The *in situ* anisotropy of the rockmass surrounding the Mine-by Tunnel is consistent with hexagonal symmetry. Described as Hudson Cracks, the fabric consists of saturated cracks of approximately 023° strike, and 35° dip. An aspect ratio of γ=0.025 best describes the observations, although the aspect ratio is not a sensitive parameter in inversion and aspect ratios between approximately γ=0.020 and γ=0.069 describe the observations almost equally well.
2. Time delays are consistent with the *in situ* rockmass being intact.
3. The *in situ* anisotropy is due to EDA-cracks, mineral alignment within the primary layering, or cracks whose orientations are governed by the mineral alignment. The orientations of these fabrics are too similar for them to be resolved separately and the lack of an explanation for the observed time delays prevents a definitive interpretation as to which of these potential fabrics is responsible. Temporal changes suggest that the *in situ* anisotropy is at least

partially due to EDA. I suggest that the anisotropy is primarily due to EDA-cracks whose orientations are influenced by the primary layering.

4. It is inconclusive whether there exist distinct differences between the *in situ* anisotropy of the granite and granodiorite. The lack of shear-wave splitting for seismic signals propagating solely through granodiorite suggests that the granodiorite is the second ever rockmass identified to have negligible *in situ* anisotropy from EDA-cracks. In contrast, the time delays for raypaths that propagated predominantly through a single lithology do not indicate any differences in the *in situ* anisotropy between the lithologies. I speculate that this may be due to EDA-cracks within the granite whose development in granodiorite is impaired by the finer grain size so that they only occur in granodiorite near where the two lithologies intermingle.

9.1.2 Excavation Effects

1. Temporal changes due to tunnel excavation and the scatter in time delays of raypaths of less than 25m length clearly demonstrates that shear waves are sensitive to excavation effects.
2. The maximum distance of observable effects from excavation is between 0.7m and 2.8m, as indicated by the onset of temporal changes. This range is consistent with a limit to the zone of excavation disturbance of about one tunnel diameter (3.5m).
3. Increases in time delays suggest that tunnel excavation creates an anisotropic fabric of the same orientation as the *in situ* fabric, indicating that the orientation of the excavation-induced fabric is governed by the *in situ* stress field or the primary layering. This result is somewhat speculative because only three raypaths show clear changes in shear-wave splitting.
4. There is no clear conclusion whether differences exist in the excavation-induced anisotropy in the granite and granodiorite. The lack of shear-wave splitting for seismic signals that propagated solely through granodiorite suggests less excavation-induced anisotropy in granodiorite. However, the time delays for raypaths with source locations predominantly within a single lithology do not indicate any differences.

9.1.3 Processing: Specific to the Shear-Wave Experiment

1. The Schmidt Hammer-nylon rod source has the benefits of known orientations and high reproducibility, with a cross-correlation coefficient of 0.90 or greater expected for repeated raypaths. However, the limited band width of 3.0kHz to 5.6kHz allows cycle skipping when cross-correlating.
2. Although cross-correlation is a practical, quantitative method to measure time delays, the effective use of cross-correlation requires: (1) rotation of the *qS1*- and *qS2*-seismograms so comparison results in a positive cross-correlation; (2) imposing a minimum time delay greater than zero; (3) rejecting measurements where one wave has a significantly smaller amplitude than the other; and (4) limiting the time delay search to a maximum of three-quarters of a shear-wave cycle.
3. The consistency of the time delays measured by cross correlation with hand-picked delays strongly suggests that both methods are indeed measuring the actual time delays between split shear waves.

9.1.4 Processing: General Importance

1. The use of multiple source orientations of a highly repeatable source with a known source radiation pattern is highly desirable for any controlled-source shear-wave experiment. The advantages over a single, non-reproducible source demonstrated in this analysis included: (1) reliable identification of polarizations and time delays; (2) distinguishing between seismic signals displaying no splitting and coincidental alignment of *qS1*- and *qS2*-wave particle motion directions with motion due to the source; (3) identification of reflected waves; (4) reliable time delay measurements using cross-correlation by selecting seismograms with the ratio of *qS1*-wave to *qS2*-wave amplitude close to unity; and (5) distinguishing between temporal change due to significant changes in the rockmass from changes due to propagation near nodal directions or diffraction around source tunnels.
2. Cross-correlation is more reliable than visual examination in searching for temporal changes for this particular dataset. I suggest the cross-correlation

will be more reliable for any dataset where the source is reproducible and the seismograms relatively uncomplicated.

3. Polarizations alone can be used to determine *in situ* fabric orientation. This result is particularly important to earthquake studies where time delays are commonly unreliable.
4. Comparison of the polarizations of model to data must be quantified because visual comparison is subjective and time consuming. Such a judgement-of-fitness algorithm should: (1) measure the number of observations that cannot be explained by a given model; (2) account for the effects of singularities; and (3) compare model polarizations to data on the same plane in which data polarizations were measured.
5. The use of progressive particle motion plots is a fast and efficient method for the visual examination of temporal changes.

9.2 Implications

9.2.1 Determining Excavation Effects

The observed temporal changes demonstrate that shear waves are sensitive to cracking induced by excavation so that shear-wave splitting can be used as method to help determine the extent of excavation disturbance and the orientation of excavation-induced cracks. Two possible applications are in minimizing excavation damage when building in nuclear waste repositories and in pillar and stope extractions in mines.

Unfortunately a more detailed evaluation of the potential of using shear waves for these purposes is not possible because the design of the Shear-Wave Experiment was not ideal for the examination of temporal changes. Specifically, not enough raypaths travelled within the rockmass of the advancing zone of excavation disturbance. This was largely due to the late conception of the Shear-Wave Experiment. Two-thirds of the Mine-by Tunnel excavation had already been completed before the commencement of the first recording sequence. The minimum separation between raypaths and the advancing tunnel would have decreased to within 2.8m for an

additional twenty raypaths if the experiment had commenced with the start of excavation.

However, this was the first experiment of its type. As such, one of the more useful aspects of the analysis is to gain insight into design improvement. It is now known that a detailed interpretation of the effects of excavation including the extent of the zone of excavation disturbance would have necessitated higher frequency seismic signals. Also a greater variety of raypath directions progressively affected by the excavation is needed to examine the asymmetries of the excavation effects. The results of a more ideal experiment could be combined with the results of other studies associated with tunnel excavation to provide a much more detailed knowledge of the effects of excavation.

9.2.2 Remote Monitoring

One purpose of this experiment was to investigate the possible use of observations of shear-wave splitting in the non-destructive remote monitoring of changes to a rockmass. This has direct applications in monitoring nuclear waste repositories. If shear-wave splitting can detect the development of cracks and the penetration of liquids into the rockmass, then it could be used to remotely monitor radioactive waste repositories where the escape of liquid carrying radioactive nuclei is to be prevented.

No significant temporal changes are observed over 117 days spanned by the recording sequences except those associated directly with an excavation sequence of the Mine-by Tunnel or relatively short raypaths that diffracted around their source tunnel. This suggests that no changes to the crack fabrics or fluid content of the rockmass significant to the maximum frequency of the seismic signals occur to the rockmass over this relatively short time interval.

However, the observed temporal changes due to the advancement of the zone of excavation disturbance suggest that longer term changes to the rockmass as subtle as small changes in the stress field may be observed. Also, changes in fluid saturation levels in the zone of excavation damage might be monitored by the comparison of *P*-wave velocities to changes in shear-wave splitting. An advantage of controlled source seismic monitoring is that path effects may be separated from source and receiver effects. The source or receiver devices may be replaced if worn out over

time, but the seismic wave propagation properties, such as the pattern of shear-wave splitting, will only indicate changes in a rockmass. Therefore, the use of controlled seismics for non-destructive remote monitoring of repositories over longer time periods is potentially extremely useful, and the possible role of shear-wave splitting observations as part of the continuous seismic monitoring has yet to be fully explored.

9.2.3 Local Monitoring

The temporal changes observed for raypaths that diffract around their source tunnel (section 5.9.2) suggest a possible method of monitoring changes to a rockmass immediately surrounding a tunnel. A controlled seismic source in the rockmass but near the free surface of a tunnel would produce seismic waves that travel around the edge of the tunnel through the most damaged part of the rockmass. A geophone within the rockmass in the radially the opposite direction from the centre of the tunnel would record the waves diffracted around the perimeter of the tunnel. The recorded wave would then have travelled through the most damaged part of the rockmass in diffracting around the perimeter of the tunnel. Changes to the rockmass near the free surface around the entire perimeter of the tunnel could then be monitored. This method would not allow detailed interpretation as to the cause of any changes, but would indicate that changes have taken place that might merit investigation.

9.3 Further Research

9.3.1 Using Induced Seismicity

The next step in this research of shear-wave behaviour within the rockmass of the 420-Level is combining the results presented in this dissertation with an analysis of shear-wave splitting in the seismic signals induced by the Mine-by Tunnel excavation. These measurements would increase the variety of raypath directions examined and allow a more detailed examination of the effects of excavation. Such a study would also allow a comparison to the effects of sources to identify any pitfalls with analyzing induced seismicity. Therefore the processing techniques and interpretation methods necessary for parameterizing anisotropy using induced seismicity would be developed.

This could be useful for any mine environment monitored by a three-component seismic network.

9.3.2 Investigating the Geological Unknowns

The analysis has revealed the many variables in this experiment that need further investigation for a fuller understanding of the *in situ* anisotropy and the effects of excavation. These include the asymmetries in excavation damage, effects of source tunnel orientation, and the precise distance from the Mine-by Tunnel of observable excavation effects.

Investigation of possible differences between the granite and granodiorite is especially important. The possible existence of distinct differences in the anisotropy of the two lithologies despite their similar mineralogies offers the opportunity to isolate and investigate properties to which anisotropy may be very sensitive. Less excavation damage within granodiorite would provide insight as to how cracks nucleate and grow due to excavation. Differences in the *in situ* anisotropy would add greater insight to the effects of grain size and shape upon anisotropy, including the dependence of EDA on grain size and shape and mineral alignment.

Also of particular importance is the need for a better understanding of anisotropy due to mineral alignment. Numerical modelling of the effects of mineral alignment should be possible using the known elastic properties of the minerals and detailed measurements of their shape, orientation, and fraction of the overall volume within the rockmass. The anisotropic effects may also be investigated using laboratory experiments where the mineral alignments in the rock samples have distinctly different orientations to any stress-relief cracking. This is needed both to determine the possible anisotropy due to mineral alignment and to more rigorously test EDA as a fabric. EDA-cracks are disturbed by excavation and therefore cannot be parameterized by direct measurements, but the anisotropy that cannot be attributed to mineral alignment may infer EDA. This modelling would be useful for any rockmass, but the development using Lac du Bonnet would be convenient because of the detailed studies of this rockmass presently taking place, its accessibility using the Underground Research Laboratory, and its homogeneity.

9.3.3 A Smaller Scale Experiment

A smaller scale shear-wave experiment is needed to produce a more detailed interpretation of the effects of excavation and investigate differences in lithology. It would be convenient to use a VSP recording geometry where triaxial accelerometers are installed down a borehole drilled perpendicularly into the rockmass from the tunnel wall. Signals would be created along the tunnel wall. This would allow the changes in the rockmass with distance from the Mine-by Tunnel wall to be examined. This experiment could be repeated both in predominantly granite and granodiorite rock to examine differences between the lithologies.

9.3.4 Alternative Rockmass

A similar shear-wave experiment is needed in a second homogeneous rockmass. The unfortunately similar orientations of the implied EDA and the mineral alignment prevented a definitive interpretation of the cause of the *in situ* anisotropy. All other studies of anisotropy in granite and granodiorite have resulted in non-unique interpretations because of similarly oriented potential fabrics. A rockmass should be sought where the potential fabrics are few and of distinctly different orientations.

9.3.5 Mine Safety

To the mining industry, potentially important applications of monitoring changes in shear-wave splitting due to changes in stress and an increase in micro-cracking are the detection of pillar deterioration and the prediction of rock bursts. Travel-time tomography has already been applied for such purposes using natural, induced, and actively produced seismicity (e.g. Young and Maxwell, 1992). The only study of using shear waves for such an application is that of Graham (1995). Shear-wave splitting was measured for similar raypaths from natural seismic events with magnitudes $M_L \geq -1.4$ as recorded by a subsurface seismic system of the President Steyn Mine, South Africa, prior to and after a magnitude $M_L=3.2$ earth tremor. No changes in splitting were found, although data was restricted by the sporadic occurrence of natural seismicity, a limit variety of raypaths, and raypath lengths greater than 115m. Monitoring using a controlled source has the advantages of high reproducibility, regular monitoring, and precisely repeated raypaths chosen to travel

only through the volume of rockmass where surveillance is desired. Investigation of the effectiveness of such monitoring can be assessed more easily than for a nuclear waste repository as the collapse of a pillar can be induced. The cost of such an investigation would be minimal if a seismic system has previously been installed for seismic monitoring.

9.3.6 An Automatic Anisotropic Estimation Technique

The success in comparing seismograms to reliably pick polarizations and time delays shows that a reliable and robust algorithm could be developed for automatic picking. The seismograms of a set would be numerically compared with the condition that the seismograms of all shear waves must all show behaviour consistent with a given polarization and time delay, or the behaviour expected for an isotropic rockmass. Such an algorithm was not developed because my initial opinion was that any automatic routine designed for this data set would be too customized for application to other data sets. However, the benefits of using multiple source orientations show that multiple source orientations should be used in any future controlled source shear-wave experiments in a mine environment. Such an algorithm may therefore be useful in the future.

References

Aki, K., & Richards, P.G., 1980, Quantitative seismology: Theory and methods, volume 1, *W. H. Freeman and Co.*, 557 p.

Aster, R.C., Shearer, P.M., & Berger, J., 1990, Quantitative measurements of shear-wave polarizations at the Anza seismic network, southern California: implications for shear-wave splitting and earthquake predictions, *J. Geophys. Res.*, **95**, 12 449-12 473.

Aster, R.C., Shearer, P.M., & Berger, J., 1991, Quantitative measurements of shear-wave polarizations at the Anza seismic network, southern California: implications for shear-wave splitting and earthquake predictions: reply, *J. Geophys. Res.*, **96**, 6415-6419.

Babuška, V., 1981, Anisotropy of Vp and Vs in rock-forming minerals, *J. Geophys.*, **50**, 1-6.

Babuška, V., & Pros, Z., 1984, Velocity anisotropy in granodiorite and quartzite due to the distribution of microcracks, *Geophys. J. R. Astr. Soc.*, **76**, 121-127.

Baptie, B., Crampin, S., & Liu, E., 1993, Displaying shear-wave splitting in cross-hole surveys for materials with combinations of EDA and PTL anisotropies, *Can. J. Expl. Geophys.*, **29**, No. 1, 227-235.

Bell, J.S., & Gough, D.I., 1979, Northeast-southwest compressive stress in Alberta: evidence from oil wells, *Earth and Sci. Lett.*, 45, 475-482.

Birch, F., 1961, The velocity of compressional waves in rocks to 10 Kilobars, part 2, *J. Geophys. Res.*, **66**, No. 7, 2199-2224.

Blenkinsop, T.G., 1990, Correlation of paleotectonic fracture and microfracture orientations in cores with seismic anisotropy at Cajon Pass Drill Hole, Southern California, *J. Geophys. Res.*, **95**, No. B7, 11 143- 11 150.

Bonner, B.P., 1974, Shear wave birefringence in dilation granite, *Geophys. Res. Lett.*, **1**, 217-220.

Booth, D.C., Abaseev, S.A., Evans, R., Crampin, S., & Chesnokov, E., 1993, Observations of shear-wave splitting near Ashkhabad, Turkmenia, *Can. J. Expl. Geophys.*, **29**, 363-370.

Booth, D.C., & Crampin, S., 1985, Shear-wave polarizations on a curved wavefront at an isotropic free-surface, *Geophys. J. R. Astr. Soc.*, **83**, 31-45.

Booth, D.C., Wyss, M., & Gillard, D., 1992, Shear-wave polarization alignments recorded above the Kaoiki fault zone, Hawaii, *Geophys. Res. Lett.*, **19**, 1141-1144.

Brocher, T.M., & Christensen, N.I., 1990, Seismic anisotropy due to preferred mineral orientation observed in shallow crustal rocks in southern Alaska, *Geology*, **18**, 737-740.

Bush, I., & Crampin, S., 1991, Paris Basin VSPs: case history establishing combinations of fine-layer (or lithologic) anisotropy and crack anisotropy from modelling shear wavefields near point singularities, *Geophys. J. Int.*, **107**, 433-447.

Carlson, S.R., & Young, R.P., 1993, Acoustic emission and ultrasonic velocity study of excavation-induced microcrack damage at the Underground Research Laboratory, *Int. J. Rock Mech. Min. Sci. & Geomech. Abstr.*, **30**, 901-907.

Chen, T.-C., Booth, D.C., & Crampin, S., 1987, Shear-wave polarizations near the North Anatolian Fault - III. Observations of temporal changes., *Geophys. J. R. Astr. Soc.*, **91**, 287-311.

Chernis, P.J., & Robertson, R.B., 1987, Natural and stress-relief microcracks in the Lac du Bonnet granite, in Katsube, T.J., & Hume, J.P., Eds., Geotechnical studies at Whiteshell Research Area, *Canada Centre for Min. Eng. Tech. Min. Res. Lab. Div.*, Report MRL 87-52 (Int).

Christensen, N.I., 1965, Compressional wave velocities in metamorphic rocks at pressures to 10 kilobars, *J. Geophys. Res.*, **70**, No. 24, 6147-6164.

Collins, D.S., Baker, C., & Young, R.P., 1994, Source parameters of the excavation-induced seismicity from the Mine-by Tunnel, *Report #RP028AECL to Atomic Energy of Canada, Ltd.*

Collins, D.S., & Young, R.P., 1993, AE/MS source location calibration and velocity results: Two surveys performed after the mine-by tunnel excavation, *Report #RP016AECL to Atomic Energy of Canada, Ltd.*

Collins, D.S., & Young, R.P., 1994, Comparison of excavation-induced microseismicity from the granite and granodiorite sections of the Mine-by Tunnel, *Report #RP026AECL to Atomic Energy of Canada, Ltd.*

Crampin, S., 1978, Seismic wave propagation through a cracked solid: polarization as a possible dilatancy diagnostic, *Geophys. J. Int.*, **107**, 417-427.

Crampin, S., 1981a, A review of wave motion in anisotropic and cracked elastic-media, *Wave Motion*, **3**, 343-391.

Crampin, S., 1981b, Shear-wave singularities of wave propagation anisotropic media, *J. Geophys.*, **49**, 43-63.

Crampin, S., 1984, An introduction to wave propagation in anisotropic media, *Geophys. J. R. Astr. Soc.*, **76**, 17-28.

Crampin, S., 1985, Evidence for aligned cracks in the Earth's crust, *First Break*, **3**, 12-15.

Crampin, S., 1987, The basis for earthquake prediction, *Geophys. J. R. Astr. Soc.*, **91**, 331-347.

Crampin, S., 1989, Suggestions for a consistent terminology for seismic anisotropy, *Geophys. Prosp.*, **37**, 753-770.

Crampin, S., 1990, Alignment of near-surface inclusions and appropriate crack geometries for geothermal hot-dry-rock experiment, *Geophys. Pros.*, **38**, 621-631.

Crampin, S., 1991a, Extensive-dilatancy anisotropy: wave propagation through fluid-filled inclusions of various shapes, *Geophys. J. Int.*, **104**, 611-623.

Crampin, S., 1991b, Effects of point singularities on shear-wave propagation in sedimentary basins, *Geophys. J. Int.*, **107**, 531-543.

Crampin, S. 1993a, Arguments for EDA, *Can. J. Expl. Geophys.*, **29**, 18-30.

Crampin, S., 1993b, A review of the effects of crack geometry on wave propagation through aligned cracks, *Can. J. Expl. Geophys.*, **29**, 03-17.

Crampin, S., 1994, The fracture criticality of crustal rocks, *Geophys. J. Int.*, **118**, 428-438.

Crampin, S., & Booth, D.C., 1985, Shear-wave polarizations near the North Anatolian Fault - II. Interpretation in terms of crack-induced anisotropy, *Geophys. J. R. Astr. Soc.*, **83**, 75-92.

Crampin, S., & Booth, D.C., 1989, Shear-wave splitting showing hydraulic dilation of pre-existing joints in granite, *Sci. Drilling*, **1**, 21-26.

Crampin, S., Booth, D.C., Evans, R., Peacock, S., & Fletcher, J.B., 1990, Changes in shear-wave splitting at Anza near the time of the North Palm Springs Earthquake, *J. Geophys. Res.*, **95**, 11 197-11 212.

Crampin, S., Booth, D.C., Evans, R., Peacock, S., & Fletcher, J.B., 1991, Comment on "Quantitative measurements of shear-wave polarizations at the Anza seismic networks, southern California: implications for shear-wave splitting and earthquake prediction", by Richard C. Aster, Peter M. Shearer and Jon Berger, *J. Geophys. Res.*, **96**, 6403-6414.

Crampin, S., Evans, R., & Atkinson, B.K., 1984a, Earthquake prediction; a new physical basis, *Geophys. J. R. Astr. Soc.*, **76**, 147-156.

Crampin, S., Hipkin, R.G., & Chesnokov, E.M., 1984b, Seismic anisotropy - the state of the Art II, *Geophys. J. R. Astr. Soc.*, **76**, 1-16.

Crampin, S., Evans, R., & Üçer, S.B., 1985, Analysis of records of local earthquakes: the Turkish Dilatancy Projects (TDP1 and TDP2), *Geophys. J. R. Astr. Soc.*, **83**, 1-16.

Crampin, S., & Kirkwood, S.C., 1981, Velocity variations in systems of anisotropic symmetry, *J. Geophys.*, **49**, 35-42.

Crampin, S., & Yedlin, M., 1981, Shear-wave singularities of wave propagation in anisotropic media, *J Geophys.*, **49**, 43-46.

Daley, T.M., McEvilly, T.V., & Majer, E.L., 1988, Multiple polarized shear wave VSP's from the Cajon Pass drill hole, *Geophys. Res. Lett.*, **15**, 1001-1004.

Douma, J., 1988, The effect of the aspect ratio on crack-induced anisotropy, *Geophys. Prosp.*, **36**, 614-632.

Feustel, A.J., & Young, R.P., 1992, Calibration of the Queen's Microseismic System at the Underground Research Laboratory, *Report #RP010AECL to Atomic Energy of Canada, Ltd.*

Feignier, B., & Young, R.P., 1992, Moment Tensor inversion of induced microseismic events: evidence of non-shear failures in the -4<M<-2 moment magnitude range: *Geophys. Res. Lett.*, **19**, 1503-1506.

Gajewski, D., 1993, Radiation from point sources in general anisotropic media, *Geophys. J. Int.*, **113**, 299-317.

Gledhill, K.R., 1993a, Shear waves recorded on close-spaced seismograms I: Shear-wave splitting results, *Can. J. Expl. Geophys.*, **29**, 285-298.

Gledhill, K.R., 1993b, Shear waves recorded on close-spaced seismograms II: The complex anisotropic structure of the Wellington Peninsula, New Zealand, *Can. J. Expl. Geophys.*, **29**, 299-314.

Graham, G., 1995, An estimation of anisotropy in the crust from three different time and distance scales, *Ph.D. dissertation*, University of Edinburgh, 280 p.

Graham, G., & Crampin, S., 1993, Shear-wave splitting from regional earthquakes in Turkey, *Can. J. Expl. Geophys.*, **29**, 371-379.

Graham, G., Crampin, S., & Fernandez, L.M., 1991, Observations of shear-wave polarizations from rockbursts in a South African gold field: an analysis of acceleration and velocity recordings, *Geophys. J. Int.*, **107**, 661-672.

Herget, G., 1987, Stresses in rock: Balkema, Rotterdam, 179p.

Holmes, G.M., Crampin, S., & Young, R.P., 1993, Preliminary analysis of shear-wave splitting in granite at the Underground Research Laboratory, Manitoba, *Can. J. Expl. Geophys.*, **29**, 140-152.

Horne, S., & MacBeth, C., 1994, Inversion for seismic anisotropy using genetic algorithms, *Geophys. Pros.*, **42**, 953-974.

Hudson, J.A., 1980, Overall properties of a cracked solid, *Math. Proc. Cambridge Phil. Soc.*, **88**, 371-384.

Hudson, J.A., 1981, Wave speeds and attenuation of elastic waves in material containing cracks, *Geophys. J. R. Astr. Soc.*, **64**, 133-150.

Hudson, J.A., 1986, A higher order approximation to the wave propagation constants for a cracked solid, *Geophys. J. R. Astr. Soc.*, **87**, 265-274.

Hudson, J.A., 1988, Seismic wave propagation through material containing partially saturated cracks, *Geophys. J.*, **92**, 33-37.

IMSL, 1987, The IMSL math/library, *IMSL Ltd.*

Kaneshima, S., 1990, Origin of crustal anisotropy: Shear wave splitting studies in Japan, *J. Geophys. Res.*, **95**, 11 121- 11 133.

Kaneshima, S., & Ando, M., 1989, An analysis of split shear waves observed above crustal and uppermost mantle earthquakes beneath Shikoku Japan: Implications in effective depth extent of seismic anisotropy, *J. Geophys. Res.*, **94**, 14 077-14 092.

Kaneshima, S., Ito, H., & Sugihara, M., 1988, Shear-wave splitting observed above small earthquakes in a geothermal area of Japan, *Geophys. J.*, **94**, 399-411.

Kaneshima, S., Maeda, N., & Ando, M., 1990, Evidence for the splitting of shear waves from waveform and focal mechanism analyses, *Phys. Earth. and Planet. Inter.*, **61**, 238-252.

Kern, H., 1978, The effect of high temperature and high confining pressure on compressional wave velocities in quartz-bearing and quartz-free igneous and metamorphic rocks, *Tectonophysics*, **44**, 185-203.

Leary, P., 1991, Deep borehole log evidence for fractal distribution of fractures in crystalline rock, *Geophys. J. Int.*, **107**, 615-927.

Li, X.-Y., & Crampin, S., 1992, Linear-transform techniques for processing shear-wave anisotropy in four-component seismic data, *Geophys.*, **58**, 240-256.

Li, Y.-G., Leary, P.C., & Henyey, T.L., 1988., Stress orientation inferred from shear wave splitting in basement rock at Cajon Pass, *Geophys. Res. Lett.*, **15**, 997-1000.

Liner, C.L., 1992, Seismos, *Leading Edge*, **11** (8), 43.

Liu, Y, 1995, Shear-wave anisotropy and the interpretation of temporal change in time delays, *Ph.D. dissertation*, University of Edinburgh, 111 p.

Liu, Y., Booth, D.C., Crampin, S., Evans, R., & Leary, P., 1993a, Shear-wave polarizations and possible temporal variations in shear-wave splitting at Parkfield, *Can. J. Expl. Geophys.*, **29**, 380-390.

Liu, E., & Crampin, S., 1990, Effects of the internal shear-wave window: comparison with anisotropy induced splitting, *J. Geophys. Res.*, **95**, 11 275-11 281.

Liu, E., Crampin, S., & Booth, D.C., 1989, Shear-wave splitting in cross-hole surveys: Modelling, *Geophys.*, **54**, 57-65.

Liu, E., Crampin, S., & Queen, J.H., 1991, Fracture detection using crosshole surveys and reverse profiles at the Conoco Borehole Test Facility, Oklahoma, *Geophys. J. Int.*, **107**, 449-464.

Liu, E., Crampin, S., Queen, J.H., & Rizer, W.D., 1993b, Behaviour of shear waves in rocks with two sets of parallel cracks, *Geophys. J. Int.*, **113**, 509-517.

Liu, E., Crampin, S., & Roth, B., 1992, Modelling channel waves with synthetic seismograms in an anisotropic in-seam seismic survey: *Geophys. Prosp.*, **40**, 513-540.

Lockner, D.A., Walsh, J.B., & Byerley, J.D., 1977, Changes in seismic velocity and attenuation during deformation of granite, *J. Geophys. Res.*, **82**, 5374-5378.

MacBeth, C., 1991, Inverting shear-wave polarizations for anisotropy using three-component offset VSPs: synthetic seismograms, *Geophys. J. Int.*, **107**, 571-583.

MacBeth, C., & Crampin, S., 1991, Comparison of signal processing techniques for estimating the effects of anisotropy, *Geophys. Pros.*, **39**, 667-689.

Martin, C.D., 1990, Characterizing in situ stress domains at AECL's Underground Research Laboratory, *Can. Geotech. J.*, **29**, 631-646.

Martin, C.D., Read., R.S., & Dzik, E.J., 1995, Near-face cracking and strength around underground openings, Mechanics of Jointed and Faulted Rock, *Balkema*, 765-776.

Martin, C.D., & Young, R.P., 1993, The effect of excavation-induced seismicity on the strength of Lac du Bonnet granite, *Rockbursts and Seismicity in Mines (Ed. R.P. Young)*, Balkema, Rotterdam, 367-371.

Maxwell, S., & Young, R.P., 1994, Wave propagation effects of an underground opening, *Report #RP025AECL to Atomic Energy of Canada, Ltd.*

McGonigle, R., & Crampin, S., 1982, A fortran program to evaluate the phase- and group-velocity surface in an anisotropic solid, *Computers & Geosci.*, **8**, 221-226.

Moos, D., & Zoback, M.D., 1983, In situ studies of velocity in fractured crystalline rocks, *J. Geophys. Res.*, **88**, 2345- 2358.

Mueller, M.C., 1992, Using shear waves to predict lateral variability in vertical fracture intensity, *Leading Edge*, **11**, 29-35.

Musgrave, M.J.P., 1970, Crystal Acoustics, *Holden-Day, Inc.*, 287p.

Numerical Algorithms Group, 1991, The NAG Fortran library, *NAG.*

Nur, A., & Simmons, G., 1969, Stress-induced velocity anisotropy in rock: An experimental study, *J. Geophys. Res.*, **74**, 6667-6674.

Peacock, S., Crampin, S., Booth, D.C., & Fletcher, J.B., 1988, Shear-wave splitting in the Anza seismic gap, southern California: temporal variations as possible precursors, *J. Geophys. Res.*, **93**, 3339-3356.

Peacock, S., McCann, C., Sothcott, J., & Astin, T.R., 1994, Seismic velocities in fractured rocks: an experimental verification of Hudson's theory, *Geophys. Prosp.*, **42**, 27-80.

Postma, G.W., 1955, Wave propagation in a stratified medium, *Geophys.*, **49**, 1637-1648.

Press, W.H., Teukolsky, S.A., Vetterling, W.I., & Flannery, B.P., 1992, Numerical recipes, *Cambridge U. Press*, 994p.

Read, R.S., & Martin, C.D., 1991, Mine-by experiment final design report, Report AECL-10430 to Atomic Energy of Canada, Ltd.

Read, R.S., Martino, J.B., & Mitchell, J.H., 1992, Mine-by experiment technical progress report 7, *Report URL-EXP-022-M056, Atomic Energy of Canada Ltd.*

Roberts, G., & Crampin, S., 1986, Shear-wave polarizations in a hot dry rock geothermal reservoir: Anisotropic effects of fractures, *Int. J. Rock Mech. Min. Sci. & Geomech. Abstr.*, **23**, 291-302.

Robertson, R.B., & Chernis, P.J., 1987, General geology of the Lac du Bonnet batholith and petrography of core samples from the WNRE research area, T.J., & Hume, J.P., Eds., Geotechnical studies at Whiteshell Research Area, *Canada Centre for Min. Eng. Tech. Min. Res. Lab. Div.*, Report MRL 87-52 (Int).

Rowlands, H.J., Booth, D.C., & Chiu, J.-M., 1993, Shear-wave splitting from microearthquakes in the New Madrid seismic zone, *Can. J. Expl. Geophys.*, **29**, 352-362.

Sammonds, P.R., Meredith, P.G., & Main, I.G., 1992, Role of pore fluids in the generation of seismic precursors to shear fracture, *Nature*, **359**, 228-230.

Savage, M.K., Peppin, W.A., & Vetter, U.R., 1990, Shear wave anisotropy and stress direction in and near Long Valley Caldera, California, 1979-1988, *J. Geophys. Res.*, **95**, 11 165-11 177.

Scholz, C.H., & Koczynski, T.A., 1979, Dilatancy anisotropy and the response of rock to large cyclic loads, *J. Geophys., Res.*, **84**, 5525-5534.

Siegesmund, S., & Kruhl, J.H., 1991, The effect of plagioclase textures on velocity anisotropy and shear wave splitting at deeper crustal levels, *Tectonophysics*, **191**, 147-154.

Slater, C., Crampin, S., Brodov, L.Y., & Kuznetsov, V.M., 1993, Observations of anisotropic cusps in transversely isotropic clay, *Can. J. Expl. Geophys.*, **29**, 216-226.

Soga, N., Mizutani, H., Spetzler, H., & Martin III, R.J., 1978, The effect of dilatancy on velocity anisotropy in Westerly Granite, *J. Geophys. Res.*, **83**, 4451-4458.

Spencer Jr., J.W., & Nur, A.M., 1976, The effects of pressure, temperature, and pore water on velocities in Westerly Granite, *J. Geophys. Res.*, **81**, 899-904.

Sprunt, E.S., & Brace, W.F., 1974, Direct observation of microcavities in crystalline rocks: *Internat. J. Rock Mech. Min. Sci. & Geomech.*, **27**, 139-150 (Abstr.).

Stuart, W.D., 1979, Strain softening prior to two-dimensional strike slip earthquakes, *J. Geophys. Res.*, **84**, 1063-1070.

Talebi, S., & Young, R.P., 1989, In-situ measurements of P and S wave velocities at the Underground Research Laboratory, *Report #RP004AECL to Atomic Energy of Canada, Ltd.*

Tilmann, S.E., & Bennett, H.F., 1973, Ultrasonic shear wave birefringence as a test of homogeneous elastic anisotropy, *J. Geophys. Res.*, **78**, 7623-7629.

Thill, R.E., & Bur, T.R., 1969, Correlation of longitudinal velocity variation with rock fabric, *J. Geophys. Res.*, **74**, 4897-4909.

Thill, R.E., Bur, T.R., & Steckley, R.C., 1973, Velocity anisotropy in dry and saturated rock sphere and its relation to rock fabric, *Int. J. Rock. Mech. Min. Sci. & Geomech. Abstr.*, **10**, 535-557.

Thomsen, L, 1988, Weak elastic anisotropy, *Geophys.*, **51**, 1954-1966.

Touloukian, Y.S., & Ho, C.Y., 1981, Physical properties of rocks and minerals, *McGraw-Hill/CINDAS*, 548 p.

Wang, C., Goodman, R.E., & Sundaram, P.N., 1975, Variations of Vp and Vs in granite premonitory to shear rupture and stick-slip sliding: application to earthquake prediction, *Geophys. Res. Lett.*, **2**, 309-311.

Wang, C., & Sun, Y., 1990, Oriented microfractures in Cajon Pass Drill Cores: Stress field near the San Andreas Fault, *J. Geophys. Res.*, **95**, 11 135- 11 142.

Wild, P., & Crampin, S., 1991, The range of effects of azimuthal isotropy and EDA anisotropy in cracked solids, *Geophys. J. Int.*, **107**, 513-530.

Winterstein, D.F., 1990, Velocity anisotropy terminology for geophysicists, *Geophysics.*, **55**, 1070-1088.

Xiong, Y., Yao, C., & Wang, P., 1993, The features of shear-wave splitting in Lulong, Northern China, and its seismic implications, *Can. J. Expl. Geophys.*, **29**, 332-340.

Yao, C., Wang, P., Lu, Y., & Chen, Y., 1993, Interpretations of shear-wave splitting in Datong area, northern China, *Can. J. Expl. Geophys.*, **29**, 341-351.

Yao, C., & Xiong, Y., 1993, Far-field radiation pattern from an anisotropic dislocation point source, *Can. J. Expl. Geophys.*, **29**, 315-323.

Yardley, G.S., & Crampin, S., 1993, Shear-wave anisotropy in the Austin Chalk, Texas, from multioffset VSP data: Case studies, *Can. J. Expl. Geophys.*, **29**, 163-176.

Young, R.P., & Collins, D.S., 1993, The spatial and temporal distribution of AE/MS source locations following the Mine-by Tunnel excavation of Round 17, *Report #RP17AECL to Atomic Energy of Canada Ltd.*

Young, R.P., & Maxwell, C., 1992, Seismic characterization of a highly stressed rock mass using tomographic imaging and induced seismicity, *J. Geophys. Res.*, **97**, 12 361-12 373.

Zatsepin, S.V., & Crampin, S., 1995, Modelling the compliance of crustal rock: I - response of shear-wave splitting to differential stress, *Geophys. J. Int.*, in preparation.

Zeng, X., 1994, Shear-wave VSP data processing for anisotropy, *Ph.D. dissertation*, University of Edinburgh.

Zeng, X., & MacBeth, C., 1993, Algebraic processing techniques for estimating shear-wave splitting in near-offset VSP data: theory, *Geophys. Pros.*, **41**, 1033-1066.

CSEG

Canadian Society of Exploration Geophysicists

March 10, 1995

Mr. Gordon Holmes
Seismology
BGS Murchison House
West Mains Road
Edinburgh, EH9 3LA
United Kingdom

Dear Mr. Holmes:

Re: Reguest to include photocopy of the following paper for your PhD Thesis

> Holmes, G.M., Crampin, S., & Young, R.P. 1993, Preliminary analysis of the shear-wave splitting in granite at the Underground Research Laboratory, Manitoba, *Can. J. Expl. Geophys.*, **29**, 140-152

The CSEG is delighted to grant you permission to include a photocopy of your paper in your PhD Thesis.

If we can be of any further assistance, please do not hesitate to contact us.

Yours truly,

Heather Payne
CSEG Office Manager

CANADIAN JOURNAL OF EXPLORATION GEOPHYSICS
VOL. 29, NO. 1 (JUNE 1993), P. 140-152

PRELIMINARY ANALYSIS OF SHEAR-WAVE SPLITTING IN GRANITE AT THE UNDERGROUND RESEARCH LABORATORY, MANITOBA

GORDON M. HOLMES[1], STUART CRAMPIN[1] AND R. PAUL YOUNG[2]

ABSTRACT

The excavation of a test tunnel at a depth of 420 m in the Mine-by Experiment at the Atomic Energy of Canada Limited's Underground Research Laboratory, Manitoba, Canada, has allowed shear-wave propagation to be examined in accurately controlled conditions in in-situ granite. This is a preliminary report of shear-wave splitting in 4.2 kHz signals from controlled shear-wave sources at distances between 7.5 m and 63 m over a wide range of azimuths and angles of incidence. Preliminary analysis indicates that about 78% of the data show the three-dimensional pattern of behaviour expected from propagation through uniform distributions of EDA cracks [(E)xtensive-(D)ilatancy-(A)nisotropy crack: stress-aligned, fluid-filled microcracks] aligned relative to the measured stress field. Some 17% of the data with raypaths near the tunnel have anomalous behaviour which is attributed to the effects of excavation damage around the tunnel opening. This damage appears to be more extensive around the advancing face of the tunnel than around the length of the tunnel. The remaining 5% of data have anomalous behaviour which has not yet been interpreted. EDA cracks are the most compliant elements of the rock mass, and the sensitivity of shear waves to this internal crack geometry demonstrated by this experiment shows that controlled-source shear-wave experiments may be used for monitoring cracking, including induced cracking, and excavation damage in radioactive waste repositories, mines, geothermal reservoirs and other subsurface operations.

INTRODUCTION

Shear-wave splitting, diagnostic of some form of seismic anisotropy, has been observed on almost all occasions that three-component records are available of impulsive, good signal-to-noise ratio, shear waves propagating in the Earth's upper crust (Crampin and Lovell, 1991). The azimuthal variation has been claimed to be caused by extensive-dilatancy anisotropy (EDA): distributions of stress-aligned fluid-filled cracks, microcracks and preferentially oriented pore space (Crampin and Lovell, 1991; Crampin, 1993a). Direct examination of EDA cracks is difficult, as such fluid-filled inclusions are the most compliant elements of the rock mass and in-situ configurations are disturbed when the rock is disturbed by drilling or excavation.

In the past, observations of in-situ shear-wave splitting have usually been limited to nearly vertical raypaths in surface recordings above local earthquakes and seismic reflection surveys and in subsurface recordings of vertical seismic profiles (VSPs). Recently, shear-wave splitting has also been studied using data from crosshole surveys (Liu et al., 1991, 1992) which offer records of more nearly horizontal raypaths but with severely limited ranges of azimuths. Thus, all previous recorded data sets showing shear-wave splitting have suffered from limitations in the directions sampled and, in the case of earthquake data, very complicated geology. As a result, the scope for geological interpretation has been limited and the behaviour of EDA cracks under external conditions is largely speculative.

This paper presents a preliminary analysis of the first recording sequence of a controlled-source shear-wave experiment as part of the Mine-by Experiment in the Lac du Bonnet granite batholith. The experimental work was performed by the Queen's University Engineering Seismology Laboratory, Kingston, Ontario, at the Underground Research Laboratory (URL), Pinawa, Manitoba, of the Atomic Energy of Canada Ltd. The Mine-by tunnel was excavated in a rock mass specifically chosen for its homogeneity, uniformity and absence of fractures. As the excavation of the tunnel proceeded, the rock mass was monitored with arrays of geophysical and geotechnical instruments, including a 16-triaxial sensor array of accelerometers. The locations of source and accelerometers were chosen to provide a comprehensive range of raypath azimuths and dips. The terminology for anisotropy is that suggested by Crampin (1989).

[1]Department of Geology and Geophysics, University of Edinburgh, Grant Institute, West Mains Road, Edinburgh EH9 3JW; also, British Geological Survey, Murchison House, West Mains Road, Edinburgh EH9 3LA

[2]Engineering Seismology Laboratory, Department of Geology and Geophysics, Queen's University, Kingston, Ontario K7L 3N6

We thank Dave Collins and Andrew Feustal for their continual assistance in these experiments. We also thank Derek Martin, Rod Read and other staff at URL for their continual support, Enru Liu for his plotting program, Brian Baptie for his assistance in modifying the program and great assistance in modelling the data and Richard Everitt for his explanation of the geology at URL. The data was collected as part of a project supported by the Canadian Nuclear Fuel Waste Management Program with joint funding by Atomic Energy of Canada Research and Ontario Hydro under the auspices of the CANDU owners group. This seismic anisotropy research was funded by the Natural Environment Research Council (UK), the Natural Sciences and Engineering Research Council (Canada), Atomic Energy of Canada Ltd. and the Association of Commonwealth Universities (UK). It is published with the approval of the Director of the British Geological Survey (NERC).

Natural microcracks

The in-situ Lac du Bonnet granite of the 420 level at URL exists in a far-field stress field that has a maximum horizontal compressive stress of 55 MPa (Read and Martin, 1991). Extensive changes to the crack structure of the granite result when the magnitude of the stress field encompassing the granite is significantly released. Such stress relief occurs by excavation or drilling when there is a zero-stress free surface, or by complete removal of in-situ stress in laboratory samples. Changes to structure include opening new microcracks (stress-relief microcracks) to form an additional crack fabric. In granite from the 420 level, the stress relief is large enough to break quartz grains (D. Martin, pers. comm.), and the effects of stress relief alter the pattern of grain boundary cracks and transgranular cracks (cracks that cross grain boundaries) so that the in-situ pattern of grain boundary cracks is not easily determined. Detailed reports on natural microcracks are being prepared but are not yet available.

Chernis and Robertson (1987) in a laboratory study of microcracks in the Lac du Bonnet granite, found they could discriminate between natural and stress-relief microcracks. The natural microcracks not affected by stress relief were less than 4 μm in aperture with rough and irregular walls and often contain debris. Chernis and Robertson conclude that high pressure alone would not be sufficient to close the natural microcracks. Chernis and Robertson did not report dimensions of the faces of the cracks, but the largest dimensions of in-situ microcracks are expected to be no more than a centimetre in diameter and possibly much smaller.

They also reported that most grain boundary cracks form around quartz grains, and may have infillings of calcite, iron oxide or clay. Ninety percent of natural cracks occur along grain boundaries. The remaining cracks that could be distinguished from stress-relief cracks occur as intragranular cracks, chiefly in feldspars. Plagioclase typically contains large numbers of pores less than 5 μm in diameter (Sprunt and Brace, 1974), which may or may not be intersected by fine intragranular cracks. Intragranular cracks within microcline may be over 1 μm in diameter.

Experiment

In media with effective seismic anisotropy there are three body waves in every direction of propagation: a quasi-*P*-wave, *qP*, with approximately radial motion, and two quasi-shear waves, the faster *qS*1 followed, after a time delay, by *qS*2. The polarizations of the three waves propagating in the same direction from a point source are approximately orthogonal [note that exact orthogonality is not expected in wave propagation from point sources in anisotropic solids (Crampin, 1981, 1989)]. The polarizations and time delays between the split shear waves can be estimated from polarization diagrams (hodograms) of the three-component particle motion. The orientation and many details of the crack parameters can be estimated from the three-dimensional patterns of polarizations and time delays if the observations cover a sufficient range of raypath azimuths and angles of incidence. The shear-wave experiment was designed to estimate these patterns of polarizations and time delays around the Mine-by tunnel by recording controlled shear-wave sources at the array of accelerometers.

Four exactly repeatable shear-wave signals were excited at each of 13 locations on the walls of the outer tunnels after most excavation sequences and recorded by the 16 accelerometers (Figure 1a). These shear-wave experiments began when the tunnel had been excavated to 27 m of the final 46 m-length, and ten recording sequences took place before the tunnel was completed (not every excavation sequence was monitored). Six additional sequences were recorded at intervals after completion in order to examine the possible longer-term effects of excavation damage on the rock mass.

The shear-wave experiment uses shear waves produced with a controlled and reproducible source at accurately known locations. Since there are believed to be no significant internal interfaces within the rock mass (with the exception of the excavation damage), the shear waves are unlikely to be disturbed by interference with internal discontinuities (Liu and Crampin, 1990) and approximately straight raypaths can be assumed. However, all recorded raypaths will have passed through the damage surrounding the tunnels in which the sources were located and the possible excavation (drilling) damage surrounding the boreholes housing the accelerometers. Disturbances to shear-wave propagation near the source are likely to have less severe effects on the waveforms of the shear waves than disturbances along the raypath or near the recorders (Yardley and Crampin, 1991). Since the diameters of the boreholes (3.2 cm) are much less than the wavelengths of the *P*- and shear waves, about 140 cm and 80 cm, respectively, the effect of the damage around the boreholes is expected to be negligible. However, the effects of such damage around the boreholes and the source tunnels will be assessed in future studies. With the possible exception of the minor effects of disturbances near source and accelerometers, the disturbance to the shear-wave propagation is expected to be due to the excavation damage around the Mine-by tunnel.

The shear-wave source

Four 40 cm-long 3.2 cm-diameter boreholes were drilled at 45° to the surface at the corners of a 29.5 cm x 29.5 cm template (Figure 1b) on the walls of the tunnels at each location. A rod was inserted in turn into each borehole and the free end pulsed with a Schmidt Hammer (Model N, total impact energy 2.207 Nm). Both steel and nylon rods were tested in the first recording sequence of the shear-wave experiment. The steel rod gave larger amplitude but emergent signals for both *P*- and shear waves and the recorded signals displayed ringing after the *P*-wave that often interfered with the shear-wave arrivals. The nylon rod produced signals with about half the amplitude of those produced by the steel rod, but the signals were impulsive, had similar

signal-to-noise ratios and had much less ringing. Consequently, nylon rods were used for all further recording sequences. The dominant frequency of both the *P*- and shear waves recorded from this source, measured over 7.5 m to 63 m raypaths, was about 4.2 kHz with corresponding wavelengths of 1.38 m ± 0.05 m for *P*-waves and 0.81 m ± 0.03 m for shear waves.

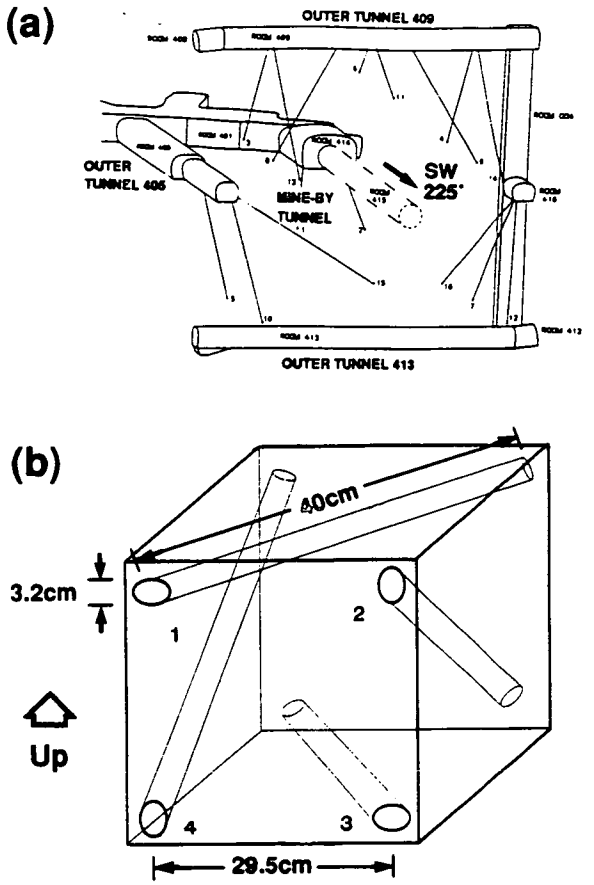

Fig. 1. **(a)** The Mine-by tunnel (Room 415) at the 420-m level at the AECL Underground Research Laboratory (after Read and Martin, 1991). Triaxial accelerometers are located at the ends of the boreholes from the outer tunnels as indicated. **(b)** Schematic illustration of the four boreholes from the templates at each of 13 source locations in the walls of the outer tunnels.

Analysis of Shear Waves

The source and receiver positions are known to better than 10-cm accuracy, and each three-component signal was rotated into the dynamic axes assuming a straight raypath: the radial component (R) showing *P*-wave polarization and the transverse-sagittal (TS) and transverse-horizontal (TH) components showing the nearly transverse polarizations of shear waves. The approximation of straight raypaths appears valid since the *P*-wave and shear-wave waveforms are largely separated by these rotations, as is shown in Figures 2 and 3. The seismograms and polarization diagrams (PDs) display shear-wave splitting typical of propagation through anisotropic or cracked solids (Crampin, 1981, 1993b). Figure 2 shows typical examples of waveforms and PDs. Polarization angles and time delays between the split shear waves were measured from PDs in the TS-TH plane normal to the radial direction. Polarizations were measured from the takeoff direction of the initial shear-wave signal and displayed in Plate Carée cylindrical equal-area projections.

Since the four source positions at each source location site are within 40 cm of each other, the four raypaths to a given accelerometer will be very close to each other and the effects of anisotropy along undisturbed raypaths are expected to be similar. This appears to be justified, as can be seen in Figure 2 which shows a typical set of four shear-wave source orientations recorded by an accelerometer. The signals show the same polarization directions for both split shear waves (although with some polarity reversals because of the different source orientations) and the same delays between the split shear waves. We attribute this compatibility between the parameters of the split shear waves as indicating raypaths through undisturbed rock. The variation of source radiation pattern means that, whatever the direction of propagation, the four sources generate both pairs of split shear waves along at least two of the raypaths. This similarity in parameters along nearly identical raypaths allows the shear-wave arrivals to be identified with great confidence and the degree of similarity provides a sensitive measure of excavation disturbance along the raypath.

With four different source orientations, the polarization of the radiated shear wave is frequently parallel to one of the anisotropic shear-wave polarizations for a particular raypath so that the other split shear waves are not excited, and polarizations may be missing, even when the polarizations and time delays are otherwise compatible. Figure 3 shows such an example. The four records show: (a) a dominant $qS1$-wave with a very low-amplitude $qS2$-wave component; (b) and (c) both split shear-waves polarizations; and (d) a small amplitude $qS1$-wave, so that the motion is principally in the $qS2$-wave direction. Note that although some polarizations are absent, those present show compatible behaviour, which we attribute to an undisturbed raypath.

Records with such missing polarizations would have been difficult to identify correctly without comparison with such multiple-source orientations along similar raypaths. Recognition of these missing events is important. Misidentifications would have led to anomalous delay times. In the case of $qS1$ not being excited, as in Figure 3d, an anomalous polarization possibly almost perpendicular to the correct $qS1$ polarization would have been identified. Anomalies could be caused by excavation damage near the source or the receiver, or by propagation near the directions of shear-wave point singularities where anomalous behaviour is expected for, possibly small, changes in raypath direction (Crampin, 1991; Wild and Crampin, 1991), although there are no point singularities to be expected in wholly hexagonal anisotropic symmetry (Crampin, 1989).

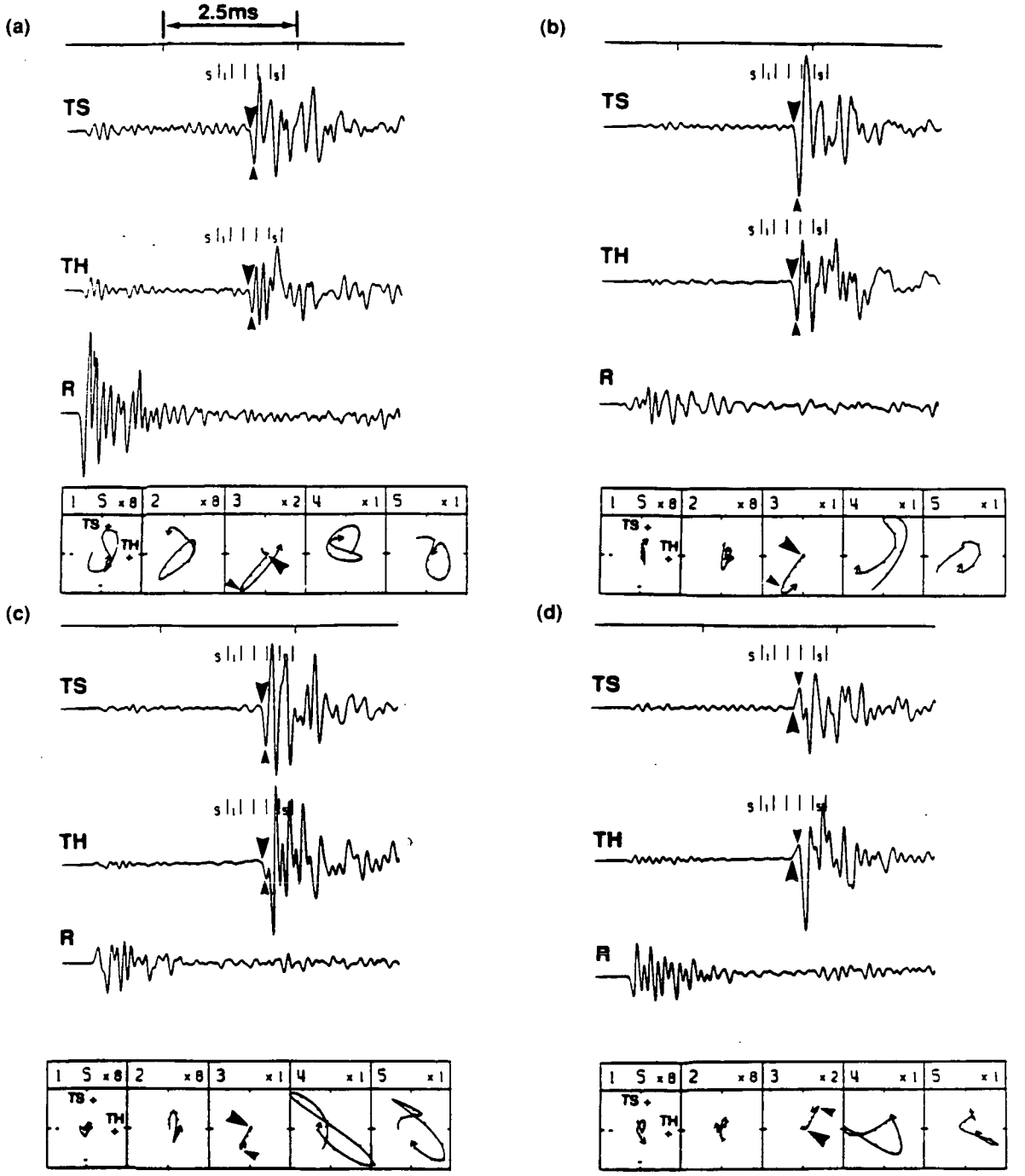

Fig. 2. Four three-component seismograms from one source location with traces rotated into the dynamic axes: from the top, transverse-sagittal (TS) direction; transverse-horizontal (TH) direction; and radial (R) direction, such that the top two channels display predominantly transverse shear-wave energy while the bottom channel displays predominantly *P*-wave energy. Time marks above the seismograms are every 2.5 μs. Polarization diagrams (PDs) of the TS-TH plane are displayed below the seismograms for the 0.25 μs time intervals marked above the shear-wave seismograms. The numbers above the PDs are the numbered time intervals and the relative multiplication factors and ticks on the PDs are every 0.02 μs. TS is represented by the vertical component of motion on the PDs and TH by the horizontal motion. Large and small arrowheads denote estimated onsets of *qS*1- and *qS*2-waves, respectively. **(a)**, **(b)**, **(c)** and **(d)** Waveforms recorded at a triaxial accelerometer for four orientations of shear-wave excitation at one source location, showing similar polarization directions and time delays on all four waveforms. The path length was 25 m and the closest approach of the raypaths to the centre of the tunnel was 16 m. Waveforms (a) to (d) correspond to source orientations 1 to 4, respectively, as presented in Figure 1b.

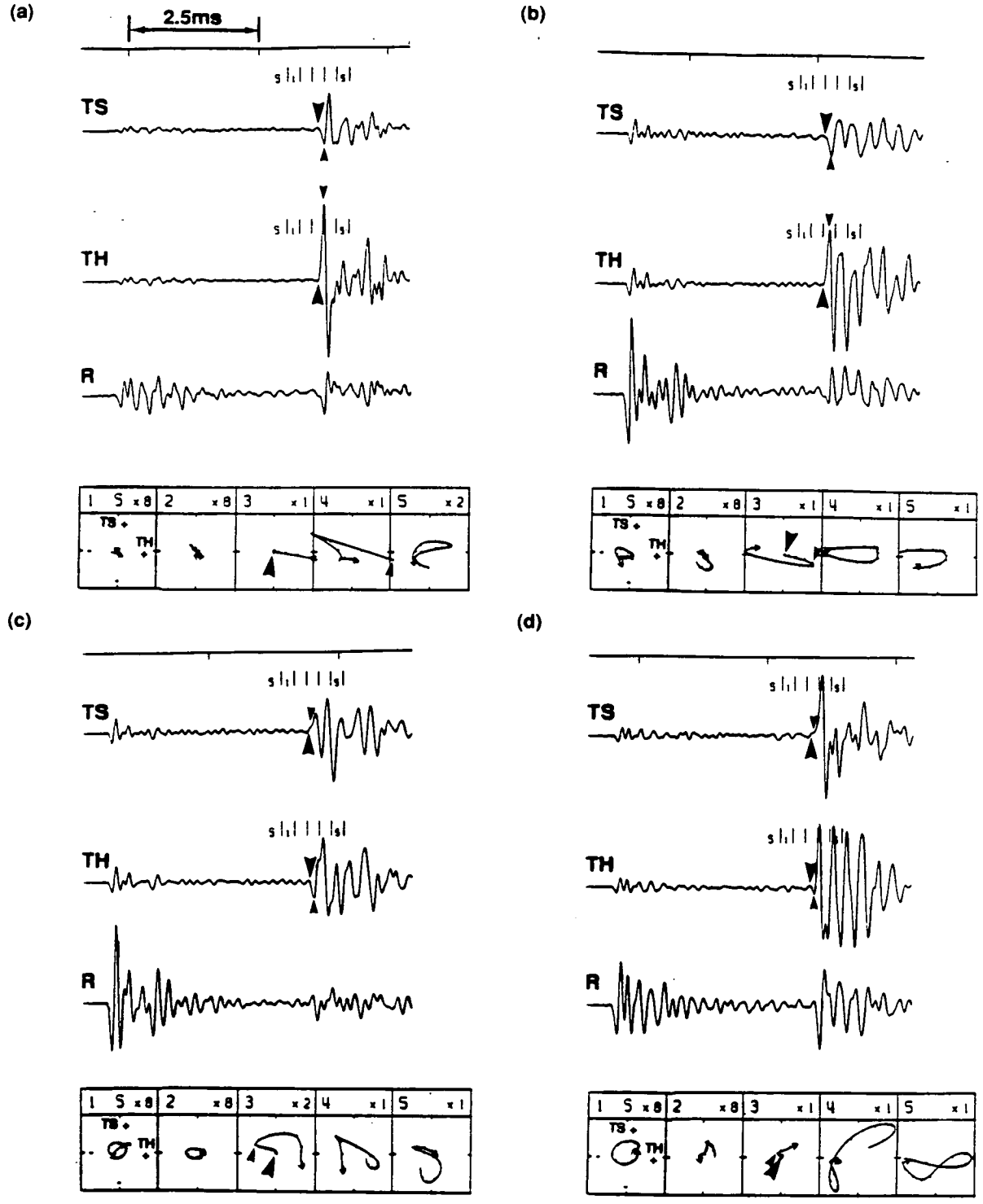

Fig. 3. Waveforms recorded at a triaxial accelerometer for four orientations of shear-wave excitation at one location where polarization directions and time delays were not similar. Notation as in Figure 3. **(a)** Minimal *qS2*-wave excitation; **(b)** and **(c)** both *qS1*- and *qS2*-waves excited; and **(d)** minimal *qS1*-wave excitation. The path length was 32 m and the closest approach of the raypaths to the centre of the tunnel was 7 m. Waveforms **(a)** to **(d)** correspond to source orientations 1 to 4, respectively, as presented in Figure 1b.

Displaying data for qualitative judgment

It is appropriate to use Plate Carée (equal-area cylindrical) projections to display polarization angles and time delays for raypaths with a wide range of azimuths and dips (Liu et al., 1989; Baptie et al., 1993). Figure 4a shows Plate Carée maps of the theoretical effects of shear-wave propagation through distributions of thin parallel horizontal microcracks, with crack density $\varepsilon = 0.01$ and an aspect ratio $\gamma = d/a = 0.001$. Crack density is defined as $\varepsilon = Na^3/v$, where N is the number of cracks of radius a and half thickness d in volume v. Polarizations displayed in the (dynamic) TS-TH plane are projected onto the V-T and R-T planes and displayed on separate projections in Figure 4a. Time delays between the split shear waves are normalized to μs/m (equivalent to ms/km) using straight-line distance.

Inversion symmetry

For an elastic wave travelling through a uniform anisotropic medium, a ray travelling in the opposite direction along a seismic ray is expected to display inversion symmetry, so that shear-wave polarizations and time delays between the split shear waves are preserved. On a Plate Carée projection, this inverted ray plots at an azimuth 180° from the original direction, with the direction of polarization in the R-T plane the same as the original ray and with the polarization in the V-T plane the mirror image about the vertical direction of the polarization of the original ray.

Inversion symmetry effectively doubles the data in an experiment with raypaths through a uniform rock mass. There are several phenomena, however, which may invalidate this symmetry. Inversion symmetry must not be invoked if there are inhomogeneities associated with excavation damage near the Mine-by tunnel, near the source or near the receiver. Application of such inversion symmetry must be used with caution as it may imprint an apparent symmetry on the data that would be incorrect and misleading if the assumption of inversion symmetry does not hold. Nevertheless, inversion symmetry can be a useful aid to recognizing anisotropic symmetry patterns in sparse data sets.

Qualitative Interpretation of Shear-wave Data

Anisotropic symmetry of the undisturbed rock mass

The initial rationale of the interpretation is that shear-wave splitting is an innate property of the intact rock mass. We seek two key results in this preliminary analysis: recognition of the underlying symmetry structure assumed to exist around the edge of the monitored volume away from the Mine-by tunnel and estimation of the extent and effects of the disturbance caused by excavation damage. Breakouts in the tunnel, and the distribution of acoustic events concentrated in the vicinity of the breakouts (Read et al., 1992a, 1992b), suggest that excavation damage is not radially symmetric about the tunnel.

Signals from straight raypaths directly obstructed by the Mine-by tunnel are not analyzed here. One triaxial accelerometer (accelerometer No. 3) was defective and did not provide any data. Quality values of 1 to 3 were assigned depending on the noise levels and impulsiveness of the shear-wave arrivals and the compatibility of the four source orientations at each source location. Quality 1 readings were highest and quality 3 readings were omitted in the analysis presented here. Unfortunately, because the first recording sequence was also used to calibrate the microseismic system, 40% of the signals created using the nylon rod were not recorded. For cases where the signal created by the nylon rod was not recorded, the signal created using the steel rod at the same location and orientation was substituted. This resulted in more quality 3 readings than would have resulted if all the signals analyzed had been created using the nylon rod. For all further recording sequences almost all signals were produced by the nylon rod.

Figure 5a shows observed polarizations and time delays along the 107 source-to-receiver raypaths with quality 1 and 2 observations. One reading is plotted from the four available from each source-to-accelerometer raypath when the readings agree and the reading with the highest quality is plotted when the four readings did not agree. Inversion symmetry has not been invoked.

Examination of Figure 5a suggests that the symmetry in the data is a reasonable fit to the model for a distribution of parallel cracks (crack density $\varepsilon = 0.02$, aspect ratio $\gamma = 0.05$) oriented 045/20. The model is shown in Figure 4b and superimposed on the observed polarizations in Figure 5b. The crack density of $\varepsilon = 0.02$ produces time delays that broadly match the average value of the observed time delays. The aspect ratio $\gamma = 0.05$, which changes the position of the abrupt change in polarizations in the equal-area plots, produces patterns of polarizations which also broadly match the observations. These crack parameters give a porosity of about 0.42% (Crampin, 1993b), nearly agreeing with porosity values of between 0.2% to 0.4% found by Wadden (1979) and Drury (1981) for the Lac du Bonnet granite.

The orientation of 045/15 for parallel cracks is approximately the anisotropy predicted by the EDA hypothesis for microcracks oriented perpendicular to the minimum stress direction. This orientation is based on the stress directions as given in Table 1 with the modification that the breakout notches indicate that σ_3 has a plunge (angle from horizontal) of about 15° rather than 11°. The model of crack planes oriented 045/20 was a slightly better fit to the data than 045/15 and the angle from the vertical of the breakout notches was greater than 20° in some places along the tunnel so the orientation of 045/20 may be perpendicular to the far-field stress. Note, however, that fitting of data to models in this preliminary analysis was by visual inspection only and an attempt at inverting the data including a goodness-of-fit evaluation is in progress. Note that near-source reflections from the walls of the outer tunnels are not considered here. The more robust analysis taking place will consider the effects of such reflections.

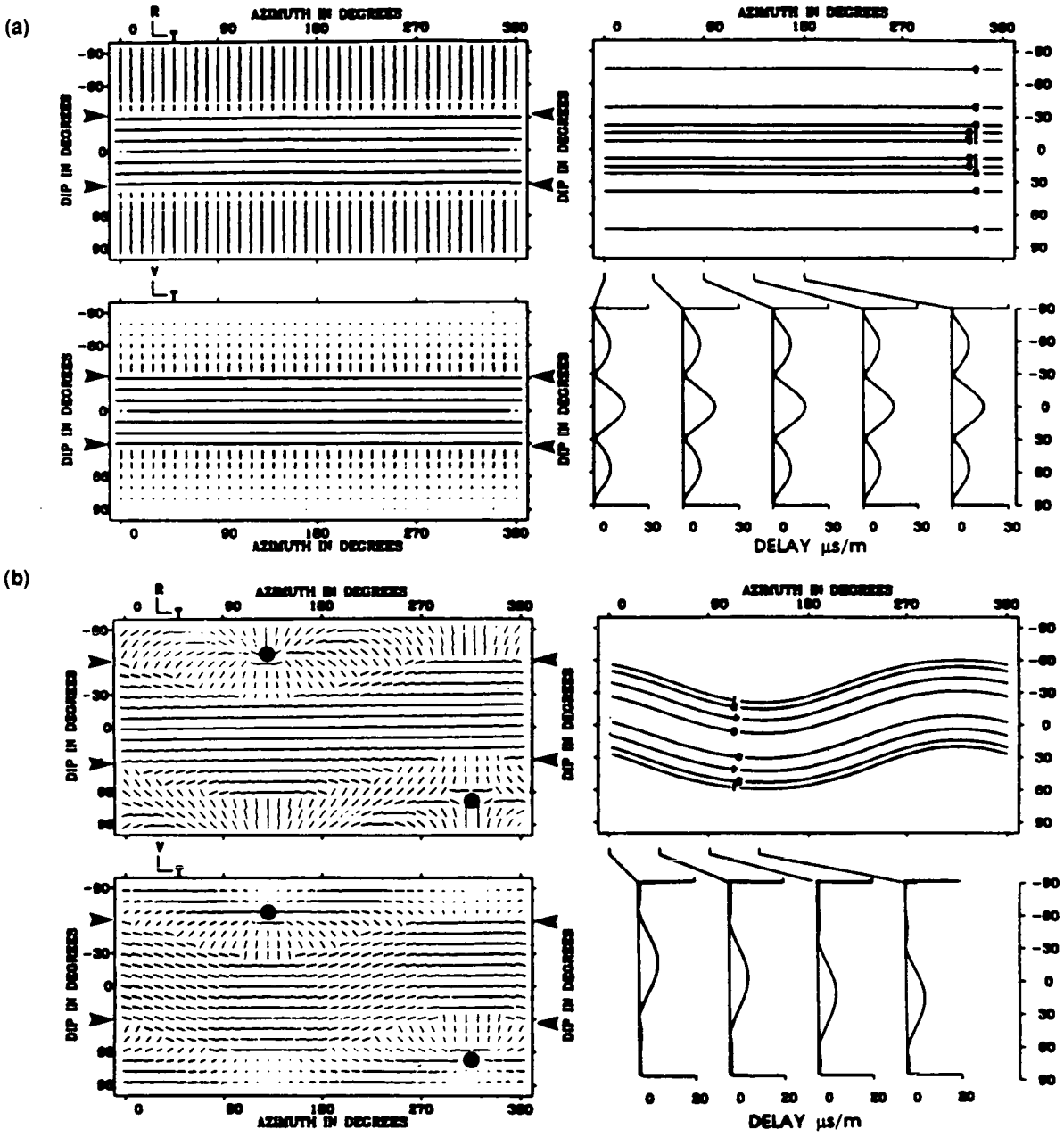

Fig. 4. The behaviour of shear-wave splitting displayed on Plate Carée (cylindrical equal-area) projections (after Baptie et al., 1993) for: **(a)** a distribution of horizontal cracks in the granite rock mass with crack density $\varepsilon = 0.01$ and aspect ratio $\gamma = 0.001$; and **(b)** a distribution of parallel cracks in the granite rock mass with crack density $\varepsilon = 0.02$ and aspect ratio $\gamma = 0.05$, striking N45°E and dipping 20° to the SE (specified as 045/20). The top left diagram of each figure displays polarizations of the leading split shear wave projected on to the horizontal radial-transverse (R-T) plane. The bottom left diagram displays the same polarizations projected on to the vertical-transverse (V-T) plane. The top right diagram displays contoured time delays between *qS*1- and *qS*2-wave arrivals normalized to 5 μs/m, and the bottom right diagrams display north-south sections of the contours at the indicated azimuths. Arrows mark the directions of line singularities and solid dots mark the directions of kiss singularities.

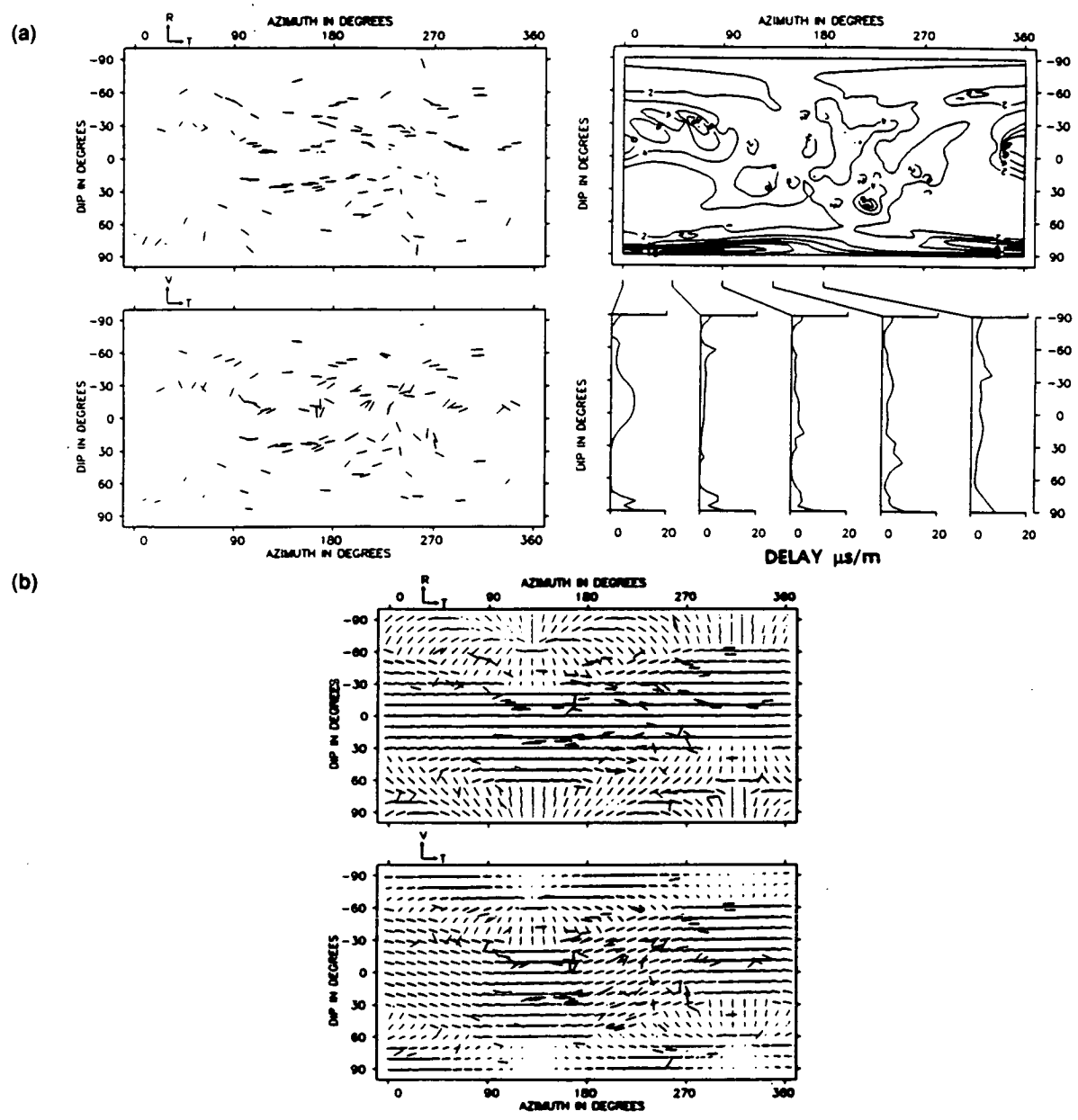

Fig. 5. **(a)** Shear-wave splitting from the first recording sequence of the shear-wave experiment displayed in Plate Carée projections for raypaths not directly obstructed by the Mine-by tunnel with the same notation as in Figure 4. Only the most consistent of the four waveforms from each station to a given accelerometer is displayed. **(b)** Polarization data from (a), above, overlain on the polarizations of the theoretical model in Figure 4b.

The contoured plot of time delays should be interpreted with caution. There are two difficulties. Time delays require identifying arrival times of both split shear waves. Both arrivals are on traces disturbed by coda. $qS1$ arrives in the coda of the *P*-wave, which in this data set is usually small and not likely to cause a problem, but $qS2$ arrives 0 to 400 μs (average 80 μs) after $qS1$ and is likely to be seriously disturbed. The other difficulty is that contouring irregular and sparse data sets which contain gaps is not an appropriate display but does allow some information about time delays to be compared with theoretical models. Improved displays for a qualitative visual comparison are being sought.

We now attempt a preliminary analysis of stress and damage anomalies along raypaths by identifying polarizations conflicting with the model in Figure 4b. We define a conflicting polarization as one which is more than 30° from

model polarizations in Figure 4b, within 20° of azimuth and dip of raypath directions, and would not fit a slight variation or small reorientation of the model. We recognize this is not an optimal technique but justify this preliminary procedure by the examination of the raypaths with conflicting polarizations.

The shear-wave parameters of 83 of the 107 observed polarizations in Figure 5 are compatible and suggest raypaths undisturbed by excavation damage. Only 24 (22%) of the 107 observed polarizations in Figure 5a conflict with the model in Figure 4b. Of these 24, at least 18 have raypaths that are probably disturbed by excavation damage. One conflicting polarization is from the shortest raypath in the experiment (7.5 m) and its polarization is possibly modified by the damage around the tunnel where the source was located. Seventeen raypaths approached the Mine-by tunnel in various ways. Two of these correspond to raypaths nearly parallel and within 12 m of the tunnel for most of their length and are likely to have traversed effects of the tunnel to a greater degree than other raypaths. Fifteen were raypaths that travelled subperpendicular to the axis of the tunnel and passed within 15 m of the excavation face of the tunnel. Stress anomalies and stress concentrations are likely to be larger in the vicinity of the excavation face than the approximately cylindrical walls of the tunnel behind the face. The 15 conflicting polarizations are likely to have been affected by the anomalous distribution of polarization directions near the face. There is also some indiciation that the effects of the face are more apparent in some directions than others, which again might be expected for excavation in a deviatoric stress field. This directional dependence is currently being studied. Only six of the conflicting polarizations are not associated with presumed excavation damage. The contribution of possible stress concentrations and/or excavation damage associated with the outer tunnels where the sources were produced has not been examined at this stage.

Figure 6a shows polarizations with the 24 conflicting data points omitted. The number of observation points has been doubled by assuming inversion symmetry along each raypath. Figure 6b shows the polarizations superimposed on the model given in Figure 4b. Figure 6c shows the time delays with the 24 conflicting data points omitted. The conflicting data points were removed in an attempt to more accurately display the time-delay pattern of the undisturbed rock mass. Symmetric points were included because inversion symmetry is valid if the data represents the undisturbed rock mass and it results in a denser data set for contouring.

Comparing the pattern of time delays of Figure 6c with the model in Figure 4b, there are some similarities in pattern with the maximum normalized time delays generally between 0 and 7 μs/m and the maximum time delays occurring between dips of 40° and -40° with similar undulations with azimuth. However, the observed time delays in Figure 6a show considerable scatter. This is expected to be because the stress-induced effects of the Mine-by tunnel and the outer tunnels are unlikely to be homogeneously distributed in space. EDA crack orientations (anisotropic symmetry), controlled by the overall stress field, are likely to be comparatively homogeneous. The EDA crack dimensions, particularly the aspect ratios, are expected to vary with the stress anomalies around the tunnels. The overall symmetry will control the shear-wave polarizations, which Figures 5b and 6b suggest has an overall consistency, but the varying crack dimensions will have the largest effect on the time-delays which display the expected scatter. It is also possible that some of the time delays do not represent the undisturbed rock mass. Very few anomalous points can greatly alter the pattern to the contoured time-delay Plate Carée projection. Note also the caution suggested in interpreting contoured time delays in the discussion of Figure 5a.

Arguments for EDA

Both data and model are preliminary, and many investigations are necessary for a more robust analysis. We suggest that there is reasonable qualitative agreement between the polarization data and the preliminary model. Many of the discrepancies between data and model are at points near line singularities where the polarization may change by up to 90° for a small change in raypath orientation, effective crack aspect ratio or crack orientation (Wild and Crampin, 1991). The line singularities in Figure 4 are where the theoretical polarizations show an abrupt change of direction (Crampin, 1989.)

We suggest that the observed polarizations are consistent with stress-aligned EDA cracks aligned perpendicular to the direction of minimum stress. Mineral fabric may also cause anisotropy. There are three very weak fabrics of similar orientation to 045/20. There exists some mineral alignment of biotite and hematite oriented 020/20 (R. Everitt, pers. notes), faint gneissic banding oriented approximately 055/25 (Read et al., 1992a, 1992b) and flow banding oriented approximately 040/30 (Read et al., 1992a, 1992b). Note, however, that the match of data and model polarizations in Figures 5b and 6b strongly indicates the presence of some form of hexagonal symmetry and very few natural fabrics possess sufficiently strong hexagonal symmetry to cause the observed shear-wave splitting. [Fluid-filled cracks are a very strong barrier to shear-wave propagation, so that comparatively weak concentrations of cracks can cause pronounced shear-wave splitting (Crampin, 1993b).] Consequently, we suggest that it is unlikely that fabric is the dominating influence aligning shear-wave polarizations, although this will need to be assessed in future investigations.

In addition, the fact that the stress anomaly around the tunnel face, where there is expected to be a considerable concentration of stress, affects rays travelling in directions subperpendicular to the tunnel's axis suggests that cracking and the stress-alignment of cracks is a dominating factor in determining the pattern of anisotropy. Polarizations corresponding to raypaths travelling within 2 m of the cylindrical opening of the tunnel, but not within 15 m of the face, are a reasonable fit to the model. This suggests that the stress-anomaly or excavation damage near the advancing face of the tunnel in some sense mends once the tunnel has advanced further, so that it causes less disturbance to the shear waves.

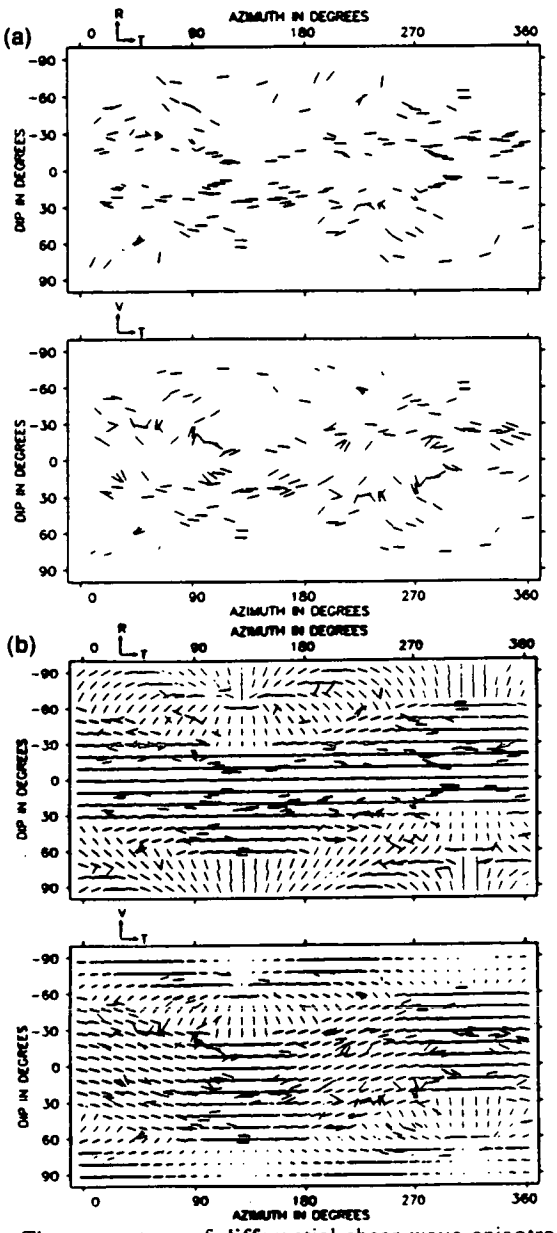

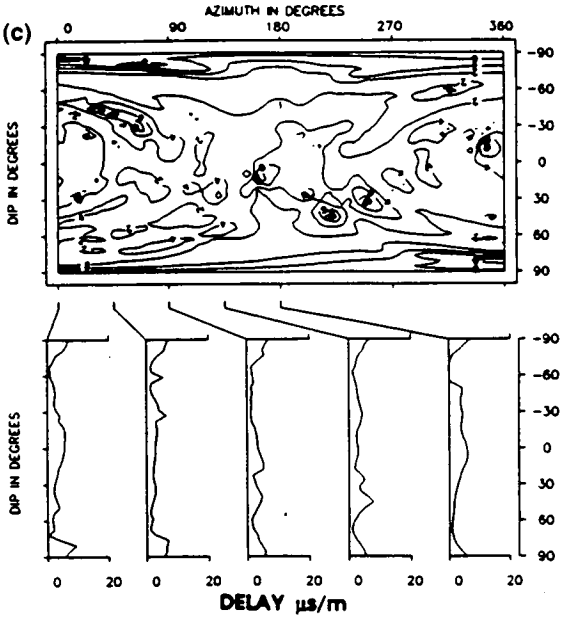

Fig. 6. **(a)** Polarizations measured from shear-wave splitting from the first recording sequence displayed in Plate Carée projections for raypaths not directly obstructed by the Mine-by tunnel, with data conflicting with the model (as specified in the text) omitted but with inversion symmetry raypaths added. **(b)** Polarization data from (a), above, overlain on the Plate Carée projections of polarizations in Figure 4b. **(c)** Contoured Plate Carée projection of time delays for the same data set as described in Figure 6a.

The percentage of differential shear-wave anisotropy assuming straight-line raypaths ranged from 0% to 4.6%, with an average of 1.2%. We have not recognized, in this preliminary analysis, any clear correlation of percentage anisotropy with the closest approach of the raypath to the tunnel. The anisotropy along a particular raypath will vary with direction. For raypaths where the polarization did not conflict with the model, the maximum anisotropy was high (4.6%), as seen in the contour plot in Figure 6a. A range of anisotropy of 1% to 5% is typical of shear-wave splitting observed in a wide range of igneous, metamorphic and sedimentary rocks in the crust (Crampin and Lovell, 1991; Crampin, 1993a).

Discussion

This paper presents a preliminary report of the first study of shear-wave splitting along raypaths covering a comprehensive range of azimuths and angles of incidence in an initially homogeneous rock mass. There are many avenues of investigation to pursue before final results can be established, but the following six conclusions are unlikely to change and are the justification for publication so soon after the completion of the experiment.

1. Shear-wave splitting is clearly visible with 4.2 kHz signals (80-cm wavelengths) for the 107 azimuths and angles of incidence through the intact homogenous granite rock mass.
2. There is qualitative agreement between approximately 80% of the raypaths and the polarizations of the split shear waves and three-dimensional patterns of polarizations expected for distributions of thin parallel fluid-filled microcracks (EDA cracks) aligned perpendicular to the minimum stress direction (strike N45°E and dip 20°SW from the horizontal). The degree of differential shear-wave anisotropy of between 0% and 4.6% is similar to that observed in a wide range of geological formations elsewhere (Crampin, 1993a).
3. About 20% of the raypaths displayed polarizations that did not agree with the model, and of these, three quarters can be attributed to effects of

excavation damage around the tunnel, particularly around the face of the tunnel. The remaining 5% have not yet been interpreted.

4. The anisotropy observed may be due to a combination of EDA and fabric anisotropy within the rock mass, although the contribution of fabric anisotropy is likely to be small.
5. The polarizations that did not agree with the model suggest that stress anomalies and excavation damage are more extensive around the face of the advancing tunnel than around the cylindrical opening of the tunnel.
6. The sensitivity of shear waves and shear-wave splitting to stress-induced changes to the in-situ rock mass has been postulated and suggests there may be practical industrial and commercial applications including the monitoring of excavation damage and thermally induced cracking within radioactive waste repositories (Crampin and Lovell, 1991).

These results are preliminary and many further investigations are indicated. The high quality of source signals, recording and known source-to-receiver geometry suggests that this experiment has the potential to answer many unresolved questions about the behaviour of EDA cracks and shear-wave splitting in crustal rocks, particularly the effects of stress on the internal structure of hard brittle rock.

Present Work

A more robust analysis of this shear-wave experiment is underway. Factors not considered in this study, such as the effects of the outer tunnels, the angle of the raypath to the source tunnel and examination of the quality 3 waveforms, will be studied. An attempt to invert the data that will also give a goodness-of-fit evaluation is underway. Most importantly, data from all 16 recording sequences will be examined, which should result in a much more detailed understanding of the effects of stress upon the rock mass and the effects of the excavation.

Revision of the Extent of Excavation Damage

The extent of the excavation damage to the Mine-by tunnel suggested by the preliminary interpretation in the main text must be revised. We have now examined repeated source-to-accelerometer raypaths as the tunnel advances and have developed a program to specify with greater precision the distance and inclination of each source-to-accelerometer raypath from the Mine-by tunnel using coordinates of the surveyed tunnel.

Signals along identical raypaths, which pass near to the tunnel and are in some cases cut by the tunnel as it advances, show very little change in the waveforms of the shear waves. Thus, anomalies previously interpreted as being the result of excavation damage around the face of the tunnel are due to some other cause.

There are several possible reasons for the lack of change of shear waveforms and shear-wave splitting around the advancing tunnel:

1. The effects of excavation damage on shear waves may be too small to be observed by the comparatively unsophisticated techniques used up to now. Reasonable estimates of excavation damage, say an increase of 10% velocity anisotropy over a distance of three metres, ought to cause recognizable changes to a 4.2 kHz shear wave, if the cracking due to excavation damage displays consistent alignments. This could lead to a change of nearly half a cycle in the shear-wave signal (5 sample points at the 50 kHz sampling rate). The consistency of the shear waves suggests that excavation damage causes changes of less than a 1 sample (2% change in velocity anisotropy) but this needs to be investigated further. If the alignments are not consistent, as seems probable, the effects would be smaller.
2. Body waves, including split shear waves, travel along minimum-time paths. Waves that would be slowed through a damaged volume will tend to take wider raypaths through faster undamaged rock to compensate for the slower speeds. If the excavation damage is small in volume, it is possible that such compensation is sufficient to hide any change caused by the damage, particularly as the path of the slower split shear wave is likely to compensate so as to keep the change in the time delay between the split shear waves small.
3. Combinations of the effects of items 1 and 2, above, are also possible and would be difficult to resolve.

More sophisticated techniques to identify the effects of excavation damage are now being developed. Note that, with the exception of the extent of the excavation damage, the analysis and conclusions in the remainder of the paper are unchanged.

References

Baptie, B., Crampin, S. and Liu, E., 1993, Displaying shear-wave splitting in cross-hole surveys for materials with combinations of EDA and PTL anisotropies: Can. J. Expl. Geophys. **29**, 227-235.

Bell, J.S. and Gough, D.I., 1979, Northeast-southwest compressive stress in Alberta: evidence from oil wells: Earth and Planet. Sci. Lett. **45**, 475-482.

Chernis, P.J. and Robertson, P.B., 1987, Natural and stress-relief microcracks in the Lac Du Bonnet granite, *in* Katsube, T.J. and Hume, J.P., Eds., Geotechnical studies at Whiteshell Research Area, Canada Centre for Min. Eng. Tech. Min. Res. Lab. Div., Report MRL 87-52 (INT).

Crampin, S., 1981, A review of wave motion in anisotropic and cracked elastic-media: Wave Motion **3**, 343-391.

_____, 1989, Suggestions for a consistent terminology for seismic anisotropy: Geophys. Prosp. **37**, 753-770.

_____, 1991, Effects of point singularities on shear-wave propagation in sedimentary basins: Geophys. J. Internat. **107**, 531-543.

_____, 1993a, Arguments for EDA: Can. J. Expl. Geophys. **29**, 18-30.

_____, 1993b, A review of the effects of crack geometry on wave propagation through aligned cracks: Can. J. Expl. Geophys. **29**, 3-17.

_____ and Lovell, J.H., 1991, A decade of shear-wave splitting in the Earth's crust: what does it mean? what use can we make of it? and what should we do next?: Geophys. J. Internat. **107**, 387-407.

Drury, M.J., 1981, Thermal conductivity, density, porosity, and mineralogy of core samples from Chalk River, Pinawa, and Atikokan: Energy, Mines and Resources (Canada), Earth Physics Branch, Internal Rep. 81-6, 13p.

Feignier, B. and Young, R.P., 1992, Moment tensor inversion of induced microseismic events: evidence of non-shear failures in the -4<M<-2 moment magnitude range: Geophys. Res. Lett. **19**, 1503-1506.

Herget, G., 1987, Stresses in rock: Balkema, Rotterdam, 179p.

Liu, E. and Crampin, S., 1990, Effects of the internal shear-wave window: comparison with anisotropy induced splitting: J. Geophys. Res. **95**, 11,275-11,281.

_____, _____ and Booth, D.C., 1989, Shear-wave splitting in cross-hole surveys: modelling: Geophysics **54**, 57-65.

_____, _____ and Queen, J.H., 1991, Fracture detection using crosshole surveys and reverse vertical seismic profiles at the Conoco Borehole Test Facility, Oklahoma: Geophys. J. Internat. **107**, 449-463.

_____, _____ and Roth, B., 1992, Modelling channel waves with synthetic seismograms in an anisotropic in-seam seismic survey: Geophys. Prosp. **40**, 513-540.

Martin, C.D., 1989, Characterizing in situ stress domains at AECL's Underground Research Laboratory: Proc. 42nd Canadian Geotechnical Conf., Winnipeg, 61-74.

Read, R.S. and Martin, C.D., 1991, Mine-by Experiment final design report: Atomic Energy of Canada Ltd., Report AECL-10430.

_____, Martino, J.B. and Mitchell, J.H., 1992a, Mine-by Experiment technical progress report 7: Atomic Energy of Canada Ltd., Report L-EXP-022-M056.

_____, _____ and _____, 1992b, Mine-by Experiment technical progress reports 1, 2, 3, 4, 5, and 6: Atomic Energy of Canada Ltd., Reports L-EXP-022-M050 to L-EXP-022-M055.

Sprunt, E.S. and Brace, W.F., 1974, Direct observation of microcavities in crystalline rocks: Internat. J. Rock Mech. Min. Sci. & Geomech., **27**, 139-150 (Abstr.).

Talebi, S. and Young, R.P., 1989, In situ measurements of *P* and *S* wave velocities at the Underground Research Laboratory: Atomic Energy of Canada Ltd., Report RP004AECL.

_____ and _____, 1990, Design of a microseismic system for the URL Mine-by Experiment: Atomic Energy of Canada Ltd., Report RP006AECL.

Wadden, M.M., 1979, Porosity measurements by the immersion technique for WN-1, -2, and CR-6, -7 samples: Geol. Surv. Can., Internal Rep. TR-7879-D6, 12p.

Wild, P. and Crampin, S., 1991, The range of effects of azimuthal isotropy and EDA anisotropy in sedimentary basins: Geophys. J. Internat. **107**, 513-529.

Yardley, G.S. and Crampin, S., 1991, Extensive-dilatancy anisotropy: relative information in VSPs and reflection surveys: Geophys. Prosp. **39**, 337-355.